

**Characterizing the Hercules Thick Disk Cloud**

by

Midshipman 1/c Aaron P. Haviland  
United States Naval Academy  
Annapolis, Maryland

---

(signature)

Certification of Adviser(s) Approval

Assistant Professor Jeffrey Larsen  
Physics Department

---

(signature)

---

(date)

Professor Debora Katz  
Physics Department

---

(signature)

---

(date)

Acceptance for the Trident Scholar Committee

Professor Carl E. Wick  
Associate Director of Midshipman Research

---

(signature)

---

(date)

Report Documentation Page			Form Approved OMB No. 0704-0188		
Public reporting burden for the collection of information is estimated to average 1 hour per response, including the time for reviewing instructions, searching existing data sources, gathering and maintaining the data needed, and completing and reviewing the collection of information. Send comments regarding this burden estimate or any other aspect of this collection of information, including suggestions for reducing this burden, to Washington Headquarters Services, Directorate for Information Operations and Reports, 1215 Jefferson Davis Highway, Suite 1204, Arlington VA 22202-4302. Respondents should be aware that notwithstanding any other provision of law, no person shall be subject to a penalty for failing to comply with a collection of information if it does not display a currently valid OMB control number.					
1. REPORT DATE <b>2009</b>	2. REPORT TYPE		3. DATES COVERED <b>00-00-2009 to 00-00-2009</b>		
4. TITLE AND SUBTITLE <b>Characterizing the Hercules Thick Disk Cloud</b>			5a. CONTRACT NUMBER		
			5b. GRANT NUMBER		
			5c. PROGRAM ELEMENT NUMBER		
6. AUTHOR(S)			5d. PROJECT NUMBER		
			5e. TASK NUMBER		
			5f. WORK UNIT NUMBER		
7. PERFORMING ORGANIZATION NAME(S) AND ADDRESS(ES) <b>United States Naval Academy,Annapolis,MD</b>			8. PERFORMING ORGANIZATION REPORT NUMBER		
9. SPONSORING/MONITORING AGENCY NAME(S) AND ADDRESS(ES)			10. SPONSOR/MONITOR'S ACRONYM(S)		
			11. SPONSOR/MONITOR'S REPORT NUMBER(S)		
12. DISTRIBUTION/AVAILABILITY STATEMENT <b>Approved for public release; distribution unlimited</b>					
13. SUPPLEMENTARY NOTES					
14. ABSTRACT					
15. SUBJECT TERMS					
16. SECURITY CLASSIFICATION OF:			17. LIMITATION OF ABSTRACT <b>Same as Report (SAR)</b>	18. NUMBER OF PAGES <b>195</b>	19a. NAME OF RESPONSIBLE PERSON
a. REPORT <b>unclassified</b>	b. ABSTRACT <b>unclassified</b>	c. THIS PAGE <b>unclassified</b>			

## Abstract

Astronomical observations show that there is an excess of faint blue stars located towards and to the left of the Constellation Sagittarius near the Galactic center, as we see it from Annapolis, indicating an asymmetry in the thick disk of the Milky Way. This region, originally discovered by Larsen and Humphreys in 1996, has been named the Hercules Thick Disk Cloud and originally had three origin theories: a galactic merger, rotation of the stellar bar, and triaxiality of the Thick Disk. This project examined the types and motions of the excess stars in order to explain their existence using the method of star counts.

We completed and analyzed a survey of Quadrants 1 and 4 of the Galaxy (those in the direction of the galactic center). Using image reduction procedures, we converted the observations into stellar catalogs organized by magnitude and color, then used data mining techniques to identify stars that appear to be part of the excess. Color and magnitude indicated the distance and type of the excess stars through the method of photometric parallax. Spectral observations, taken by collaborators at the University of Minnesota, were to be used to determine the motion of the excess stars due to the gravitational effects from the Galaxy. We then incorporated the data into an updated model of the Galaxy and applied an optimization technique known as a 'genetic algorithm' to find the best fit parameters of the galactic model.

This model helped us to better study the galactic asymmetry and the ranges of color, magnitude, and spatial motion of these excess stars. We showed that the excess is located entirely above the galactic plane, which suggests that the Hercules Thick Disk Cloud is the remnant of a galactic merger.

Key Words: Astronomy, Hercules Thick Disk Cloud, Galaxy, Star Count, Color, Photometric Parallax

## Contents

<b>Chapter 1:</b>	<b>Background</b>	<b>6</b>
<b>Section 1:</b>	The Search for Galactic Asymmetry: Developing a Star Count Model of the Galaxy	6
<b>Section 2:</b>	Discovery of the Milky Way and a Historic Model	7
<b>Section 3:</b>	Geography of the Milky Way (as it is Currently Understood)	10
<b>Section 4:</b>	Astronomical Observables	13
<b>Section 5:</b>	Modern Star Counts: Galactic Models	20
<b>Section 6:</b>	Discovery of the Galactic Asymmetry	31
<b>Chapter 2:</b>	<b>Observations</b>	<b>37</b>
<b>Section 1:</b>	Data Available for this Project	37
<b>Section 2:</b>	Observations from the CTIO 1.0-m telescope in La Serena, Chile	40
<b>Chapter 3:</b>	<b>Data Processing</b>	<b>43</b>
<b>Section 1:</b>	Image Reduction	43
<b>Section 2:</b>	Photometric Reduction	51
<b>Section 3:</b>	Star-Galaxy Discrimination	58
<b>Section 4:</b>	Catalog Creation and Star Counts	66
<b>Chapter 4:</b>	<b>Data Analysis</b>	<b>71</b>
<b>Section 1:</b>	Analysis of Count Ratios	71
<b>Section 2:</b>	Photometric Parallax Plot	78
<b>Section 3:</b>	Running the Genetic Algorithm	84
<b>Section 4:</b>	Spectral Classification/Proper Motions	96



<b>Section 5: Other Data Mining Techniques</b>	100
<b>Chapter 5: Conclusions and Directions for Future Work</b>	110
<b>Appendix A Genetic Algorithm</b>	114
<b>Appendix B. Presentation of Star Count Data</b>	118
<b>Appendix C. PerlScript Coding for Data Analysis</b>	172
<b>Index of Tables and Figures</b>	186
<b>Bibliography</b>	192

## Acknowledgements

I first began conducting research with Assistant Professor Jeffrey Larsen in the fall semester of my second-class year, when I was one of a contingent of midshipmen working on his Near Earth Asteroid project. I am very honored that he offered me the chance to continue working on the project that was his doctoral thesis. Professor Larsen has been one of my great mentors here at the Naval Academy and I will always be indebted to his hard work and confidence.

Professor Debora Katz provided the voice of reason when we made our big plans. I thank her for delving into this project and providing me with some of the most helpful critiques and suggestions that I received all year. Most especially, I thank her for her endless supply of patience and support, including sitting through several nerdy discussions on the latest in science fiction.

Thank you also to the project collaborators, Roberta Humphreys and Juan Cabanella, who blazed the trails that I have followed. This project could not have existed without all their hard work.

My thanks go out to the U.S. Naval Academy Trident Scholar Committee, who have allowed me to pursue this research over the last year and offered very helpful critiques and suggestions. I am also very grateful to the Office of Naval Research and the National Science Foundation for providing the funding to travel to the Cerro Tololo Inter-American Telescope in La Serena, Chile.

I would especially like to thank my parents, who have provided more help to me over the years than a son could ever ask for. Whether it was driving up to see me on a

lonely Saturday during plebe year or giving me with the right words of encouragement at just the right time, I know that I could not have made it through four years at Annapolis without them. And as for my sister and brother, I could not ask for a better pair of friends and traveling companions.

Finally, this project is dedicated to the memory of my cousin, Laurel Blair Salton Clark. A Navy doctor, an astronaut, and a member of the space shuttle Columbia's last voyage, Laurel traveled to the stars that I have only been able to look at through a telescope. Wherever she is, I hope that she can be proud of this project.

*Silently, one by one, in the infinite meadows of heaven, Blossomed the lovely stars, the forget-me-nots of heaven.*

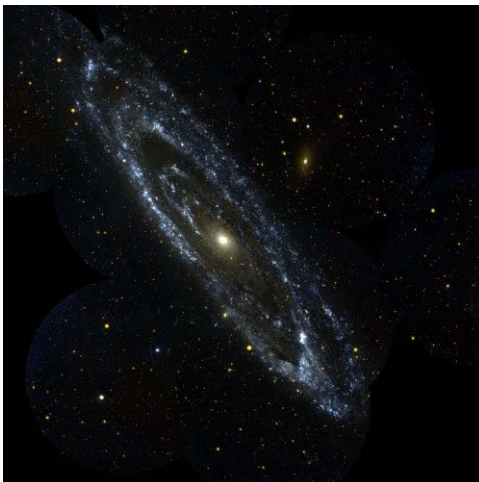
- Henry Wadsworth Longfellow

## Chapter 1: Background

### 1.1 The Search for Galactic Asymmetry:

#### Developing a Star Count Model of the Galaxy

In 1996, researchers at the University of Minnesota discovered an excess population of stars in the Thick Disk of our Galaxy. Based on our current understanding of galactic formation, the Galaxy should be roughly symmetrical. Therefore, this project addresses the question of how that excess stellar population was most likely formed along with the asymmetric nature of the thick disk and inner halo of the Milky Way. We use the method of star counts to create catalogs of stars organized by position, brightness, and color, and then use them to update and analyze a model of the galaxy. We then used a genetic algorithm driver to optimize the counts with the goal of gaining an improved understanding of the inner halo and thick disk. These results, when analyzed, have valuable implications for the formation and early history of our Galaxy. In order to describe this process, we first summarize our current understanding of the structure of a



barred spiral galaxy (Figure 1), of which the Milky Way Galaxy is one, as well as how astronomers have come to understand its shape despite the limitation of living inside of it. We then describe the method of star counts, the data used, and the history of the excess.

**Figure 1: NASA Image of the barred spiral Andromeda Galaxy, with a structure similar to the Milky Way**

## 1.2 Discovery of the Milky Way and a Historic Model

Understanding the structure of our galaxy is a classic example of trying to see the forest from among the trees. An observer in another galaxy would clearly be able to see that the Milky Way is a disk-shaped spiral galaxy, just as Earth-bound astronomers can see that many other galaxies have a clearly spiral shape. However, living within the Milky Way puts astronomers at a disadvantage in terms of vantage point.<sup>1</sup> If the Milky Way's disk were a Frisbee, we would be living at about two-thirds of the distance from the center to the outer edge, able to stare at the Frisbee material around us but having to use observations to determine the structure on which we live.<sup>2</sup> In fact, the only way that we could determine our position would be by examining the amount of "Frisbee-material" in the space surrounding us. As we looked towards the center of the disk, we would see more Frisbee, whereas we would see less Frisbee if we looked towards the outer edge. If we looked "up" and "down" perpendicular to the disk plane, we would see almost no Frisbee. Similarly, if we saw more stellar material in one direction in the sky than in the opposite direction, then we would realize that we live on the edge of a stellar distribution. This method is the basic idea behind the star count method developed by the astronomer William Herschel in the 18<sup>th</sup> century.

William Herschel (1738-1832) first became famous in 1781 when he discovered the planet Uranus and was subsequently appointed as King George III's personal astronomer. With the vast wealth of the English king, Herschel was able to build large

---

<sup>1</sup> Henbest, Nigel and Heather Couper, *The Guide to the Galaxy*, Cambridge: Cambridge University Press, 1994, pp 57.

<sup>2</sup> *The Dorling Kindersley Science Encyclopedia*, London: Dorling Kindersley, 1997.

20-foot telescopes and even a 40-foot-long telescopic tube.<sup>3</sup> To achieve his lifelong goal of making an accurate map of the stars, Herschel engaged in a process called “star-gauging,” whereby he observed 700 separate regions of the sky and counted the number of stars in each.<sup>4</sup> Unfortunately, Herschel’s procedure and analysis of the data were limited to the astronomical knowledge of the time. A method for measuring the distance between stars was not developed until 1838,<sup>5</sup> so Herschel made the assumption that all stars have the same absolute magnitude and that their apparent brightness falls off according to the inverse square law.<sup>6</sup> He took the distance between the Earth and the star Sirius to be the standard unit of measurement, dubbed a “siriometer.”<sup>7</sup> Therefore, if a star is one-fourth as bright as Sirius, then it is two siriometers away from the Earth. Herschel also assumed that the density of stars is the same in all areas of space, that there are no obstructing objects or materials between our planet and the stars, and that we should be able to see to the edge of our galaxy.<sup>8</sup> Following these assumptions, Herschel used a process of star counting similar to our “Frisbee observation” method. When he pointed his telescope toward the center of the Galaxy along the disk, he observed more stars than when he pointed it toward the galaxy’s edge.

The result of Herschel’s lengthy analysis was the “grindstone model” shown in Figure 2, in which the galaxy is a disk-like structure that is 1000 siriometers (9000 light-years) across and 100 siriometers (900 light-years) deep. The sun is close to but not exactly at the center of the galaxy. However, Herschel was troubled by the long, jagged,

---

<sup>3</sup> Henbest, *Guide*, pp 9.

<sup>4</sup> Mihalas, Dimitri and James Binney, *Galactic Astronomy: Structure and Kinematics*, 2<sup>nd</sup> ed., New York: W. H. Freeman and Company, 1981, pp 4.

<sup>5</sup> Henbest, *Guide*, pp 10.

<sup>6</sup> Mihalas, *Galactic*, pp 209.

<sup>7</sup> Henbest, *Guide*, pp 10.

<sup>8</sup> Tucker, Andrew R., MIDN, USN, “Exploration of Asymmetric Galactic Stellar Populations Using Star Counts, Galactic Models, and Genetic Algorithms,” United States Naval Academy, Fall 2007, pp 1.

empty tunnels protruding from the edges of his model. As he continued his studies of astronomy later in his life, he focused on binary star systems and concluded that not all stars have the same absolute magnitude, thus refuting one of the underlying assumptions of his model. Herschel eventually disowned the grindstone model and died believing that he had failed to produce an accurate stellar map.<sup>9</sup> We now know that the largest problem with the model was not accounting for the scattering of light as it travels across space, also known as interstellar extinction.

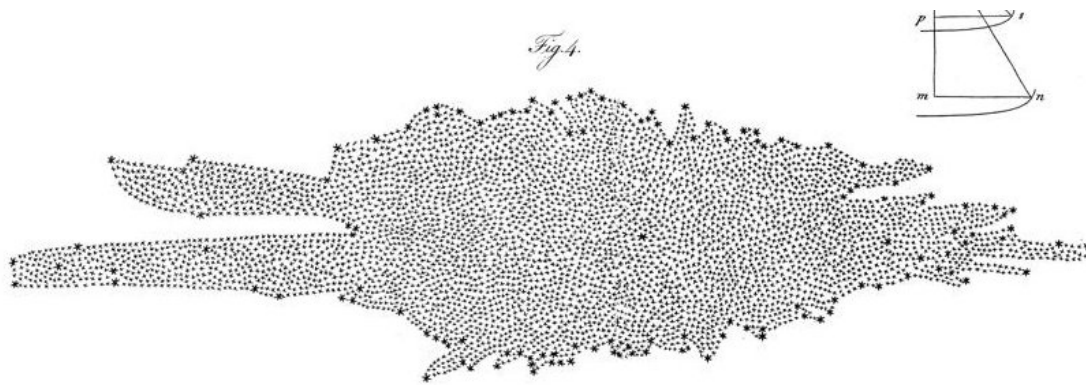


**Figure 2: Herschel's "grindstone model" of the disk of the Milky Way**

---

<sup>9</sup> Henbest, *Guide*, pp 11.

### 1.3 Geography of the Milky Way (as it is currently understood)

As we currently understand it, our galaxy is a barred spiral disk that is 100,000 light-years in diameter, 1,000 light-years thick, and contains approximately 100 billion stars. Unlike interstellar gas, the stellar main disk appears to be relatively continuous, but detailed studies indicate that it is in fact a series of overlapping populations, of which two are dominant.<sup>10</sup> The *thin disk* is only 500 light-years thick and contains younger stars whose orbits are nearly circular. The stars closest to the galactic core have the fastest orbital speeds. The *thick disk*, on the other hand, surrounds the thin disk and is 4,000 light-years thick. Its stars are older, have fewer massive elements, and their motions are mostly circular but not as regular as those of the thin disk. The thick disk was discovered statistically by Gilmore and Reid at the Royal Observatory at Edinburgh in 1983.<sup>11</sup> Since the thin disk has a higher concentration of dust and nebulous gas than the area above or below it, star formation occurs almost exclusively in the thin disk, which explains why the stars in the thin disk are younger than in the thick disk. However, astronomers are currently not certain if the thick disk was formed or if the Milky Way captured and absorbed many smaller, older galaxies in an act of galactic cannibalism and spread the stars in a disk with its gravity over time.<sup>12</sup>

Our solar system is located between 26,000 and 27,000 light-years from the Galactic center, an area that is not too chaotic in its motions and not too diffuse in its concentration of materials. The Sun makes one full revolution around the center every

---

<sup>10</sup> Than, Ker, "The New Tourists Guide to the Milky Way," Space.com, 27 Feb. 2006, <[http://www.space.com/scienceastronomy/060227\\_mm\\_milky\\_way\\_tour.html](http://www.space.com/scienceastronomy/060227_mm_milky_way_tour.html)>, Accessed 18 Dec. 2007.

<sup>11</sup> Gilmore, G., and N. Reid, "New light on faint stars. III – Galactic structure towards the South Pole and the Galactic thick disc," *Royal Astronomical Society, Monthly Notices*, vol. 202, Mar. 1983, p. 1025-1047.

<sup>12</sup> Quinn, P. J., and Jeremy Goodman, "Sinking satellites of spiral systems," *Astrophysical Journal*, Part 1, vol. 309, Oct. 15, 1986, p. 472-495.



225 million years. Closer to the center of the galaxy, the density of stars is higher, the stars themselves are younger, and they have shorter periods of rotation. The rate of rotation of the core suggests that there is a supermassive black hole at the galaxy's center which astronomers have dubbed Sagittarius A\*. A 27,000 light-year-long bar of 30 million stars rotates around the core and apparently plays a role in feeding the black hole.<sup>13</sup>

Surrounding the disk of the spiral galaxy is a halo of older stars formed earlier through collapse of a gas cloud and globular clusters of stars that rotate around the disk in elliptical orbits.<sup>14</sup> The inner halo is 100,000 light-years in diameter, 1,000 light-years thick, and contains 170 star clusters and a dozen small galaxies, including the Large and Small Magellanic Clouds.<sup>15</sup> After observing an unexplained source of gravity that holds the star clusters together and maintains a relatively uniform velocity of the galactic disk, astronomers have also concluded that, in addition to the stars, there must be a substantial amount of invisible dark matter. This dark matter is arranged in a spherical component called the corona. Figure 3 shows a rudimentary model of the Galaxy as astronomers currently understand it.

---

<sup>13</sup> Than, "New Tourists."

<sup>14</sup> Hester, Jeff, George Blumenthal, Bradford Smith, David Burstein, Ronald Greeley, and Howard G. Voss. *21<sup>st</sup> Century Astronomy*, Second Edition. New York: W. W. Norton & Company, 2007, pp 558.

<sup>15</sup> Oort, J. H., "Some Problems Concerning the Structure and Dynamics of the Galactic System and the Elliptical Nebulae NGC 3115 and 4494," *Astrophysical Journal*, vol. 191, p. 273.

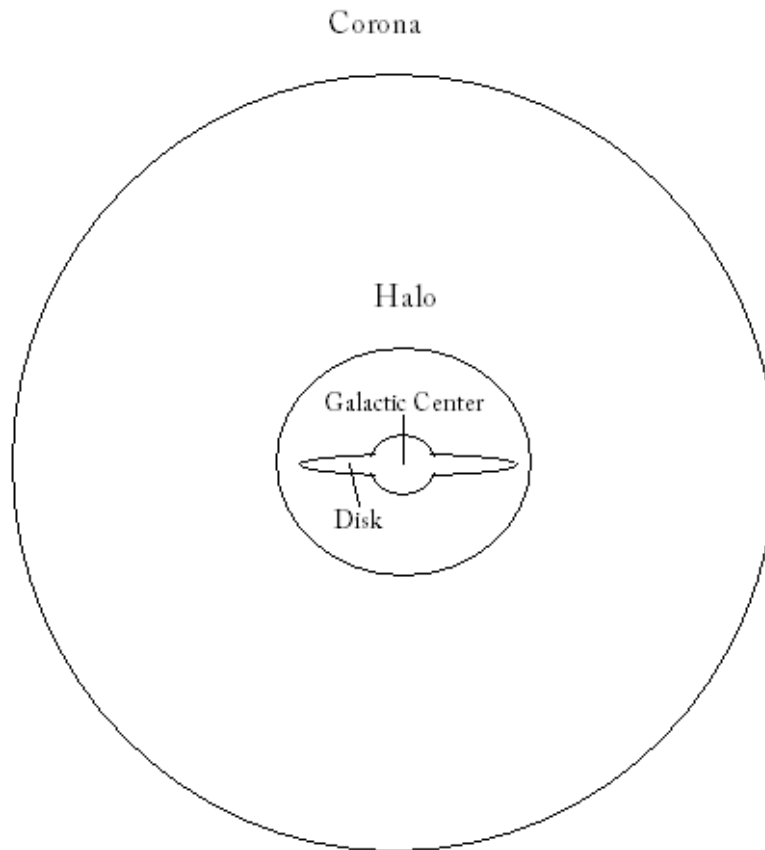


**Figure 3: Edge-on model of the Milky Way galaxy. “Halo” refers to the stellar halo and “corona” to the extended dark matter halo. The scaling term “kpc” stands for kiloparsecs.**

## 1.4 Astronomical Observables

### 1. Photometric Parallax

Examining large numbers of stars requires a series of properties (or observables) that we can measure. The power, or energy per unit time, that a star emits is its luminosity and the more luminous a star is, the brighter it appears at a set distance. To allow direct comparison of brightness, the absolute magnitude is defined as the brightness of a star which would be perceived by an observer located 10 parsecs away from the star. Since light is emitted in all directions, the intensity falls off with the square of the distance from the star (the inverse square law). Therefore, a star that has the same absolute magnitude as another star but is twice the distance away will have one-fourth the apparent brightness. Apparent magnitude is the brightness of a star as we see and measure it in the sky. Magnitudes themselves are based on a negative logarithmic scale similar to the magnitude scale developed by Hipparchos in Ancient Greece where observed stars were sorted by brightness. A 1<sup>st</sup> magnitude star has the brightness emitted by a  $2 \times 10^{28}$  W star observed from a distance of 10 parsecs ( $1 \text{ pc} = 3.26 \text{ ly} = 3.09 \times 10^{16} \text{ m}$ ) and the scale moves down by logarithmic factors of 2.5. A 1<sup>st</sup> magnitude star is 2.5 times brighter than a 2<sup>nd</sup> magnitude and a 2<sup>nd</sup> magnitude star is 2.5 times as bright as a 3<sup>rd</sup> magnitude. So, somewhat counter-intuitively, a fainter star has a higher magnitude.<sup>16</sup> The equation relating absolute magnitude,  $M$ , to apparent magnitude,  $m$ , through distance,  $d$ , is:

$$m - M = 5 \log\left(\frac{d}{D}\right) = 5 \log(d) - 5 \quad (\text{Equation 1})$$

The distance  $d$  is in parsecs while the standard distance  $D$  is equal to 10 parsecs.

---

<sup>16</sup> Mihalas, *Galactic*, pp 209.

Stars also have inherent color, determined by their temperature. Since they emit as near-perfect blackbodies, the wavelength (and therefore color) in which the greatest amount of light is emitted is given by Wien's Law,  $\lambda_{peak} = \frac{2900}{T} \mu\text{m}\cdot\text{K}$ . The peak wavelength ( $\lambda_{peak}$ ) is inversely proportional to the absolute temperature ( $T$ ). A higher temperature will decrease the wavelength and move the color of radiation emitted from the red end of the electromagnetic spectrum towards the blue end. "In between" stars are bluer than cooler stars.<sup>17</sup>

Color is defined as a comparison of apparent magnitudes taken through filters allowing only certain ranges of wavelengths to pass through. A blue filter, for example, will only allow the blue portion of the spectrum to pass through and will absorb all other wavelengths. When collecting data, a star is observed using first a blue filter and then a green (visual) filter. The absolute magnitude in the blue filter is labeled as B and the magnitude through the green/visual filter is V. Therefore, the color magnitude on the blue side of the spectrum is measured by the difference between the magnitudes under the two different color filters, B-V. Due to the inverse scale of magnitudes, a small B-V value indicates a bluer color, while a larger B-V value suggests a redder color.

Based on observations of millions of stars, astronomers have concluded that all ordinary, hydrogen-burning stars fall on a main sequence relationship of color versus inherent luminosity. This relationship, which falls on the Hertzsprung-Russel Diagram shown in Figure 4, shows that blue stars are hotter and have a higher absolute magnitude, while red stars are cool and have a lower absolute magnitude. Astronomers classify stars by a letter based spectral class system that is based on color and temperature. Due

---

<sup>17</sup> Henbest, *Guide*, pp 124.

to their interrelatedness on the H-R Diagram and with Wien's Law, astronomers use the descriptors color, temperature, and spectral class synonymously.

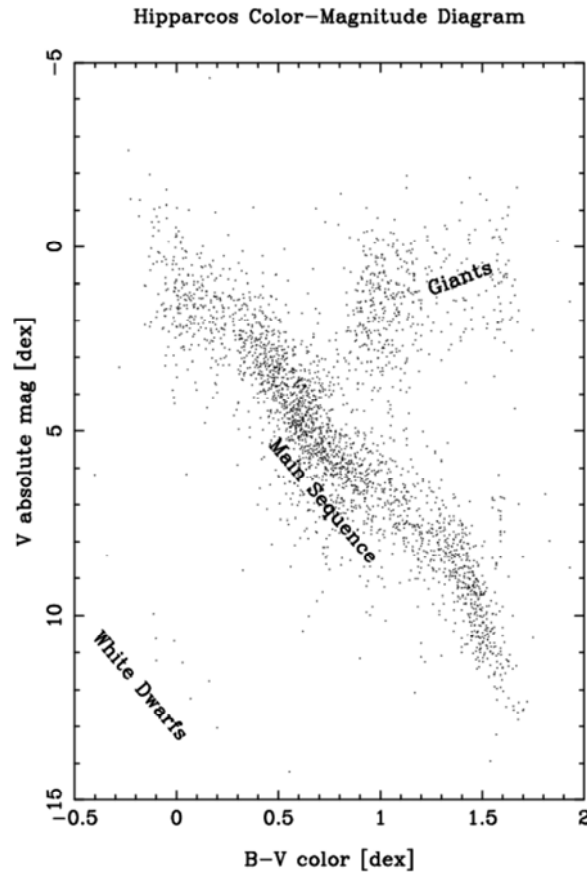


**Figure 4:** Hertzsprung-Russell Diagram of data from the Hipparcos Catalog, showing the relationship between absolute magnitude and color (which is substituted by Spectral Class)

Returning to Equation 1 relating magnitude and distance:

$$m - M = 5 \log\left(\frac{d}{D}\right) = 5 \log(d) - 5 \quad (\text{Equation 1})$$

Astronomers must know the apparent and absolute magnitude in order to calculate distance to the star. We can easily observe the apparent magnitude through a telescope, but absolute magnitude is more difficult to calculate. Using the method of photometric parallax, we measure the B-V color of the stars, assume that these stars are main

sequence, and plot the B-V color onto the Hertzsprung-Russell Diagram in order to find the absolute magnitude.

This process is based on the assumption that color is completely independent of distance. However, we have not yet accounted for interstellar and atmospheric extinction, the scattering of light as it travels through space and through our atmosphere. Extinction often causes blue light to be scattered more than red light. As a result, the received light is moved preferentially toward the red end of the EM spectrum. In general, this reddening,  $E(B-V)$ , and obscuration,  $A(V)$ , are accounted for by the Universal Extinction Law, where.

$$\frac{A(V)}{E(B-V)} \equiv 3.2 \quad (\text{Equation 2})$$

In this project, we will use the extinction estimates of Schlegel, Finkbeiner, and Davis (1998). By a careful microwave and infrared study of dust, they were able to make a map of longitude and latitude of  $E(B-V)$ . An image of their extinction map is presented in Figure 5. The structure of dust and gas extinction is filamentary, but the maps sample to resolutions of two arcminutes. <sup>18</sup>  $A(V)$  comes from an all-sky map and the assumption that the obscuration is similar to the disk star distribution.

---

<sup>18</sup> Schlegel, David J., Douglas P. Finkbeiner, and Marc Davis, "Maps of Dust Infrared Emission for Use in Estimation of Reddening and Cosmic Microwave Background Radiation Foregrounds," *Astrophysical Journal*, vol. 500, p. 525.

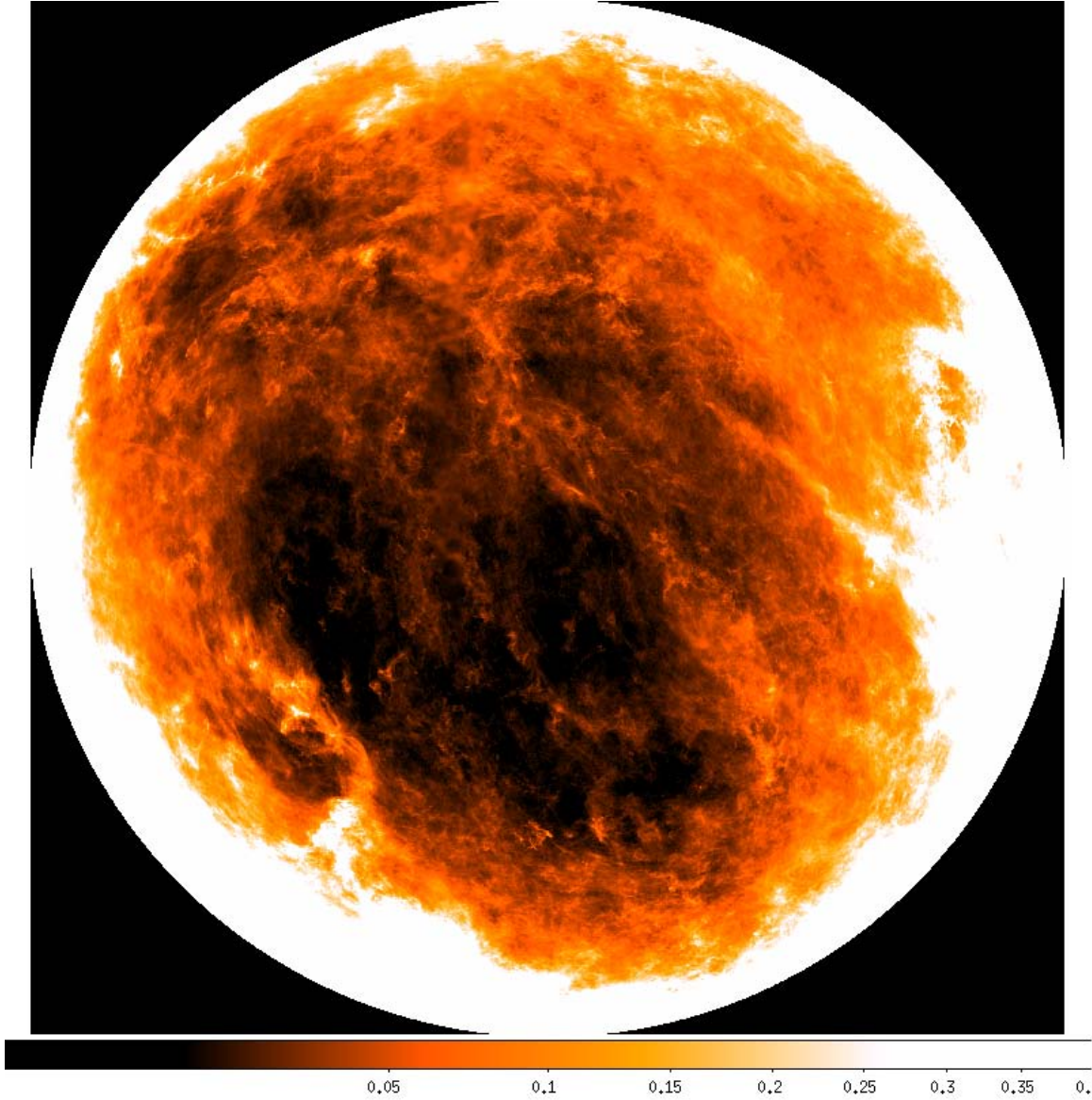


**Figure 5: Orthographic Projection of Schlegel, Finkbeiner, and Davis (1998) from our database.**  $E(B-V)$  scale in magnitudes is projected on the bottom of the figure and the map covers the Northern Galactic Hemisphere. A similar map exists for the Southern sky.

Once we have accounted for extinction and possess an accurate color of the star, we can use the photometric parallax method to calculate the correct distance from our Sun to the star. Combining distance with position in the sky, we can determine the position of a star in the Galactic coordinate system.

## 2. *Stellar Motion*

Astronomers can also observe the motion of stars in the sky through a variety of techniques. From an Earth-bound standpoint, there are two types of motions that we can observe for stars: radial motion and proper motion.

Radial motion is the movement of stars along the line of sight the observer. We measure the Doppler shift of spectral lines in the outer layers of a star to determine if the star is moving toward or away from us and at what velocity. Since there is a standard wavelength of light,  $\lambda$ , for hydrogen, helium, and other stellar elements in our rest frame, there is a standard basis of comparison for the difference between the observed and standard wavelengths,  $\Delta\lambda$ , as a function of radial velocity,  $v$ . The relationship is given by:

$$\frac{v}{c} = \frac{\Delta\lambda}{\lambda} \quad (\text{Equation 3})$$

where  $\Delta\lambda$  the shift in wavelength,  $\lambda$  is the standard spectrum wavelength for hydrogen,  $c$  is the speed of light, and  $v$  is the radial velocity of the star (either toward or away from us).

The proper motion, on the other hand, is calculated simply by observing the gradual change in angular position of a star's position in the sky with respect to the other stars and knowing the star's distance (which is estimated using the absolute magnitude or a stellar parallax). However, due to the gradual motion of stars, proper motion observations must be done over a period of decades. Many astronomers acquire their proper motion data using a comparison of stars surveyed first in 1950 in Epoch I of the Palomar Observatory Sky Survey (POSS I) and then again in 1985 in Epoch II (POSS II).



The proper motion catalog constructed from these survey results is the U.S. National Observatory B 1.0 Catalog.<sup>19</sup> Although no specific proper motion observations were made in this project, much of Larsen and Humphreys' original studies of the excess stars involved these stars.

---

<sup>19</sup> Monet *et al.*, 2003.

## 1.5 Modern Star Counts: Galactic Models

After Herschel's death, astronomers continued to improve upon the star count method but found limits to its utility. Soon thereafter, the star count method became a mostly forgotten technique, and, as a result, the mathematical formalism of the star count has not changed much during the past 150 years. However, one major difference between Herschel's method and the star counts now completed by astronomers is the incorporation of the method of photometric parallax. Instead of falsely assuming that all stars have the same absolute magnitude, we make the more accurate assumption that most stars are main sequence. By measuring their color and plotting it against the H-R Diagram, we find the absolute magnitude and are then able to calculate a more accurate distance.

We used four different filters in this project: Johnson's ultraviolet (U), blue (B), visual or green (V), and the Cousins-Kron system for red (R).<sup>20</sup> We observed the magnitudes of stars under each of these filters and subtracted the color magnitudes in various combinations: U-B, B-V, and V-R. Each of these measurements represents the magnitude of the star within a specific spectral range.

### A. Seelinger's Fundamental Equation of Stellar Statistics and its Variables

When observing a field of stars, we denote the solid angle of the observation as  $\Omega$ . In this area, the number of stars in a unit area of the sky (areal density) we observe is a function of apparent magnitude and color, represented as  $A(m_V, S_{B-V})$ . Examples of these are presented in Figure 6.

---

<sup>20</sup> Bessell, M. S., "UBVRI passbands," *Astronomical Society of the Pacific*, Publications (ISSN 0004-6280), vol. 102, Oct. 1990, p. 1181-1199.

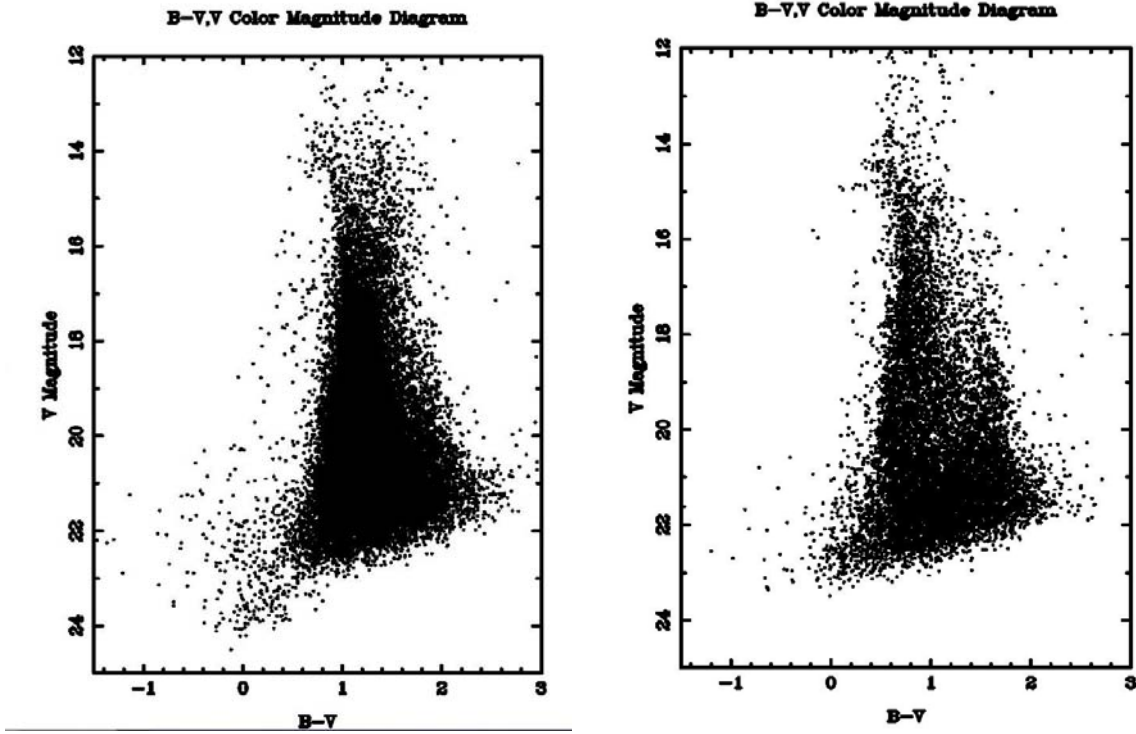


Figure 6: Color magnitude diagrams in the B-V band. The left image shows a denser cluster of B-V stars than the right image and come from a line of sight more towards the center of the Galaxy.

According to Hugo von Seelinger's Fundamental Equation of Stellar Statistics, these plots the areal density of several stellar populations, indexed by  $i$ , depend on the functions for the spatial density distribution of stars,  $D(r)$ , multiplied by the luminosity function  $\Phi(M_V, S_{B-V})$ , where  $M_V$  is the absolute magnitude of stars in the band V. The stellar populations are indexed by  $i$  as into 1) galactic core, 2) halo, 3) thin disk, and 4) thick disk. When the areal density is applied over a solid angle  $\Omega$  to a limiting distance  $R_{max}$ , Seelinger's equation is:<sup>21</sup>

$$A(m_v, S_{B-V}) = \sum_{i=1}^N A_i(m_v, S_{B-V}) = \Omega \sum_{i=1}^N \int_0^{R_{Max}} \int_{M_{Min}}^{M_{Max}} \Phi_i(M_v, S_{B-V}) D_i(\vec{r}) r^2 dr$$

(Equation 4)

<sup>21</sup> Larsen, Jeffrey Arthur, *The Shape of the Galaxy*, University of Minnesota: August 1996, pp 3.

In its basic form, the Seelinger Equation says that when we go out to a certain distance away from our Sun, we should expect to find this many stars and what types (colors) they are.

### *1. Angle of Observation*

The angle of observation  $\Omega$  is the square angle of the area being observed. Seelinger's integrates to find the stars in a unit of volume, so we must combine the angular area under observation with the distance range to find the volume element. After the observer selects a spatial direction based upon longitude ( $l$ ) and right ascension ( $b$ ), the model begins to move a distance  $r$  away from the sun. As an incremental distance  $dr$  is added, the model adds an incremental volume element,  $\Delta V$ , as shown in Figure 7. Since the total volume within the cone is calculated using the equation  $V = \frac{1}{3}\Omega r^3$ , where  $\Omega$  is the square angle of the area being observed, the equation for incremental volume element from distance  $r_1$  to  $r_2$  is:

$$\Delta V = V_2 - V_1 = \frac{1}{3}\Omega(r_2^3 - r_1^3) \quad (\text{Equation 5})$$

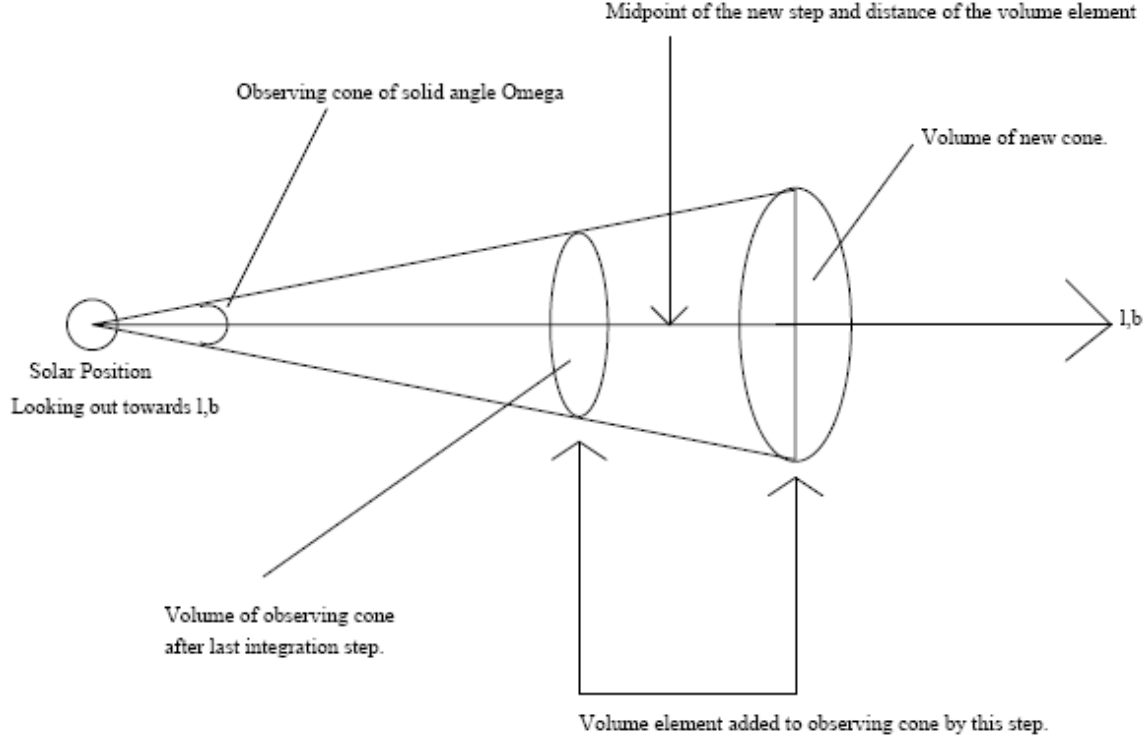


**Figure 7: Volume calculation for the galactic model developed by Larsen and Humphreys  
(GALMOD)**

## 2. Density Function and Stellar Population

This volume element is then scaled by the density function,  $D_i(\vec{r})$ . As an example, the disk is modeled in Equation 5 as a double exponential in both radius in the plane from the galactic center ( $r$ ) and height above the plane ( $z$ ). These functions are normalized to give a relative density of stars in the solar neighborhood.  $N_0$  is the normalization constant unique to the disk.

$$D_i(\vec{r}) = N_0 e^{\left( -\frac{r}{R_H} - \frac{z}{Z_H} \right)} \quad (\text{Equation 6})$$

At the center of the Galaxy, where stars are most concentrated,  $r = 0$  and  $z = 0$ .

Therefore,  $D_i(\vec{r}) = N_0 e^0 = N_0$ , which is the maximum possible density in the distribution.

This function is only an estimate of the behavior of the Galactic disk, which in reality is

much more complicated and random. However, it does present a useful model that is statistically accurate for a large number of stars.

Separate density function equations can also be written for the Galactic core, the halo, and the thin and thick disks. These structures are assigned a number and indexed by the variable  $i$ . The Seelinger Equation finds the integral for each of the structures within an area of space and sums them up to get the distribution of a certain magnitude and color of stars.

### 3. The Luminosity Function

The luminosity function,  $\Phi(M_V, S_{B-V})$ , predicts the relative number of stars of each absolute magnitude and color in a given volume of space. For our Galactic model, we used the disk and halo/thick disk luminosity function developed by Gilmore, Reid, and Wielen and presented in Figure 8.

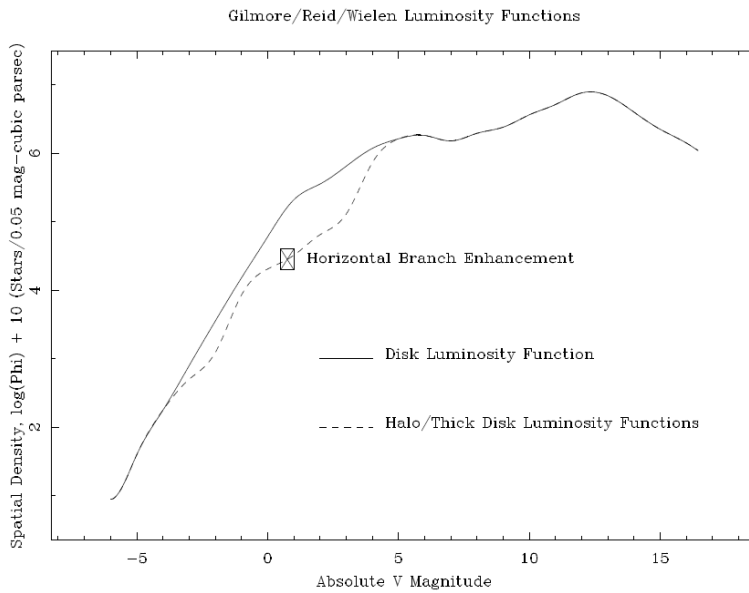


**Figure 8: Luminosity function used in the GALMOD**

It should be noted that the color term  $S_{B-V}$ , of which luminosity is a function, is not presented in Figure 8. This is because the color term is already used in plotting out the distance to the star using the method of photometric parallax. This is implied but not explicitly stated in Seelinger's Equation.

#### 4. *Practical Use*

Seelinger's equation has the observed areal density,  $A(m_V, S_{B-V})$ , as the answer to an integral whose component functions,  $D_i(\vec{r})$  and  $\Phi(M_V, S_{B-V})$ , we wish to find. Once a star count field is taken, the goal is to solve for the spatial distribution,  $D_i(\vec{r})$ , and luminosity functions,  $\Phi(M_V, S_{B-V})$ , by inverting the areal density equation. However, this equation is extremely complicated and difficult to work with for large amounts of data. Also, observing stellar populations from a particular angle does not mean that we can easily classify what specific Galactic structure they belong to. Without a computing device to catalog and analyze the data, astronomers were unable to use star counts to discover any meaningful results other than some observations of the galactic plane.

However, the introduction of computers in the 1970's brought star counts to the forefront of modern astronomy once again. Astronomers realized that, instead of directly solving the fundamental equation, they could instead create a statistical model which could be compared to collected data. In a surge of renewed popularity, researchers used the star count method to detect the thick disk in 1983<sup>22</sup> and the bar situated at the galactic

---

<sup>22</sup> Gilmore and Reid, "New light on faint stars," 1983.

core in 1994<sup>23</sup>, as well as to observe the merging of the Sagittarius Dwarf into the Milky Way in 1994<sup>24</sup> and, of course, the Hercules Thick Disk Cloud studies in this project.

Various astronomical teams have developed their own galactic models over the past few decades. This project modernized a model known as GALMOD first developed by Larsen in 1996 to analyze the Automated Plate Scanner (APS) star counts of the Palomar Observatory Sky Survey, Epoch I (POSS I). The model is based upon the previously discussed equation for areal density (Equation 4).

From the data collected in 1996, Larsen found different color-magnitude relationships among the separate structures of the Galaxy. These relations are plotted in a color-magnitude diagram in Figure 9.

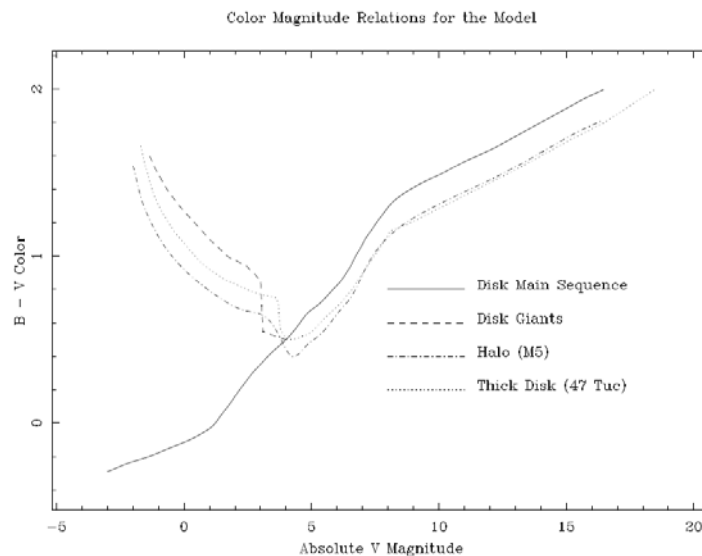


**Figure 9: Color-magnitude relations used in GALMOD (Larsen 1996). The Halo and Thick Disk Populations have redder, bright stars since they represent older populations.**

<sup>23</sup> Weinberg, Martin D., “Kinematic signature of a rotating bar near a resonance,” *The Astrophysical Journal*, Part 1 (ISSN 0004-637X), vol. 420, no. 2, p. 597-611.

<sup>24</sup> Ibata, R. A., G. Gilmore, and M. J. Irwin, “A Dwarf Satellite Galaxy in Sagittarius,” *Nature*, vol. 370, no. 6486/Jul 21, p. 194, 1994.



### B. Galactic Coordinates

To portray an accurate view of the galaxy, GALMOD must also be able to convert a set of Earth-centered coordinates into coordinates that are based upon the center of the galaxy. Galactic latitude ( $b$ ) and longitude ( $l$ ) are defined from our sun with respect to the center of the galaxy, so that  $l = 0^\circ$ ,  $b = 0^\circ$  is the direction of the center. The longitude increases counterclockwise of the galaxy. Astronomers classify the galaxy into four quadrants of longitude, as shown in Figure 10. Quadrant 1 (Q1) contains all space from  $l = 0^\circ - 90^\circ$ , Quadrant 2 (Q2) contains  $l = 90^\circ - 180^\circ$ , Quadrant 3 (Q3) encompasses  $l = 180^\circ - 270^\circ$ , and Quadrant 4 (Q4) has  $l = 270^\circ - 360^\circ$ . Since the galaxy becomes sparser as a function of distance way from the center, the data in this project focuses on Quadrants 1 and 4.<sup>25</sup>

---

<sup>25</sup> Larsen, *Shape*.

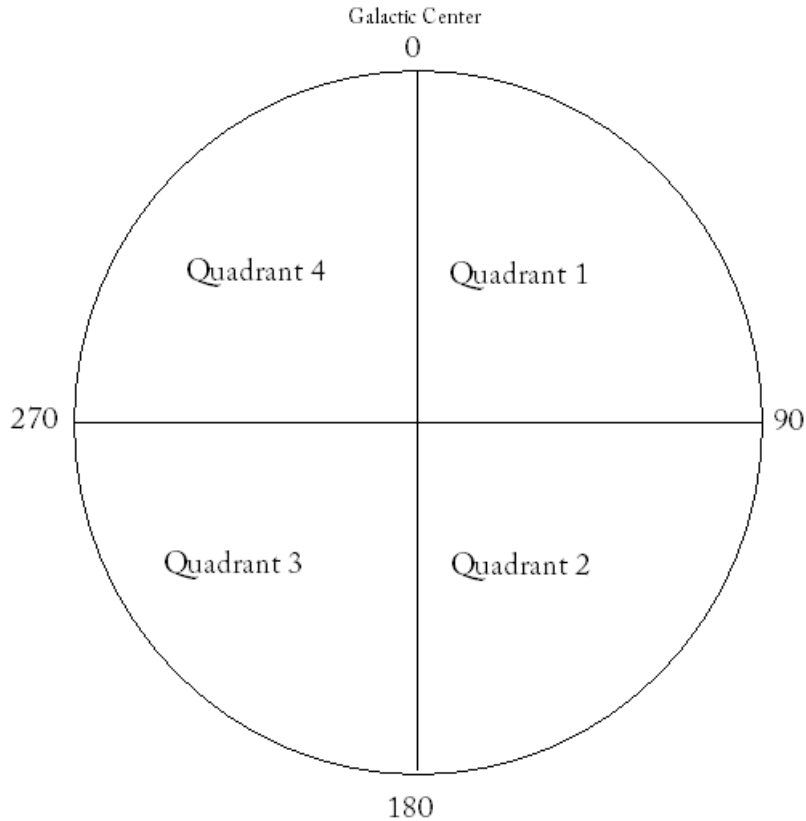


**Figure 10: Coordinate scheme of the galaxy, centered around our solar system.**

The conversion from a sun-centered to a galactic core-centered coordinate system depends upon an angular, geometric relationship. This new galactocentric coordinate system will be based upon the distance along the galactic plane from the galactic center to the observation point,  $R$ , the angle along the galactic plane relative to the Sun-Center line,  $\Phi$ , and the perpendicular height above the galactic plane,  $Z$ . The galactocentric coordinates will then be  $(R, \Phi, Z)$ . One of the parameters to be defined for the galaxy are the coordinates of our sun, where  $\Phi = 0^\circ$ , the distance of the sun above or below the galactic plane is  $Z_0$ , and the radius of sun from the galactic center is  $R_0$ . Figure11 defines this relationship.

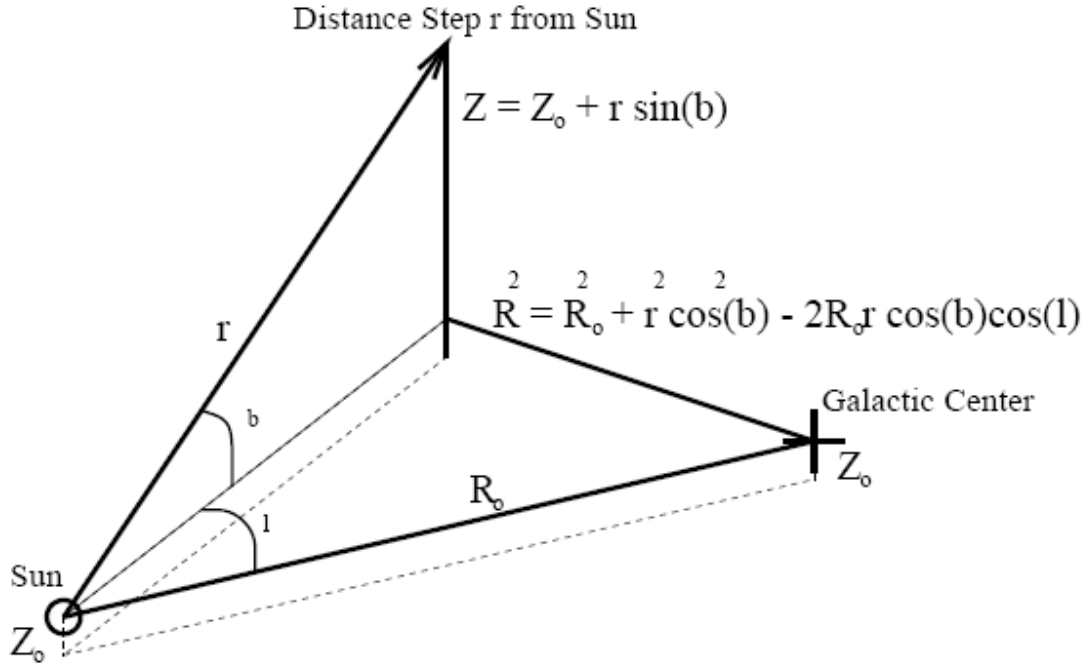


**Figure 11: Mathematical conversion between solar-relative ( $r, l, b$ ) and galactic relative coordinates ( $R, Z$ ).**

After determining the number of stars per magnitude per unit volume, the next step of the galactic model is to categorize these stars by color, according to a defined relationship for different stellar populations of the Galaxy. Since the main sequence is single valued, knowing the absolute magnitude of a star tells us its color.

### C. Global Parameters

Once the galactic model has been fully developed, the next step is to obtain a set of global parameters that define the galaxy and to search for any areas of the galaxy that deviate from a smooth, symmetric fit.<sup>26</sup> These parameters are especially useful in the density function, as in Equation 6 when we use the constants  $R_H$  for disk length,  $Z_H$  for disk height, and  $N_0$  for the density normalization of the disk. The parameters to be

<sup>26</sup> Larsen, *Shape*, pp 135.

searched for are listed in Table 1. A genetic algorithm, described in Appendix B, is used as a driver to find the optimum values for these parameters.

Parameter	Description
<i>Adopted Parameters</i>	
$Z$	Solar Distance Above Midplane
$R$	Solar Distance from Galactic Center
$R_{H,Disk}$	Radial Scale Length of Disk
$N_{0,Disk}$	Disk Density Normalization
$Z_{H,Disk,Max}$	Disk Scale Height, Dwarf Maximum
$Z_{H,Disk,Giants}$	Disk Scale Height, Giants
<i>Derived Parameters</i>	
$R$	Halo “deVancouleurs’ radius”
$c/a$	Halo Axial Ratio
$N_{0,Halo}$	Halo Density Normalization
$R_{H,Thick}$	Thick Disk Radial Scale Length
$Z_{H,Thick}$	Thick Disk Scale Height
$N_{0,Thick}$	Thick Disk Density Normalization

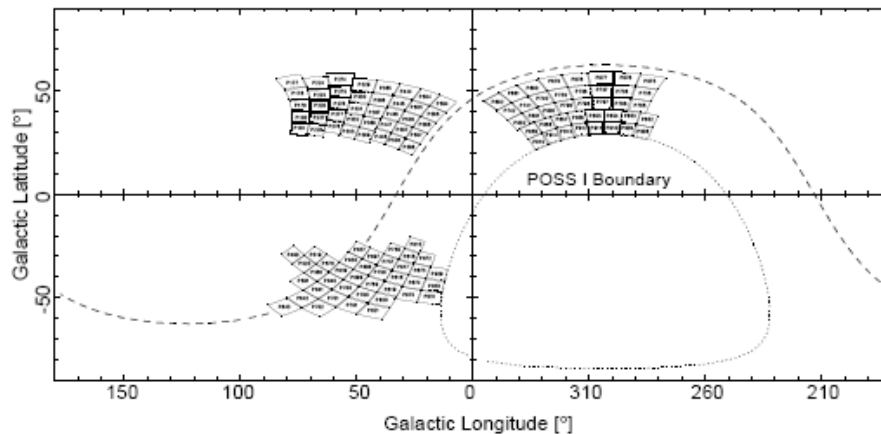
**Table 1: Structural parameters to be optimized by the genetic algorithm.**

## 1.6 Discovery of the Galactic Asymmetry

Humphreys and Larsen (1996) used magnitude-limited star count data collected from the Automated Plate Scanner (APS) Catalog at the University of Minnesota as well as the previously discussed galactic model known as GALMOD. Their data consisted of stellar catalogs created from 88 astronomical plates of  $16 \text{ deg}^2$  area sampling the entire sky visible from the Palomar Observatory with  $|b| > 20^\circ$ . The model used Seelinger's formula from Section 5 for a three-component galaxy, accounting for the thin disk, thick disk, and halo. Larsen and Humphreys then used a genetic algorithm to customize the fit and derive the global parameters for their Galaxy model. The expectation was that this model, symmetric by nature, would match the observed star counts from the Galaxy. Instead, they found an asymmetry in the structure of our Galaxy. When examining four paired fields at an altitude range of  $b = 30^\circ\text{-}40^\circ$  and longitude  $l = 20^\circ\text{-}45^\circ$  in Q1 and Q4, they found a 30% excess of blue stars in Q1 than in Q4 (Larsen and Humphreys, 1996). Since blue stars at these apparent magnitudes largely are well above the disk like the thick disk and halo, Larsen and Humphreys concluded that the asymmetry was associated with these components.<sup>27</sup>

---

<sup>27</sup> Humphreys, Roberta M., Juan Cabanela, and Jeffery A. Larsen, "Support for a Meeting on 'The Fate of the Most Massive Stars,'" National Science Foundation, 23-28 Mar. 2004, pp 2.



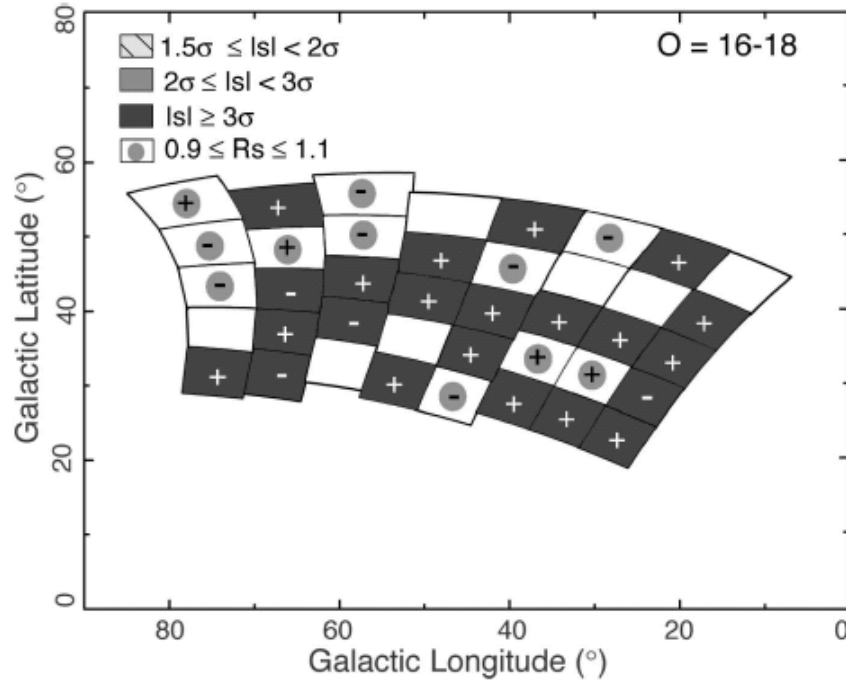


**Figure 13: A map of the star excess against the galactic ( $l, b$ ) coordinates. The “+” areas trace the asymmetry**

Their findings showed Humphreys, Parker, and Larsen analyzed this new set and found a 20-25% excess of blue and intermediate colored stars, mostly of magnitude 18-18.5, in an area of Q1 located at  $b = 30-40$  and  $l = 20-60$ . The ratios of Quadrant 1 star counts divided by Quadrant 4 star counts are organized by stellar field in Figure 13. In terms of distance from our solar system, this large grouping is located 1-2 kiloparsecs from our sun and 0.5-1.5 kpc above the galactic plane. The excess appeared to end at  $l = 60$ , though the group continued to taper off with stars of magnitude fainter than 18.5.<sup>29</sup>

As a part of the project, Larsen also wrote a genetic algorithm as a driver for the data to find the values of the global parameters. He combined these derived parameters

<sup>29</sup> Larsen, Jeffrey A. and Roberta M. Humphreys. “Fitting a Galactic Model to an All-Sky Survey” in *The Astronomical Journal*, vol. 125 (April 2003): pp 1346.

with other accepted parameter values from professional sources to get the total global parameters listed in Table 2.

Parameter	Values
<i>Adopted Parameters</i>	
$Z$	20 pc
$R$	8 kpc
$N_{0,Disk}$	1.00
$Z_{H,Disk,Max}$	325 pc
$Z_{H,Disk,Giants}$	250 pc
<i>Derived Parameters</i>	
$R_{H,Disk}$	3.5 kpc
$c/a$	0.55
$N_{0,Halo}$	0.0022
$R_{H,Thick}$	4.7 kpc
$Z_{H,Thick}$	929 pc
$N_{0,Thick}$	0.028

**Table 2: Adopted and Derived Parameter Values from GALMOD**

Recent efforts by astronomers have focused on finding tidal tails left over from other galactic mergers in the outer halo (Martinez-Delgado *et al.* 2007, Bell *et al.* 2007), so there had been little follow-up study of the stellar excess until recently. Interestingly, the presence of another excess in the same direction in extremely faint counts has been reported by a separate team of astronomers led by V. Belokurov,<sup>30</sup> but they associated their finding with a much more distant area of the Milky Way that they call the Hercules-Aquila cloud. We believe that the Belokurov discovery is unrelated to the Larsen-Humphreys excess and comprises a separate structural feature in the more distant halo of

---

<sup>30</sup> Belokurov, V., *et al.*, “The Hercules-Aquila Cloud” in *The Astrophysical Journal*, vol. 657 (10 March 2007): pp. L89.



the Milky Way Galaxy. The Larsen and Humphreys excess has since been confirmed using the Sloan Digital Sky Survey.<sup>31</sup>

Based on available data, Larsen, Humphreys, and Parker proposed three possible causes of the asymmetry.

1. The Milky Way is a galactic cannibal whose gravitational forces ripped apart a significantly smaller galaxy in the distant past. The apparent asymmetry in this area of the galaxy could be the stellar remnants of that event. However, the wide area over which the asymmetry is spread and the fact that there is no overlap with the path of the Sagittarius dwarf through the halo seemed to make a galactic merger remnant the least likely explanation.<sup>32</sup>
2. The bar located at the center of the galaxy has stirred up the stars in this part of the galaxy and the observed clump is simply left over in the bar's gravitational wake.<sup>33</sup> If this theory is correct, then spectral observations should show a lag in the rotational velocities of Q1 stars compared to those in Q4.<sup>34</sup>
3. Either the thick disk or the halo simply has a triaxial shape, meaning that the radii in each of the three coordinate directions for the density functions are different.<sup>35</sup> This theory will be supported if future observations show that the

---

<sup>31</sup> Juric, Mario *et al.*, "The Milky Way Tomography with SDSS. I. Stellar Density Distribution," *The Astrophysical Journal*, Volume 673, Issue 2, (The American Astronomical Society, February 2008), pp 864-914.

<sup>32</sup> Cabanela, J.E., Jeffrey Larsen, and Roberta M. Humphreys. "Mapping the Asymmetric Thick Disk: A Search for Triaxiality." Moorhead, MN: Minnesota State University, 2007.

<sup>33</sup> Sellwood, J. A., "Bars and Dark Matter Halo Cores," *The Astrophysical Journal*, vol. 587, issue 2, pp. 638-648.

<sup>34</sup> Cabanela, *et al.*, "Mapping the Asymmetric Thick Disk."

<sup>35</sup> Parker *et al.*, "I. The Star Counts," pp. 1346.

stellar excess extends out to greater longitudes than previously observed.<sup>36</sup> If this hypothesis were true, then astronomers would need to revisit our overall understanding of galactic dynamics. A triaxial shape in the thick disk might also indicate a triaxiality in the dark matter corona and would raise a number of questions about galactic formation.

One of the reasons that astronomers have not been able to quickly confirm this galactic asymmetry is that the photographic-based APS catalog was large and contained very faint stars. Until recently, large CCDs had a very hard time observing this much sky to these faint magnitudes. The National Science Foundation funded a study by Humphreys, Larsen, and Dr. Juan Cabanela to collect more data.

---

<sup>36</sup> Cabanela, *et al*, "Mapping the Asymmetric Thick Disk."

## Chapter 2: Observations

### 2.1 Data Available for this Project

The data from this project comes from several sources:

- The Steward Observatory 90-inch telescope at Kitt Peak, AZ, used to study the U, B, V, and R magnitudes for a stellar catalog in the northern sky. The four observing runs included Larsen and Katz in May 2007 and Larsen in September 2006 (data unusable due to persistent clouds), September 2007, and May 2008.
- 1.0-m SMARTS Consortium telescope near La Serena, Chile, also to study the U, B, V, and R magnitudes for a stellar catalog in the Southern sky. The two observing runs were Cabanela and Humphreys in April 2006 and Larsen, Humphreys, and Haviland in October 2008.
- NOAO Hydra Multi-object Spectrograph in Chile to study the radial motions of the observed stars in the southern sky; observing run conducted by Humphreys in April 2008
- Smithsonian Astrophysical Observatory Hectospec Multi-Object Spectrograph (on MMT Telescope) on Mt. Graham, AZ, to study the radial motions of observed stars in the northern sky; observing runs conducted by Humphreys in June 2007, October 2007, May 2008, and September 2008.

As an additional resource, the U.S. Naval Observatory B 1.0 catalog of proper motions is also available to compare the observed proper motions of the stars.



**Figure 14: 90-inch telescope in the foreground at Kitt Peak, AZ, with the 4-meter telescope in the background**



**Figure 15: 1.0-m SMARTS Consortium telescope near La Serena, Chile**

## 2.2 Observations from the CTIO 1.0-m Telescope in La Serena, Chile

In October 2008, Larsen, Humphreys, and Haviland went on an observation run to La Serena Chile in order to complete our CCD catalogs of the Southern sky. We had time reserved on the 1.0-m telescope at the Cerro-Tololo Inter-American Observatory (CTIO), where we carried out observations from 8 pm (local time) to 6 am each night from October 19<sup>th</sup>–25<sup>th</sup>. Haviland personally conducted observations on three full nights, including the night photographed in Figure 16.



**Figure 16: Nighttime view of the 1.0-m telescope at the CTIO Observatory during Haviland's observations.**

Each stellar field was photographed through four different color filters: Johnson U, B, V, and Cousin's Kron R. Since the amount of light received varies with color, we altered the exposure time depending on the color filter being used to reach similar

limiting magnitudes. Exposures in the U band ran for 400 seconds, exposures in the B band for 485 seconds, V band for 160 seconds, and R for 190 seconds. Throughout the night, we also took flat images, zeros, and darks that would later be used for calibration in the image reduction process (described in section 3.1). The night of October 20<sup>th</sup>-21<sup>st</sup> was somewhat overcast, so we took our images to collect as much light as possible and went back to the same field on the next clear night to take calibration images. This allowed us to calibrate our deeper images despite the clouds during image reduction using a process called differential photometry.

The greatest problems encountered were mechanical errors in the telescope, particularly in focusing the image. The U filter required a different focus than the other color bands, but the device for changing the focus was imprecise and prone to mechanical failure. Our observation team spent much of the first two nights experimenting with the focus and figuring out the optimum numerical values to be used. The telescope did have a technician on hand to offer assistance, but we still occasionally had to learn it by trial and error. Mechanical failures also caused problems with keeping the telescope steady. A telescope needs to track at sidereal rates, but mechanically can drift. We used a guiding CCD and an auto-tracker to compensate. In each field, we picked a large, clear star to image on and slaved the drives to keep this star stationary on the CCD. During this run, the control system still drifted at times, particularly in the vertical direction. As a result, the stars in some of the fields (especially during the longer U and B exposures) were smeared vertically across the image, making some of the stars indistinguishable from galaxies.

When an image was clearly smeared, we usually retook the exposure, but were not always able to due to time constraints. Another difficulty in using a 1.0-meter telescope was that we needed to photograph nine different sub-fields in order to cover a full square degree. Unlike the 4-meter telescope, where we could have photographed an entire field in one exposure, using the 1.0-meter was a very time-intensive process. However, getting reservation time on the 4-meter is very difficult due to higher demand, whereas time on the 1-meter was guaranteed by the observatory.



**Figure 17: View from inside the dome of the 1.0-meter telescope.**  
(Courtesy of Jeffrey Larsen)



## Chapter3: Data Processing

### 3.1 Image Reduction

During the Palomar Observatory Sky Survey, Epoch I (1950), which comprised the dataset for Larsen and Humphrey's original detection, astronomers used photographic plates that were manually fitted in and out of the end of the telescope. Later, as technology improved, these plates were scanned into digital images. The development of the CCD has greatly simplified data collection and allowed astronomers to control the telescope entirely from a central room, which was our method in this project. The CCD camera came into widespread use amongst astronomers in the 1980's. Almost every telescope now has a CCD camera, which is a high-sensitivity digital camera attached to the focus point of the telescope. The camera has a transparent window through which light shines onto a CCD chip, which is a large cluster of photodiodes that make up the pixels of the digital image. Light causes electron movement on the semiconductor wafers and the readout of freed electron in the pixel registers can be used to create an image from the CCD. A voltage is applied across the CCD that reenergizes the CCD plate and allows a new image to be taken after the old image is stored to digital memory.<sup>37</sup> CCD digital images can be much more easily analyzed using computer programs rather than manually using the older plates. During our project, this allows us to quickly analyze the large numbers of stars in each field.

---

<sup>37</sup> Martinez, Patrick and Alain Klotz, *A Practical Guide to CCD Astronomy*, trans. by André Demers (Cambridge: Cambridge University Press, 1998), p. 1.

Unfortunately, the CCD is not without its own required calibration. We had to account for temperature variations, sensitivity variations among the pixels, electronic bias, and other sources of error in the CCD. An example of a raw, uncalibrated CCD image is shown in Figure 18.

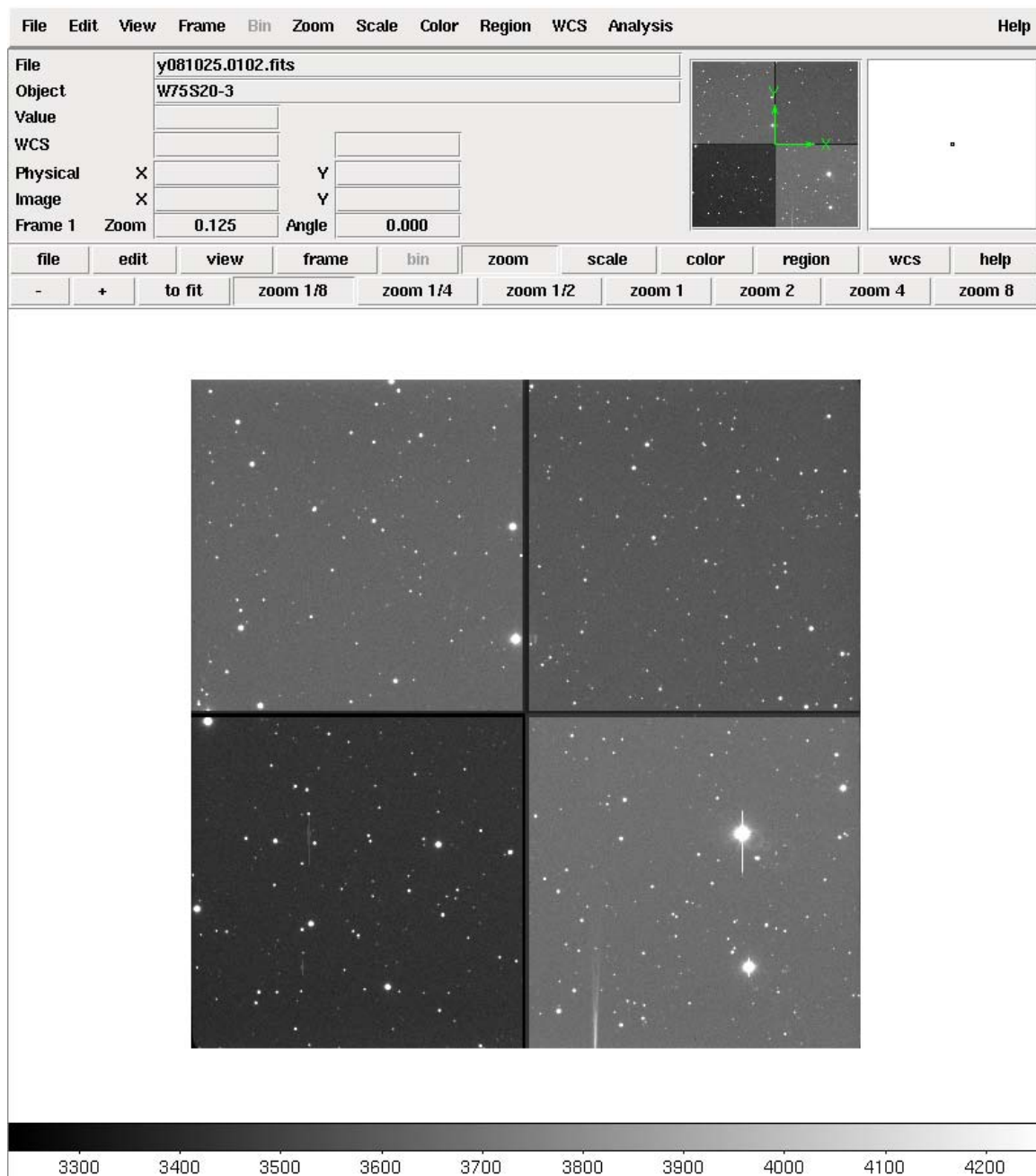
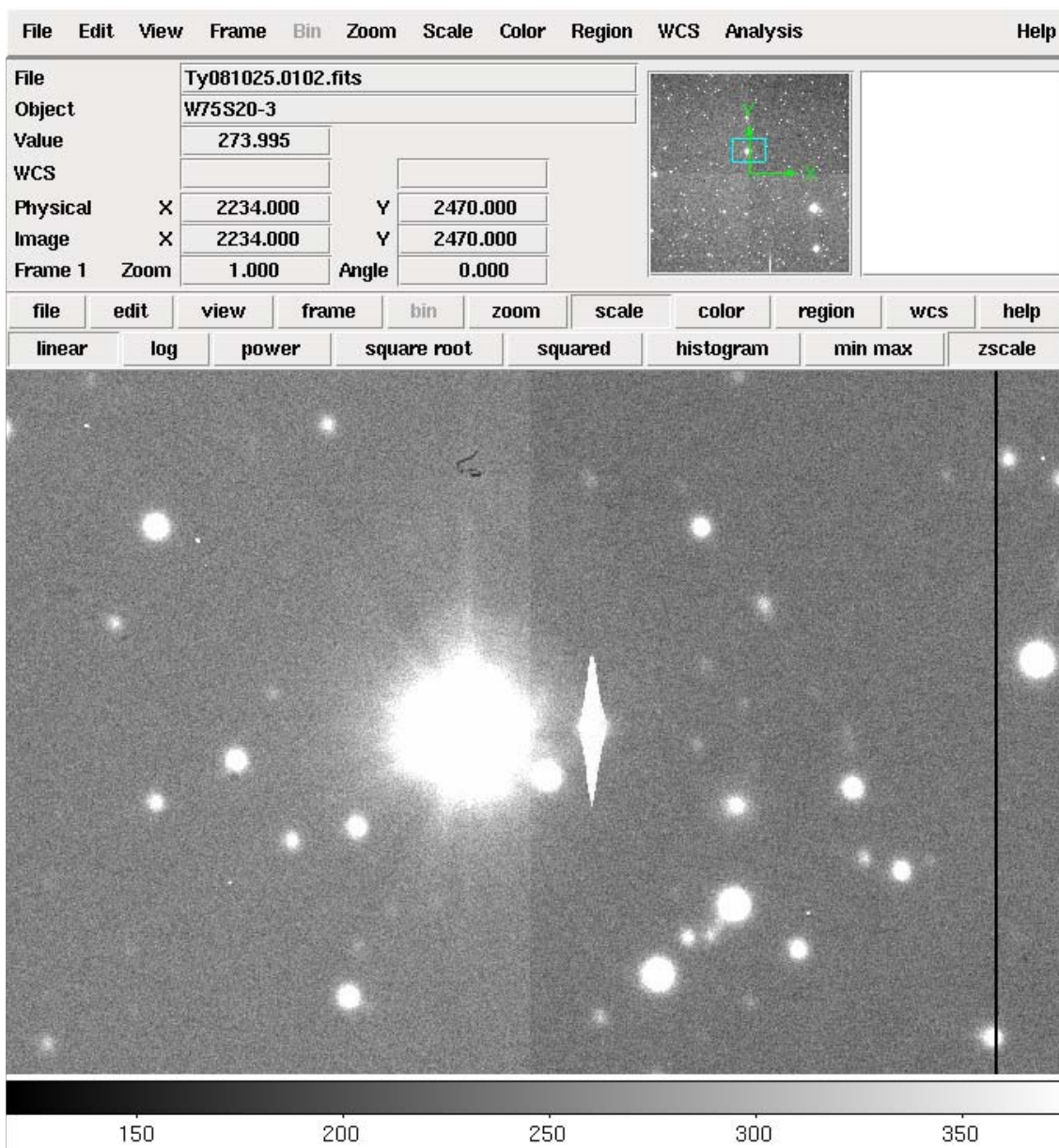


Figure 18: Raw CCD image (no calibration)

In addition, the convenience of using multiple amplifiers to speed readout time create false images through E-M induction, also known as “cross-talk.” Electromagnetic induction among separate sides of the CCD plate produced a ghost image of a bright star on the opposite side of the image in Figure 19. Fortunately, ghost images like this are easily identifiable and can be filtered out from the digital image.



**Figure 19: Example of Cross-talk.** Electromagnetic induction causes the ghost image to appear on the other side of the CCD plate.

The first step of image reduction is to trim down the image and remove the overscan separating the data sections. A trimmed down image is shown in Figure 20:

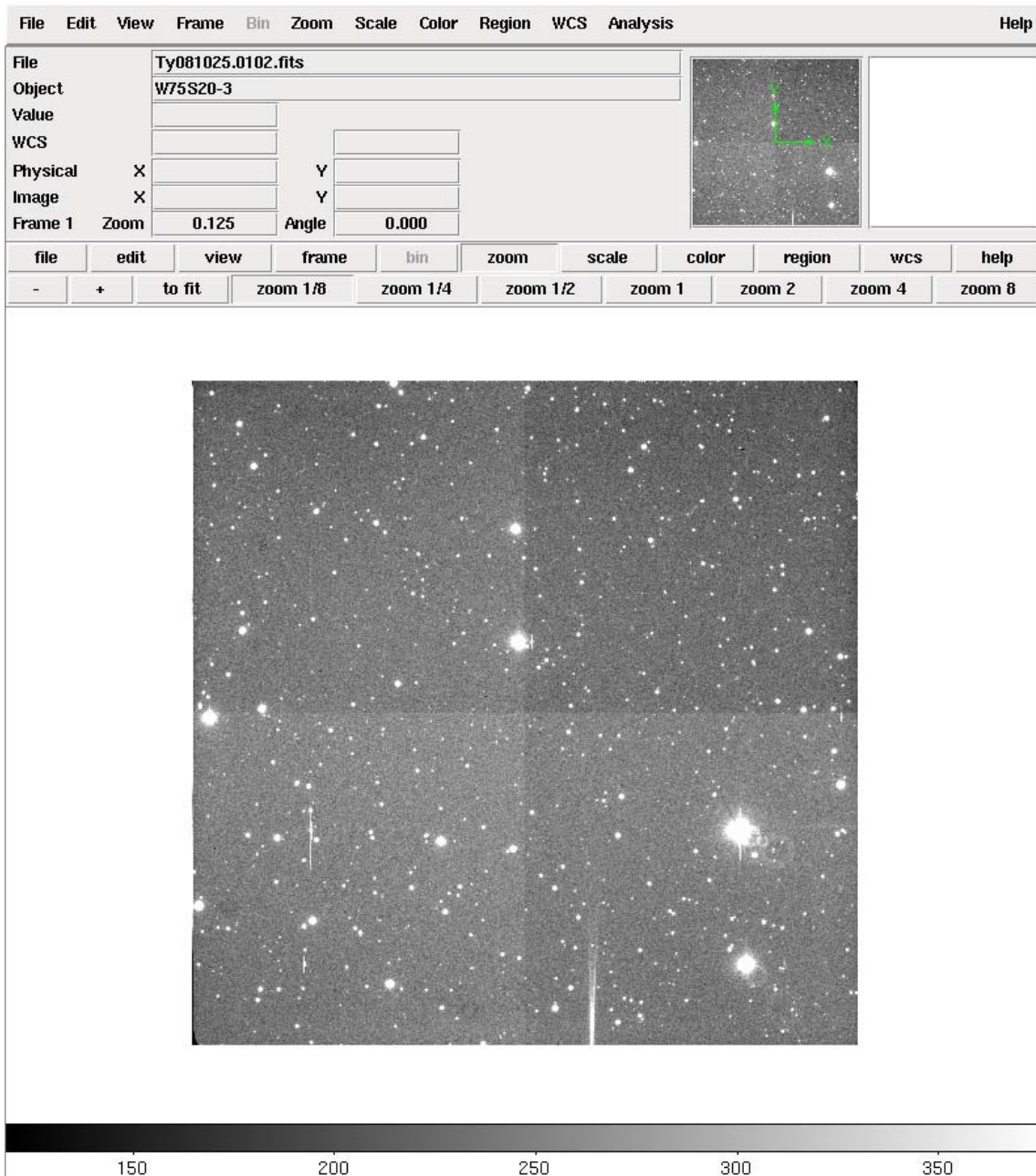


Figure 20: Trimmed CCD image.

Applying a voltage to a CCD frees electrons before the CCD is exposed to the image. Therefore, we needed a bias image, also known as a zero, to remove the

underlying background level from each image. Since this bias level is presumably constant over a long period of time, we took one set of bias images (with zero exposure time for each image) before each observation run and subtracted the average bias image from each raw image.<sup>38</sup>



**Figure 21: Zero-Bias Image**

<sup>38</sup> Howell, Steve B., *Handbook of CCD Astronomy* (Cambridge: Cambridge University Press, 2000), p. 59.



We also took dark images with the shutter closed, but over longer periods of time to account for a buildup of thermal noise during exposure. During the image reduction process, we averaged out the many different dark images to produce a single dark calibration image. Along with the bias, we subtracted the dark image from the raw image.<sup>39</sup> (Physically, there is no visual difference between a dark and a bias image except that there are a few more counts in the dark due to the thermal background. We scaled this excess to exposure time and subtracted it from the image to be calibrated.)

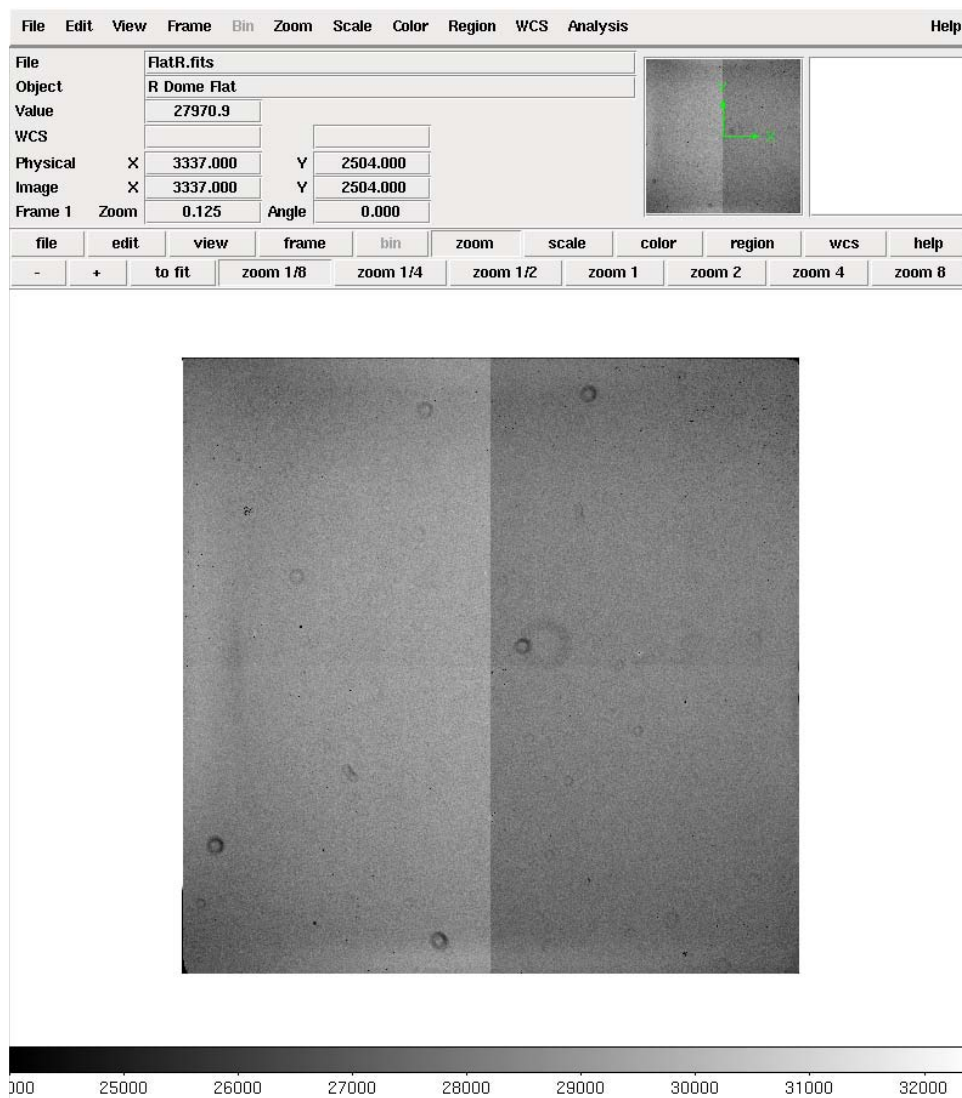


**Figure 21: Flat Field.**

<sup>39</sup> Ibid., p. 59.

We took the flat field images with the shutter open with the goal of accounting for variations among the pixels, including damage that may have occurred to the CCD while in the camera. To get a flat field, our telescope shone a constant light level over the entire CCD camera to see which pixels were not properly measuring the image. Each color filter required a separate flat field calibration, so this time-intensive procedure was completed at the beginning of the night before the sky darkened for observations.

When these image reduction techniques are combined together on a pixel by pixel basis, the result can be described by the equation:<sup>40</sup>

$$\textit{Final Reduced Image} = (\textit{Raw Image} - \textit{Bias Image} - \textit{Dark Frame}) / (\textit{Flat Field})$$

An example of a final, successfully calibrated image is shown in Figure 23. This image can now be measured for objects, classified, photometrically calibrated, and astrometrically calibrated. Each step will be discussed in the next few sections.

---

<sup>40</sup> Ibid., p. 60.

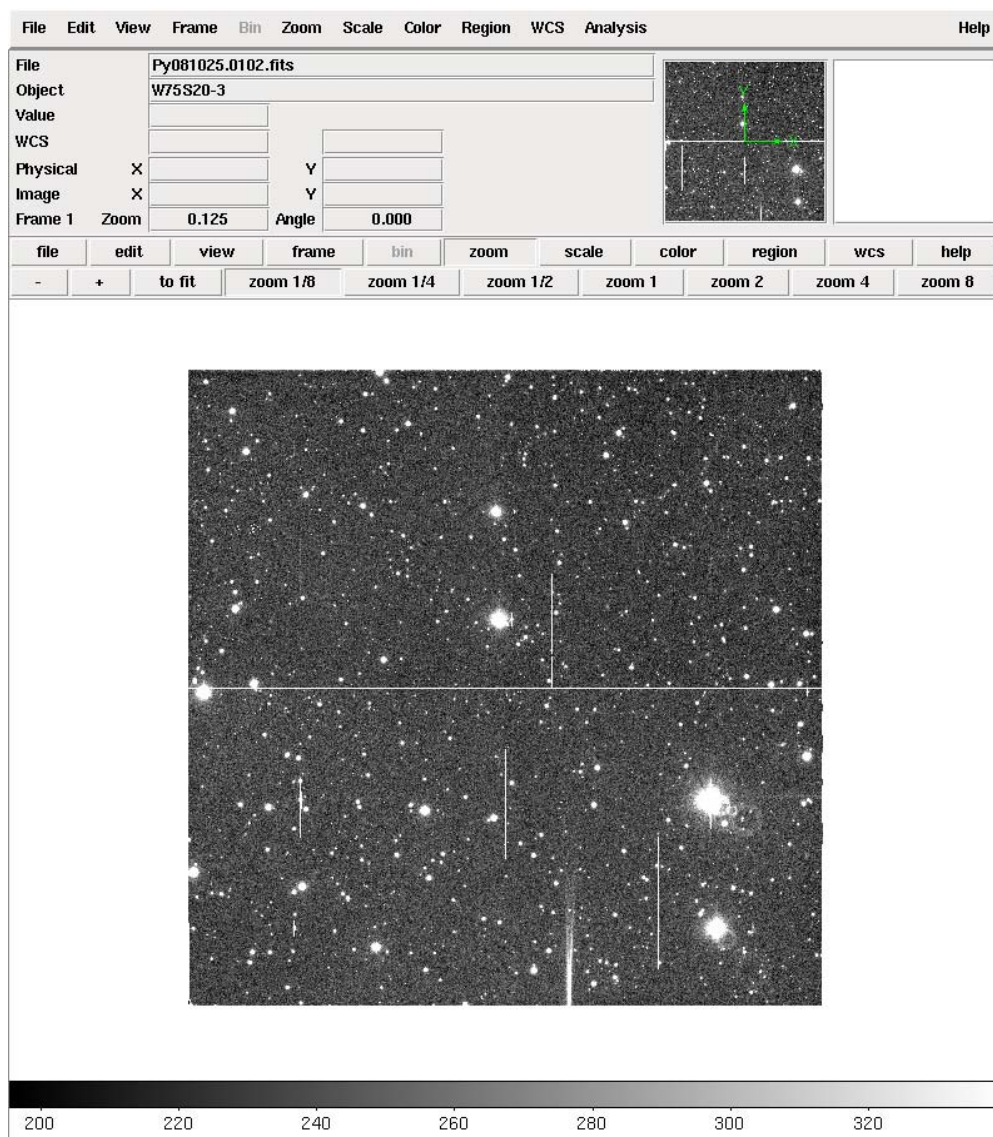


Figure 23: A successfully calibrated CCD image.



### 3.2 Photometric Reduction

After the image reduction steps had been completed, it was necessary to calibrate the photometric sensitivity of our data. Most of the need for calibration comes from extinction, which (as discussed in Section 1.4) is the process by which light is absorbed and scattered as it travels from its source to the observer. Some extinction takes place as light travels across outer space and is scattered by interstellar dust, but stellar extinction is minor compared to atmospheric extinction. The more atmosphere between the observer and the star, the greater is the level of extinction and the smaller the apparent brightness of the observed objects. The atmosphere also causes a reddening in the spectrum of light. Due to atomic energy levels of the atmospheric molecules, blue light scatters more than red light, as evidenced by how the sky is blue during the day and red when the sun sets.

With both atmospheric extinction and reddening, the effect increases as the distance through the atmosphere increases, which happens as the telescope points lower in the sky. Ideally, we would make our observations from a satellite above the atmosphere, but this is not practical for most astronomers. Therefore, we have to calibrate our telescopic observations from beneath the atmosphere to remove atmospheric effects. The distance from the ground to the atmosphere, which is referred to as the “airmass,” is not the same depending on what angle you make your observations from compared to the zenith (straight up in the sky,  $90^\circ$  to the horizon). Airmass is literally a ratio of the distance from the ground to the outer edge of the atmosphere at a certain angle to the distance from the ground to the atmosphere at zenith. When the airmass is

1.7, there is 1.7 times as much atmosphere to cross than at when the telescope is at zenith. The shortest distance between the ground and the atmosphere is looking straight up ( $0^\circ$ ), while the longest is in the direction of the horizon ( $90^\circ$ ). The airmass,  $X$ , is therefore a function of the secant of the elevation.

$$X(0^\circ) = \sec(0^\circ) = 1$$

$$X(90^\circ) = \sec(90^\circ) = \infty$$

The airmass function is accurate until about  $5^\circ$  above the horizon.

For our analysis, we use the Hardie Method for photometric calibration<sup>41</sup> and change the notation so that it is more amenable to CCD analysis.:

Let  $V$ ,  $B$ ,  $R$ , and  $U$  be the bandpass magnitudes of stars from the calibrated images. These are the values that we want.

Let  $v$ ,  $b$ ,  $r$ , and  $u$  be the instrumental magnitudes of stars from the un-calibrated images. These are the values that we have from our observations.

Let  $K_V$ ,  $K_{VB}$ ,  $K_{UB}$ , and  $K_{VR}$  be the extinction coefficients that describe the amount of light per airmass lost due to atmospheric extinction.

Let  $C_V$ ,  $C_{BV}$ ,  $C_{UB}$ , and  $C_{VR}$  be the first order color terms that measure the shift in color due to atmospheric reddening. More specifically,  $C_V$  measures how much fainter the  $V$  magnitude is due to scattering. (For our purposes, we only use the first order color terms and leave out the second order terms, which are smaller values of no more than magnitude 0.05.)

Let  $Z_V$ ,  $Z_{BV}$ ,  $Z_{UB}$ , and  $Z_{VR}$  be the zero points in the conversion of electron input values from the CCD to photon magnitude outputs. These values measure

---

<sup>41</sup> Hardie, Robert H., "Photoelectric Reductions," *Astronomical Techniques*, ed. William A Hiltner (Chicago: Chicago Press, January 1964), pp. 178.

detector gain (or quantum efficiency) and lock our calibration to the absolute photon flux from the targets.

Hardie's equations for photometric calibration are:

$$V = v - K_V X + Z_V + C_V(B-V)$$

$$B-V = C_{BV}[(b-v) - K_{BV}X] + Z_{BV}$$

$$U-B = C_{UB}[(u-b) - K_{UB}X] + Z_{UB}$$

$$V-R = C_{VR}[(v-r) - K_{VR}X] + Z_{VR}$$

In order to make these conversions from observed to calibrated bandpass magnitudes, we used observations of the same stars at different airmasses ( $X$ ) to calculate the extinction coefficients ( $K$ 's), which are independent of the other variables. We take three clear images (sometimes two, based on weather conditions) of the same area of the sky but taken at different times, so the airmass in each image is different. We identify a distinct star in each image and plot the star's magnitude over the airmass of each image. The slope of the magnitude loss ( $\Delta V$ ) over the airmass equals the extinction coefficient,  $K$ . We carry this procedure out for the four different bandpasses ( $V$ ,  $B-V$ ,  $U-B$ , and  $V-R$ ) to get the four extinction coefficients,  $K_V$ ,  $K_{BV}$ ,  $K_{UB}$ , and  $K_{VR}$ . An example is shown in Figure 24.

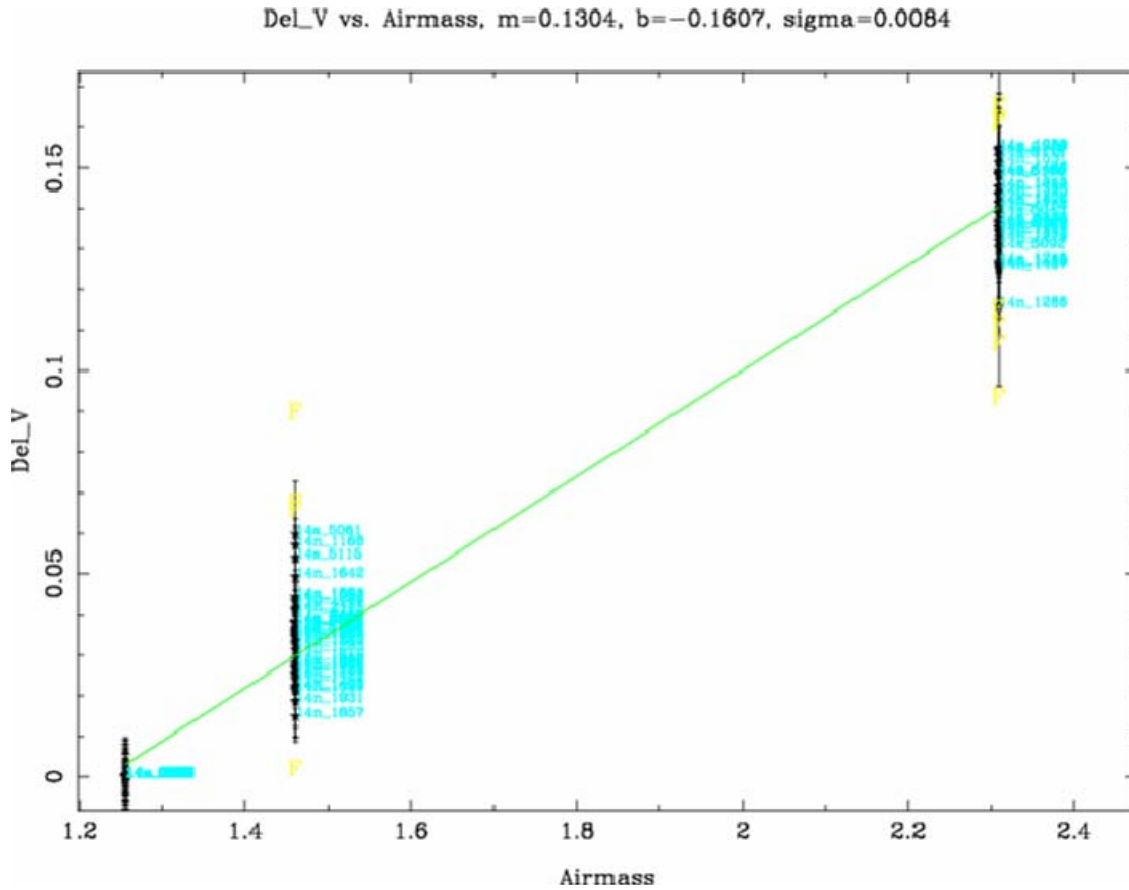


**Figure 24: Stellar Magnitude lost (Del\_V) versus Airmass. The slope of the best fit line is the extinction coefficient,  $K$ .**

To calculate the color terms ( $C$ 's) and zero points ( $Z$ 's), we take observations of stars in a standard field that have been carefully calibrated by previous observers to bootstrap our observations (Figure 25). The slope of the best fit line through the true color to instrumental color plot is the color term,  $C$ , while the intercept of the line is the zero point,  $Z$ .

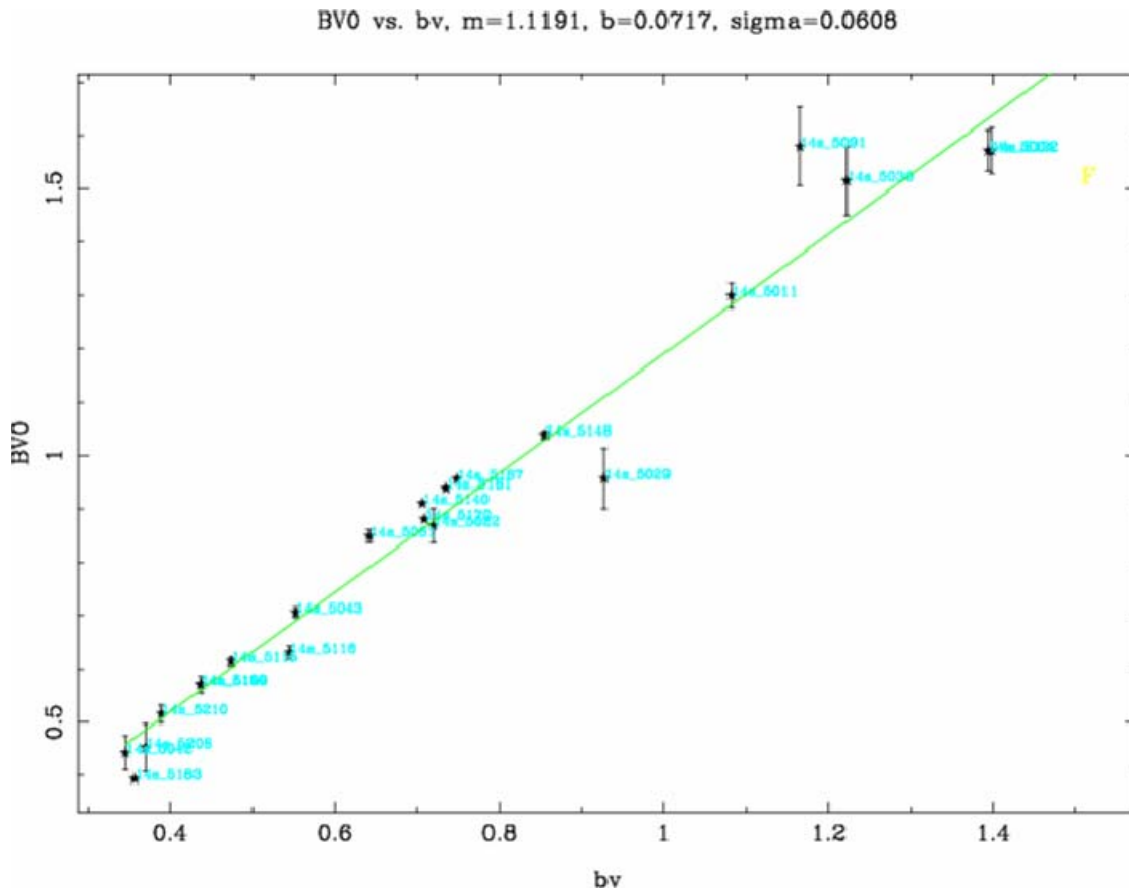


**Figure 25: True color versus instrumental color of standard star fields. The slope is the color term (C), while the y-intercept is the zero point, Z.**

As previously mentioned, we also used differential photometry to gather data on overcast nights. All the stars that we intended to examine were still visible through the CCD but their apparent magnitudes were greatly reduced in brightness. To account for this brightness difference, we took various calibration images on the following, compared the overcast brightness values to the clear values, and added a magnitude offset to the field on the overcast night to find what the apparent brightness should have been if it had been a clear night.

Using our calibration stars and the preceding analysis, we found the following photometric solutions to Hardie's equations during our data reductions:

	$K_V$	$\sigma$ (# of stars)	$K_{B-V}$	$\sigma$ (# of stars)	$K_{V-R}$	$\sigma$ (# of stars)	$K_{U-B}$	$\sigma$ (# of stars)
12-Sep-07	0.1486	0.0341	0.2583	0.0230	0.082	0.0165	0.1495	0.1649
13-Sep-07	0.1968	0.0087	0.1026	0.0343	0.0448	0.0086	0.2597	0.0452
14-Sep-07	0.1369	0.0057	0.1399	0.0118	0.2155	0.0299	0.2972	0.0666

**Table 3: Extinction Coefficients from September 2007 observation run at Kitt Peak, AZ**

	$C_V$ (Sigma)	$Z_V$ (Amp)	$C_{B-V}$ (Sigma)	$Z_{B-V}$ (Amp)	$C_{V-R}$ (Sigma)	$Z_{V-R}$ (Amp)	$C_{U-B}$ (Sigma)	$Z_{U-B}$ (Amp)
12-Sep-07	0.0413	24.753	1.1471	0.0999	0.9128	0.0562	1.0240	-1.4172
13-Sep-07	-0.0469	24.900	1.1840	-0.0903	0.9285	0.1222	0.9682	-1.1059
14-Sep-07	-0.0410	24.7580	1.1748	0.1552	0.9116	0.2575	0.9920	-1.3377

**Table 4: Color Terms from September 2007 observation run at Kitt Peak, AZ**

	$K_V$	$\sigma$ (# of stars)	$K_{B-V}$	$\sigma$ (# of stars)	$K_{V-R}$	$\sigma$ (# of stars)	$K_{U-B}$	$\sigma$ (# of stars)
2-May-08	-0.0473	24.82	1.1178	0.0859	0.9314	0.1687	0.9540	-1.1026
3-May-08	-0.0621	24.76	1.0966	0.1517	-0.9696	0.0988	0.9076	-0.9488
5-May-08	-0.0618	24.77	1.1097	0.1768	0.9658	0.0933	0.9554	-1.1914
6-May-08	-0.0800	24.68	1.0745	0.3668	0.906	0.2741	0.9118	-1.4301

**Table 5: Extinction Coefficients from May 2008 observation run at Kitt Peak, AZ**

	$C_V$ (Sigma)	$Z_V$ (Amp)	$C_{B-V}$ (Sigma)	$Z_{B-V}$ (Amp)	$C_{V-R}$ (Sigma)	$Z_{V-R}$ (Amp)	$C_{U-B}$ (Sigma)	$Z_{U-B}$ (Amp)
2-May-08	0.1613	0.0067	0.0805	0.034	0.0753	0.0186	0.2411	0.1447
3-May-08	0.1653	0.0057	0.0929	0.0307	0.0371	0.0123	0.2045	0.1162
5-May-08	0.1267	0.0011	0.0976	0.0436	0.0352	0.0535	0.2769	0.0750
6-May-08	0.146	0.0088	0.0873	-	0.04	-	0.25	-

**Table 6: Color Terms from May 2008 observation run at Kitt Peak, AZ**

	$K_V$	$K_{B-V}$	$K_{V-R}$	$K_{U-B}$
19-Oct-08	0.05	0.167	0.031	0.238
20-Oct-08	0.666	0.48	0.76	0.76
21-Oct-08	0.237	0.10	0.08	0.26
22-Oct-08	0.179	0.12	0.06	0.23
23-Oct-08	0.198	0.11	0.04	0.26
24-Oct-08	0.22	0.04	0.16	0.15
25-Oct-08	0.16	0.21	0.06	0.27
26-Oct-08	0.10	0.04	0.01	0.34
27-Oct-08	0.15	0.12	0.05	0.24

**Table 7: Extinction Coefficients from October 2008 observation run at La Serena, Chile**

	$C_V$ (Sigma)	$Z_V$ (Amp)	$C_{B-V}$ (Sigma)	$Z_{B-V}$ (Amp)	$C_{V-R}$ (Sigma)	$Z_{V-R}$ (Amp)	$C_{U-B}$ (Sigma)	$Z_{U-B}$ (Amp)
19-Oct-08	0.0843	23.057	0.8268	-0.0799	0.9	0.1048	0.9128	-0.9072
21-Oct-08	0.1002	23.126	0.8803	-0.1806	0.9321	0.1649	0.8929	-0.8351
22-Oct-08	0.1029	23.0106	0.8258	-0.0547	0.9535	0.0931	0.9387	-1.0675
23-Oct-08	0.0759	23.0161	0.7975	-0.0562	0.9184	0.1085	0.8016	-0.7008
25-Oct-08	0.0942	23.0428	0.8868	-0.1409	0.9087	0.1808	0.8109	-0.8777
26-Oct-08	0.117	22.9445	0.8473	-0.1127	0.8888	0.1498	1.1905	-1.3043
27-Oct-08	0.0998	22.9726	0.8674	-0.1474	0.8806	0.1417	0.9038	-0.8457

**Table 8: Color Terms from October 2008 observation run at La Serena, Chile**

Although there is some variation among the observed values depending on weather conditions for each night, our values were consistent with the average values that we should find at USNO at Kitt Peak, AZ:

$C_V$	$=$	$-0.02$	$K_V$	$=$	$0.15$
$C_{BV}$	$=$	$1.14$	$K_{BV}$	$=$	$0.11$
$C_{VR}$	$=$	$0.95$	$K_{VR}$	$=$	$0.05$
$C_{UB}$	$=$	$0.90$	$K_{UB}$	$=$	$0.25$

as well as the values for CTIO near La Serena, Chile:

$C_V$	$=$	$0.096$	$K_V$	$=$	$0.163$
$C_{BV}$	$=$	$0.847$	$K_{BV}$	$=$	$0.123$
$C_{VR}$	$=$	$0.912$	$K_{VR}$	$=$	$0.052$
$C_{UB}$	$=$	$0.877$	$K_{UB}$	$=$	$0.245$

### 3.3 Star-Galaxy Discrimination

One of the difficulties in observing stars in vast regions of the sky is distinguishing between stars and galaxies. Although galaxies are composed of billions of stars, they are located much farther away and can sometimes be confused with stars. However, we can generally distinguish between the two based on their angular width. For a star with a diameter of  $10^8\text{m}$  located between  $10^{16}\text{m}$  and  $10^{19}\text{m}$  away, the expected angular size is:

$$\theta = \text{size} / \text{distance} = 10^8\text{m} / (1-1000) \times 10^{16}\text{m} = 10^{-8} \text{ to } 10^{-11} \text{ radians}$$

On the other hand, a typical galaxy with a diameter of 100,000 light-years located between 50 and 10,000 light-years away has an angular size of:

$$\theta = \text{size} / \text{distance} = 10^5\text{Ly} / (50-10000) \times 10^6\text{Ly} = 10^{-3} \text{ to } 10^{-6} \text{ radians}$$

Even though galaxies are located much farther away from our position than stars, galaxies nevertheless tend to have a much larger angular size than stars, on the order of two to eight orders of magnitude. A pixel in a CCD camera has a width of 0.6 arc minutes, or  $2.9 \times 10^{-6}$  radians. A star should take up only a single pixel of space on a CCD (what is called a “point object”) while a galaxy will take up multiple pixels (“extended object”). However, atmospheric bulk motions and diffraction limits both cause smear across our images.

The size of objects on a CCD are measured by the full width at half maximum (FWHM), which equals the distance from one-half the peak value through the peak to the half-value point on the opposite side (Figure 26). Atmospheric seeing obviously highly smears the point objects far more than the already extended objects. Figure 15 shows the digital image of a galaxy with a FWHM of 6 pixels, while Figure 16 shows a star that has



been smeared out to have a FWHM of 4.2 pixels. Given the similar FWHM values, it is sometimes not easy to distinguish between galaxies and smeared stars, but this technique helps: All point objects will smear identically while extended objects will smear non-uniformly.

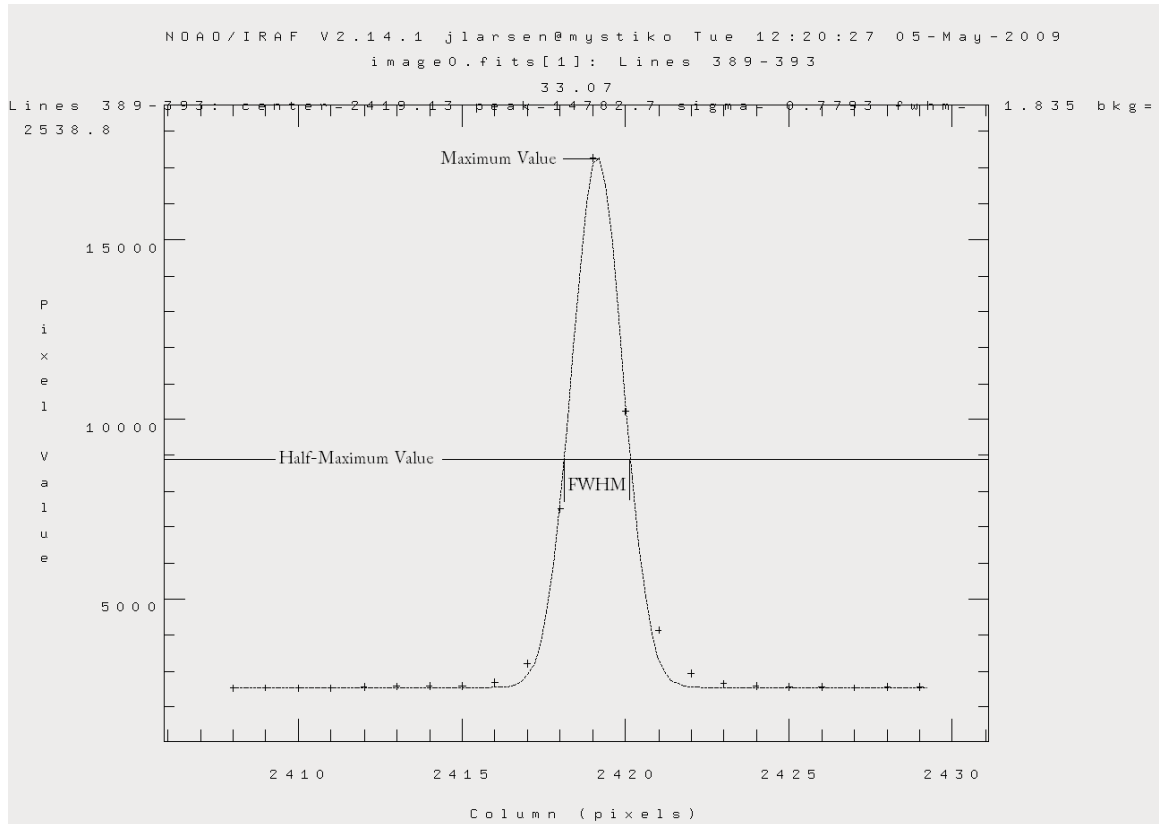


**Figure 26: Diagram of the FWHM**

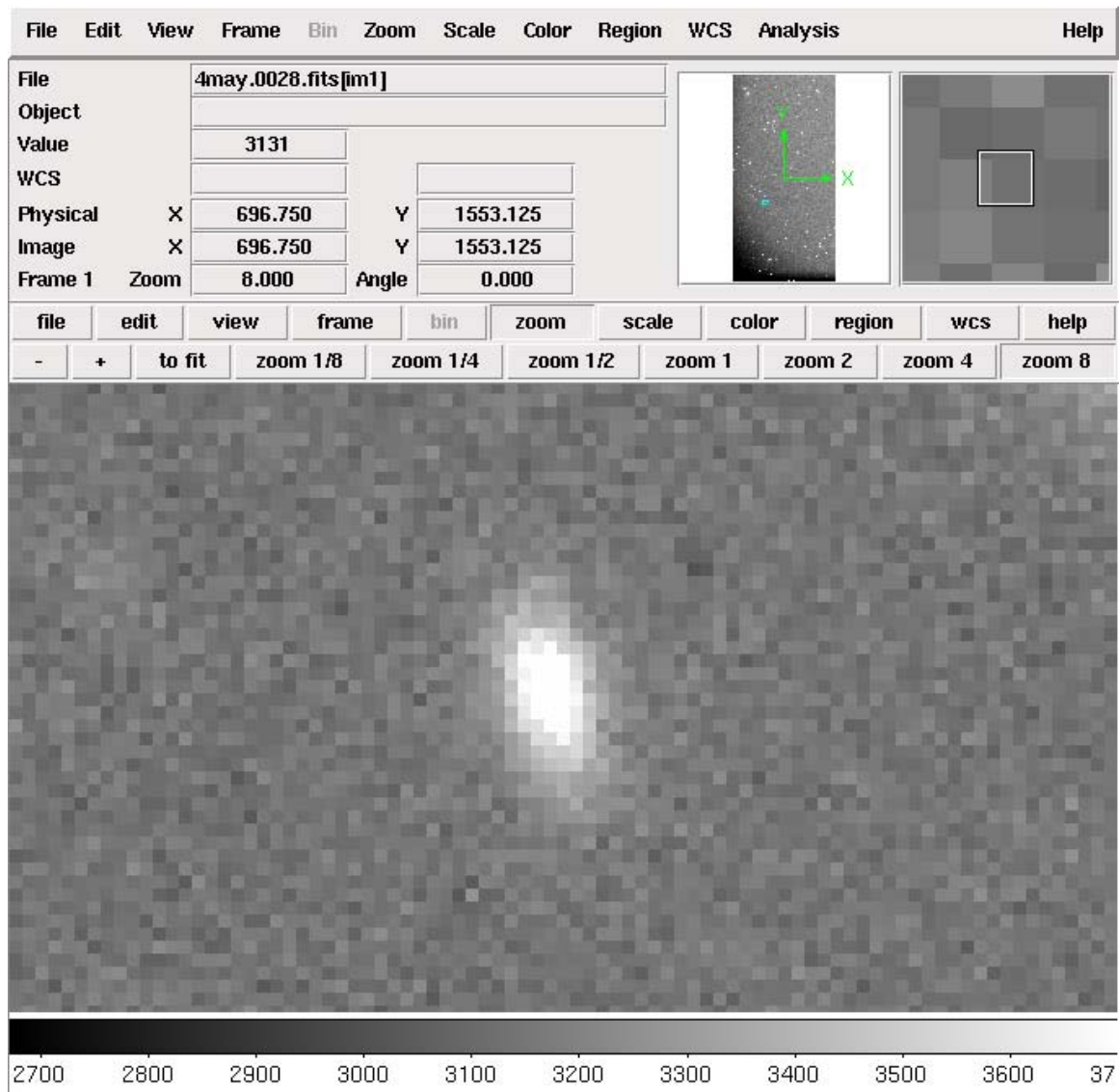
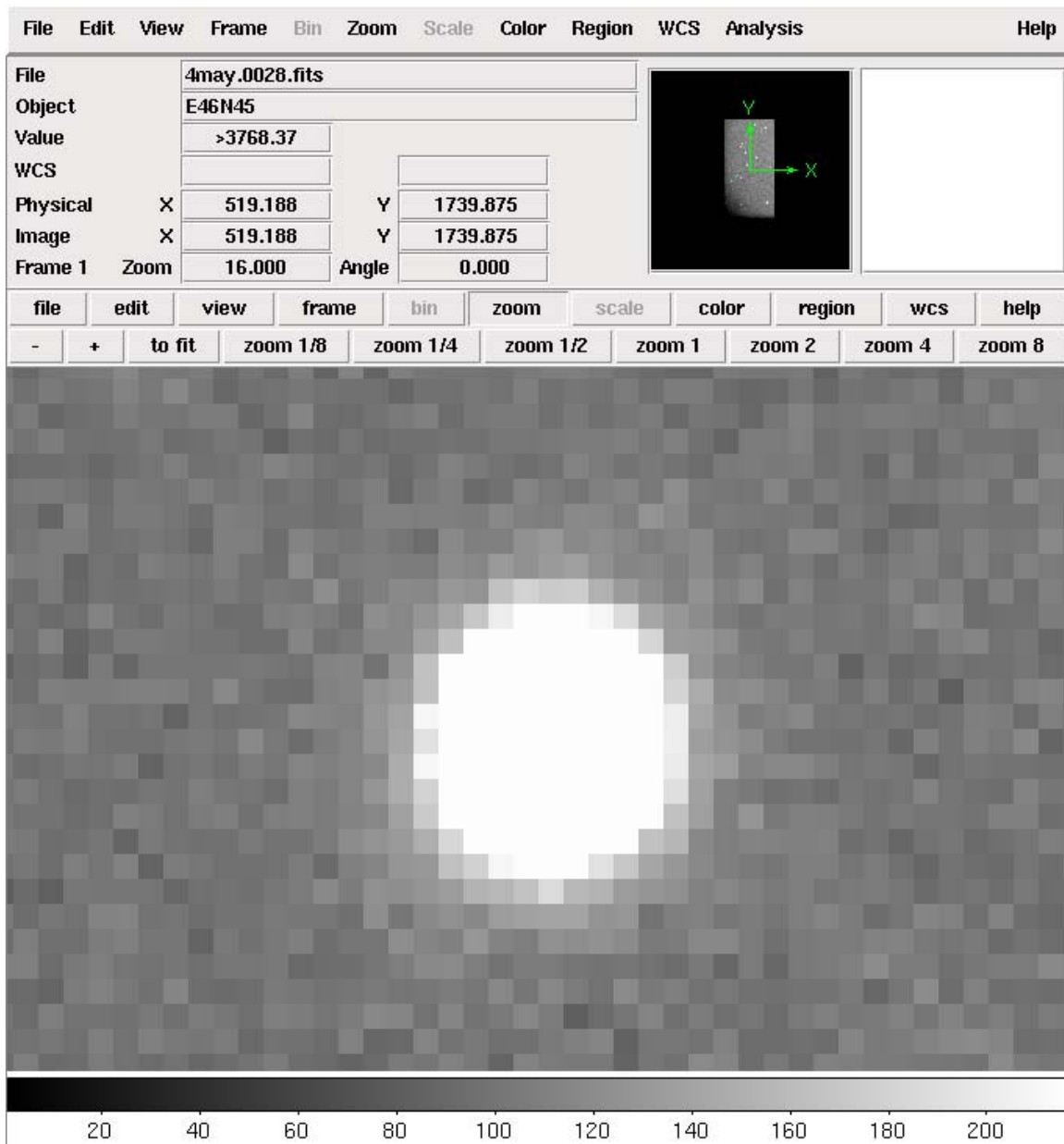


Figure 27: CCD image of a galaxy with a FWHM of 6 pixels. The distinctive vertical oval shape is the galaxy's disk.



**Figure 28: CCD image of a star with a FWHM of 4.2 pixels. The star's core gives it its round shape and atmospheric effects smear the image out.**

Most of the contaminating factors that confuse the star and galaxy populations can be removed by examining image parameters to look for deviations from the point star trend. We isolated three parameter spaces that we used to separate the populations in a

program called autocalib.pl and Haviland performed the actual classification for all images.

### 1. *Maximum Surface Brightness versus Area*

Due to smearing, stars have light profiles that peak near the image center while galaxies have a more uniform brightness across a given area. Therefore, if star and galaxy profiles of the same size are examined, the galaxies will be fainter. The separation of star-galaxy populations along this parameter space is shown in Figure 29. As one moves up the plot at a given area (for example, at 2000 pixels on the horizontal axis), galaxies are located above the locus and stars are below it.

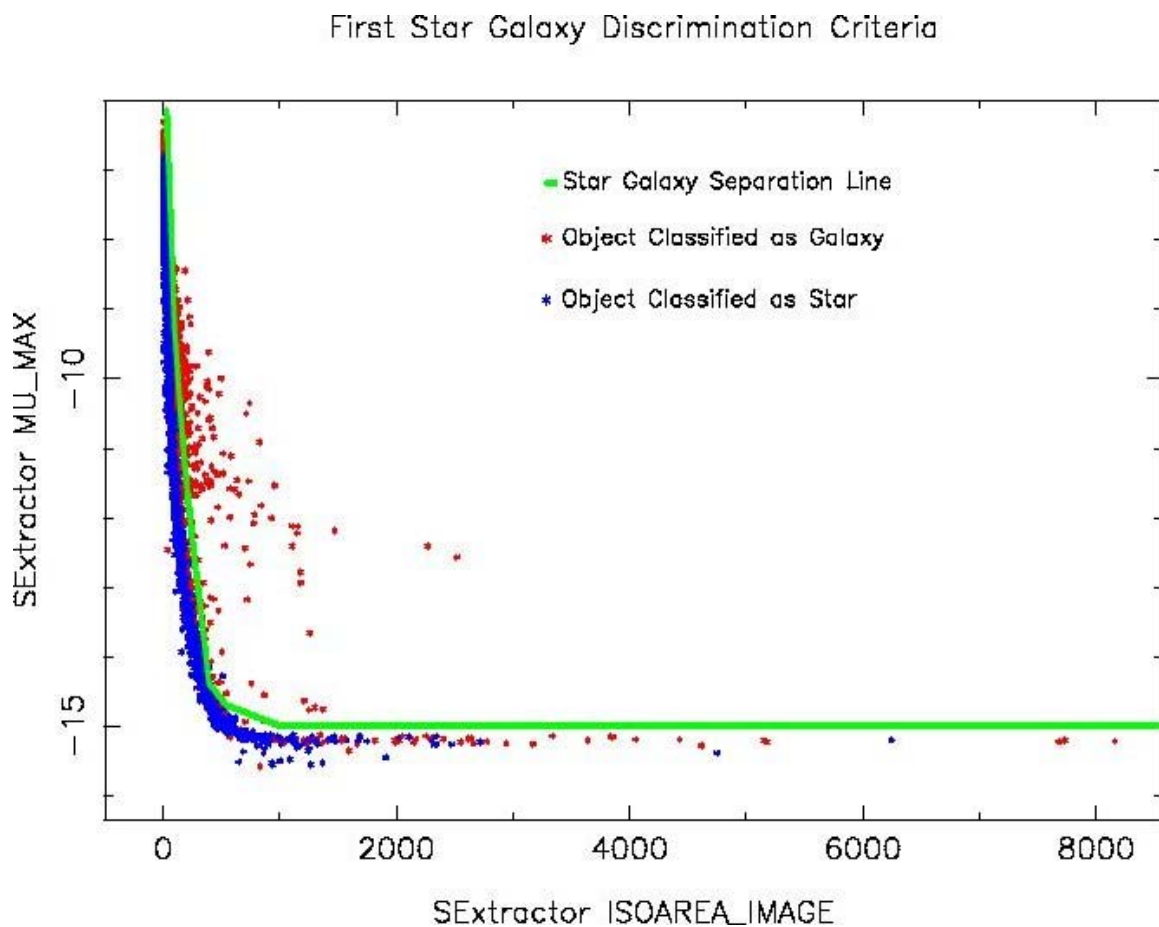


**Figure 29: Star-Galaxy Test on Maximum Surface Brightness versus Area**

## 2. *Isophotal Magnitude versus Aperture Magnitude*

Isophotal magnitude is magnitude over the entire object. Aperture magnitude is the magnitude over a particular, predefined area of the sky, in this case equal to two times the FWHM of an average star. Since galaxies can have light spread out across a larger area than this aperture, the aperture magnitude will be fainter for galaxies than for stars because galaxies are missing more light. This parameter space is shown in Figure 30:

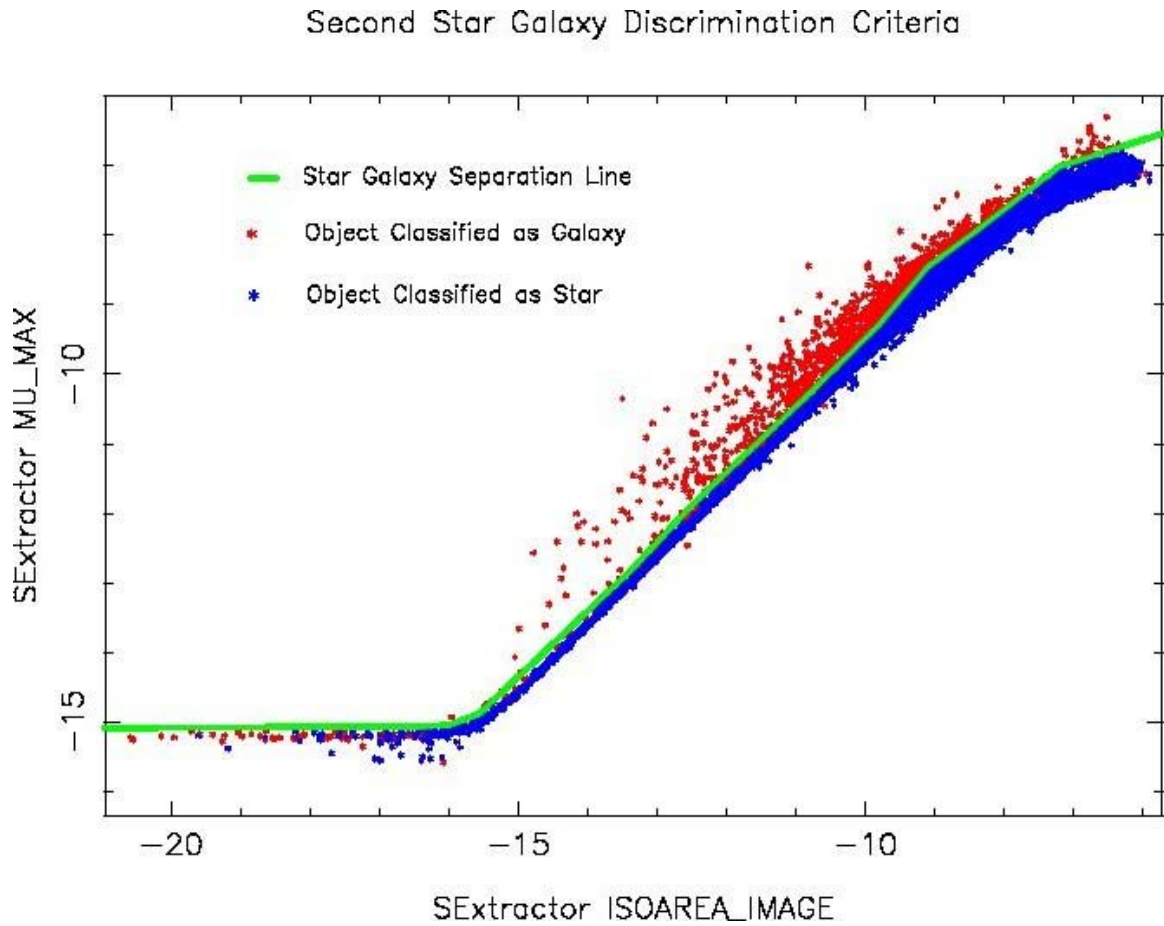


**Figure 30: Star-Galaxy Test on Isophotal Magnitude versus Aperture Magnitude**

### 3. XY Image Moment versus Peak Surface Brightness

As point objects, stars are relatively round, even when smeared out, while galaxies take on different shapes and therefore have very different XY moments of the intensity distribution. This parameter space is shown in Figure 31.

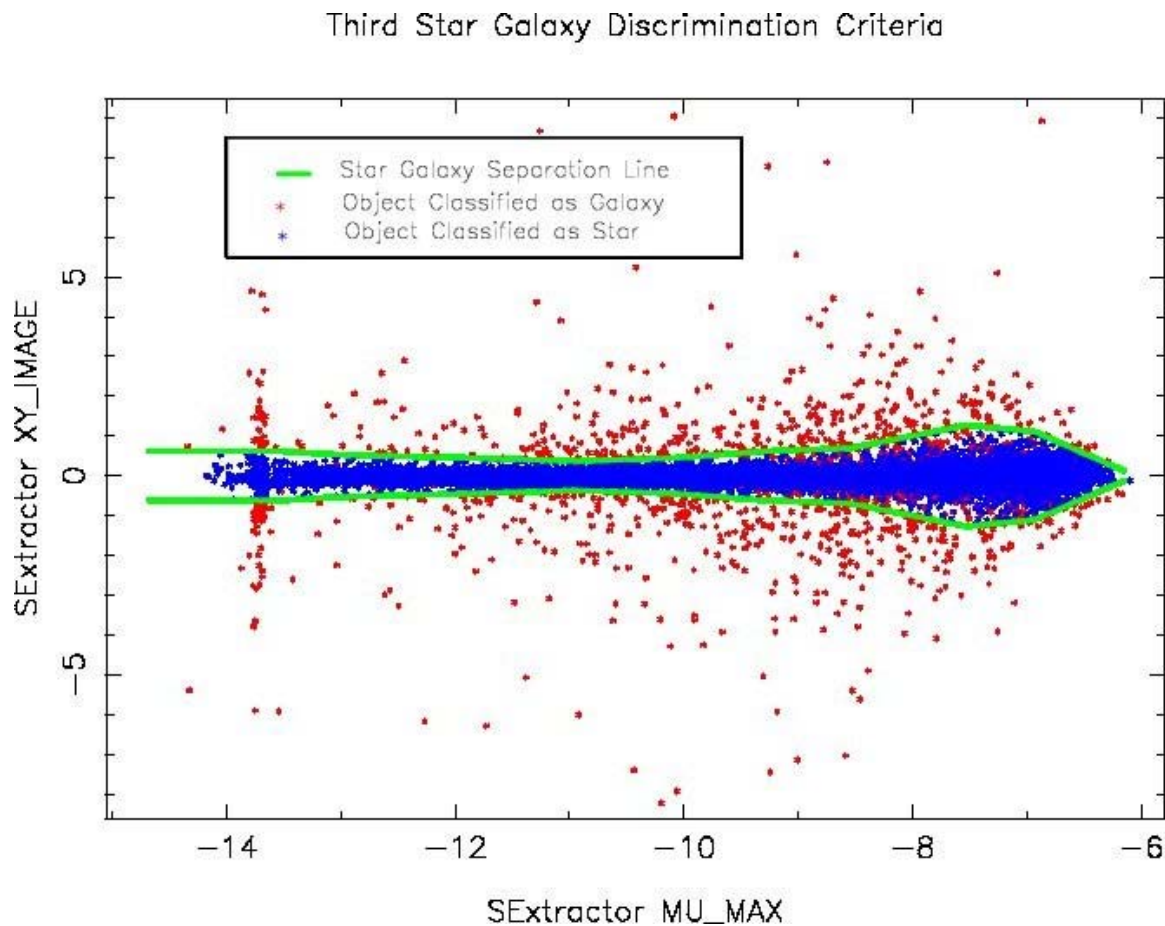


**Figure 31: Star-Galaxy Test on XY Image Moment versus Peak Surface Brightness.** Objects at zero on the vertical axis are perfectly round. Objects further to the right on the horizontal axis are fainter than objects to the left. The objects located around the bulge on the right of the figure are images that have a greater chance of statistical variation.

I conducted these tests on images in the R and V color bands and used the computer program autocalib.pl to draw in the star-galaxy cutoff line in each of these three

parameter spaces. Each image was examined four different times in each of the parameter spaces and with each of the three tests for 12 total tests. In each test, we assigned each star candidate the number zero and each galaxy candidate the number 1. The final “score” for an object is the average of these numbers over the 12 tests and appears as one of the columns in the stellar catalog. In the final analysis, all objects with a score of less than 0.4 were considered to be stars, while those with scores of 0.4 or higher were discarded as galaxies.

### 3.4 Catalog Creation and Star Counts

Following star-galaxy discrimination, Larsen also performed final astrometric calibrations on the images using a customized version of his MOSSUR package from Spacewatch for the 90 Prime and Y4KCam instruments. The calibrations involved using the USNO-B 1.0 catalog to identify catalog stars and a 13-term polynomial to map out right ascension and declination on the images (allowing for cross terms and distortion on the edges of the images).

The actual object detection and generation of the stellar catalogs required the use of a software program called Source Extractor (or SExtractor) developed by Bertin and Arnouts in 1996.<sup>42</sup> We applied the program to each of the calibrated images, which then identified objects in the images (Figure 32), analyzed the objects, and organized them into a catalog. SExtractor works by taking previously calibrated images and matching the objects among the four different color filter images. By comparing the magnitudes of a star at different color values, the program is able to find the overall color and stellar classification of the star. The magnitudes at different colors, along with the position, are incorporated into the stellar catalog through cross matching.

A sample catalog is shown in Table 3 and the stars are organized by numerical name, right ascension, declination, apparent V magnitude, U-B color, B-V color, and V-R color. The error for each of these columns is also included. Whenever a star does not have any color reading within a particular range, the value 99.99 is inserted to rule out any analysis of the value in the computer program.

---

<sup>42</sup> Bertin, E. and S. Arnouts. "SExtractor: Software for source extraction." *Astronomy and Astrophysics Supplement*, v. 117, June 1996, p. 393-404.



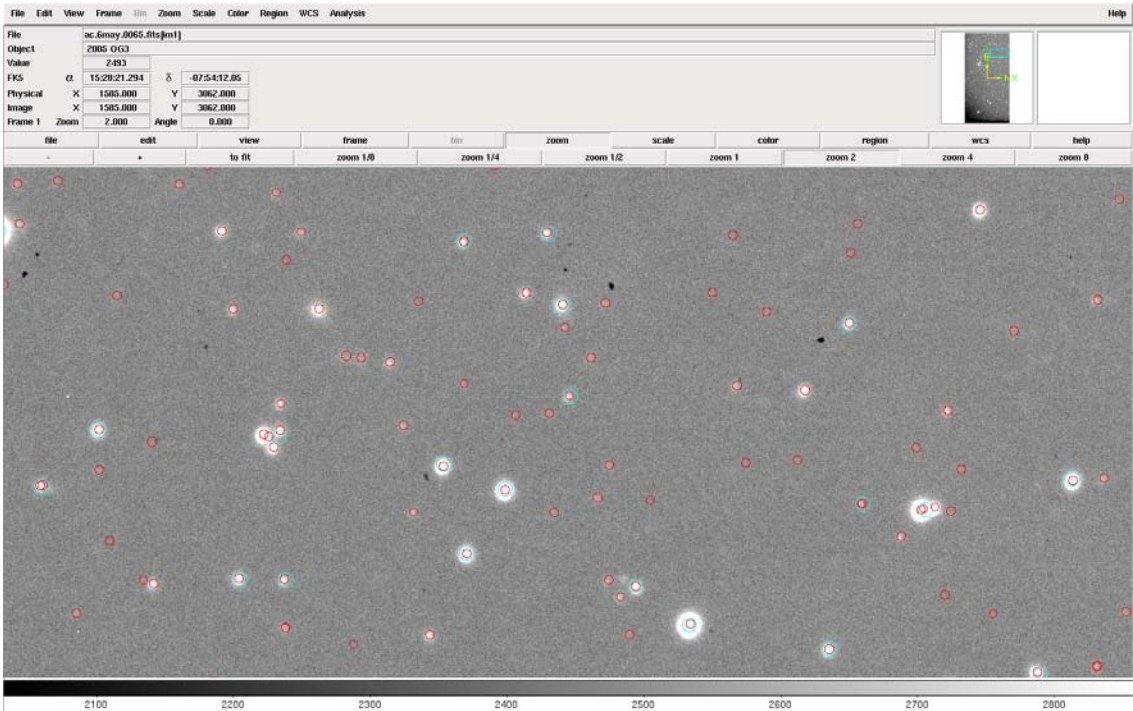


**Figure 32:** The SExtractor program analyzes images, identifies objects, and sorts the object data into a stellar catalog, as in Table 9.

Name	RA	Dec	err(RA)	err(Dec)	S/G test	V mag	err	UB	err	BV	err	VR	err	s/g	
000001	258.708096	-2.034296	0.000072	0.000015	00.00	4	22.24	00.12	99.99	99.99	-0.76	00.14	02.29	00.11	1
000002	258.708241	-2.096549	0.000041	0.000012	00.00	4	22.28	00.16	99.99	99.99	00.06	00.21	01.29	00.17	1
000003	258.708347	-1.968896	0.000094	0.000014	00.00	4	21.72	00.09	99.99	99.99	-0.84	00.10	02.35	00.08	1
000004	258.708578	-1.972424	0.000031	0.000025	00.00	4	21.32	00.07	99.99	99.99	01.64	00.20	02.02	00.08	1
000005	258.708601	-1.947149	0.000061	0.000044	00.00	4	21.56	00.09	99.99	99.99	00.37	00.14	01.59	00.09	1
000006	258.708689	-2.261104	0.000029	0.000021	00.00	4	21.56	00.10	99.99	99.99	01.19	00.19	01.22	00.11	1
000007	258.708691	-2.280543	0.000028	0.000025	00.00	3	22.28	00.15	99.99	99.99	01.94	00.13	01.65	00.16	1
000008	258.708851	-2.352433	0.000038	0.000030	00.00	4	21.74	00.11	99.99	99.99	01.56	00.10	01.18	00.12	1
000009	258.708920	-2.108061	0.000069	0.000017	00.00	4	22.58	00.17	99.99	99.99	01.43	00.17	01.03	00.21	1
000010	258.708944	-2.257450	0.000042	0.000034	00.05	4	22.78	00.17	99.99	99.99	01.49	00.16	01.09	00.20	1
000011	258.708994	-2.289925	0.000017	0.000011	00.00	3	18.04	00.01	00.01	00.02	00.89	00.01	00.65	00.01	1
000012	258.709105	-1.989559	0.000018	0.000011	00.00	4	19.25	00.02	99.99	99.99	01.41	00.05	01.01	00.02	1
000013	258.709111	-2.372904	0.000034	0.000027	00.00	4	19.24	00.02	00.83	00.17	01.16	00.03	00.84	00.02	1
000014	258.709147	-1.879641	0.000040	0.000004	00.05	4	16.63	00.00	01.27	00.02	01.13	00.00	00.95	00.00	1
000015	258.709197	-1.875621	0.000032	0.000009	00.05	4	17.77	00.00	00.35	00.02	00.77	00.01	00.78	00.01	1
000016	258.709288	-1.944704	0.000020	0.000010	00.00	4	21.60	00.11	99.99	99.99	02.12	00.09	01.89	00.11	1
000017	258.709345	-2.206680	0.000023	0.000021	00.00	3	22.79	00.24	99.99	99.99	01.94	00.20	01.65	00.25	1
000018	258.709378	-2.063034	0.000037	0.000023	00.00	4	22.28	00.15	99.99	99.99	00.65	00.24	01.17	00.17	1
000019	258.709467	-1.985162	0.000029	0.000029	00.00	4	21.12	00.08	99.99	99.99	00.73	00.14	00.86	00.09	1
000020	258.709508	-2.363133	0.000079	0.000103	00.00	4	21.52	00.09	00.39	00.28	00.99	00.16	01.02	00.11	1
000021	258.709518	-1.923353	0.000017	0.000014	00.15	4	17.19	00.00	00.45	00.02	00.96	00.01	00.68	00.00	1
000022	258.709574	-1.960198	0.000015	0.000014	00.00	4	19.21	00.02	00.45	00.08	00.70	00.03	00.69	00.02	1
000023	258.709613	-2.157168	0.000036	0.000049	00.00	4	22.05	00.13	99.99	99.99	01.02	00.22	00.81	00.16	1
000024	258.709627	-2.199309	0.000031	0.000023	00.00	4	19.27	00.02	01.21	00.16	01.00	00.04	00.86	00.02	1
000025	258.710040	-2.231960	0.000027	0.000071	00.00	4	20.78	00.06	00.21	00.19	00.82	00.10	00.90	00.07	1
000026	258.710066	-1.977393	0.000020	0.000029	00.00	4	21.56	00.10	99.99	99.99	01.67	00.10	01.34	00.12	1
000027	258.710194	-2.021233	0.000034	0.000029	00.00	4	21.52	00.10	99.99	99.99	00.59	00.16	00.89	00.13	1
000028	258.710291	-1.941738	0.000024	0.000012	00.00	3	22.86	00.21	99.99	99.99	02.49	00.17	02.35	00.21	1
000029	258.710315	-1.883793	0.000009	0.000024	00.00	4	21.95	00.13	99.99	99.99	01.48	00.12	01.10	00.15	1
000030	258.710339	-2.175036	0.000031	0.000015	00.00	4	19.00	00.01	01.02	00.13	01.04	00.03	00.78	00.02	1
000031	258.710395	-2.311612	0.000094	0.000052	00.00	4	21.75	00.11	99.99	99.99	01.62	00.10	01.26	00.12	1
000032	258.710484	-2.170825	0.000029	0.000009	00.00	3	22.69	00.24	99.99	99.99	01.84	00.21	01.53	00.26	1
000033	258.710515	-1.928709	0.000030	0.000018	00.00	4	21.04	00.07	99.99	99.99	00.79	00.13	00.75	00.09	1
000034	258.710573	-2.365600	0.000053	0.000059	00.05	4	22.83	00.33	99.99	99.99	01.71	00.28	01.37	00.35	1

"E20N20.gen3.finalcat" 37036 lines, 3925818 characters written

**Table 9: Sample Stellar Catalog Data from the field E20N20, showing right ascension, declination, U-B, B-V, and V-R color, and the star/galaxy test.**

Tables 10 and 11 summarize the directions to all observed fields used in this project, as well as the size of the observed field and the date and location at which the fields were observed. KPNO stands for the Kitt Peak National Observatory in Arizona while CTIO stands for the Cerro Tololo Inter-American Observatory in Chile.

Field	Date Observed	Telescope	Field size (square degrees)	# of objects	Right Ascension (J2000)	Declination	Galactic longitude (l)	Galactic latitude (b)
E20N20	May 2006	KPNO	1.02	37036	259.3	-1.78	20.63	18.79
E20N32	May 2006	KPNO	1.02	22228	248.87	4.16	20.53	30.79
E20S47	October 2008	CTIO	0.84	7758	324.1	-28.01	21.01	-48.24
E23N40	May 2008	KPNO	0.75	15191	243.01	9.99	23.34	38.68
E25N40	May 2006	KPNO	1.02	18869	243.61	11.48	27.31	35.71
E25S40	October 2008	CTIO	0.95	9984	317.5	-22.78	26.04	-41.16
E27N37	May 2008	KPNO	0.75	13695	247.16	11.48	25.38	38.83
E27S37	October 2008	CTIO	0.84	9753	315.02	-20.33	28.09	-38.19
E30N20	May 2006	KPNO	1.02	54106	263.68	6.49	30.51	18.89
E33N40	May 2008	KPNO	0.75	11538	246.11	16.62	32.67	38.75
E33S40	October 2008	CTIO	0.53	5143	319.84	-17.04	34.21	-41.28
E35N32	May 2006	KPNO	1.02	27412	254.53	15.58	35.34	30.89
E35S32	May 2006	KPNO	1.02	24987	312.67	-12.39	36.06	-33.06
E42N40	May 2006	KPNO	1.02	21436	248.53	23.59	42.09	38.99
E44N40	September 2007	KPNO	0.75	9228	249.09	24.96	43.97	38.9
E45N20	May 2006	KPNO	1.02	49282	269.74	19.31	45.43	19.02
E45S20	May 2006	KPNO	1.02	41543	306.09	1.08	45.9	-20.96
E48N45	May 2008	KPNO	0.75	12108	244.28	28.6	47.26	43.96
E50N31	May 2006	KPNO	1.02	26739	260.16	27.32	50.23	30.09
E50S31	May 2006	KPNO	1.02	27056	317.82	-0.64	51.19	-31.87
E53N42	May 2008	KPNO	0.75	8900	248.52	32.02	52.77	41.03
E55N42	May 2006	KPNO	1.02	21255	248.65	33.61	54.87	41.2
E55S42	October 2008	CTIO	0.74	5681	329.34	-3.2	56.67	-42.84
E60N20	May 2006	KPNO	1.02	35504	275.42	32.42	60.32	19.27
E60S20	May 2006	KPNO	1.02	40657	313.67	12.99	61.06	-20.69
E65N31	May 2006	KPNO	1.02	28576	263.82	39.78	65.08	30.36
E75N20	May 2006	KPNO	1.02	39162	281.47	45.73	75.28	19.54

**Table 10: Summary of Observed Quadrant 1 Fields used in this project**

Field	Date	Telescope	Field size (square degrees)	# of objects	Right Ascension (J2000)	Declination	Galactic longitude (l)	Galactic latitude (b)
W20N20	April 2006	CTIO	0.95	20773	234.07	-30.77	340.86	18.91
W20N32	May 2006	KPNO	1.02	18031	226.12	-21.17	341.02	30.87
W20N47	May 2008	KPNO	0.75	9277	217.55	-8.8	341.29	45.74
W20S20	May 2006	KPNO	1.02	25640	279.09	-55.39	340.52	-21.09
W25N40	May 2006	KPNO	1.02	13315	217.95	-16.53	336.19	38.97
W25S40	October 2008	CTIO	0.53	4620	317.31	-60.51	335.17	-41.18
W27N37	May 2008	KPNO	0.75	10870	218.16	-20.06	334.21	35.81
W27S37	October 2008	CTIO	0.21	1377	314.61	-20.2	28.09	-37.78
W30N20	April 2006	CTIO	0.95	23465	224.84	-36.09	330.97	18.98
W30S20	May 2006	KPNO	1.02	22356	272.72	-64.23	330.46	-21.01
W33N40	May 2008	KPNO	0.75	10573	212.69	-19.21	328.9	38.88
W35N32	April 2006	CTIO	0.95	8554	213.88	-27.27	326.19	31.05
W35S32	October 2008	CTIO	0.95	12473	302.57	-70.19	325.23	-32.97
W42N40	April 2006	CTIO	0.95	11850	205.24	-21.43	319.46	39.17
W42S40	October 2008	CTIO	0.95	5383	333.21	-72.04	317.77	-40.98
W45N20	April 2006	CTIO	0.95	18530	208.18	-41.43	316.13	19.22
W45S20	October 2008	CTIO	0.95	20134	252.84	-76.83	315.4	-20.79
W50N31	April 2006	CTIO	0.95	9504	199.95	-31.5	311.27	30.3
W53N32	May 2008	KPNO	0.75	6380	196.2	-20.92	308.74	41.21
W55N42	April 2006	CTIO	0.95	13274	194.53	-20.87	306.66	41.38
W60N20	April 2006	CTIO	0.95	11953	189.14	-42.79	301.12	19.5
W60S20	April 2006	CTIO	0.95	11192	172.17	-82.32	300.34	-20.41
W65N31	April 2006	CTIO	0.95	5317	184.91	-31.38	296.39	30.6
W65S31	October 2008	CTIO	0.95	4275	71.92	-82.02	294.95	-31.39
W75N20	April 2006	CTIO	0.95	8745	170.75	-39.76	286.13	19.82
W75S20	May 2008	KPNO	0.75	11222	122.79	-72.18	285.37	-20.14

**Table 11: Summary of Observed Quadrant 4 Fields used in this project**

## Chapter 4: Data Analysis

### 4.1 Analysis of Count Ratios

Our goal was to differentiate between three theories for the excess: a galactic merger, interaction with the Stellar Bar rotation, and triaxial shape in the Galactic thick disk. The causes and expected signatures for each of the origins are:

1. If the asymmetry were caused by a galactic merger, we would probably see the excess in only one quadrant. The merger could be passing through the Galactic Plane, but it is unlikely that it would be on either side of the Plane in equal amounts.
2. If the origin involved the rotation of the stellar bar, the asymmetry would only be at galactic longitudes of  $45^\circ$  or less and would extend both above and below the Galactic Plane or closer to the Galactic center.
3. If a previously unknown triaxial shape exists in the thick disk, we would see the asymmetry existing both above and below the Galactic Plane and extending to large distances from the center of the Galaxy.

To explore these hypotheses, we counted ratios from 11 fields from the highest longitudes, whose distribution is shown in Figure 33. A count ratio is simply the number of stars in one field divided by the number of stars in another. To make the comparison equal, we selected stars for the ratio from a restricted range of color and magnitude. The number must also be normalized by the area on the sky if they are not equal.

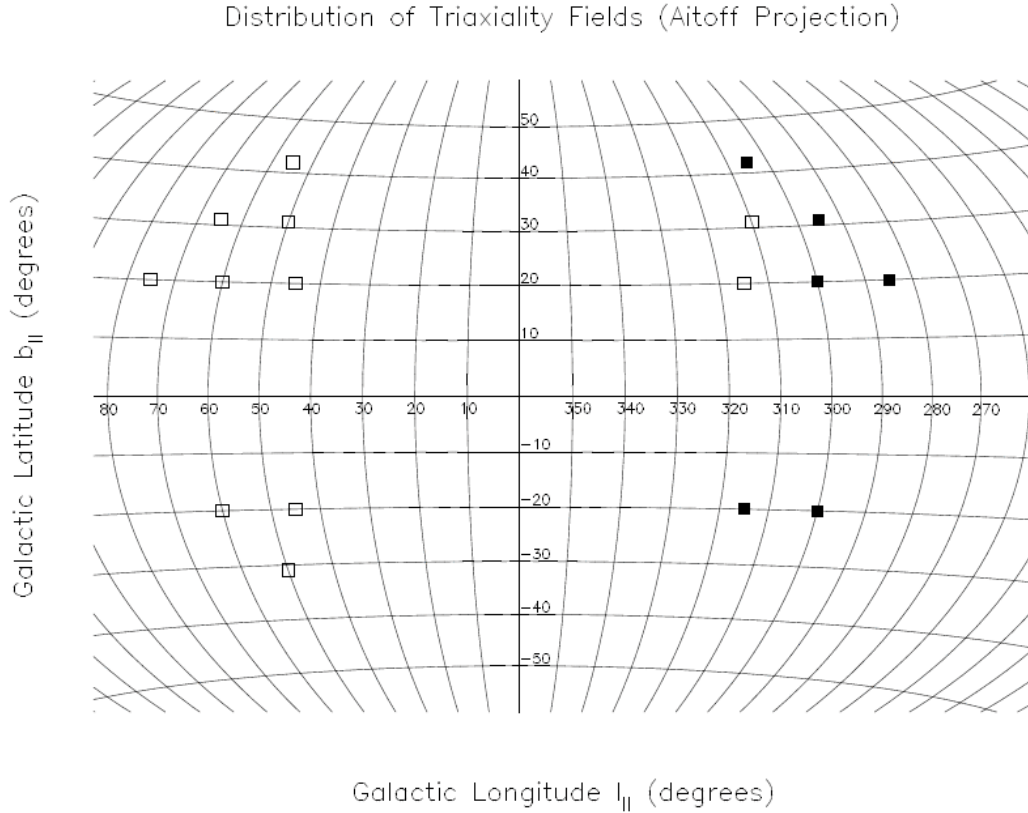


**Figure 33: Aitoff projection of the stellar fields analyzed for the ratio study**

We computed our ratios with certain cuts for volume and magnitude. For magnitude, we used  $16 < V < 19$ ,  $17 < V < 18$ , and  $18 < V < 19$ . The bright ranges were necessary because the CTIO fields tend to not probe as faint as the KPNO fields. For the color cuts, we observed the stars in this range and counted the stars between  $B-V = -2$  (where no stars are observed in all fields) and an identifiable feature on each image. For our project, we decided to identify the peak  $B-V$  color in each image as our upper color limit, since it contains a reasonable number of thick disk stars. We wrote a computer program that binned selected stars by color and magnitude, then found the peak bin. If the bin to the left was lower than the bin to the right, we extrapolated the peak color as lying closer to the right of the peak bin. This computer program, although never exact,

has proved to be the most accurate method to estimate the peak color. Figure 34 shows the medial color bin diagram for the field E20N20, where the B-V peak color is 0.80.

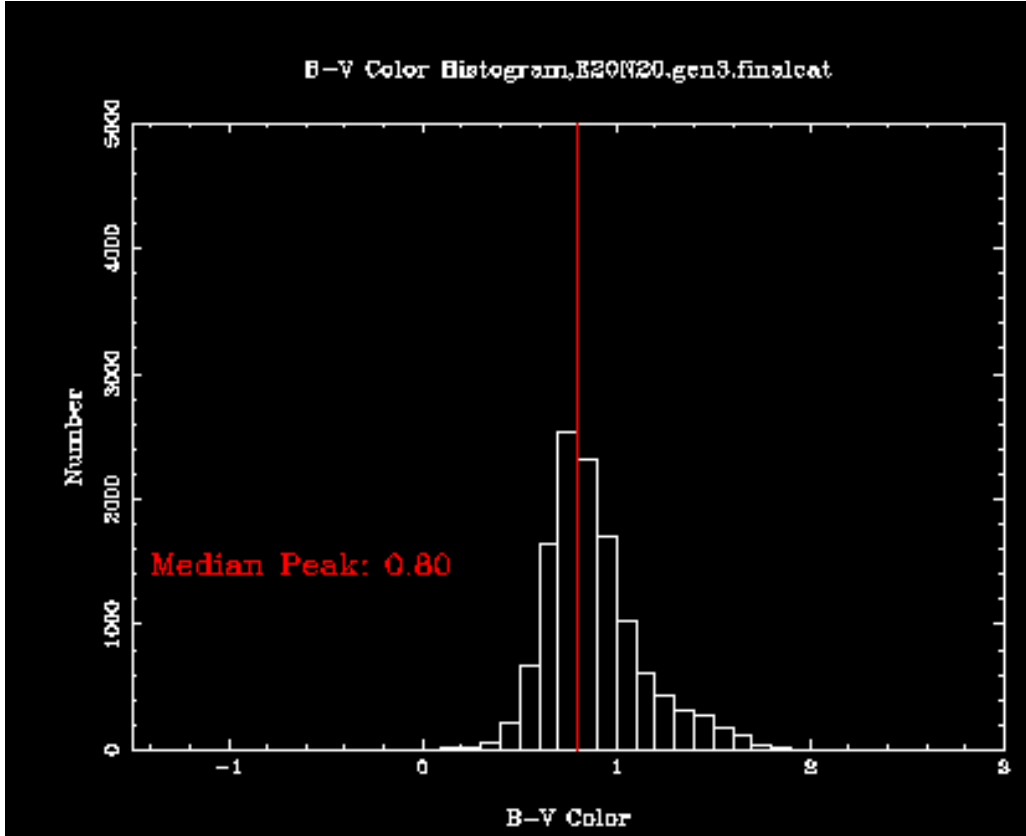


Figure 34: Color bin analysis of the field E20N20, used to find the peak color by analyzing the median color bins.

After developing this technique, we created a PerlScript-based program that counted the number of stars between  $B-V = -2$  and the peak  $B-V$  color as well as between two magnitude limits. The program, entitled `completepeak.pl` (see Appendix D), counted stars over the magnitude ranges  $16 < V < 19$ ,  $16 < V < 17$ ,  $17 < V < 18$ , and  $18 < V < 19$  and gave a numerical value with counting and systematic errors. We then used these numbers to develop star count ratios of complementary fields of Quadrants 1 and 4, as well as the northern and southern quadrants.

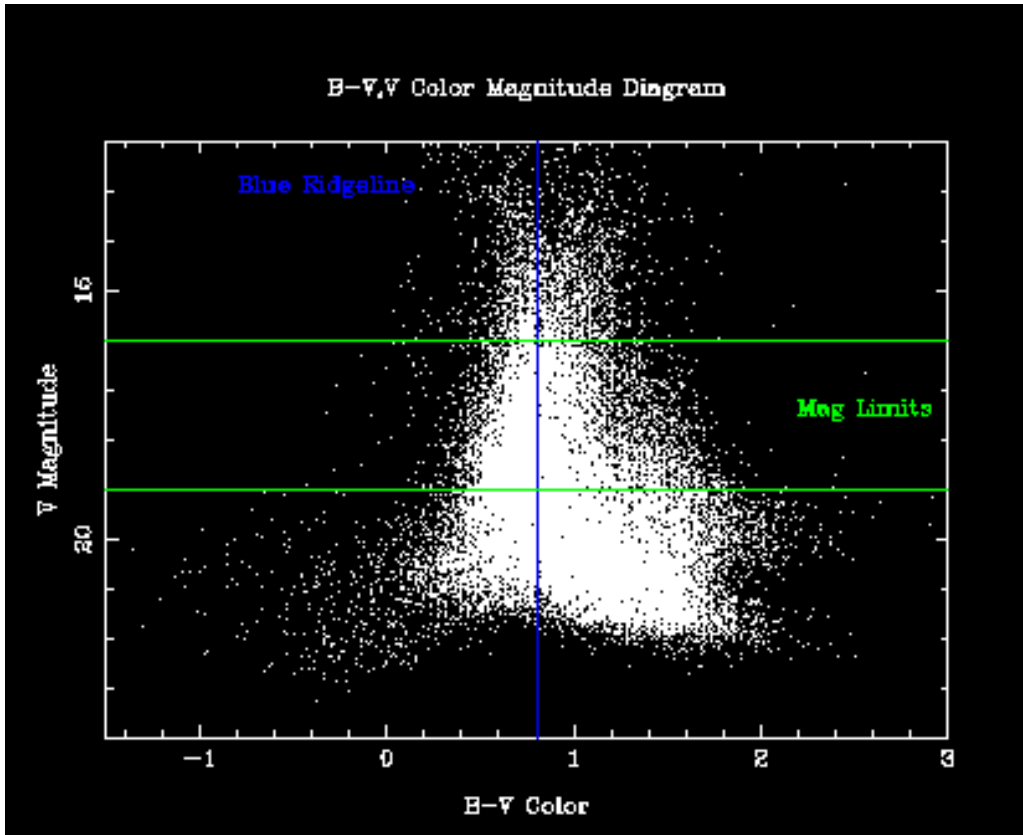


Figure 35: Magnitude-Color Diagram of the field E20E20 covering magnitudes  $16 < V < 19$ . The horizontal lines represent the magnitudes limits, while the vertical line represents the peak color.



Field Ratio	$l_1 / l_2$	$b_1 / b_2$	GALMOD Ratio Predictions			Observed Count Ratios		
			$16 < V < 19$	$17 < V < 18$	$18 < V < 19$	$16 < V < 19$	$17 < V < 18$	$18 < V < 19$
Quadrant 1 / Quadrant 4 ratios above the Galactic Plane								
E45N20 / W45N20	45/315	+20/+20	1.00	1.00	1.00	1.14 ± 0.04	1.21 ± 0.02	1.00 ± 0.05
E50N31 / W50N31	50/310	+31/+31	1.00	1.00	1.00	1.22 ± 0.08	1.28 ± 0.09	1.08 ± 0.09
E55N42 / W55N42	55/305	+42/+42	1.00	1.00	1.00	1.02 ± 0.08	0.98 ± 0.11	0.99 ± 0.10
E60N20 / W60N20	60/300	+20/+20	1.00	1.00	1.00	1.03 ± 0.04	1.01 ± 0.07	0.93 ± 0.06
E65N31 / W65N31	65/295	+31/+31	1.00	1.00	1.00	1.01 ± 0.07	1.07 ± 0.11	0.82 ± 0.09
E57N20 / W75N20	75/285	+20/+20	1.00	1.00	1.00	1.01 ± 0.04	0.97 ± 0.07	0.96 ± 0.07
Quadrant 1 / Quadrant 4 ratios below the Galactic Plane								
E45S20 / W45S20	45/315	-20/-20	1.00	1.00	1.00	0.94 ± 0.03	1.01 ± 0.06	0.87 ± 0.04
E60S20 / W60S20	60/300	-20/-20	1.00	1.00	1.00	1.00 ± 0.04	0.89 ± 0.05	1.17 ± 0.07
Quadrant1 ratios above/below the Galactic Plane								
E45N20 / E45S20	45/45	+20/-20	0.94	0.94	0.97	1.13 ± 0.04	1.18 ± 0.06	1.10 ± 0.05
E50N31 / E50S31	50/50	+31/-31	0.97	0.97	0.98	1.13 ± 0.04	1.17 ± 0.11	1.04 ± 0.09
E60N20 / E60S20	60/60	+20/-20	0.94	0.93	0.96	0.90 ± 0.05	0.86 ± 0.06	0.84 ± 0.05
Quadrant 4 ratios above/below the Galactic Plane								
W45N20 / W45S20	315/315	+20/-20	0.94	0.94	0.97	0.94 ± 0.04	0.94 ± 0.06	0.92 ± 0.05
W60N20 / W60S20	100/100	+20/-20	0.94	0.93	0.96	0.82 ± 0.05	0.73 ± 0.04	1.00 ± 0.07

Table 12: Observed Ratios

We developed ratios, normalized by area of the observed sky, of the complementary stellar fields, including Quadrant 1 over Quadrant 4 and the northern quadrant fields over the southern fields. The Galactic model, GALMOD, predicts what the each of the ratios should be in a perfectly symmetric Galaxy and from our position several thousand light-years above the Galactic Plane. Since we are above the Galactic Plane, we see more stars looking down onto the plane from the southern sky than looking above the Plane from the northern sky.

In our analysis, we found a statistically significant ratio of Quadrant 1 to Quadrant 4 stars in the northern sky. Within the V magnitude range  $16 < V < 19$ , the ratio of stars in E45N20 compared to W45N20 was  $1.14 \pm 0.04$ . Within the same regions, E50N31 / W50N31 showed a ratio of  $1.22 \pm 0.08$ . Observed fields extending out to greater Galactic longitudes, including  $55^\circ$ ,  $60^\circ$ ,  $65^\circ$ , and  $75^\circ$ , showed no ratios greater than 1.00 outside of the error margin.

Comparing Quadrant 1 above to below the Galactic Plane also showed greater-than-expected ratios at the same longitudes. Between V Magnitudes 16 and 19, the ratio E45N20 / E45S20 was  $1.13 \pm 0.04$  with an expected ratio of 0.94. In the same magnitude range, E50N31 / E50S31 had a ratio of  $1.13 \pm 0.04$  with an expected ratio of 0.97. As before, this excess does not extend out to  $60^\circ$ .

These comparisons proved that there is an excess of stars at lower longitudes in Quadrant 1 above the Galactic Plane. When we examined the ratios of Quadrant 1 to Quadrant 4, both below the Galactic Plane, we found no evidence for the excess. The ratio E45S20 / W45S20 at V magnitudes  $16 < V < 19$  was  $0.94 \pm 0.03$  with an expected ratio of 1.00. The ratio E60S20 / W60S20 at the same magnitudes was  $1.00 \pm 0.04$ , also

with an expected ratio of 1.00. The final comparisons of Quadrant 4 fields above to below the Galactic Plane also showed expected ratios. We expected  $W45N20 / W45S20$  to be 0.94 and found it to be  $0.94 \pm 0.04$ . Similarly, we expected  $W60N20 / W60S20$  to be 0.94 and found it to be  $0.82 \pm 0.05$ .

In the final analysis of our count ratios, the excess stars can only be found in Quadrant 1 above the Plane. As discussed in our signatures for the origin theories, both the stellar bar and the triaxial theories require that the stellar excess extends below the Galactic Plane. Since our analysis rules both of these theories out, the most likely origin must therefore be the galactic merger.

## 4.2 Photometric Parallax Plot

We used the program `photometric parallax.pl` (discussed in Appendix D) to find the distance to each star via the method of photometric parallax. By plotting the galactocentric coordinates and the distance on the same image, we developed a position map of all the stars in our fields of view. The resultant image appeared as a top-down view of the Galactic plane from an overhead perspective (up the  $z$ -axis). The stars shown in the image represent a slice of the galaxy between two  $z$ -axis positions (specified in the arguments) above or below the Galactic plane. The zero coordinates mark the location of the Sun. Figure 36 shows a diagram of the observed stellar locations between 2.0 and 2.5 kiloparsecs above the Galactic Plane. The density of stars is denoted by a color spectrum on the right of the figure.

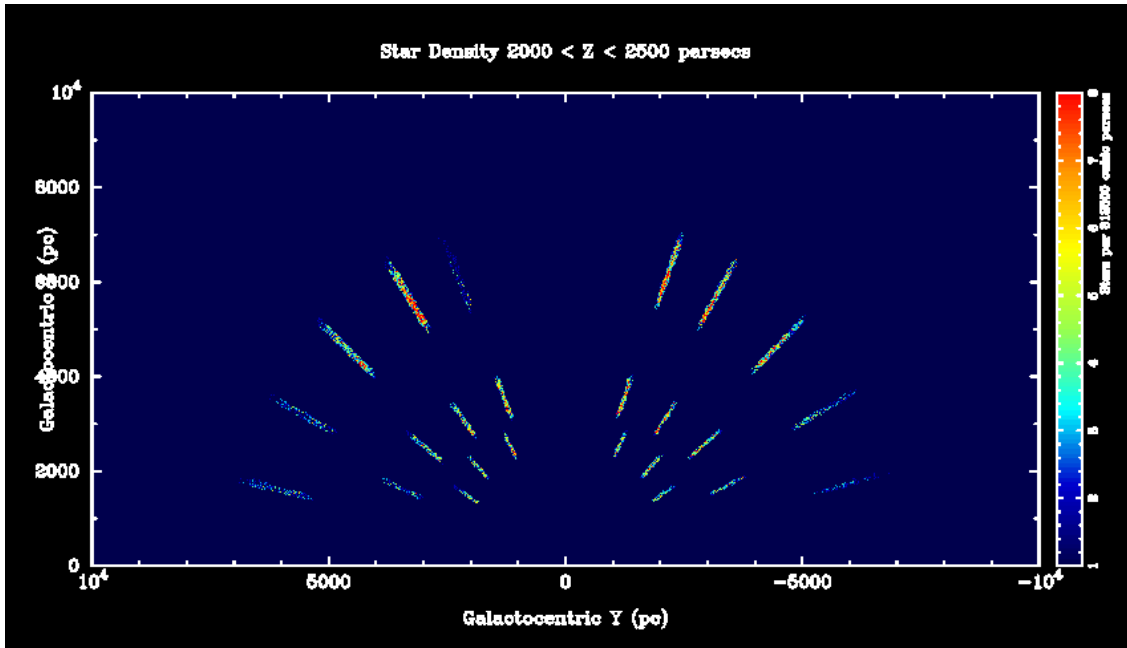


Figure 36: Overhead view of the Galaxy, measuring star density in the measured stellar fields at a height of 2-2.5 kiloparsecs above the Galactic Plane.

We used the program `scan.pl` (see Appendix D) to develop a series of 500 parsec-thick slices of the Galaxy, ranging from 0 to 500 kiloparsecs. Viewing the images in sequence shows how the density of stars changes with increasing distance above the Galactic Plane.

We then developed a parallel program call `plinking.pl`, which we used to show how the fields of view in our observation sampled the Galaxy in both the x-y plane (the view of the galaxy from above the Galactic Plane looking downwards) and the y-z plane (a side view of the Galaxy, looking straight at the edge of the Galactic Plane). The resultant images shown in Figures 37 and 38 give a sense as to the volume of space being samples. The fields of observation extend outward in a cone shape similar to Figure 7 in Section 1.5 showing the GALMOD calculation for volume across space. Although the area of sky being surveyed is still very small, the number of samples shown by the green dots in the images gives a sense of the high number of star counts dealt with in this project.

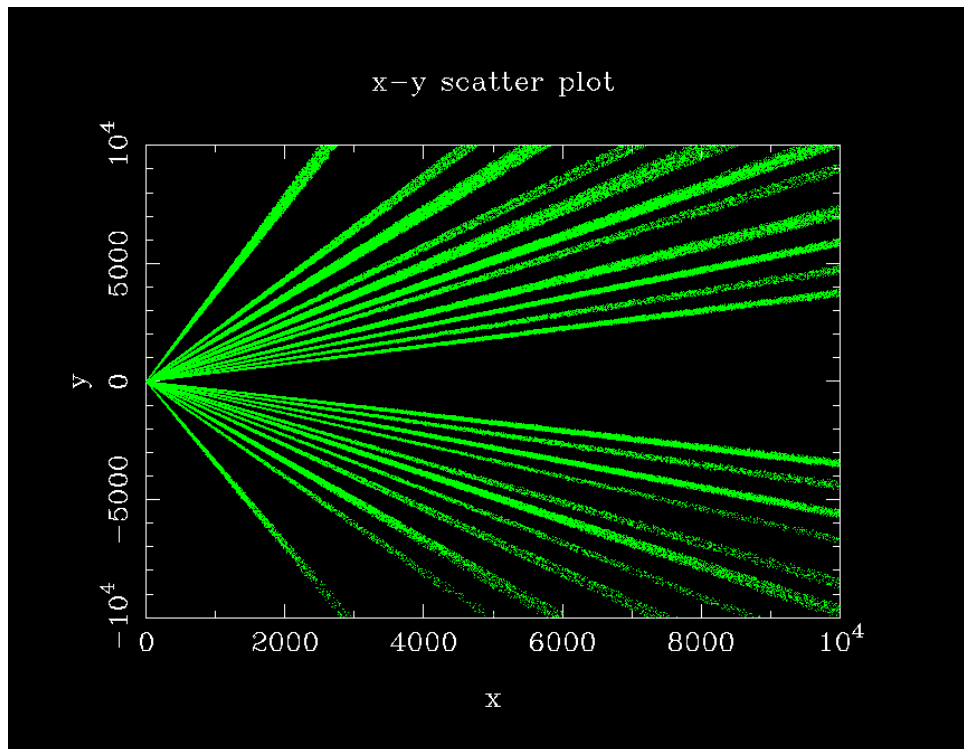


Figure 37: Field of view where the sun is at the origin and the Galactic Center is in the positive y-axis direction. The x-y scatter plot represents an overhead view of the Galaxy.

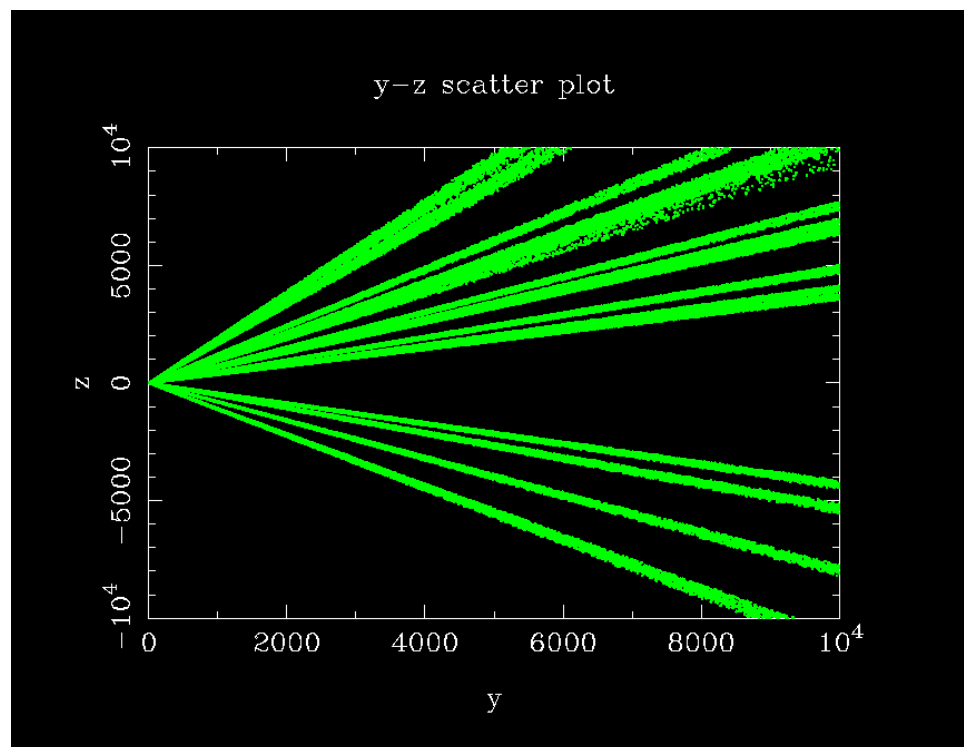


Figure 38: Field of view where the sun is at the origin and the Galactic Center is in the positive y-axis direction. The y-z scatter plot represents a side view of the Galaxy.

Unfortunately, Figures 37 and 38 do not provide any assistance in data mining and characterizing the excess. Figure 36 does provide an overhead view of the complementary fields and shows some difference, but the excess appears as a low contrast feature for what should be a high contrast structure. Although it does offer a distances scale, it is not clear enough to calculate the distance to or the size of the stellar excess.

In order to locate the stellar excess, we designed a program that compares parallax distances of complementary stellar fields and the number of stars at each distance. We took two complementary stellar fields and separated the stars in each of them into bins of 400 parsecs of distance away from our Sun. In other words, all stars between 0 and 400 parsecs from our sun fell into one bin, and those between 400 and 800 parsecs fell into another bin. We then subtracted the stars in one bin from the Quadrant 1 field by the stars in the same bin in the Quadrant 4 field. This allowed us, for example, to see how many more stars Quadrant 1 had than Quadrant 4 between 800 and 1200 parsecs away from our Sun. We documented these results on a graph of star count number versus distance in parsecs. Finally, we computed the Poisson error of the number of stars in each field at each distance bin and checked to see if the difference in the number of stars was significant.

Figure 39 shows this program being run on the fields E25N40 and W25N40. The green dots represent the number of stars in E25N40 subtracted by the number of stars in W25N40. The lines surrounding the horizontal axis represent the  $\sigma$ -error at each distance. Between 800 and 3200 parsecs, the data show that the E25N40 has a statistically significantly greater number of stars than W25N40 in several contiguous bins

at more than  $2\sigma$ . Therefore, we concluded that the excess exists at longitude  $l = 25^\circ$ .

When this same program was performed on fields at a much greater longitude, such as E75N20 and W75N20 in Figure 40, we did not observe a statistically significant deviation between the two fields. Therefore, we concluded that the excess does not exist at longitude  $l = 75^\circ$ .

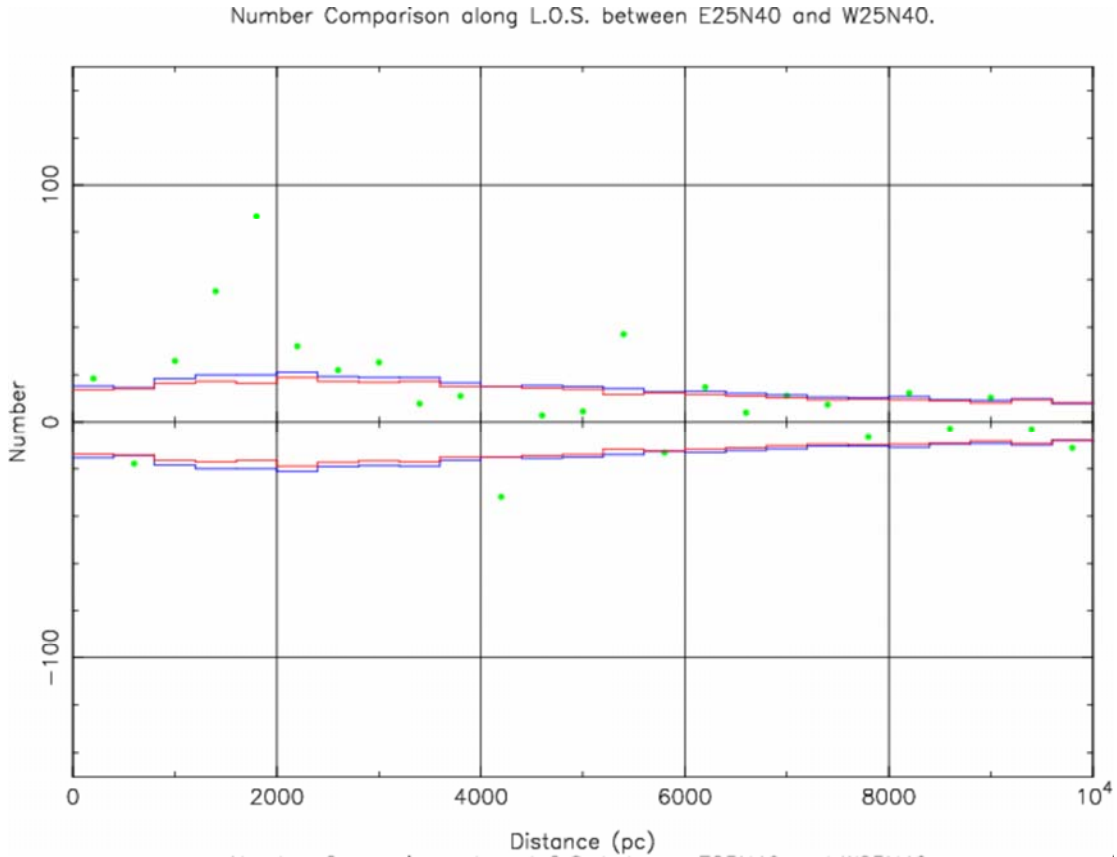


**Figure 39: Difference between objects in E25N40 and W25N40 over distances from our Sun. The Fourier lines show the sigma error at varying distances. The lines points outside of the error lines indicate the presence of the excess between 800 and 3200 parsecs from our Sun.**



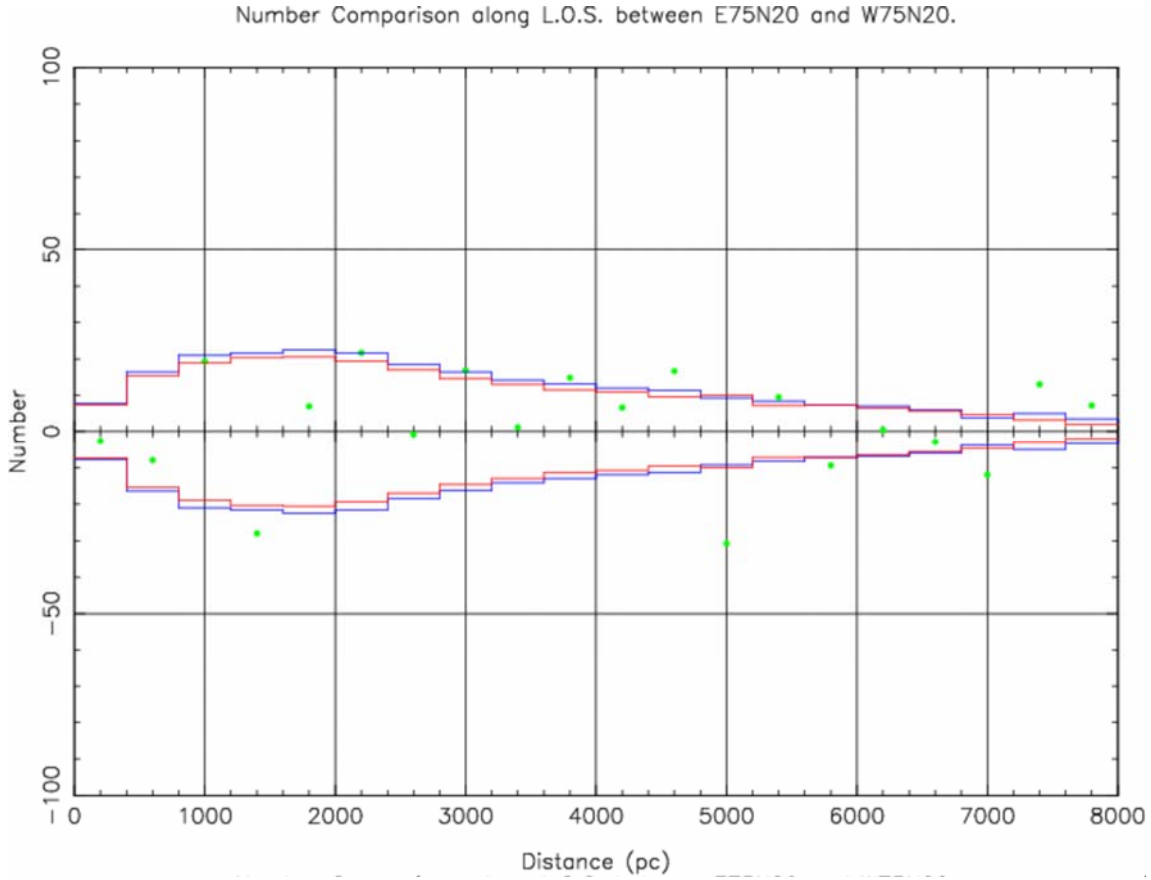


**Figure 40: Difference between objects in E75N20 and W75N20 over distances from our Sun. The Fourier lines show the sigma error at varying distances. Most of the points fall within the error lines, so the plot does not indicate the presence of the excess at this position in the sky.**

Our results from the comparison of E25N40 to W25N40 suggested that the excess is located between 800 and 3200 parsecs from our Sun. Further results showed that the excess is relatively thin and may be only 1500 parsecs thick. However, since the excess fields span a latitude change of only  $10^\circ$ , its thickness shrinks down to 1000 parsecs. Therefore, we surmised that the excess must be tube-like in shaped and has a tidal tail. Both these results, limited size and presence of a tidal tail, are indicators of a galactic merger, further supporting our conclusion about the origin of the excess.

### 4.3 Running the Genetic Algorithm

As mentioned in Section 1.5, the goal of the genetic algorithm is to find the best fit values for the parameters of a galactic model (listed in Table 1) that fit self-consistently with the CCD data for the first comparison. From this galactic model, we look at deviations in the data in order to identify the stellar excess. This task is not difficult since we already have the already have the genetic algorithm written by Larsen in 1996 in order to drive the galactic model.<sup>43</sup> Most of the genetic algorithm program is based on the work of Michaelowicz.<sup>44</sup> For our project, two changes needed to be made. Instead of the O-E bandpass used with the original photographic plates, we use the B-V color bandpass. Additionally, original photographic surveys using the POSS I Data used large plates which could be trimmed down to a uniform 16 square-degree area. The new data has variable survey area that must eventually be normalized during image reduction for comparison. In order to compare the new model with the original from Larsen's thesis, we placed our data into similar bins of width 0.2 V magnitude and 0.2 B-V color. We ran the program at the end of the project on 7 different workstations. The process, which originally took two weeks on an SGI Power Challenge multi-processor supercomputer in 1996, took only 7 hours using the PC's in the Naval Academy astronomy laboratory.

The principles of the genetic algorithm are discussed in further detail in Appendix B, but basically we used a payoff statistic to compare the actual color-magnitude data to the GALMOD showing what the data should look like in a symmetric Galaxy and based on our Sun's position relative to the Galactic Plane. Figure 41 shows the evolution of the

---

<sup>43</sup> Larsen, *Shape*, 135.

<sup>44</sup> Michaelowicz, *Genetic Algorithms*, 1.

genetic algorithm plotting the fitness of the parameter solutions to the generation of solutions for a population size of 100 in one of our runs. The blue dots represent the fitness of the best solution, while the green dots represent all other population members. Crossover changes the fitness of the solutions for either better or worse, causing some green dots to move far lower down in fitness than the blue dot. In some cases, a mutation causes the fitness of a solution to drastically decrease (the red dots). Most of the green dots lie near the best solution, indicating that the population tends to favor the fit parameters from the first generation. Figure 41 shows the overall fitness increasing slightly over succeeding generations.

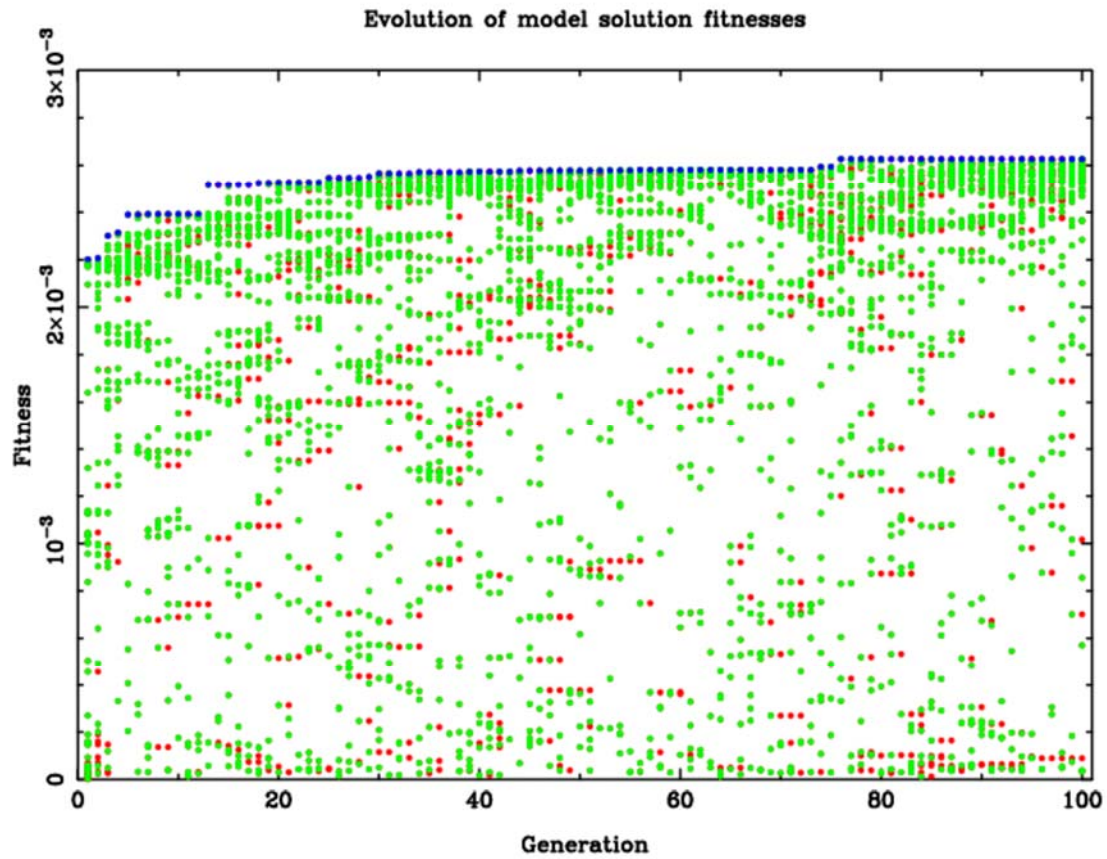


Figure 41: Fitness plot of the Genetic Algorithm solutions over succeeding generations

Over the course of the project, we conducted 14 runs of the genetic algorithm over three separate fields. The results are summarized in Table 13. The relatively slow evolution of the fitness solution as a function of generation is shown in Figure 42.

Computer	Disk Scale Height c/a	Halo scale length	Halo normalization	length	Thick Disk scale height	Thick Disk normalization
Phobos_1	3952.4952	0.5963	3046.9279	0.0002	4657.7876	1492.3731
Phobos_2	3361.3786	0.4507	4397.8623	0.0016	3676.2852	993.9245
Deimos_1	3548.8390	0.4520	4278.2683	0.0019	4664.054	972.1384
Deimos_2	3427.8462	0.7295	4772.6767	0.0004	4971.4721	1050.5007
Europa_1	3475.6677	0.5856	4850.2765	0.0003	4352.2419	1294.9549
Europa_2	3028.8054	0.4954	4800.7333	0.0007	4861.0478	1340.8232
Io_1	3055.8283	0.6579	2571.3000	0.0003	4171.5006	1366.442
Io_2	3600.0673	0.7664	3495.2187	0.0005	4888.3377	1034.2051
Ganymede_1	3316.0734	0.5121	3101.0092	0.0024	4812.0714	845.7681
Ganymede_2	3952.4952	0.5958	2828.2765	0.0002	4657.7876	1492.3731
Callisto_1	3185.7879	0.5375	2561.1310	0.0005	4598.6874	1371.289
Callisto_2	3269.4668	0.4672	2262.4538	0.0008	4405.8822	1351.2228
Mystiko_1	3671.6535	0.6027	3451.7662	0.0015	4877.5535	802.4593
Mystiko_2	2982.8736	0.6028	3210.7515	0.0004	3972.6154	1415.0169
<b>Mean</b>	<b>3416.3770</b>	<b>0.5751</b>	<b>3544.9037</b>	<b>0.0008</b>	<b>4540.5232</b>	<b>1201.6779</b>
<b>Sigma</b>	<b>310.20076</b>	<b>0.0976</b>	<b>907.05199</b>	<b>0.0007</b>	<b>382.51022</b>	<b>240.7776775</b>

Computer	Distance from Galactic Center	Distance above Galactic Mid-Plane	Normalization of Disk Luminosity Function	Scale height disk giants	Scale height disk dwarves	Overall fitness of best solution
Phobos_1	8000.0000	20.5000	1.0000	250.0000	325.0000	0.002727
Phobos_2	8000.0000	20.5000	1.0000	250.0000	325.0000	0.002607
Deimos_1	8000.0000	20.5000	1.0000	250.0000	325.0000	0.002618
Deimos_2	8000.0000	20.5000	1.0000	250.0000	325.0000	0.002715
Europa_1	8000.0000	20.5000	1.0000	250.0000	325.0000	0.002800
Europa_2	8000.0000	20.5000	1.0000	250.0000	325.0000	0.002773
Io_1	8000.0000	20.5000	1.0000	250.0000	325.0000	0.002750
Io_2	8000.0000	20.5000	1.0000	250.0000	325.0000	0.002684
Ganymede_1	8000.0000	20.5000	1.0000	250.0000	325.0000	0.002577
Ganymede_2	8000.0000	20.5000	1.0000	250.0000	325.0000	0.002727
Callisto_1	8000.0000	20.5000	1.0000	250.0000	325.0000	0.002751
Callisto_2	8000.0000	20.5000	1.0000	250.0000	325.0000	0.002783
Mystiko_1	8000.0000	20.5000	1.0000	250.0000	325.0000	0.002627
Mystiko_2	8000.0000	20.5000	1.0000	250.0000	325.0000	0.002698
<b>Mean</b>	<b>8000.0000</b>	<b>20.5000</b>	<b>1.0000</b>	<b>250.0000</b>	<b>325.0000</b>	<b>0.002703</b>
<b>Sigma</b>	<b>0</b>	<b>0</b>	<b>0</b>	<b>0</b>	<b>0</b>	<b>7.07E-05</b>

**Table 13: Summary of the results of the genetic algorithm (organized by computers on which the we ran the genetic algorithm)**

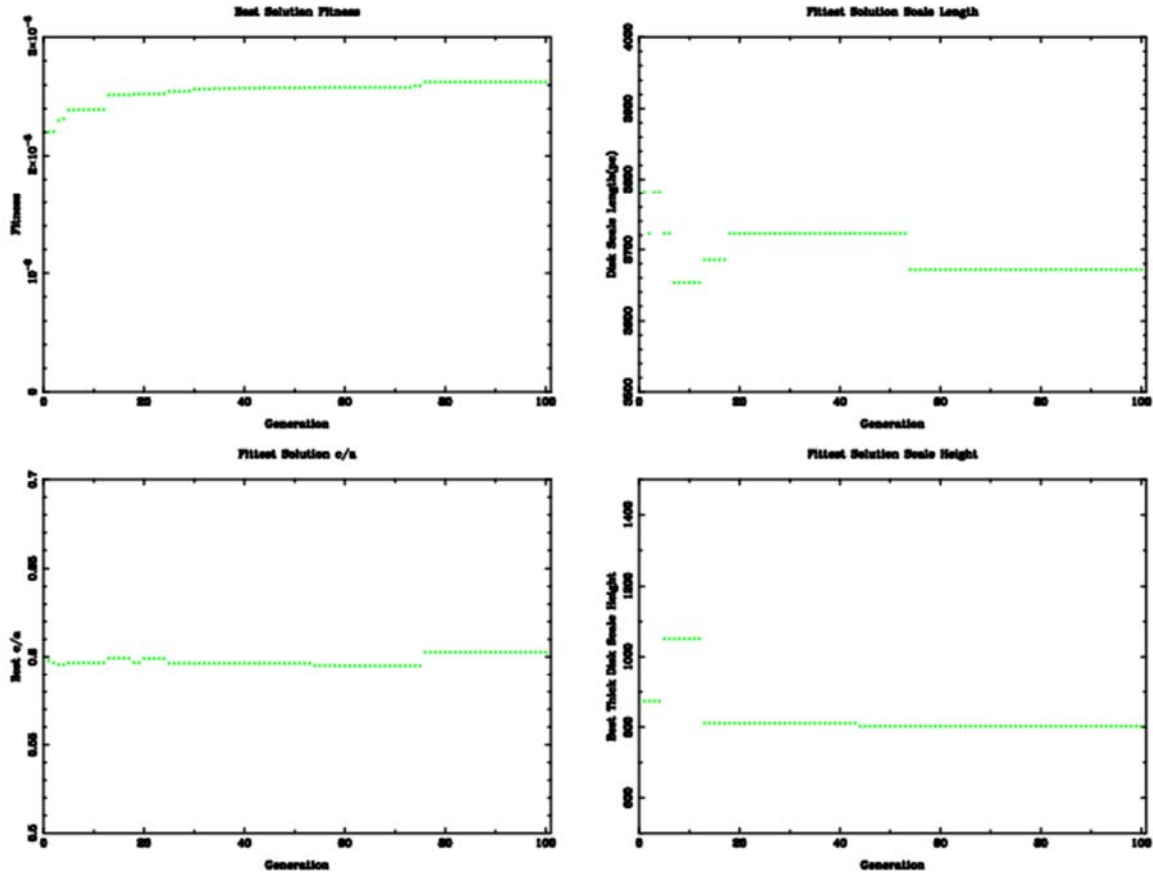


Figure 42: Evolution of the fitness solution for different parameters over succeeding generations.

When our mean and sigma values of the best fit parameters are compared to Larsen's original data on the 7 parameters in Table 2, we find overall agreement between the two sets of data. The halo normalization for our data seems too small and so the Halo can look like the Thick Disk towards the center of the Galaxy. However, we would need to include data on Quadrants 2 and 3 in order to separate out the two structures, a project that will be completed in the future.

In Figures 43 and 44, we examine histogram values of the data at different B-V color values, with each diagram representing a different magnitude range for the

Quadrant 1 field E25N40 and the Quadrant 4 field W25N40. We see in Figure 44 that the observed number of stars roughly matches what was expected from the Galactic Model in Quadrant 4. However, Figure 43 shows that the observed number of stars was significantly greater than the expected values in Quadrant 1, again providing further evidence for the excess.

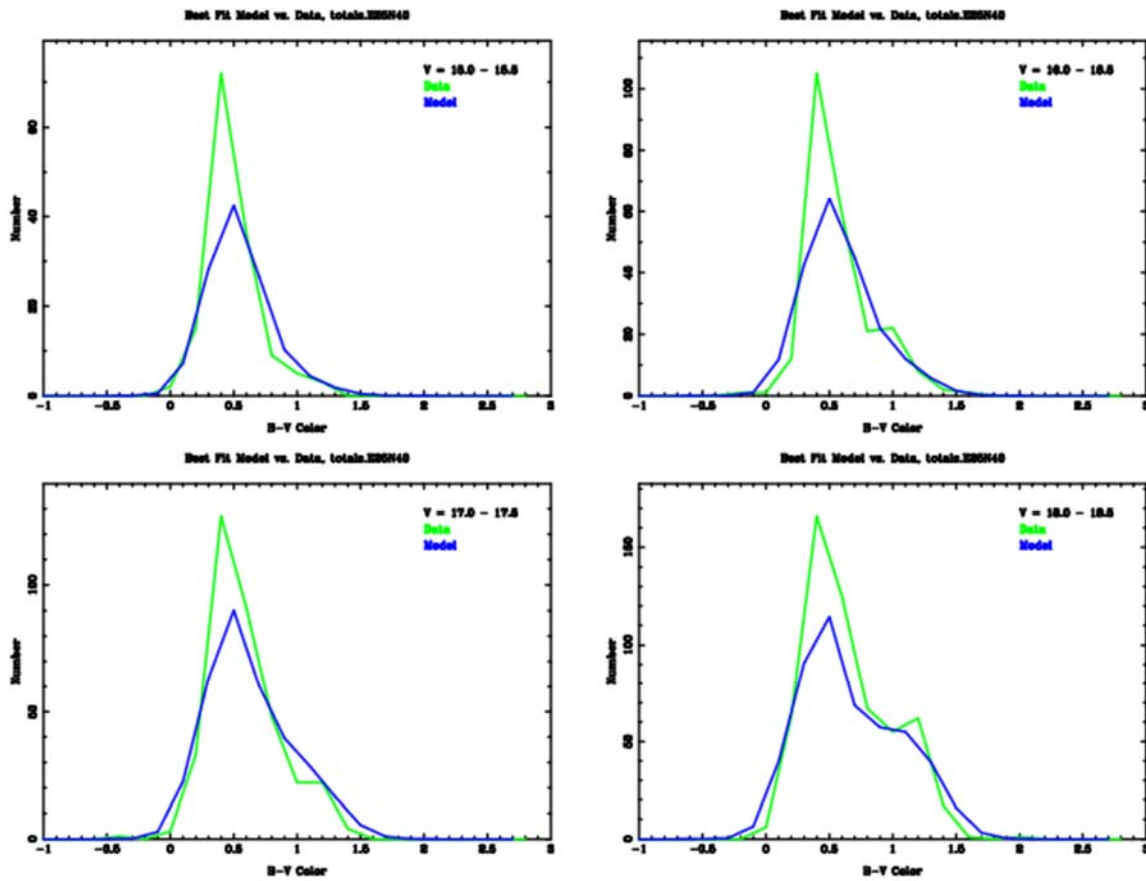


Figure 43: Model of Predicted versus Observed stars at different magnitudes for the field E25N40. The comparison shows a large under-prediction in the colors of the excess.

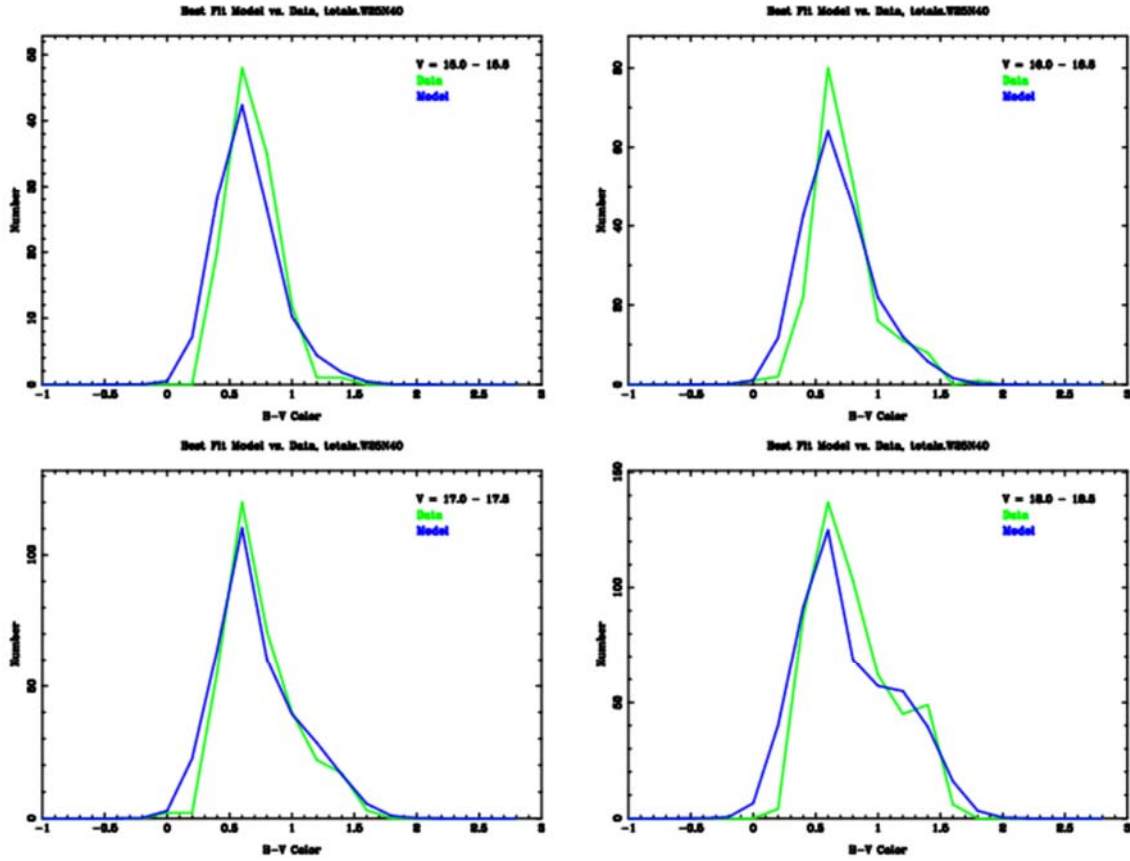


Figure 44: Model of Predicted versus Observed stars at different magnitudes for the field W25N40. The prediction is much closer to the observed results, indicating that the excess is not present in the field.

The thick disk and the halo have very similar behavior in these directions towards the center of the Galaxy. As a result, we effectively underestimated the number of Halo stars present and overestimated the number of Thick Disk stars. In Figures 45 through 48, showing histogram values of color of E25N40 stars at different magnitude ranges, the Halo size should be equal to the Thick Disk, but instead we observe very few Halo stars over the full range of color. The model will need to be corrected by adding data observed in the directions of Quadrants 2 and 3 in order to develop a better model of the Halo.



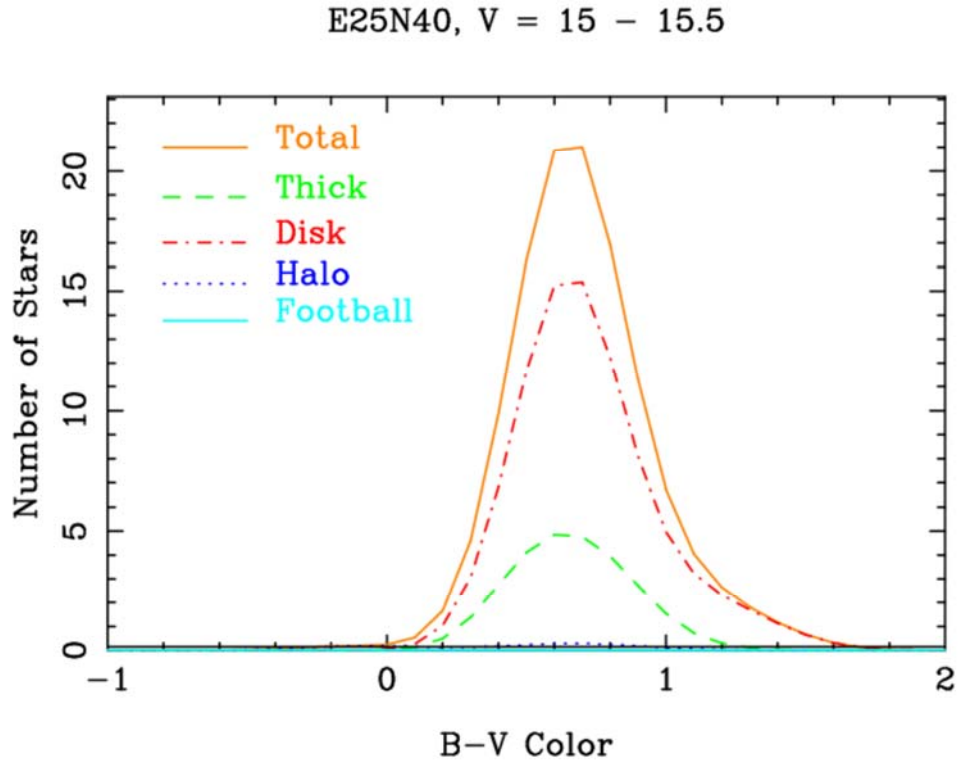


Figure 45: Component by component model prediction of the star in E25N40 between  $V$  magnitudes 15 and 15.5

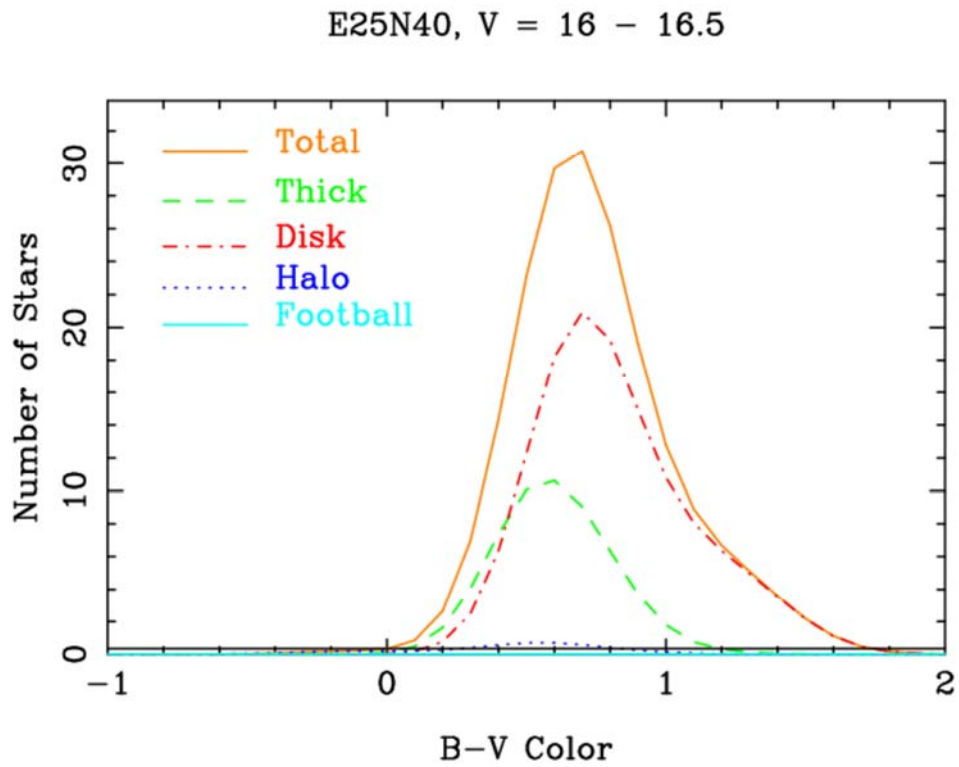


Figure 46: Component by component model prediction of the star in E25N40 between V magnitudes 16 and 16.5

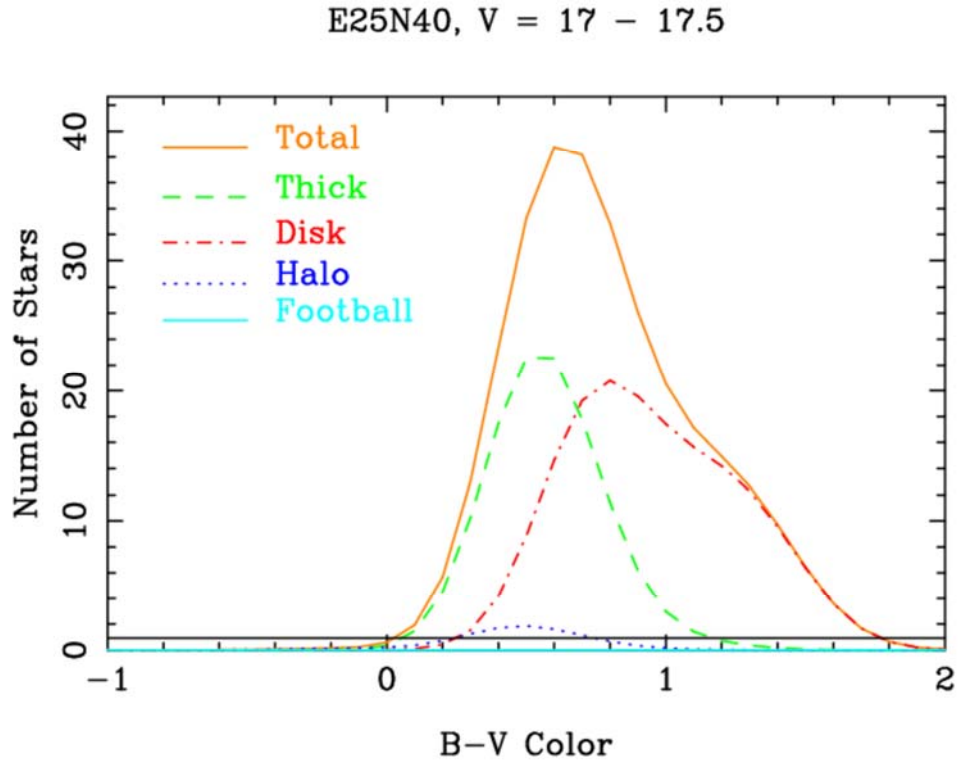


Figure 47: Component by component model prediction of the star in E25N40 between  $V$  magnitudes 17 and 17.5

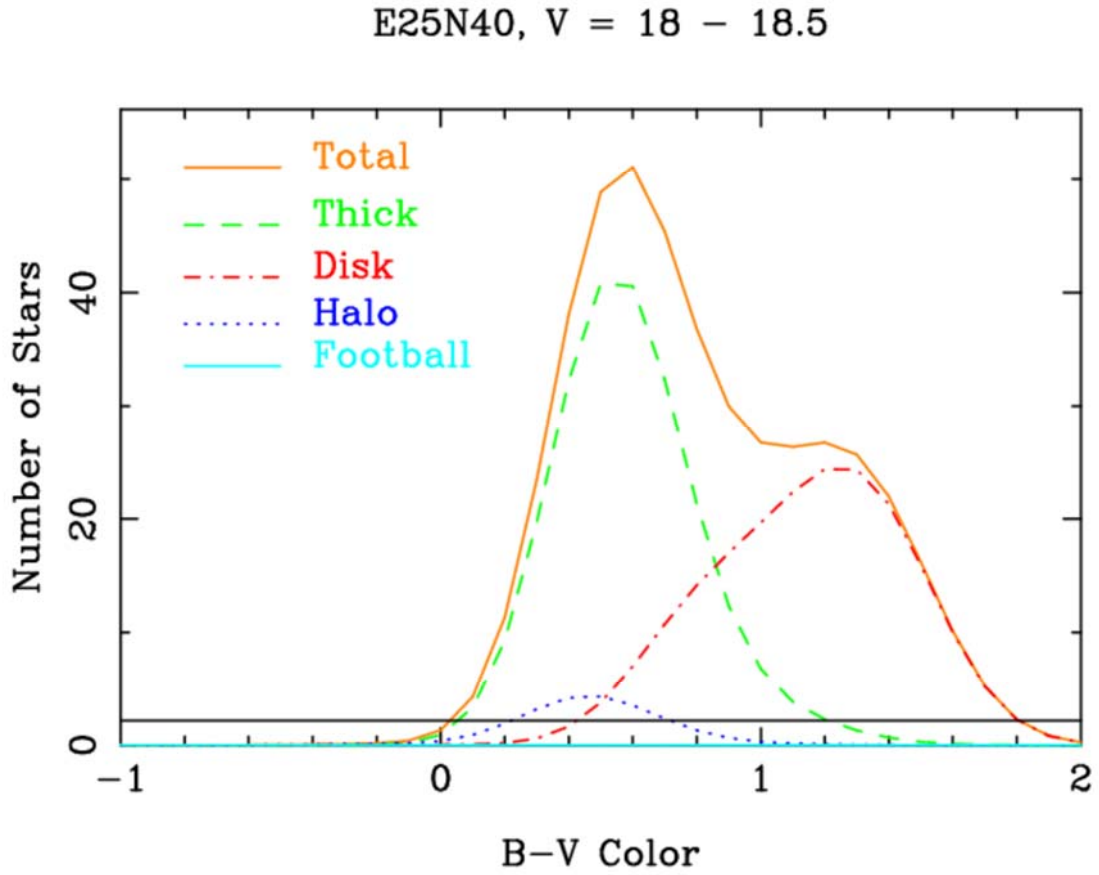
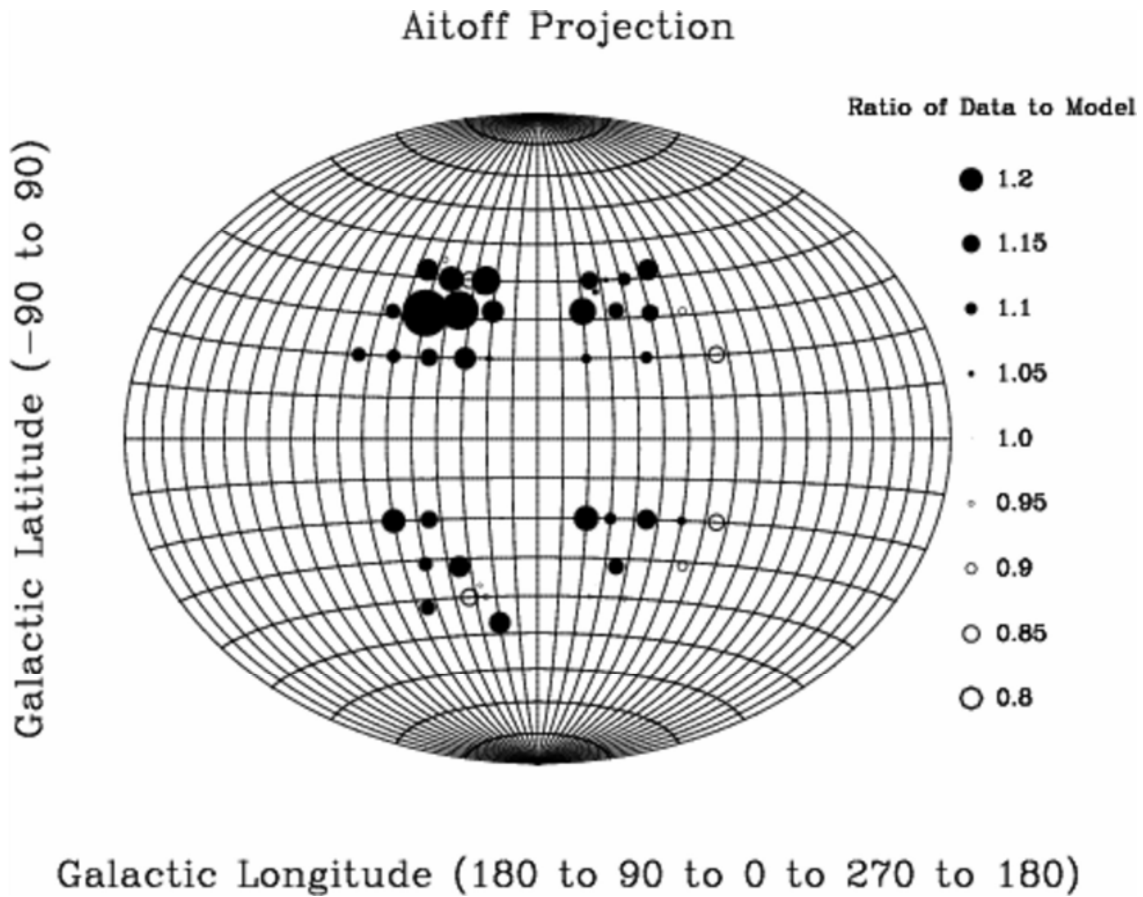


Figure 48: Component by component model prediction of the star in E25N40 between  $V$  magnitudes 18 and 18.5

Fortunately, the problem of identifying Halo stars did not limit our ability to plot the overall excess. Figure 49 presents an Aitoff projection of fields where the observed data deviated from the Galactic Model by more than 5 percent. Our underestimated halo is the reason why most of the ratios in the plot are positive. However, the deviations in Quadrant 1 above the Galactic Plane are clearly larger than the ratios in the other

quadrants. Therefore, an initial analysis of the Genetic Algorithm results supports the presence of the stellar excess and confines the excess to higher latitude fields.



**Figure 49:** Aitoff projection showing how the Ratio of Observed Data to Genetic Algorithm predictions varies from field to field. The large ratios in Quadrant 1 above the Galactic Plane indicate the presence of the excess. The positive ratios in all other fields indicates an underestimation in the number of halo stars throughout the inner Galaxy.

#### 4.4 Spectral Classification / Proper Motions

Besides position and stellar classification, another method of astronomical analysis is to look at the motion of the stars. As discussed in Section 1.4, proper motion is the observed movement of stars in the plane of the sky, while radial motion is the forward/backward motion along the line of sight as observed by shifts in the Doppler spectrum. The combination of proper and radial motions an important discriminator that, when analyzed with the distance to the stars, can be used to find the spatial motion of stars.

Figure 50 diagrams the proper motions of stars in the field E75N20 as observed from the USNO-B 1.0m telescope. The vertical axis represents the proper motion along the axis of declination in terms of micro-arcseconds ( $\mu\text{asec}$ , or  $10^{-6}$  arcseconds) per year. The horizontal axis represents proper motion along the axis of right ascension, also in micro-arcseconds per year. The cloud of points, each representing the proper motion of a star in the particular field, is not centered for two reasons. First, the overall rotation of the Galaxy gives stars a different speed depending on their distance from the Galactic center. Stars that are further from the Galactic center orbit with greater speeds than those located closer to the center. Second, these observations are made from the perspective of our Solar System, which has its own specific velocity with respect to the Galactic center.

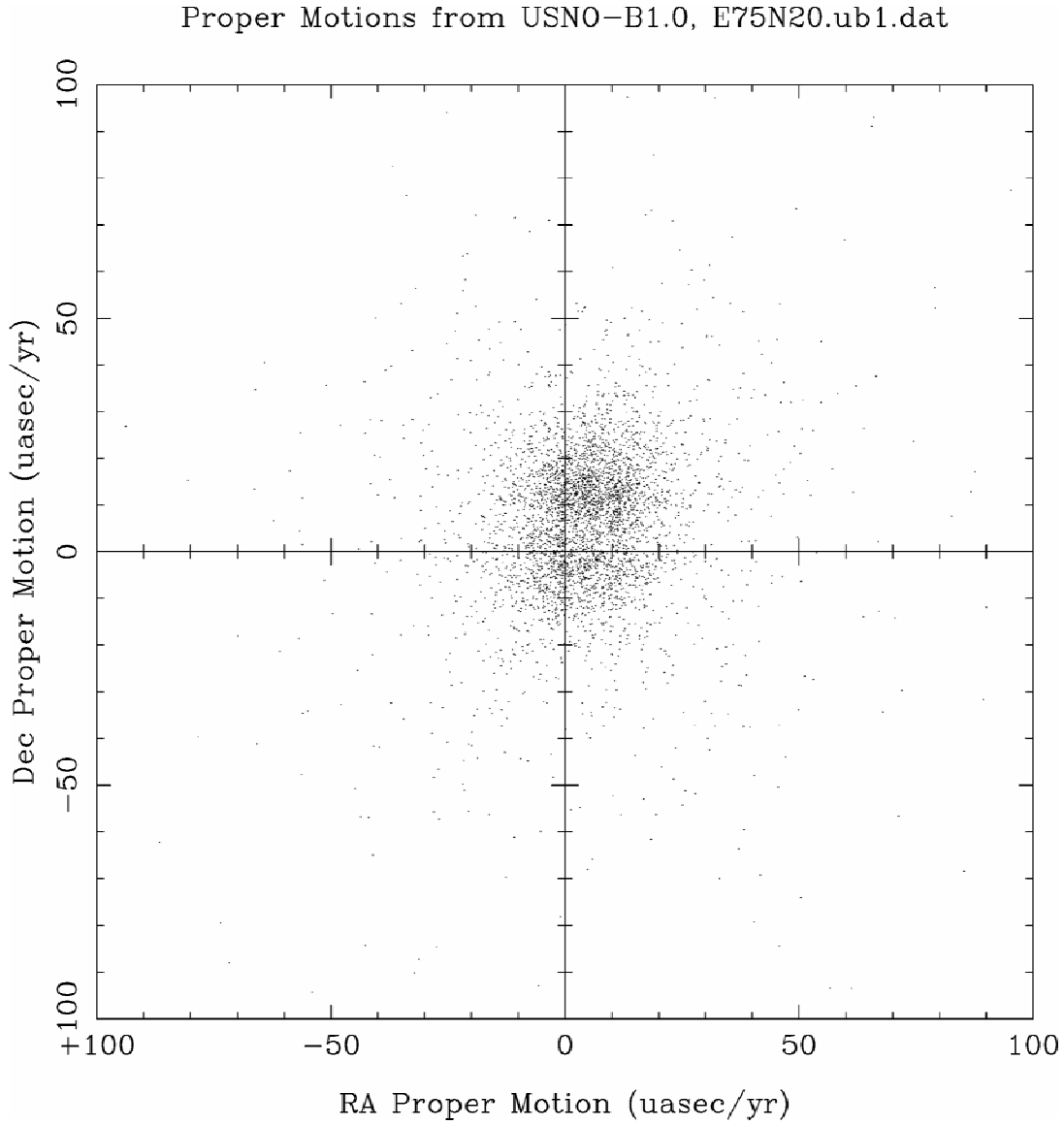


**Figure 50: Proper motions of stars in the Quadrant 1 field E75N20**

Proper motion measures the angular velocity ( $\mu$ ) to a star, but we cannot measure the actual, translational velocity ( $v_t$ ) without knowing the distance from our position to the star ( $r$ ). The two are related by the equation:

$$\mu = v_t / r$$

If we know the distance to a star from the method of photometric parallax, we can then multiply it by the angular velocity (the proper motion) to find the translational velocity.<sup>45</sup>

However, the proper motion represents by no means the complete picture of stellar motion. Proper motion represents motion across the sky perpendicular to the line of sight. Radial motion ( $v_r$ ), calculated via the Doppler shift, represents motion parallel to the line of sight. These components are used to find the velocity ( $v$ ) using the equation:

$$v = (v_t^2 + v_r^2)^{1/2} \quad (\text{Equation 7})$$

The angle of motion to the line of sight is:

$$\tan\theta = v_t / v_r \quad (\text{Equation 8})$$

Studies by Parker *et al.* used observations from the W/YN and CTIO 4-meter telescopes and analyzed the spectra of 700 Thick Disk candidate stars. They found that, on average, Quadrant 1 stars rotate 80-90 kilometers per second slower about the Galactic center than corresponding Quadrant 4 stars.<sup>46</sup> This difference was enough to suggest that the stars were members of separate populations, but it did not offer evidence for any of the three formation hypotheses.

At the outset of the project, we planned on acquiring more data on the radial velocities in of Thick Disk candidate stars and combining the data with proper motions in order to make a more complete velocity map of the Hercules Thick Disk Cloud. Our collaborators at the University of Minnesota and Minnesota State University completed observations in Fall 2008, but bugs in the National Laboratory's reduction package

---

<sup>45</sup> Carroll, *An Introduction to Modern Astrophysics*, 17.

<sup>46</sup> Parker *et al.*, "The Kinematics" (2004), pp. 1346-1361.



prevented them from properly reducing the data and finding the radial velocity values within the timeline of this project.

Fortunately, as discussed in Section 4.1, we only needed position information on the stellar excess in order to conclude that the most likely origin was a galactic merger. The radial velocity information will instead be used in future studies that characterize the Hercules Thick Disk Cloud in greater detail.

## 4.5 Other Data Mining Techniques

In its most basic form, the method of star counts utilizes arrays of color versus magnitude to analyze stellar observations. The data can be mined using various methods, one of which is to present the data as a color-magnitude diagram. Figure 51 shows a scatter plot of stars' magnitude (V) versus their B-V color in a Quadrant 1 Field known to contain an excess (E25N40), while Figure 52 shows the same diagram for a complementary Quadrant 4 field (W25N40). We easily observe the peak structure in both diagrams at the B-V color of 0.6 and the stars belonging to the thick disk in the parallel peak at B-V color 1.5.

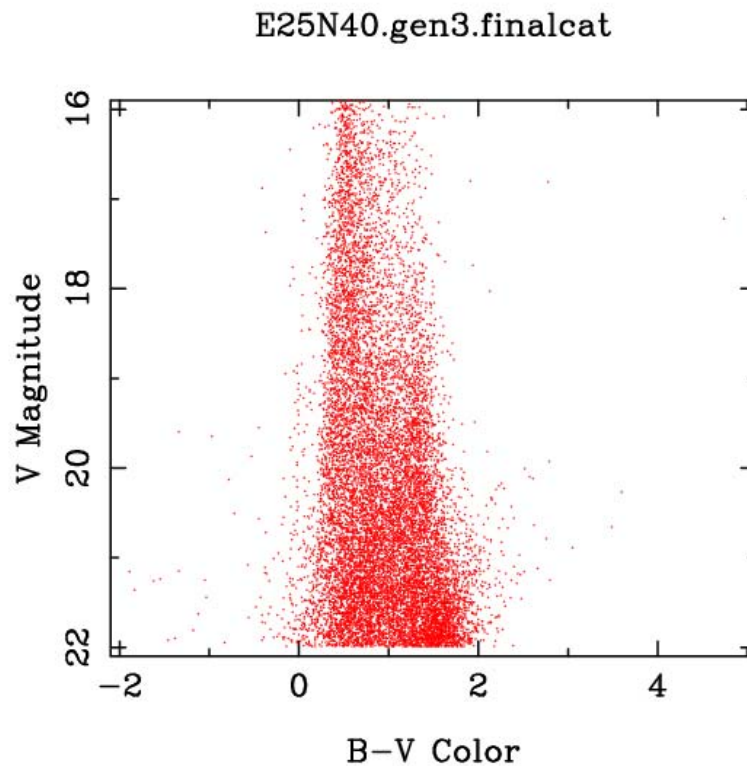
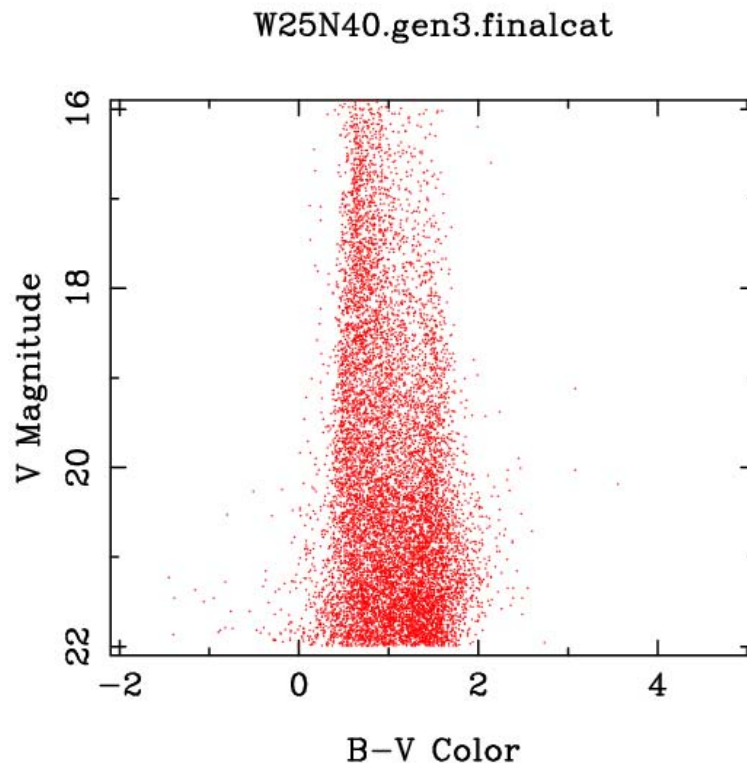


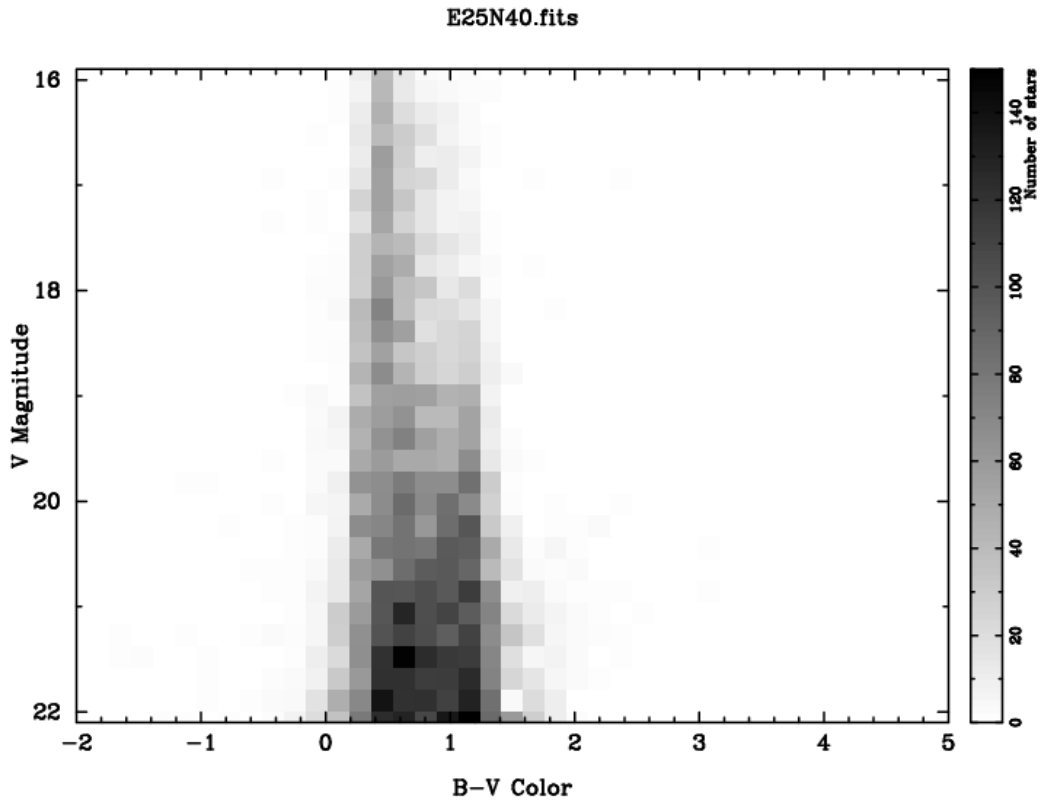
Figure 51: Scatter plot of Magnitude (V) versus B-V Color of stars in the Quadrant 1 Field E25N40



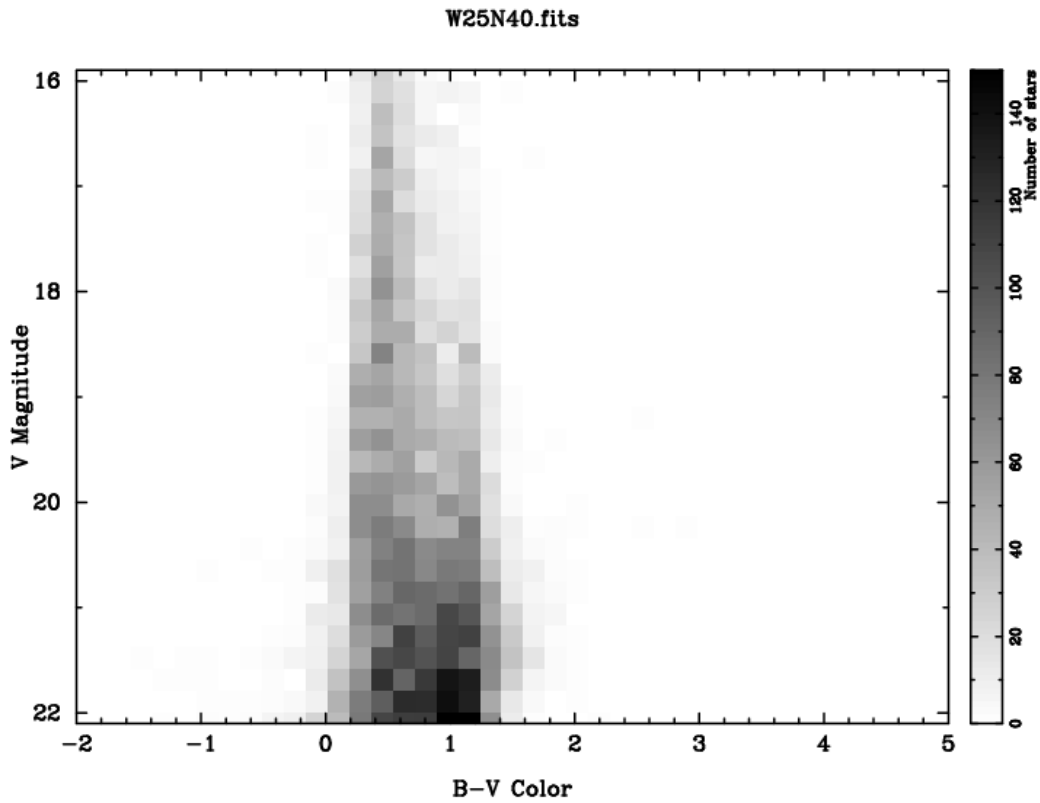
**Figure 52: Scatter plot of Magnitude (V) versus B-V Color of stars in the Quadrant 4 field W25N40**

Although the scatter plot forms color-magnitude diagrams do present a good amount of detail about the stellar composition of the observed fields, they have some weaknesses when used for comparative analysis such as our numeric presentations. Strikeovers are points where stars with identical colors and magnitudes plot over each other, thereby preventing us from seeing how many points are on each portion of the diagram. A more useful tool is to use a two-dimensional histogram of the data represented as an image. In the histograms in Figures 53 and 54, the data from the previous figures have been divided into bins of 0.2 V magnitude by 0.2 B-V color

magnitude. The number of stars in each bin, which forms a pixel in an image, is indicated by a grayscale described on the right of the diagram.

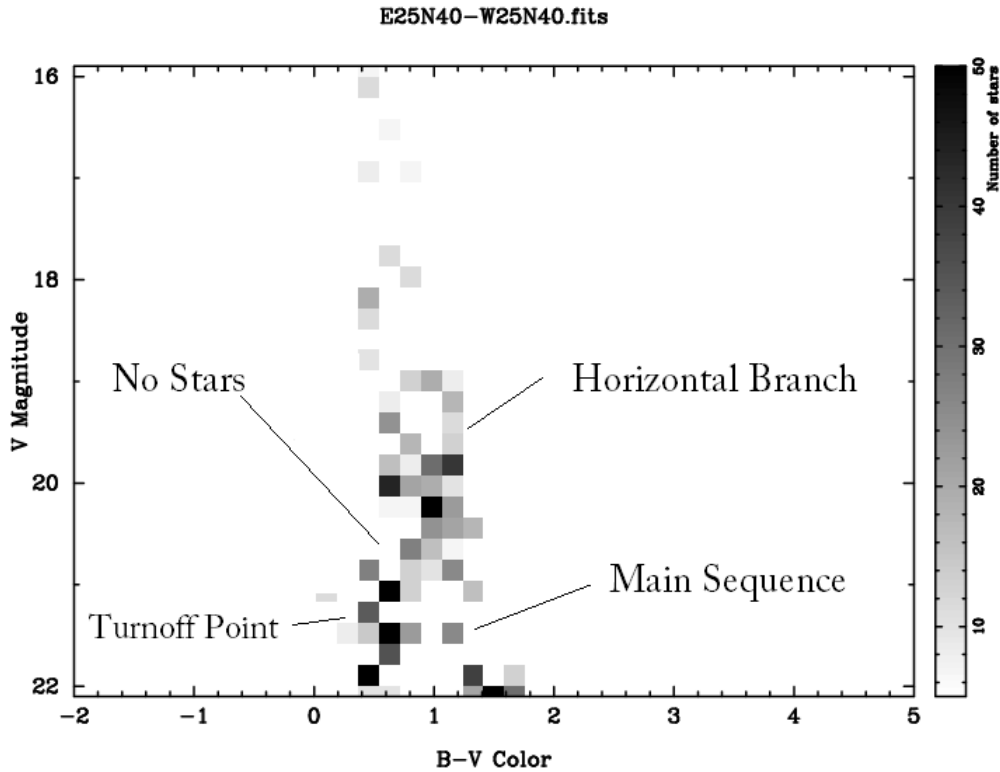


**Figure 53: V Magnitude versus B-V Color Histogram for the Quadrant 1 Field E25N40.** The grayscale puts white pixels on bins with no stars and very dark pixels on bins with many stars.



**Figure 54: V Magnitude versus B-V Color Histogram for the Quadrant 4 Field W25N40.**

The usefulness of the histogram method proves itself when we simply subtract the histogram image W25N40 from E25N40. In other words, the number of stars in each bin in the Quadrant 1 field is subtracted by the number of stars in the equivalent bins in Quadrant 4. The difference image, as plotted in Figure 55, shows that there are an excess number of stars in the Quadrant 1 field over the B-V color range.



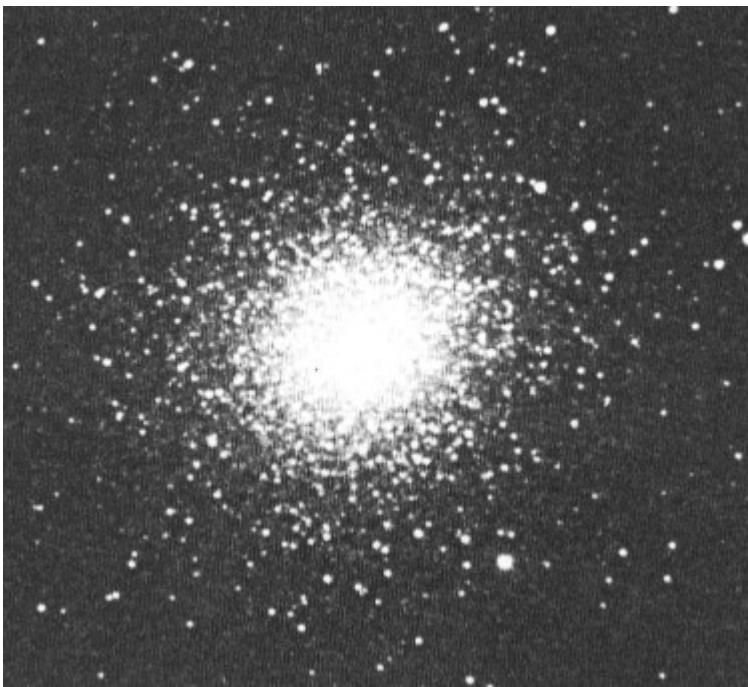
**Figure 55:** Histogram difference between E25N40 and W25N40, showing an excess number of stars in E25N40. No negative values existed for any pixel in E25N40 that had more than 50 stars initially.

Figure 55 gives an overall view of the structure of the stellar excess. The brighter stars (those with lower magnitude values around  $V = 20$ ) are more red in color ( $0.8 < B-V < 1.2$ ), while fainter stars ( $V = 21.5$ ) are more blue ( $0.4 < B-V < 0.8$ ). The excess is 20 – 40% greater in Quadrant 1 versus Quadrant 4, is more than  $2\sigma$  compared to Poisson errors over many pixels.

Observing structure in color-magnitude diagrams is not an unexpected occurrence for astronomers. As discussed in Section 1.4, most stars follow the main sequence described in the Hertzsprung-Russell Diagram, which relates color as a function of absolute magnitude. Stars usually follow a specific pattern in their lives as they convert hydrogen into helium in their cores and move along the main sequence band. For most of our plots, we have been unable to observe any structure because we are observing stars

spread out randomly over great distances. The random distances cause a smearing effect that gives rise to the vertical bands in Figures 53 and 54.

The best observations of structure in color magnitude diagrams are made when looking at globular clusters, which are spatially tight groupings of stars orbiting our galaxies. Since the globular cluster stars formed together, there is little deviation among their distances as we see them. Figure 56 shows an image of the globular cluster M2. Figure 57 shows a color-magnitude histogram of the similar globular cluster M67, where the main sequence structure is very apparent.



**Figure 56: Image of the globular cluster M2**

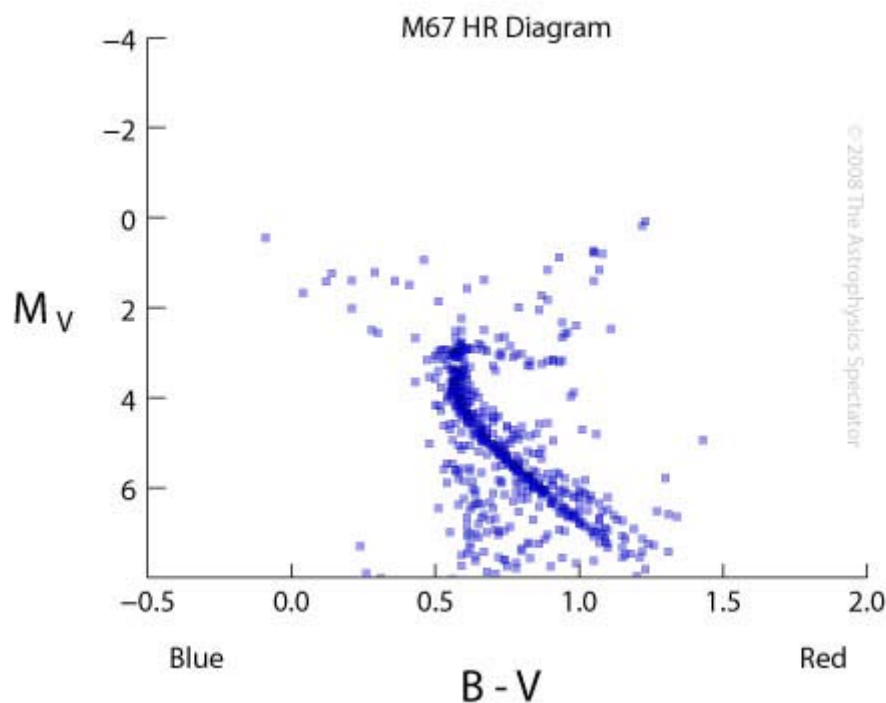


**Figure 57:** Color-Magnitude diagram showing the structure of the globular cluster M67

Notice that in the main sequence in Figure 57, brighter stars are bluer than fainter stars. However, our analysis of the excess in Figure 55 shows quite the opposite effect. Oppositely oriented color-magnitude groupings, however, are not unheard of and usually occur in older, more evolved populations of stars. An example of this is shown in the 47 Tuc HR Diagram in Figure 58. Stars brighter than a V magnitude of +4 are older, have run out of hydrogen, and have evolved off of the main sequence. Between magnitudes +4 and +2, the stars begin to burn helium and thereby becoming bluer again, forming a horizontal branch on the diagram. The turnoff color is the bluest (smallest  $B - V$ ) color still on the main sequence and can provide a clue as to the cluster's age.



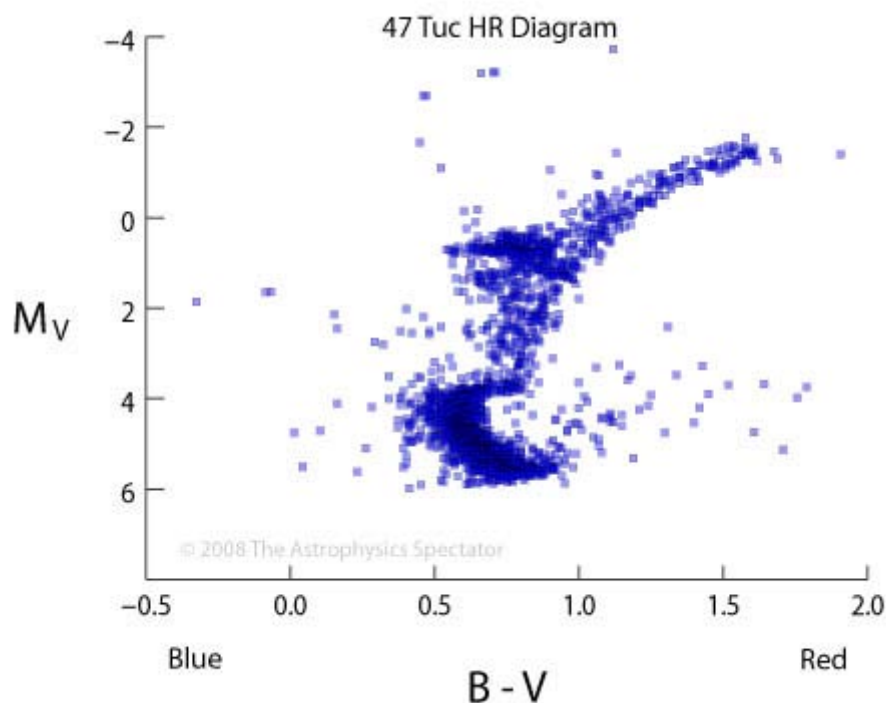


**Figure 58: Color-Magnitude Diagram of 47 Tuc, showing an older population of stars that has evolved off of the main sequence.**

In Figure 55 of the measured stellar excess in E45N20, we observe a turnoff point from the main sequence at V magnitude of 21.5 and a possible horizontal branch at V of 20.5. By the time we reach a V magnitude of 20, there are almost no blue stars in the image. The position at which the turnoff exists can help to provide an estimate of the age of the population of stars in the excess. Although we have insufficient statistical power to do anything more than make a rough conclusion about the age, this turnoff point occurs at V magnitude 21 at a B-V color value between 0.3 and 0.5.

Stellar age is based off of the principle that bluer stars are brighter and hotter and therefore burn more fuel than cooler, fainter, redder stars. If a population of stars forms at a set time, the bluer stars will burn fuel faster than the redder stars and will therefore

die off sooner. Stellar populations with a larger proportion of red stars to their overall star number are therefore usually older populations. This is why the blue stars in the 47 Tuc HR Diagram in Figure 58 have grown old and evolved off of the main sequence, while the red stars have stayed on the main sequence. As a population of stars ages and evolves, the turnoff point for main sequence to non-main sequence stars moves down the V magnitude axis to fainter and fainter magnitudes. Figure 59 shows series of time-evolved main sequences (isochrones) whose turnoff points we used to estimate the age of the Hercules Thick Disk Cloud. Our turnoff color is approximately  $B-V = 0.2 - 0.4$ , which when placed on this isochrone indicates an age of 1 to 3 billion years.

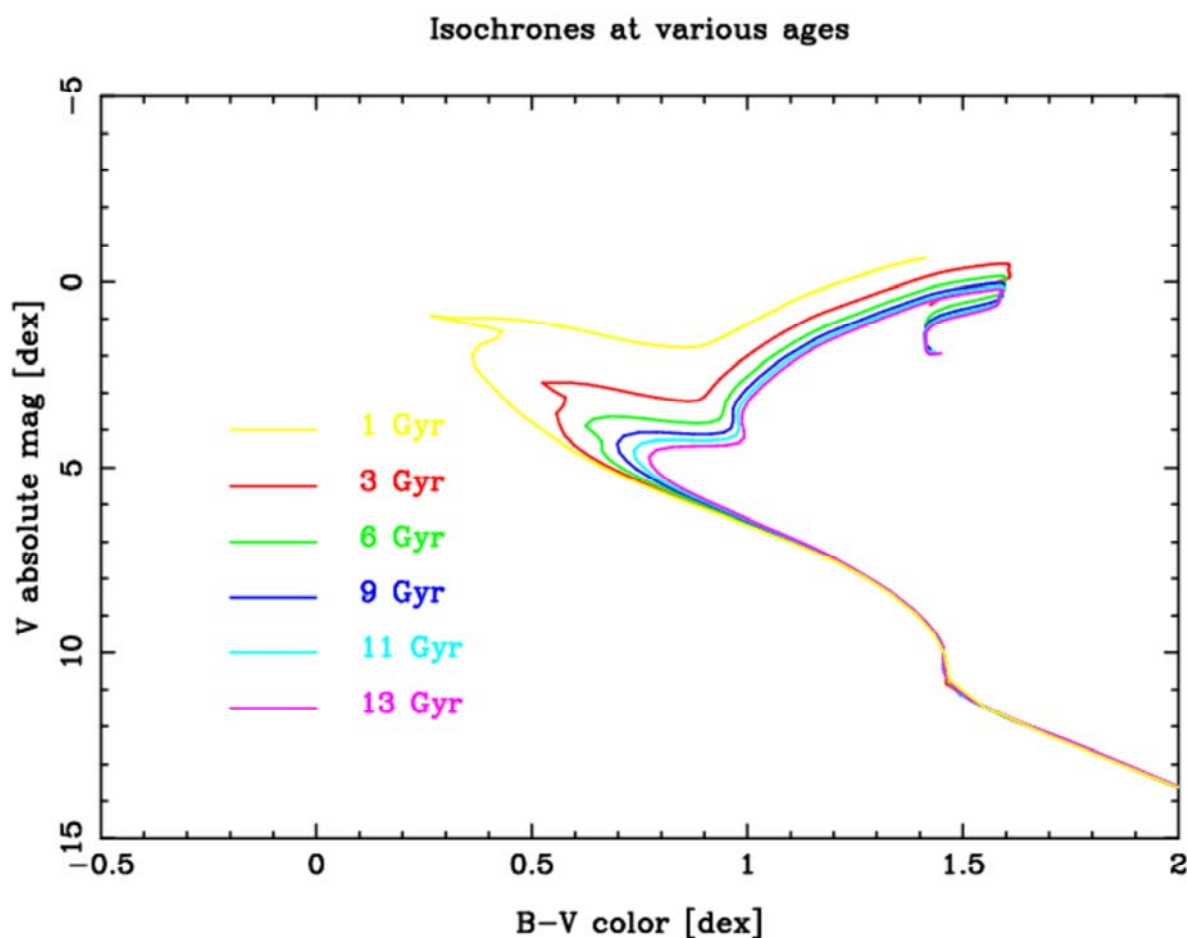


**Figure 59:** Diagram of various turnoff points in the color-magnitude diagram, with estimated ages on the right-side scale based on the V magnitude of the turnoff point. Our turnoff color is approximately  $B-V = 0.2 - 0.4$ .

To make this estimate viable, we assumed star formation for the stellar excess stopped when our Galaxy stripped away its gases by dynamical friction during the galactic merger. The excess stars have continued aging without producing new stars ever since the galactic merger, so the age should be accurate. To improve upon our age estimate of 1 to 3 billion years, future work will have to focus on refining the isochrone technique. We will have to add statistics through additional observation of the 20 – 21 V magnitude range in order to make a more accurate determination of the turnoff color.

## Chapter 5: Conclusions and Directions for Future Work

Figure 60 shows the Aitoff Projection of all observed fields in this project. Table 12 from Section 4.1 is reprinted to show the count ratios of data again.

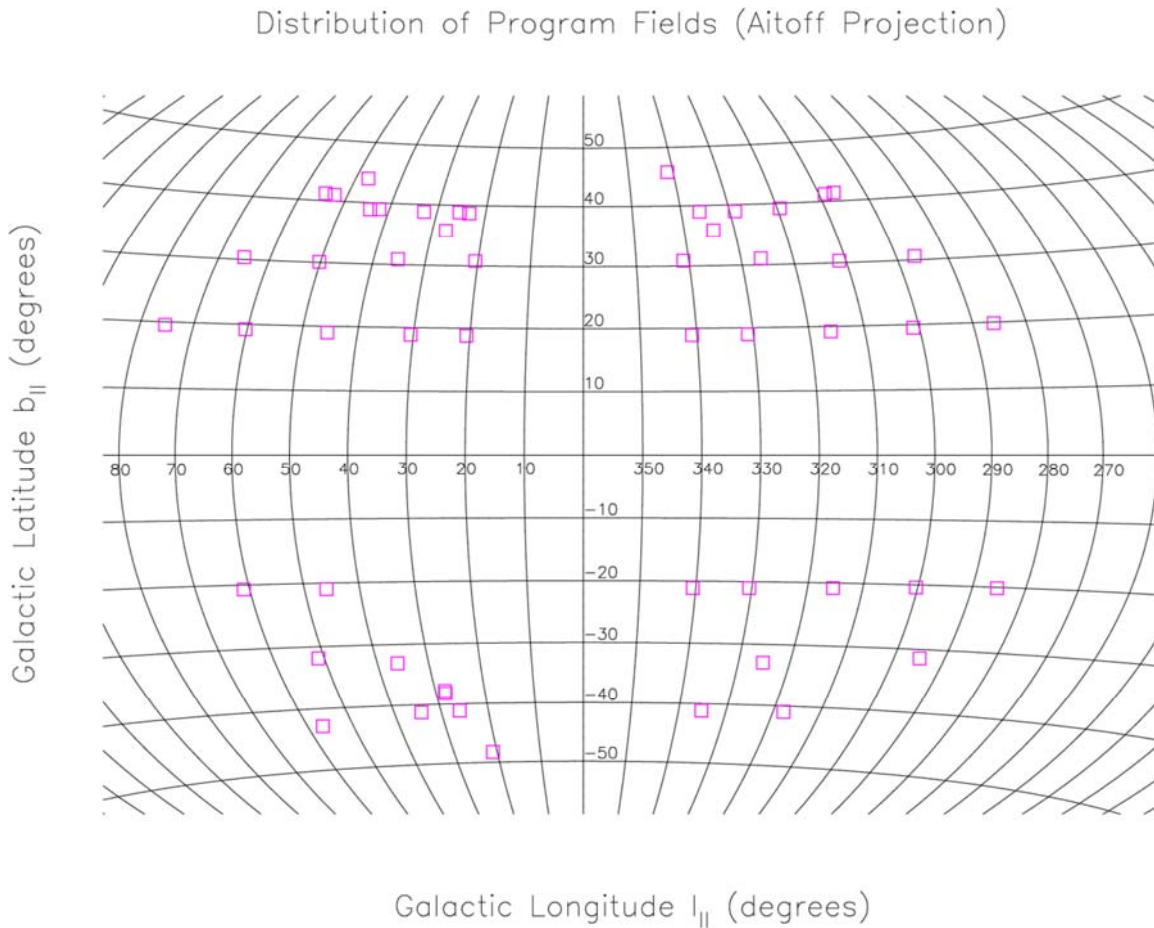


**Figure 60: Aitoff projection of the stellar fields analyzed over the course of the project**

Field Ratio	$l_1 / l_2$	$b_1 / b_2$	GALMOD Ratio Predictions			Observed Count Ratios		
			$16 < V < 19$	$17 < V < 18$	$18 < V < 19$	$16 < V < 19$	$17 < V < 18$	$18 < V < 19$
Quadrant 1 / Quadrant 4 ratios above the Galactic Plane								
E45N20 / W45N20	45/315	+20/+20	1.00	1.00	1.00	1.14 ± 0.04	1.21 ± 0.02	1.00 ± 0.05
E50N31 / W50N31	50/310	+31/+31	1.00	1.00	1.00	1.22 ± 0.08	1.28 ± 0.09	1.08 ± 0.09
E55N42 / W55N42	55/305	+42/+42	1.00	1.00	1.00	1.02 ± 0.08	0.98 ± 0.11	0.99 ± 0.10
E60N20 / W60N20	60/300	+20/+20	1.00	1.00	1.00	1.03 ± 0.04	1.01 ± 0.07	0.93 ± 0.06
E65N31 / W65N31	65/295	+31/+31	1.00	1.00	1.00	1.01 ± 0.07	1.07 ± 0.11	0.82 ± 0.09
E57N20 / W75N20	75/285	+20/+20	1.00	1.00	1.00	1.01 ± 0.04	0.97 ± 0.07	0.96 ± 0.07
Quadrant 1 / Quadrant 4 ratios below the Galactic Plane								
E45S20 / W45S20	45/315	-20/-20	1.00	1.00	1.00	0.94 ± 0.03	1.01 ± 0.06	0.87 ± 0.04
E60S20 / W60S20	60/300	-20/-20	1.00	1.00	1.00	1.00 ± 0.04	0.89 ± 0.05	1.17 ± 0.07
Quadrant1 ratios above/below the Galactic Plane								
E45N20 / E45S20	45/45	+20/-20	0.94	0.94	0.97	1.13 ± 0.04	1.18 ± 0.06	1.10 ± 0.05
E50N31 / E50S31	50/50	+31/-31	0.97	0.97	0.98	1.13 ± 0.04	1.17 ± 0.11	1.04 ± 0.09
E60N20 / E60S20	60/60	+20/-20	0.94	0.93	0.96	0.90 ± 0.05	0.86 ± 0.06	0.84 ± 0.05
Quadrant 4 ratios above/below the Galactic Plane								
W45N20 / W45S20	315/315	+20/-20	0.94	0.94	0.97	0.94 ± 0.04	0.94 ± 0.06	0.92 ± 0.05
W60N20 / W60S20	100/100	+20/-20	0.94	0.93	0.96	0.82 ± 0.05	0.73 ± 0.04	1.00 ± 0.07

**Table 12: Observed Ratios**

From the ratios in Table 12, we found that the most positive stellar ratios occur when comparing Quadrant 1 above the Galactic Plane to Quadrant 4 below the Plane and Quadrant 1 above the Plane to Quadrant 4 above the plane. The ratios of Quadrant 1 below to Quadrant 4 below and Quadrant 4 above to Quadrant 4 below are roughly what they should equal based on predictions made by the galactic model. As discussed in section 4.1, our analysis of the ratios of the 11 highest longitudes shows the stellar excess is confined to only Quadrant 1 above the Galactic Plane. Both the stellar bar and the thick disk triaxiality origins required the excess to extend significantly below the Galactic Plane. By ruling out these two possibilities, we conclude that the Hercules Thick Disk Cloud was most likely formed as the result of a galactic merger. Preliminary analysis of the color-magnitude turnoff point we discovered allows us to make an estimate that the merger took place between 1 to 3 billion years ago. From our analysis using the method of photometric parallax, we conclude that the excess is a cloud or a stream about 1.5 kiloparsecs wide and located between 800 and 3200 parsecs from our Sun.

Future work in studying the stellar excess will focus on mapping the motions of the stars and determining the overall trajectory of the Hercules Thick Disk Cloud. A more accurate pinpointing of the color-magnitude turnoff point will allow us to make a more precise estimate of the age of the excess. Further analysis of the shape of the excess may tell us more information about the type of object that was absorbed by our galaxy during the galactic merger.

For years, most astronomers have focused on studying extragalactic objects because they lacked the mathematical tools to analyze and understand our own Galaxy. The study of the Hercules Thick Disk Cloud represents a strong attempt to better

understand our own stellar neighborhood, despite the limitation of not being able to observe it from the outside. Few can guess what new surprises await as astronomers refocus their attention on the Milky Way.

## Appendix A: Genetic Algorithm

To find the multi-dimensional parameters underlying a star count model for the Galaxy, astronomers need to employ some kind of optimization technique. An enumerated search would randomly pick out different sets of parameters to test and would eventually find the optimal set of solutions, but only after ten million iterations for a reasonable match and one trillion iterations for an exact match, so this is an expensive proposition. A gradient search is ruled out because the luminosity functions and color lookup tables are numerical, causing the GALMOD to be non-analytical. A combination of these two methods, known as an iterated search, would also take too long, as would a method developed in the 1980's called simulated annealing. In his initial research in 1996, Larsen settled on the Genetic Algorithm.<sup>47</sup>

Genetic algorithms are mathematical procedures for finding a solution or set of solutions in a variety of situations. The algorithm program takes potential model parameters and treats them as a set of genes on a chromosome. One generation's chromosomes recombine in different patterns to form the next generation of chromosomes, with better model fits having a higher probability of being continued into the next generation. The algorithm takes the most fit of these combinations and allows them to reproduce into the next generation. Thus, natural selection and survival of the fittest ensures that the algorithm finds the most optimal solutions.<sup>48</sup>

The global parameters (our model variables) to be solved for are known as *genes* and each variable on a particular population member is a *chromosome*. The model

---

<sup>47</sup> Larsen, *Shape*, 135.

<sup>48</sup> Mihalas, Dimitri and James Binney, *Galactic Astronomy: Structure and Kinematics*, 2<sup>nd</sup> ed. (New York: W. H. Freeman and Company, 1981), pp 15.

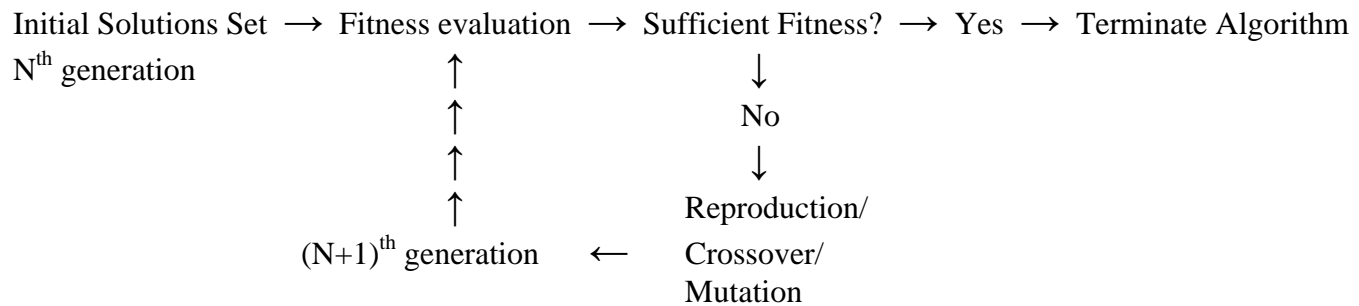


produced by the chromosomes is a *phenotype*. Two population chromosomes interact and recombine to produce offspring, with recombination controlled by the *single point crossover* method, where part of one solution and part of another are integrated at a single point. Random *mutations* will change certain parameters in the chromosomes to decrease the likelihood that a solution finds the actual best fitness. The population is allowed to reproduce over time and the solutions of higher fitness value are allowed to survive, while those of lower value die off and are removed from the population (“survival of the fittest”). Over time, the average fitness value of all chromosomes in the population increases and the genes converge to the same set of parameter values. When 80% of the population converges same set of values, the algorithm cuts off and gives the most common values as the optimal set of solutions. Though the solutions may not be the mathematical absolute best, they still produce a relatively good set of parameters in a reasonably short amount of time.<sup>49</sup>

The diagram below shows the steps of the genetic algorithm, beginning at the  $n^{\text{th}}$  generation and running through an initial evaluation for fitness of the chromosomes. Depending on performance standards, the algorithm will either stop if the fitness (accuracy) of the solutions is sufficient or will modify the solutions to make a new generation. If modification occurs, the “chromosomes” of solutions reproduce via gene crossover (integrating separate solutions) and develop mutations (new random values) amongst the solutions. This new  $(n+1)^{\text{th}}$  generation will be evaluated for its fitness again and the algorithm will either stop or go through another iteration of reproduction, crossover, and mutation. The mutation cycle will continue until the fitness level is adequate to stop the algorithm.

---

<sup>49</sup> Larsen, *Shape*, 136-137.



The increasing level of fitness over succeeding generations is modeled in Figure

61.

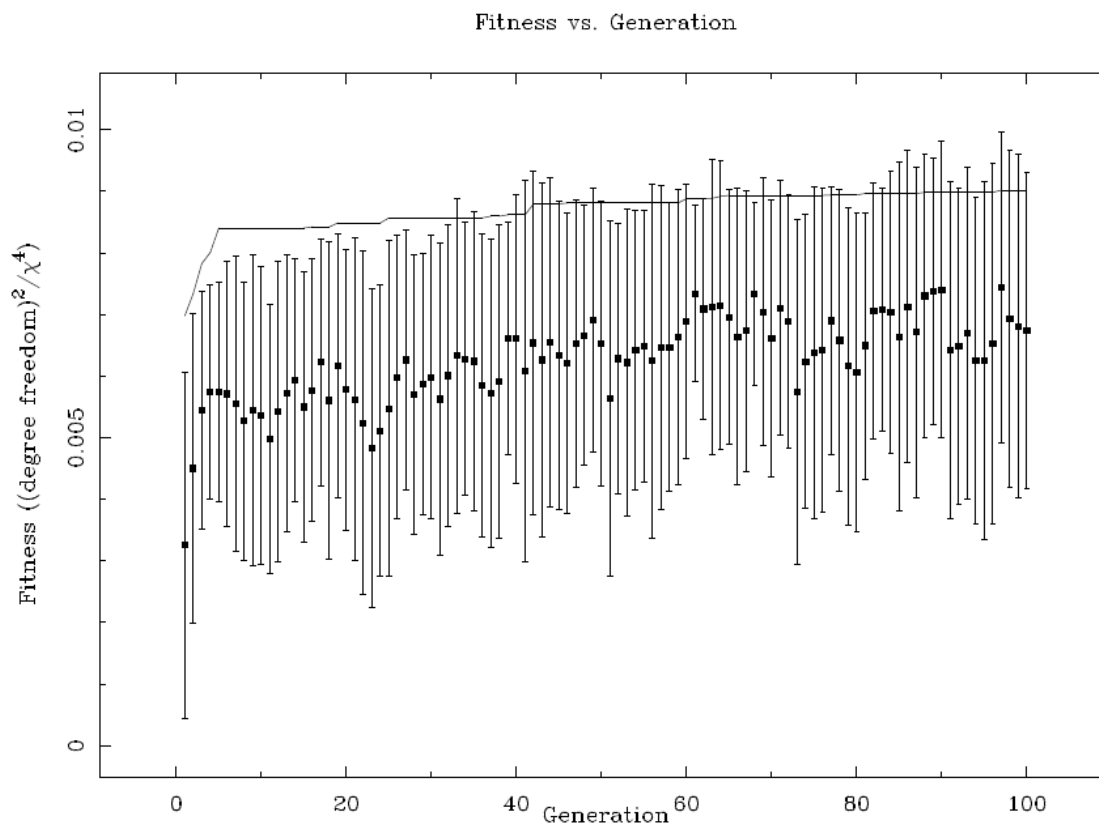


**Figure 61: Evolution of Population Fitness by a Genetic Algorithm over time**

When applied to the galactic model, the genetic algorithm compiles a population set of random solutions and assigns a fitness value to each solution. The fitness value in

this application is determined by comparing the proposed model to the observed data in the fitness function.<sup>50</sup> This forms a modified  $\chi^2$  statistic that is used on all bins with more than 5 stars each in the model.

$$\chi_{Field}^2 = 2 \times \sum_{M_V, S_{B-V}} \frac{(A_{Field, Model}(M_V, S_{B-V}) - A_{Field, Data}(M_V, S_{B-V}))^2}{(A_{Field, Model}(M_V, S_{B-V}) + A_{Field, Data}(M_V, S_{B-V}))}$$

(Equation 10)

where  $M_V$  is the absolute V magnitude,

$S_{B-V}$  is the B-V color magnitude,

$A_{Field, Model}(M_V, S_{B-V})$  is the galactic model distribution, and

$A_{Field, Data}(M_V, S_{B-V})$  is the observed distribution

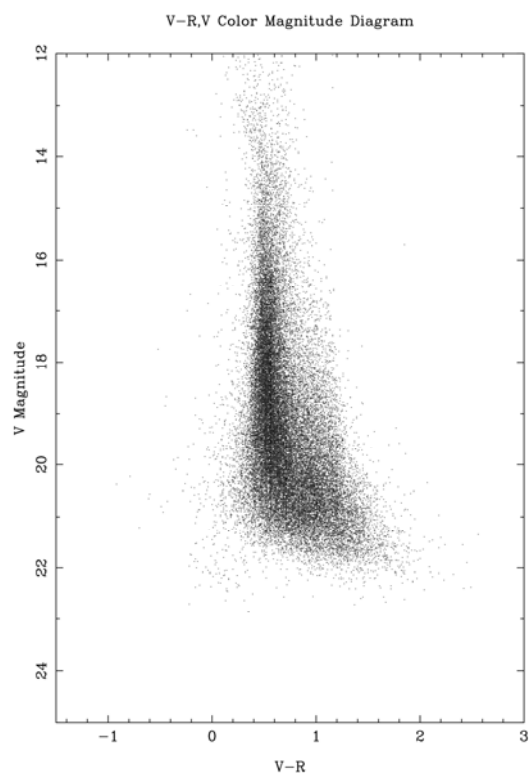
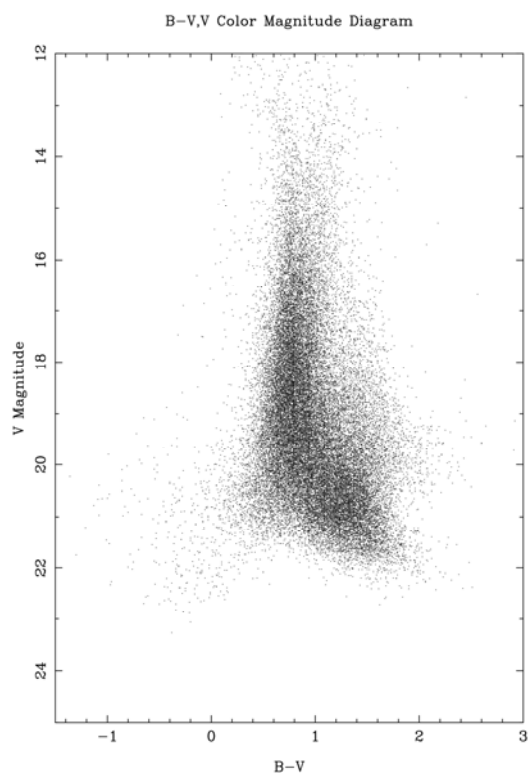
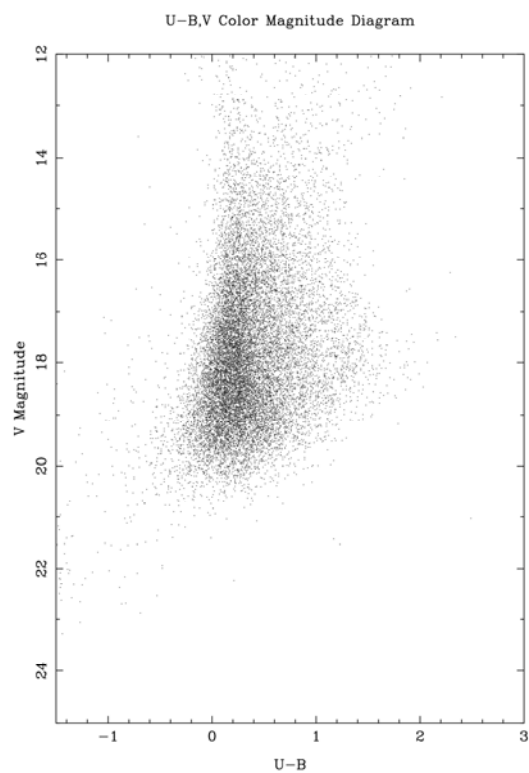
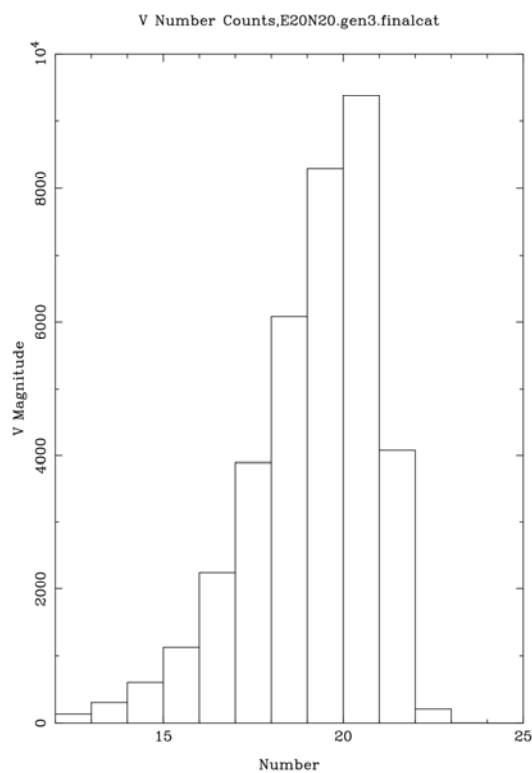
---

<sup>50</sup> Larsen, *Shape*, pp. 141/

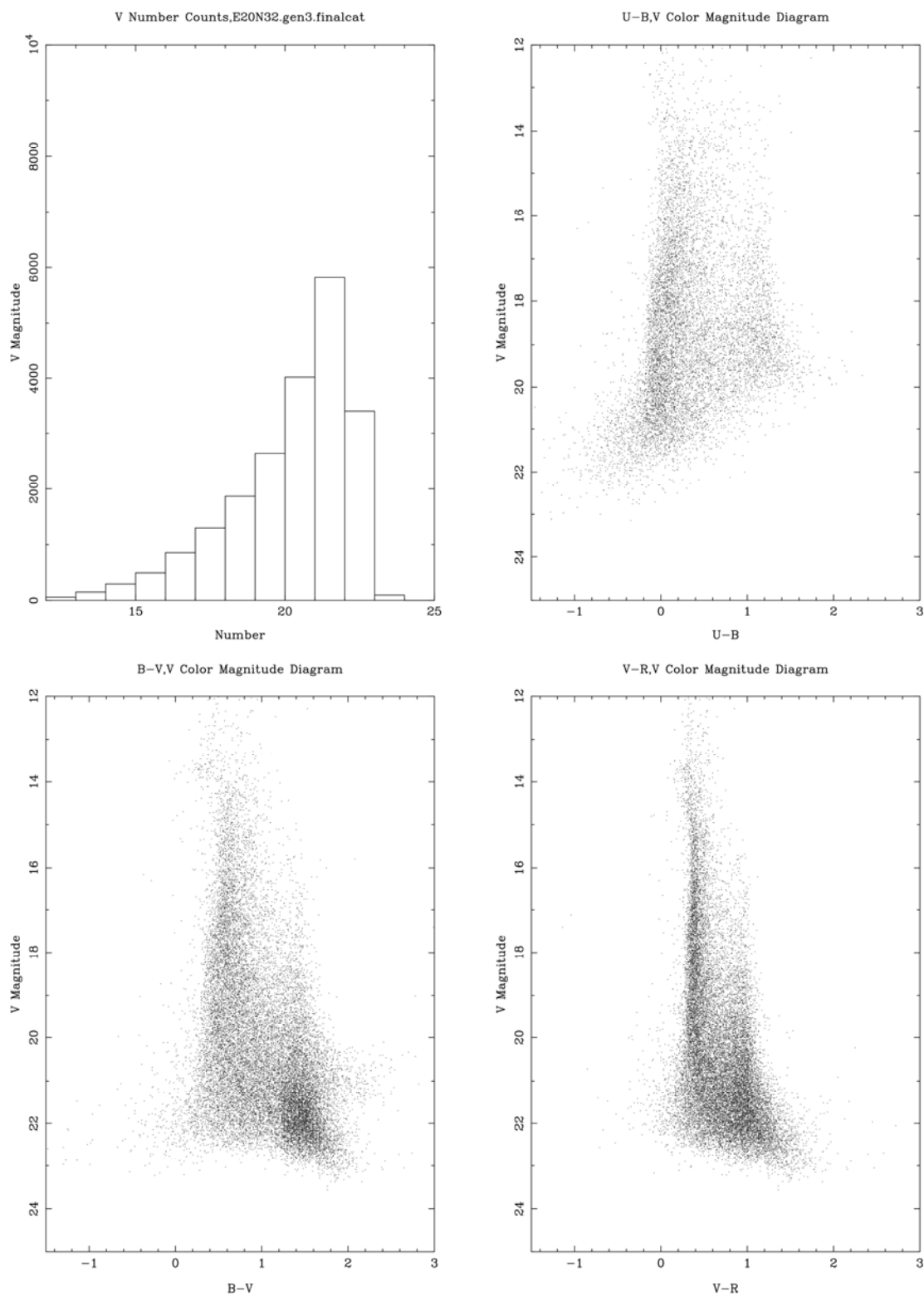
## Appendix B: Presentation of Star Count Data

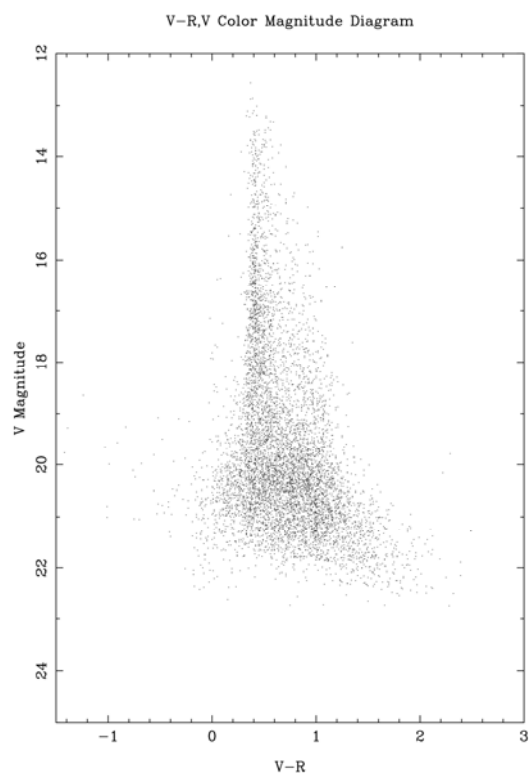
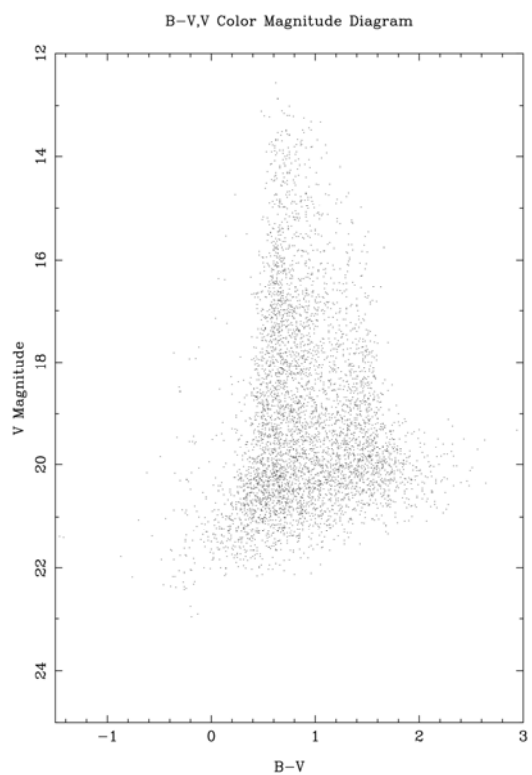
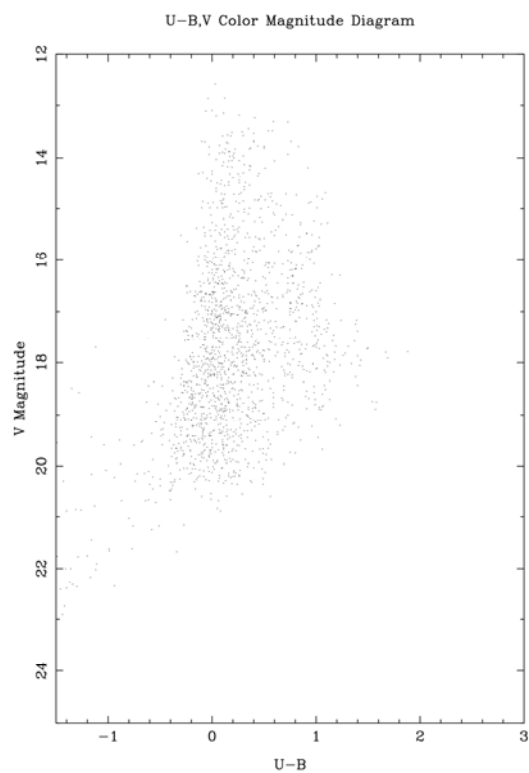
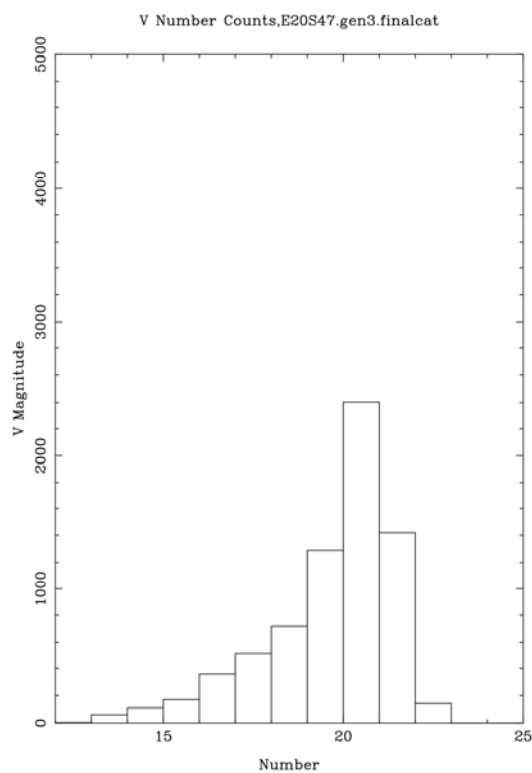
The following data are from the observed fields listed in Table 12 and mapped out in the Aitoff projection in Figure 60. Each field is represented in four plots

1. The first plot is the V magnitude of observed stars for this field against the number of star counts in each magnitude. It is used to show the distance the observed field stars extend out to and consequently the faintest magnitudes observed by the CCD.
2. The second plot is the V magnitude against U-B color. These data can be used for population discrimination when analyzing proper and radial motion, so its use is outside the bounds of this report.
3. The third plot is the V magnitude against the B-V color. These data are the main discriminator in both star counts models and the method of photometric parallax.
4. The final plot is the V magnitude against the V-R color. These data are not as commonly used, but they are occasionally utilized to check B-V photometry, since the V-R and B-V colors for main sequence stars are correlated.

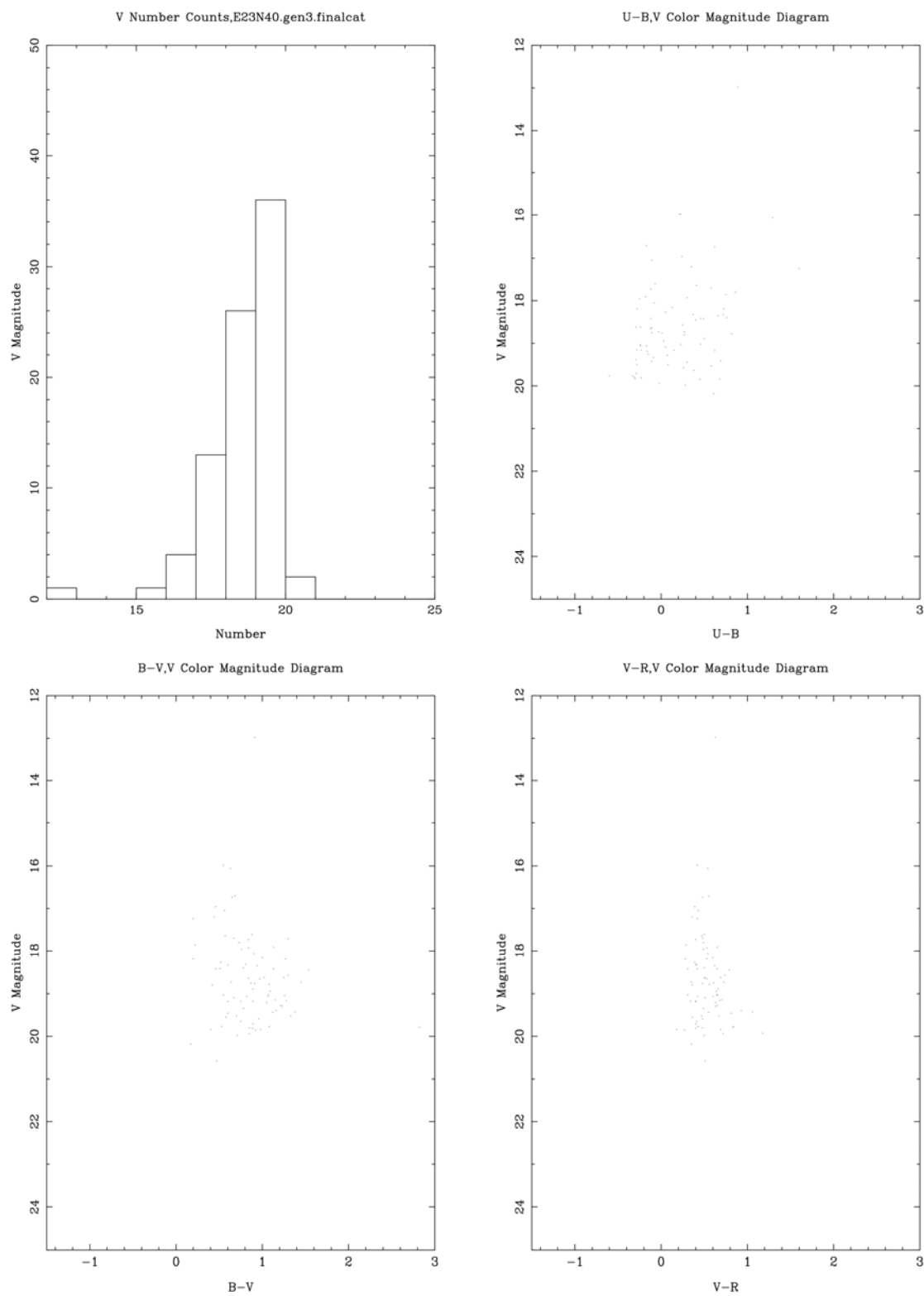
**E20N20**

# E20N32

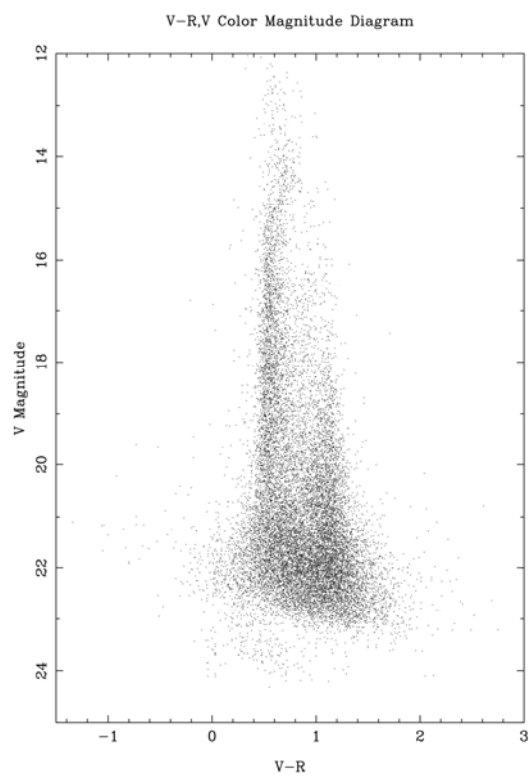
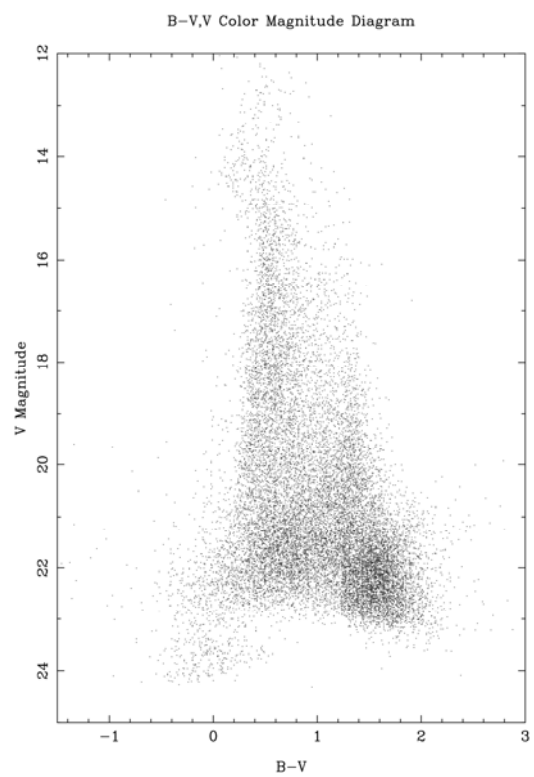
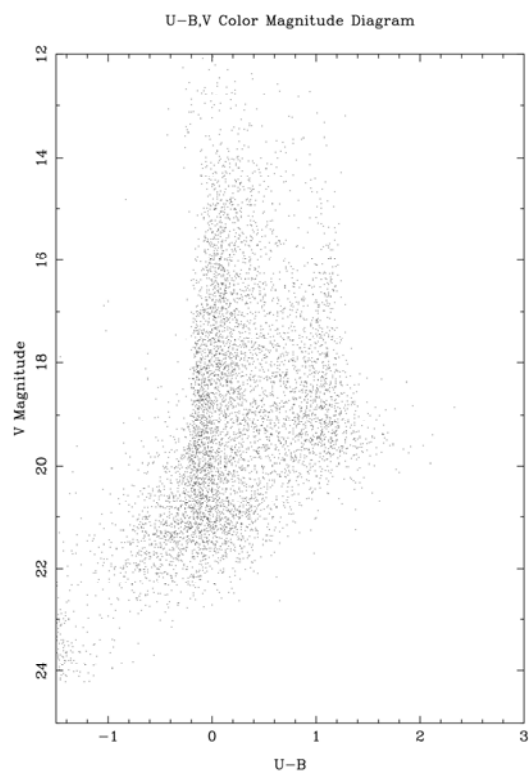
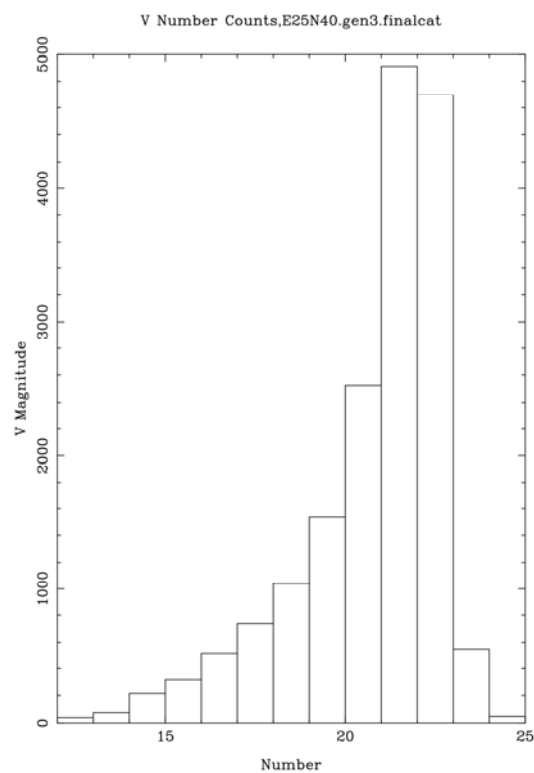


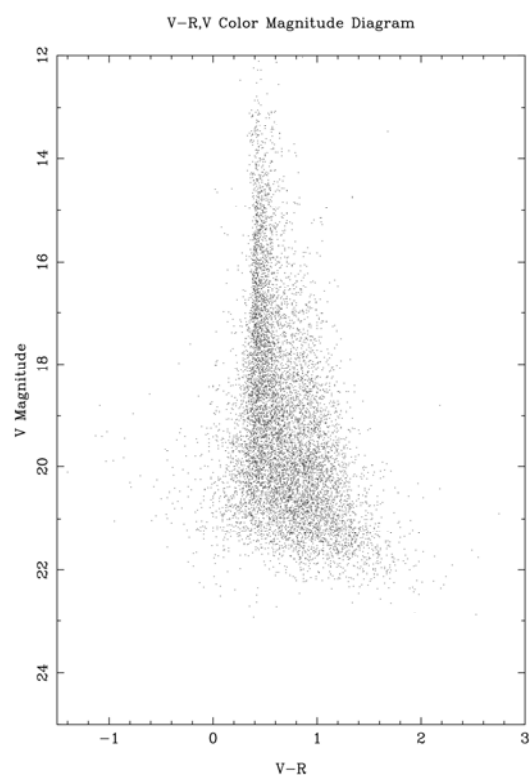
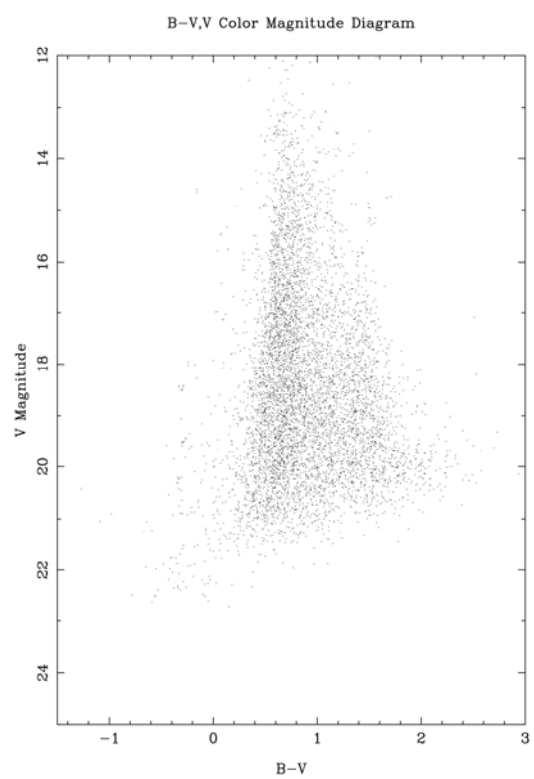
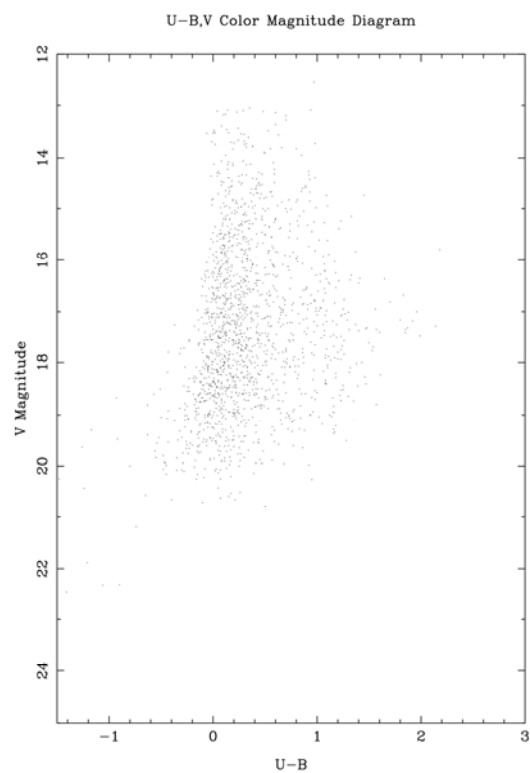
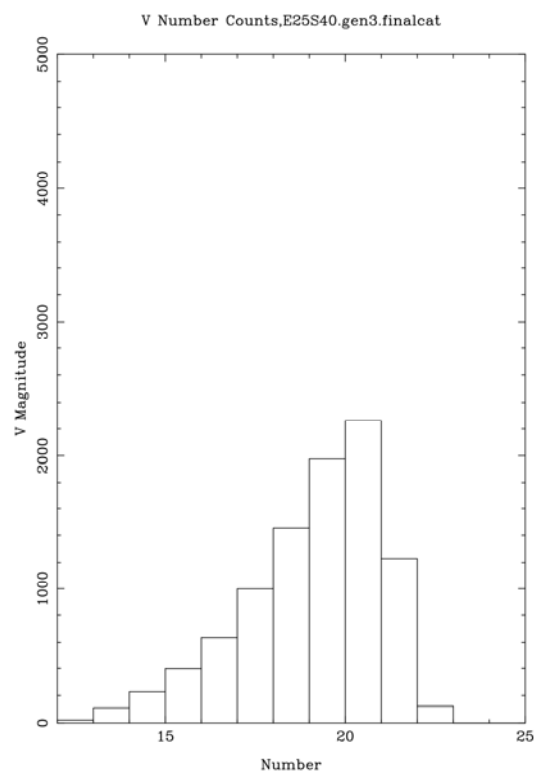
**E20S47**

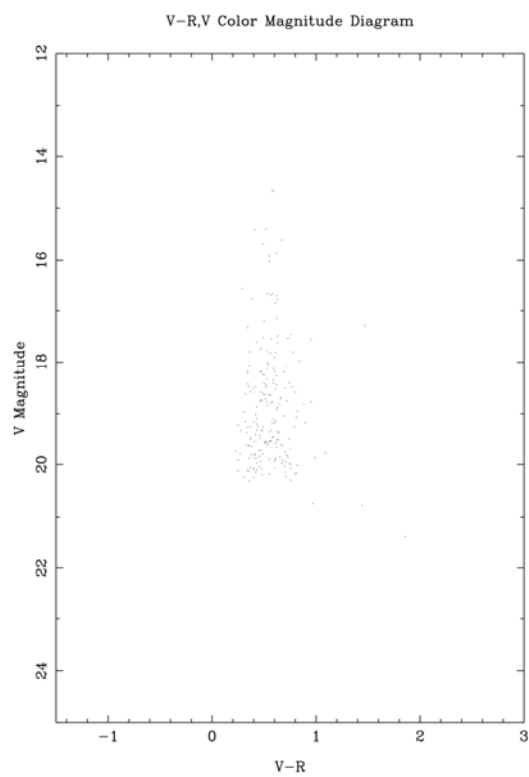
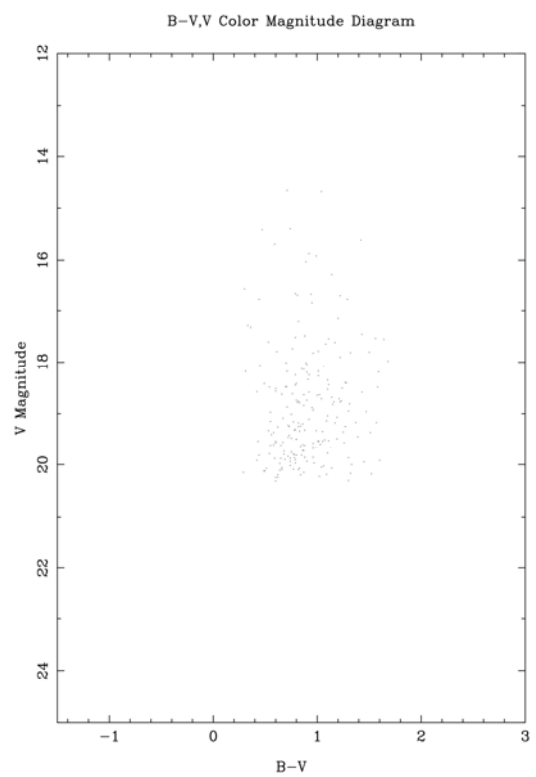
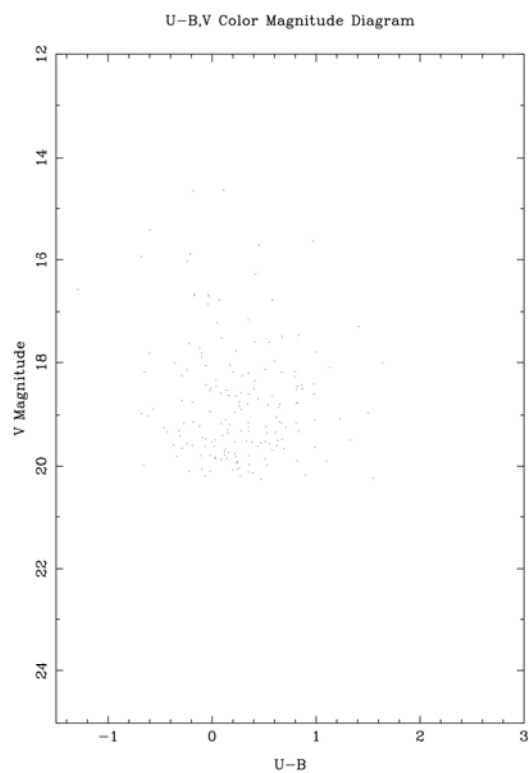
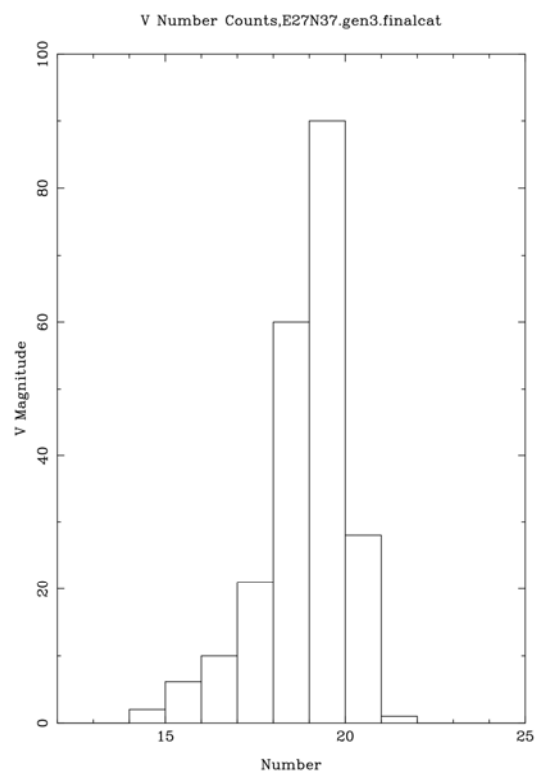
# E23N40

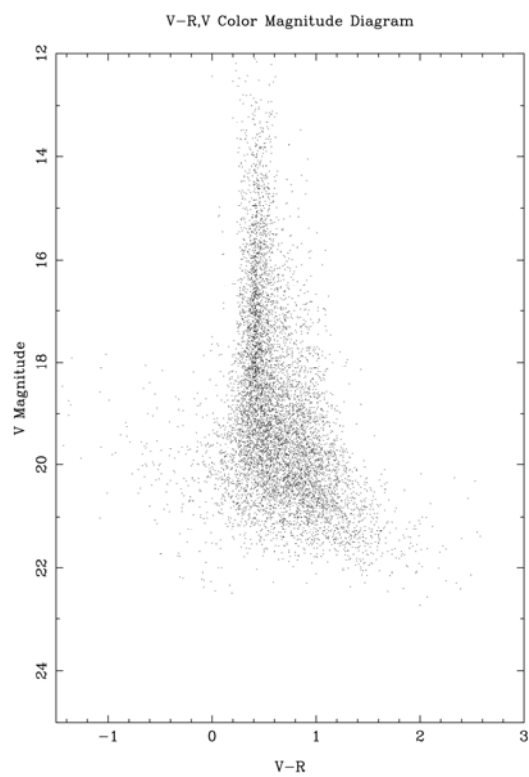
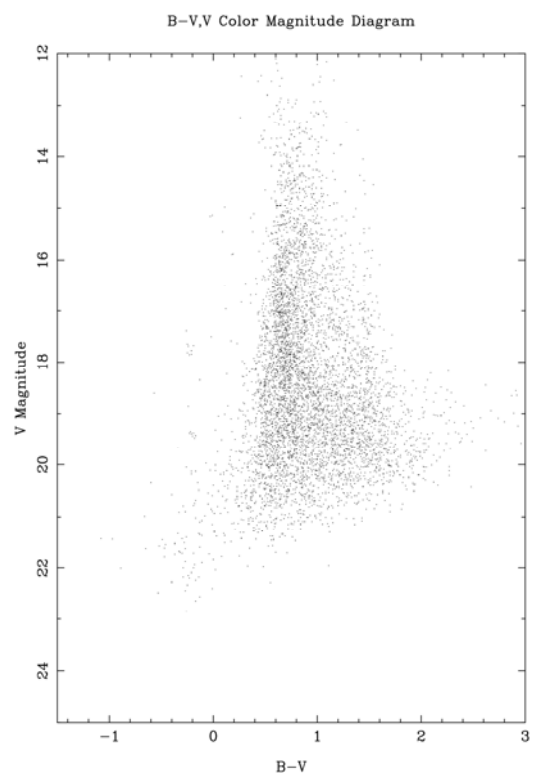
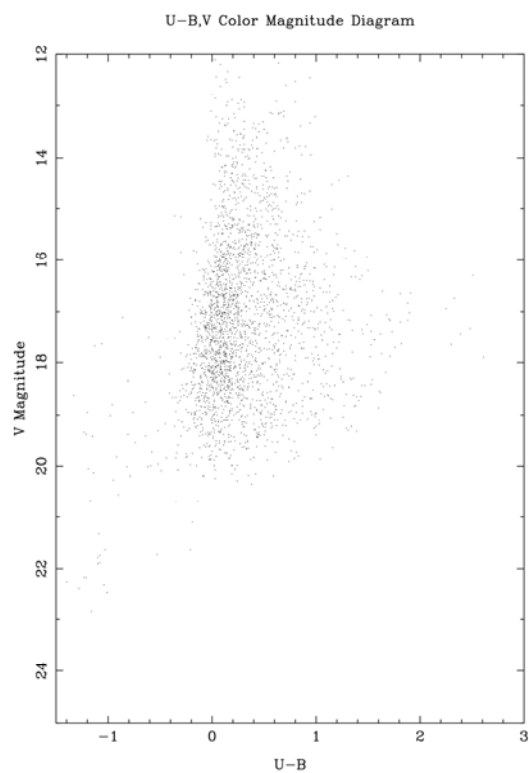
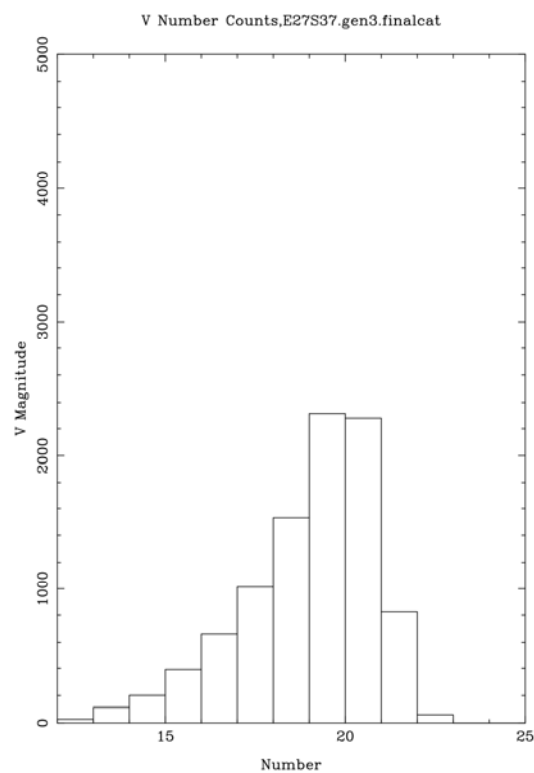


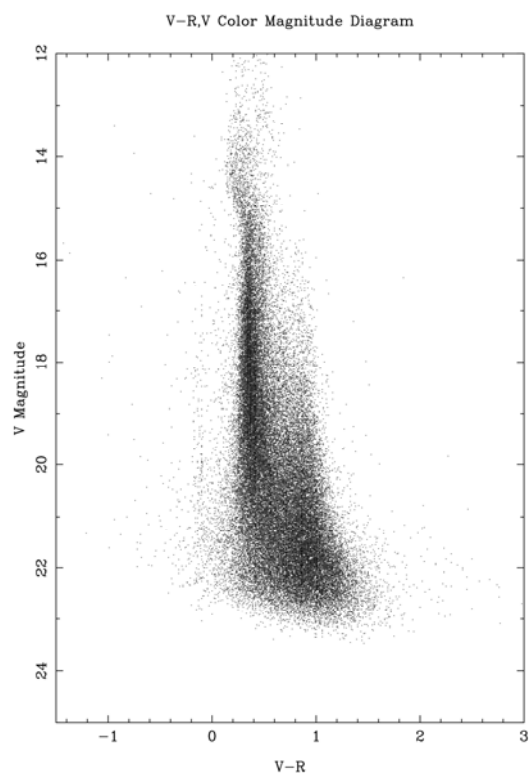
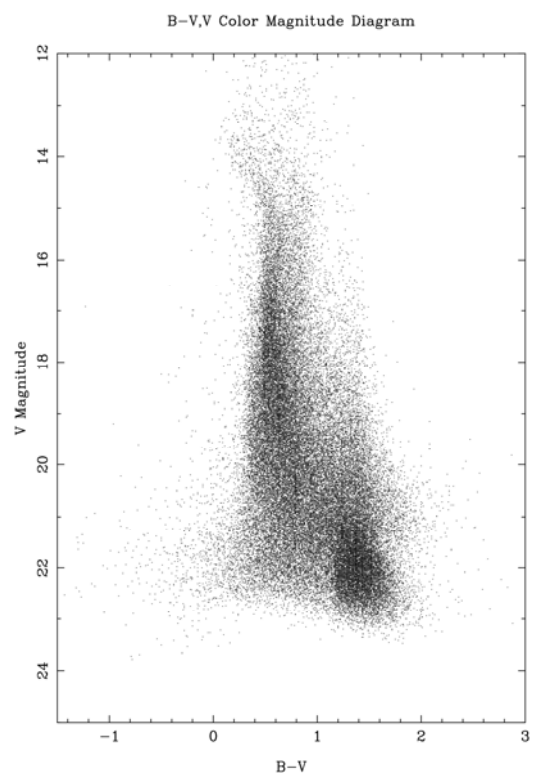
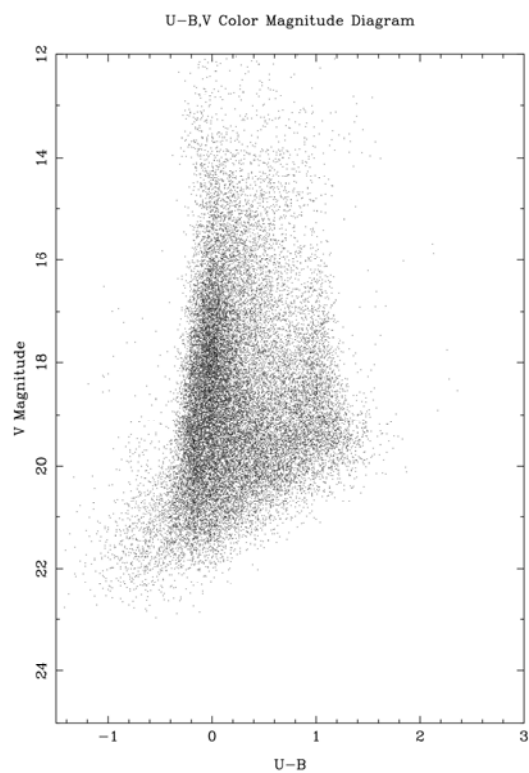
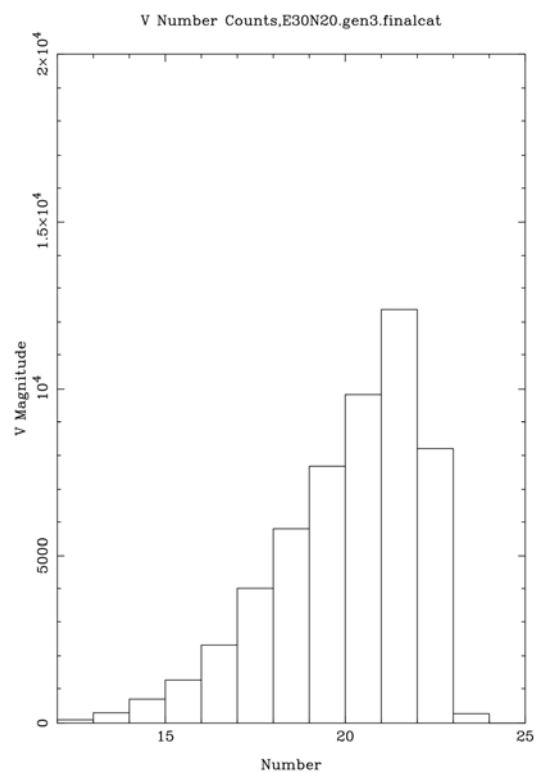


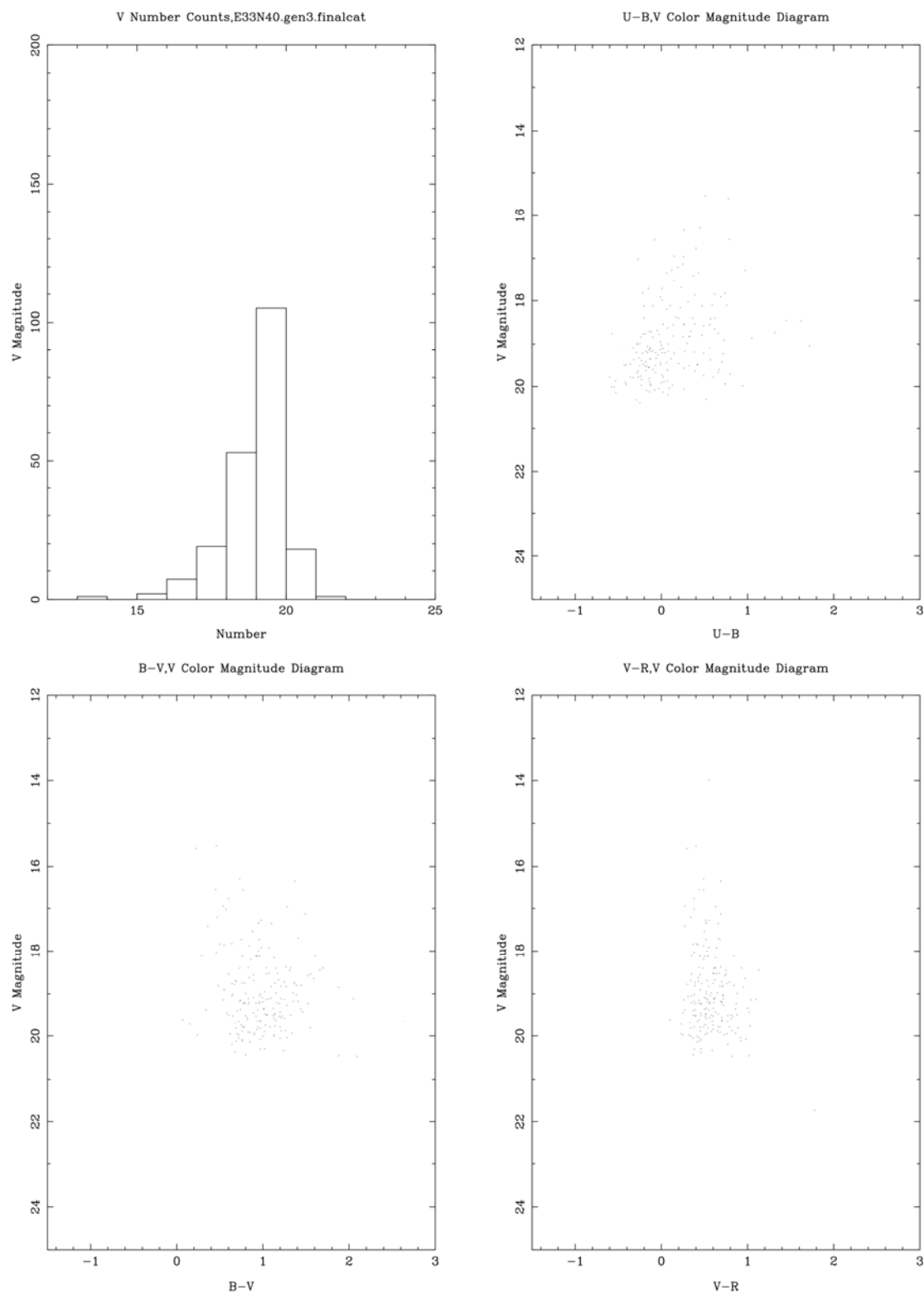
**E25N40**

**E25S40**

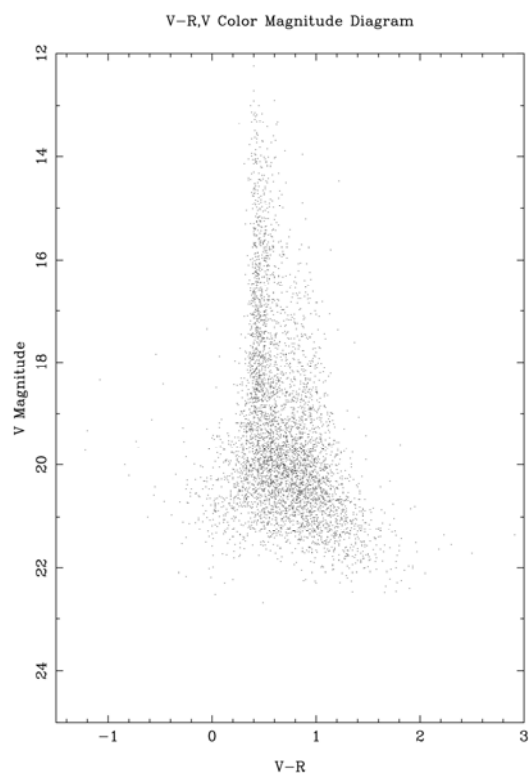
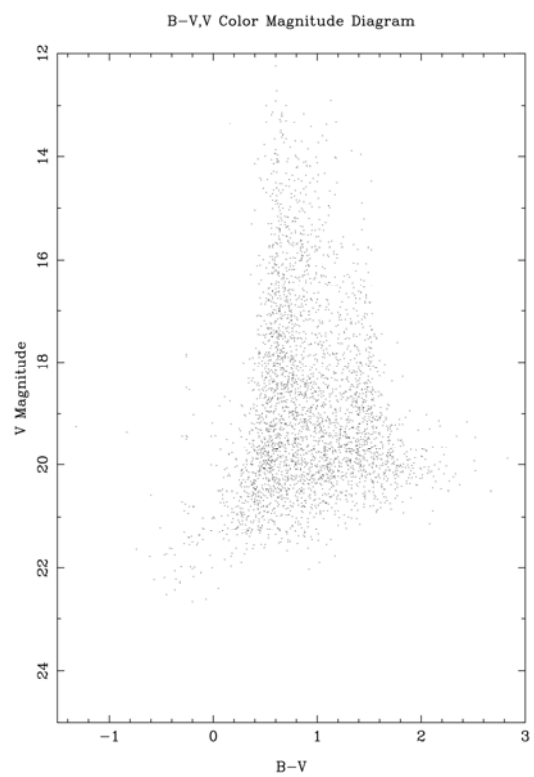
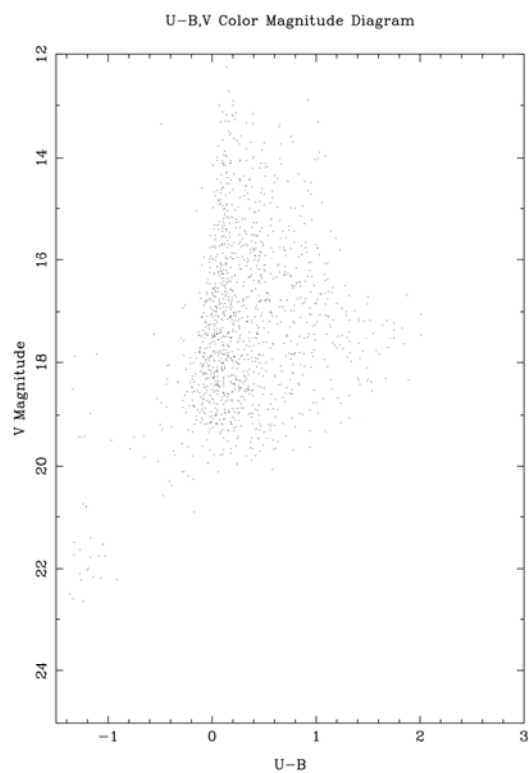
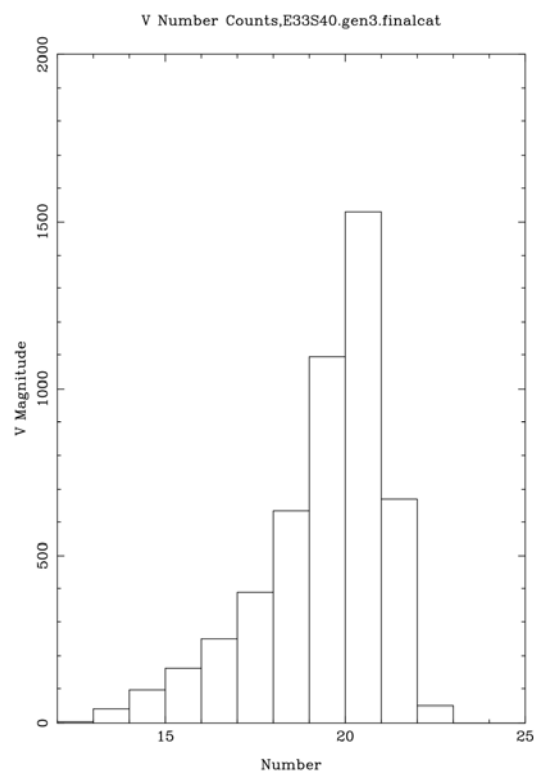
**E27N37**

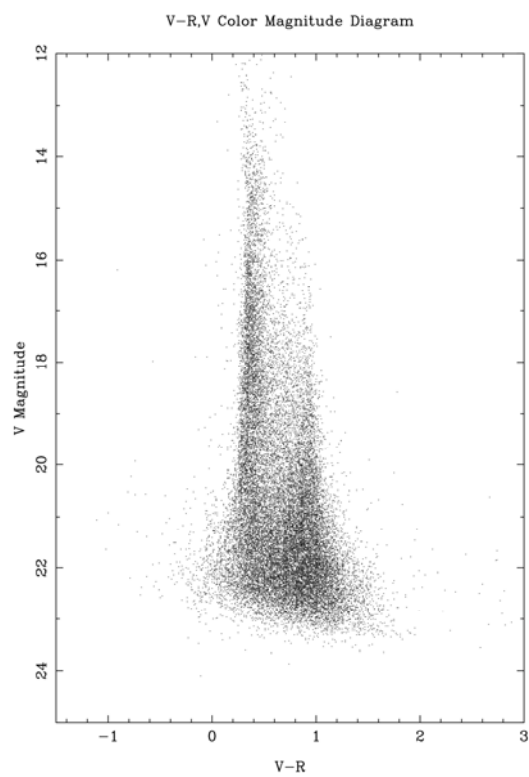
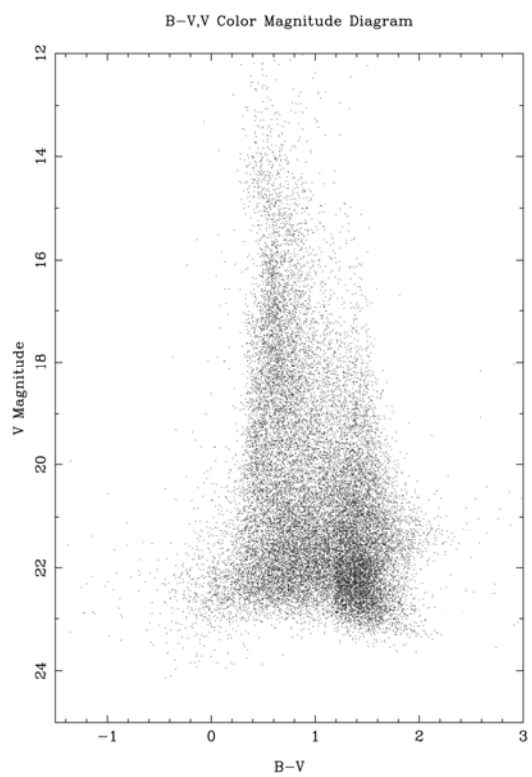
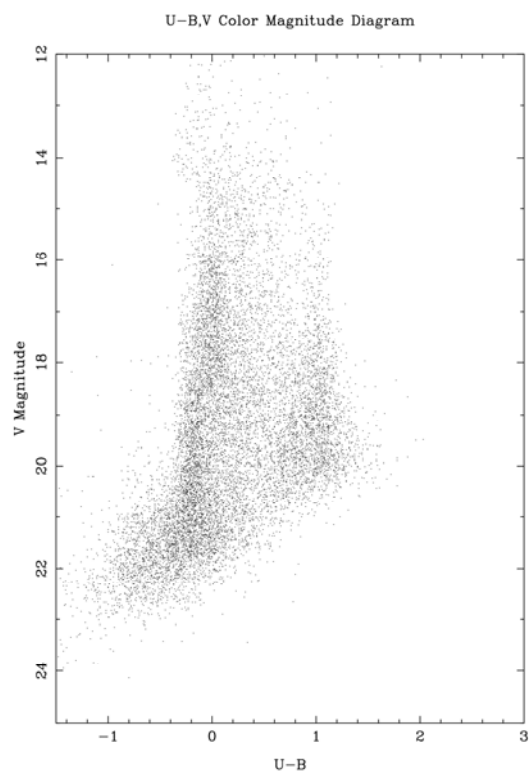
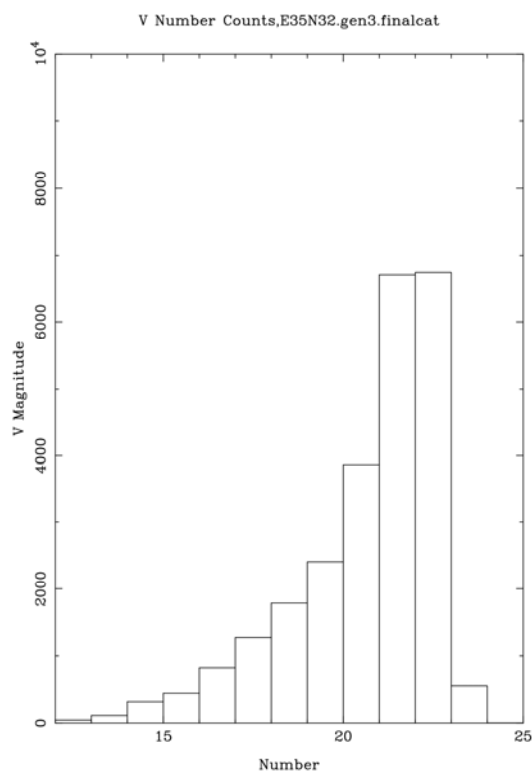
**E27S37**

**E30N20**

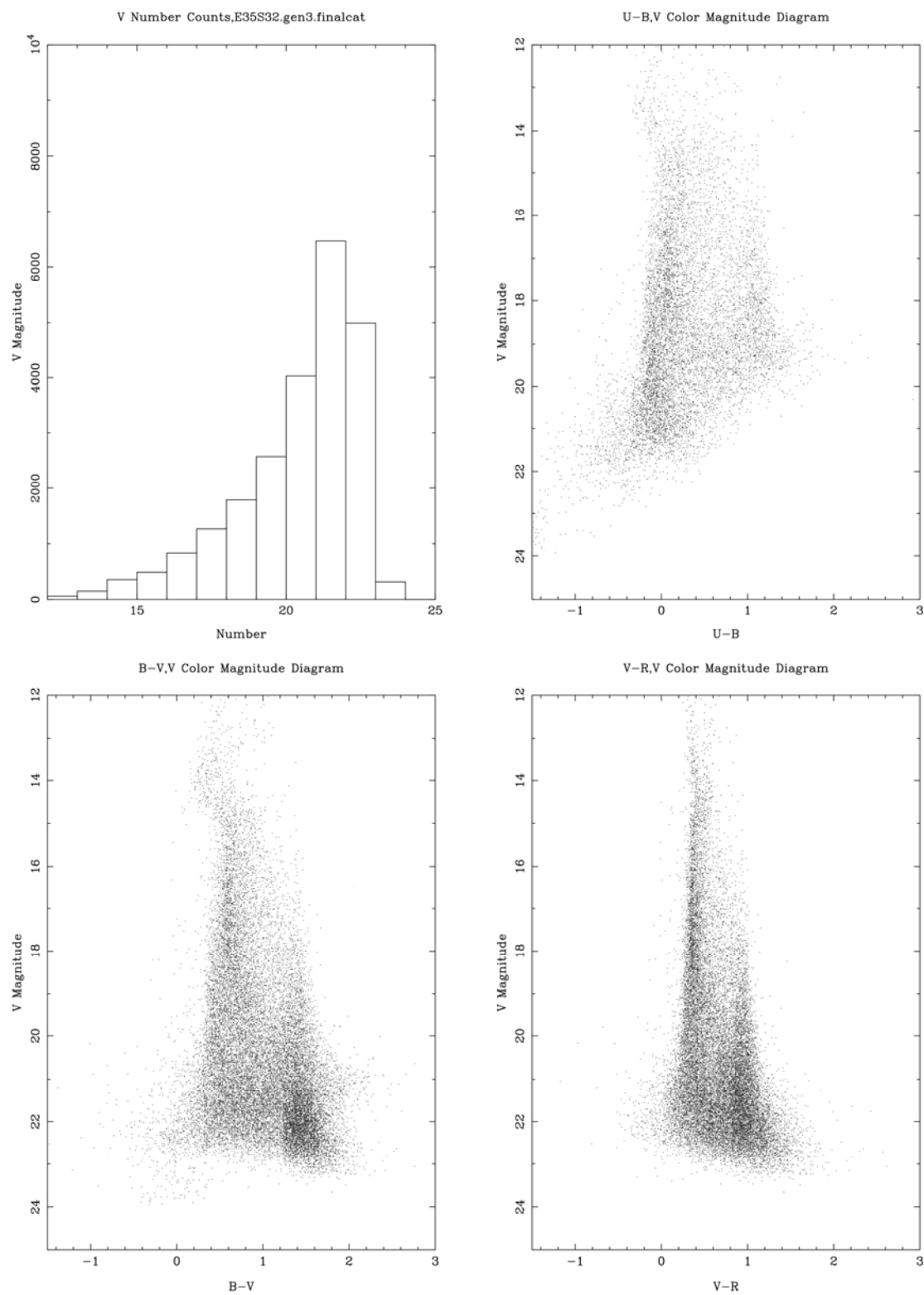
**E33N40**

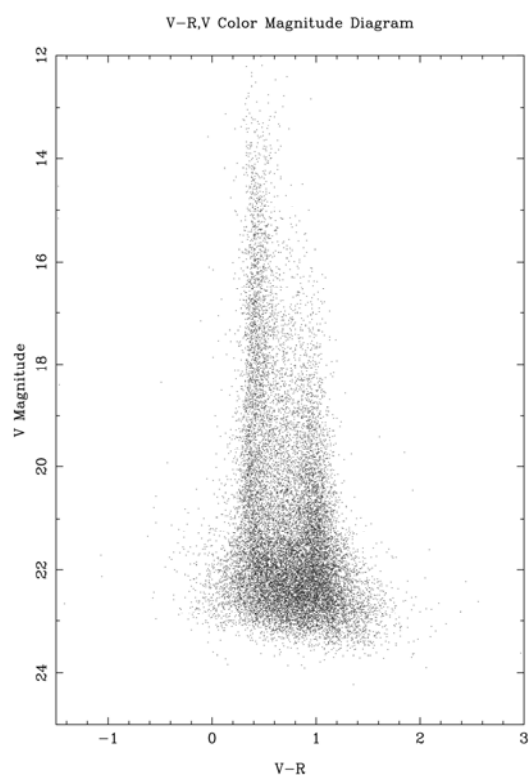
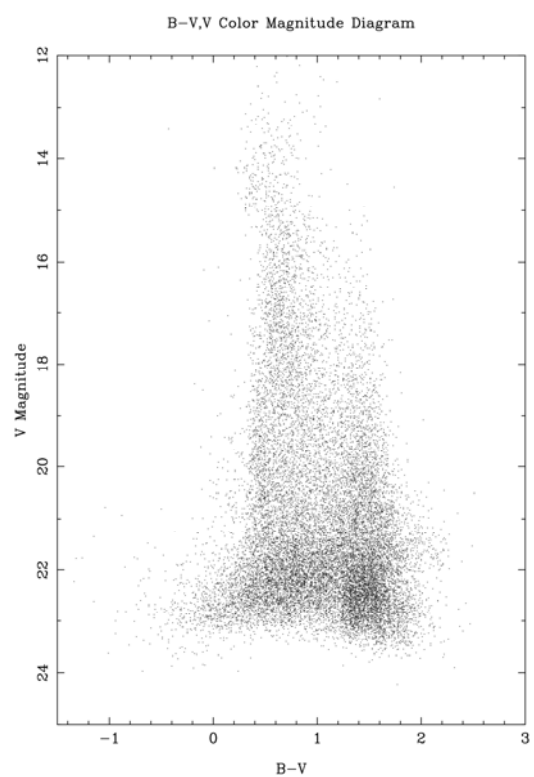
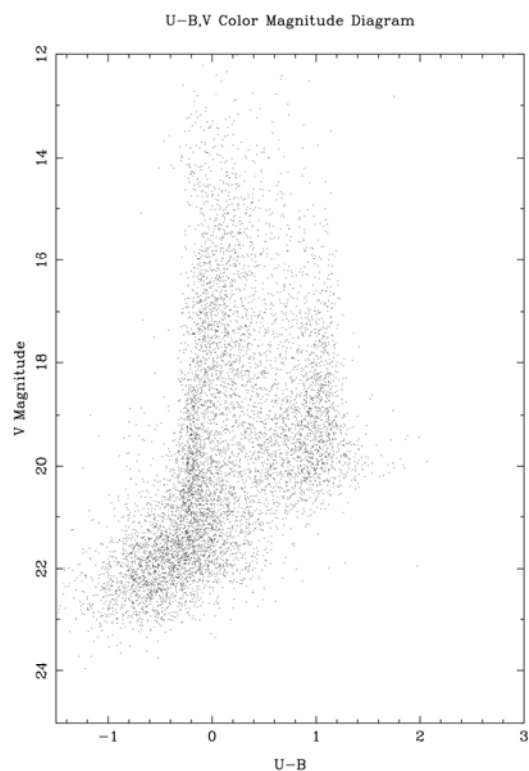
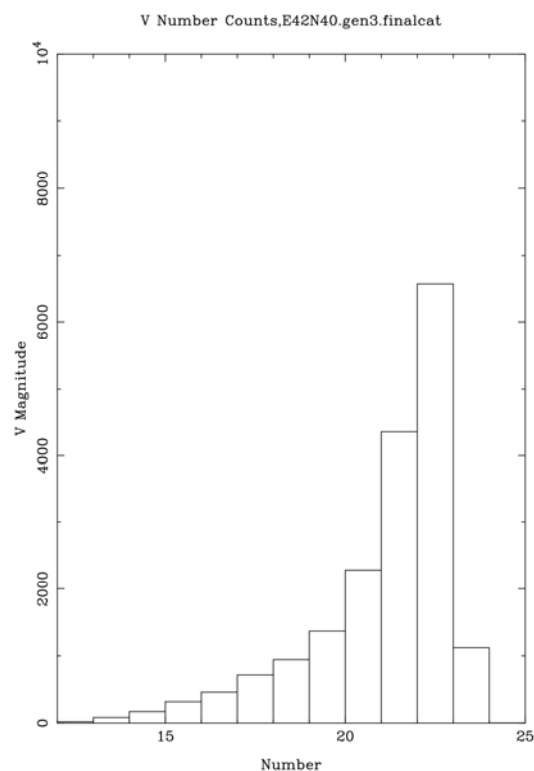
# E33S40

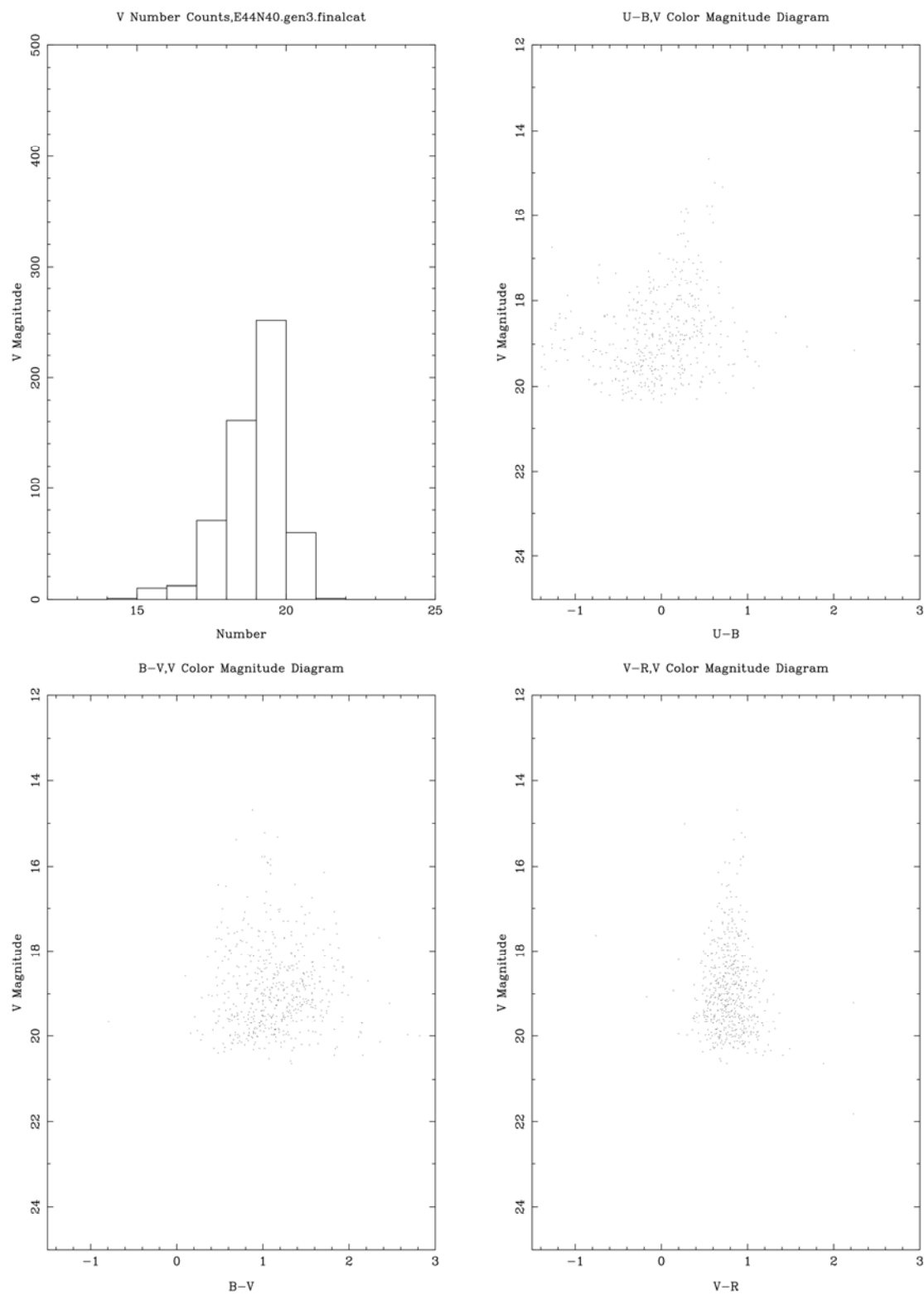


**E35N32**

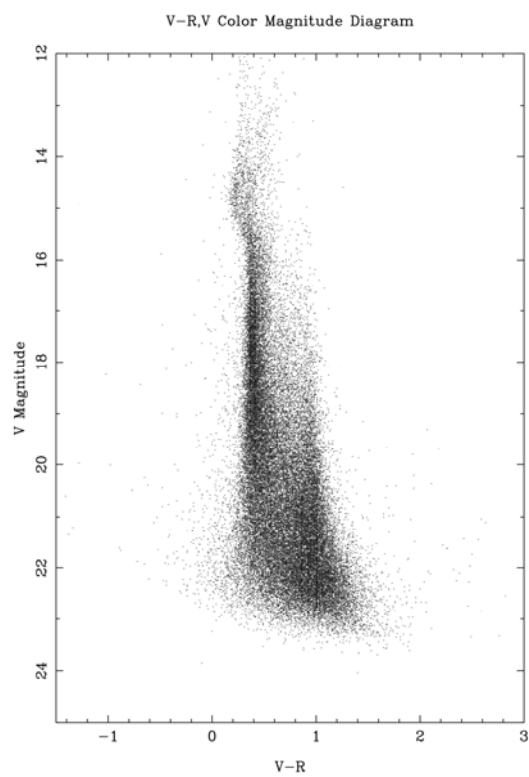
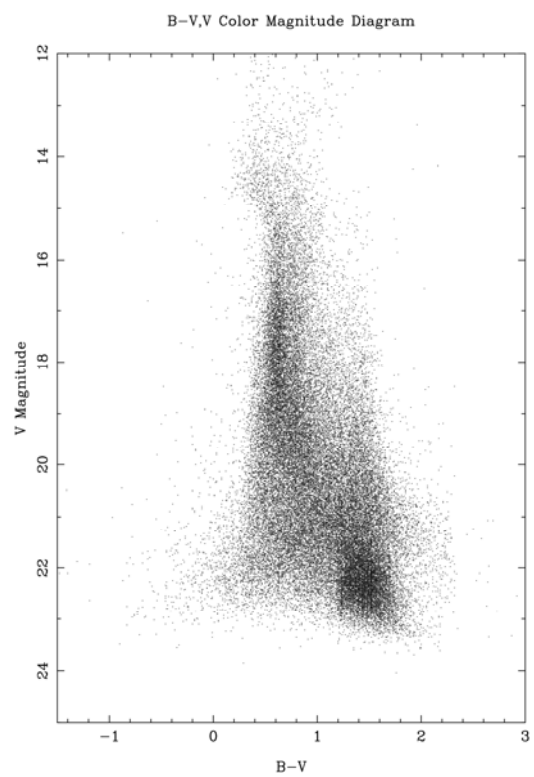
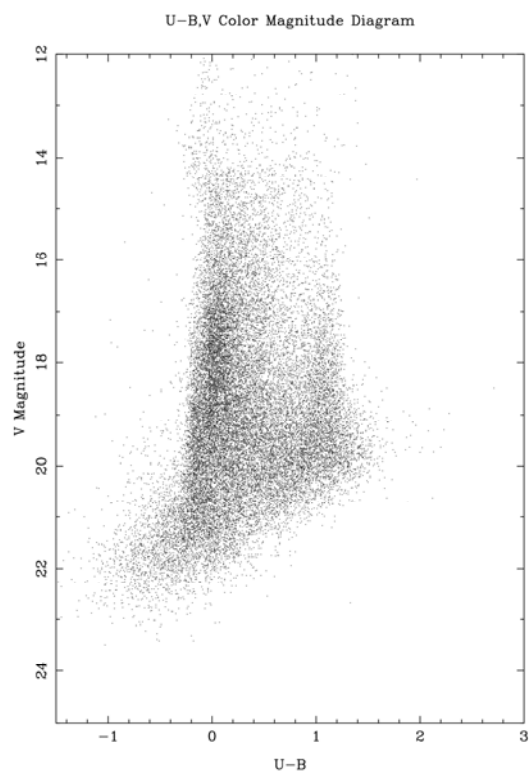
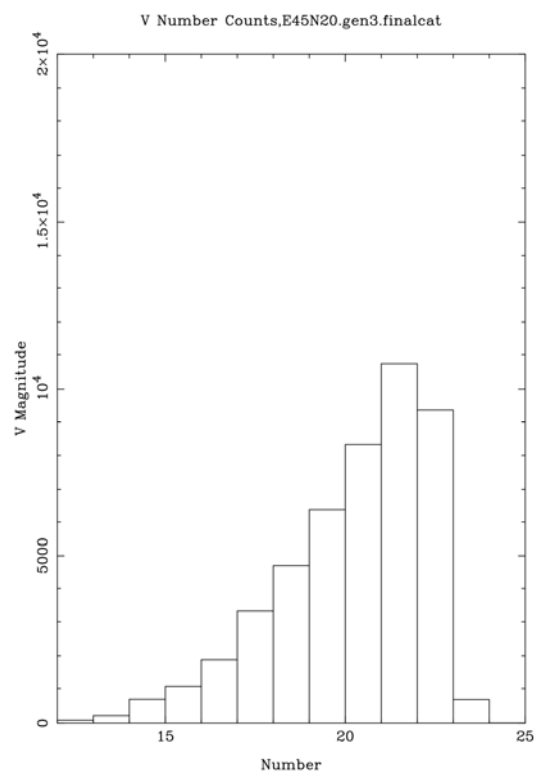


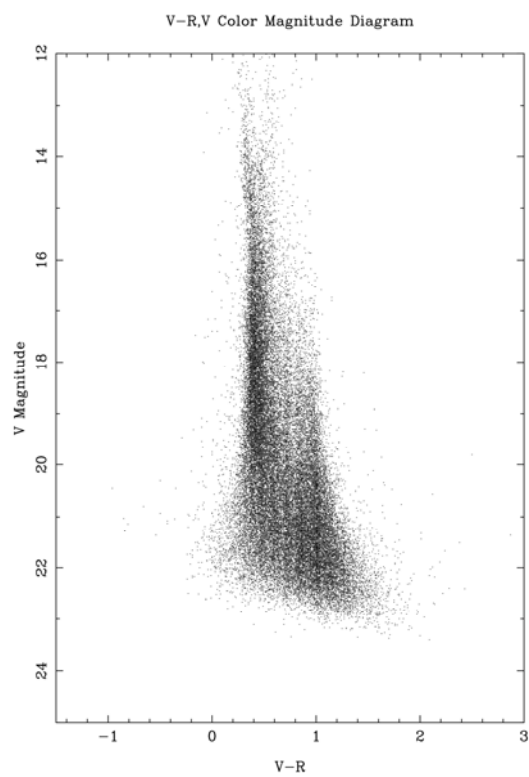
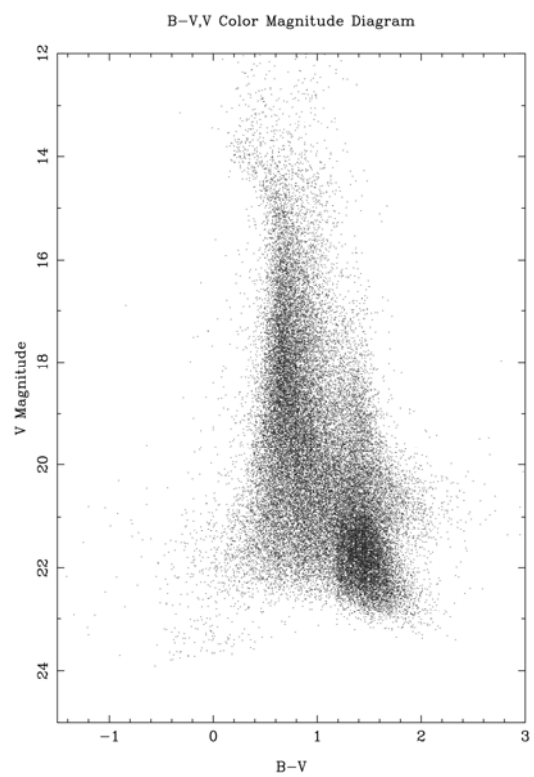
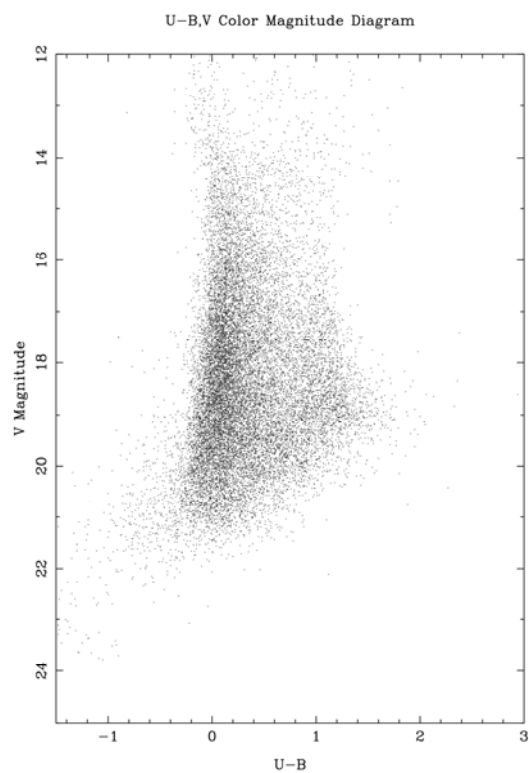
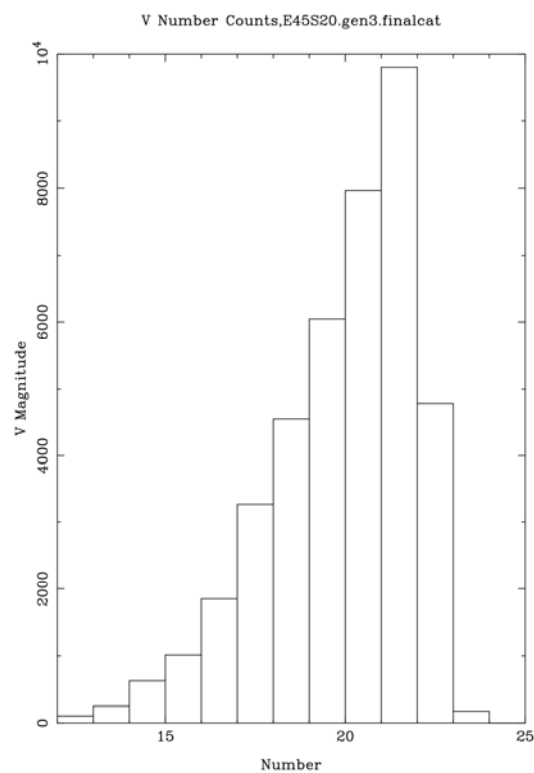
**E35S32**

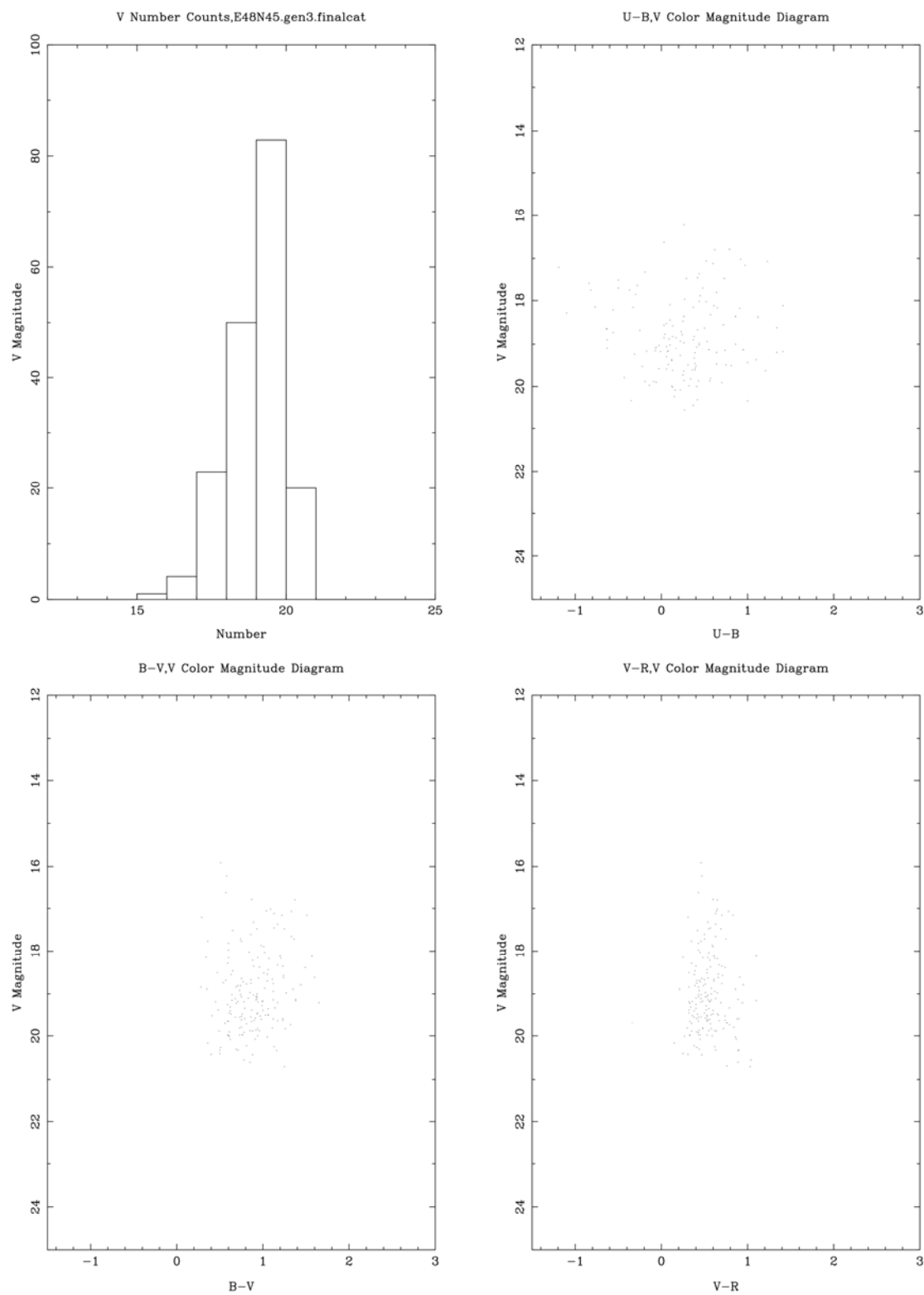
**E42N40**

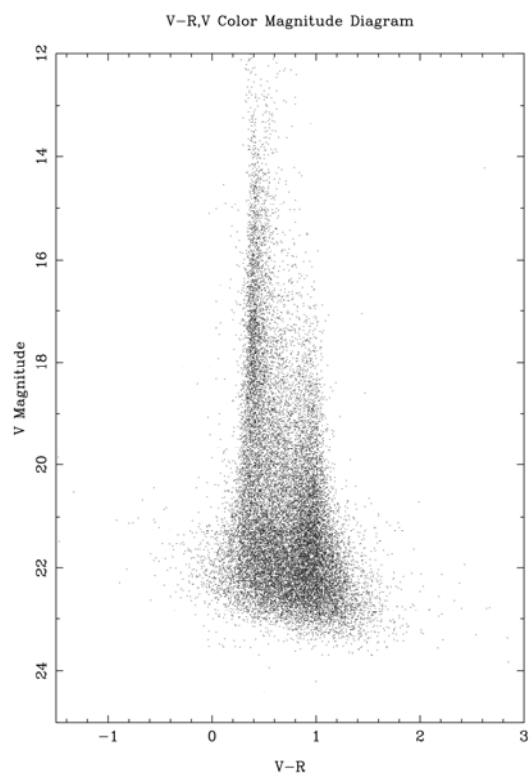
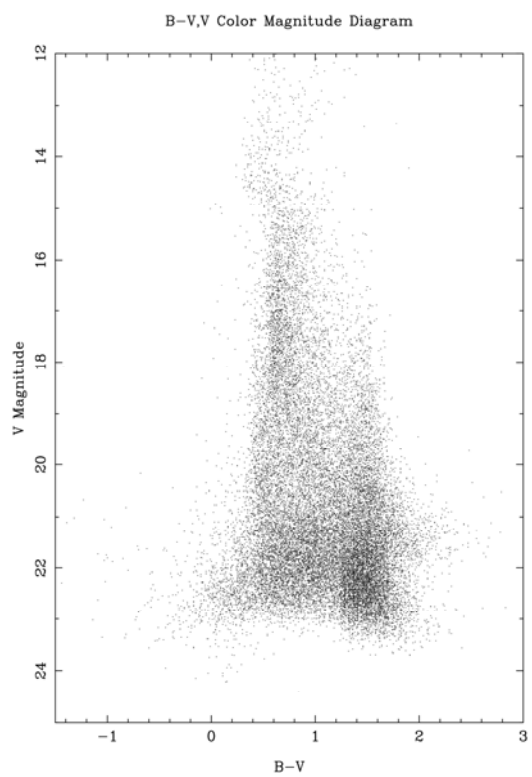
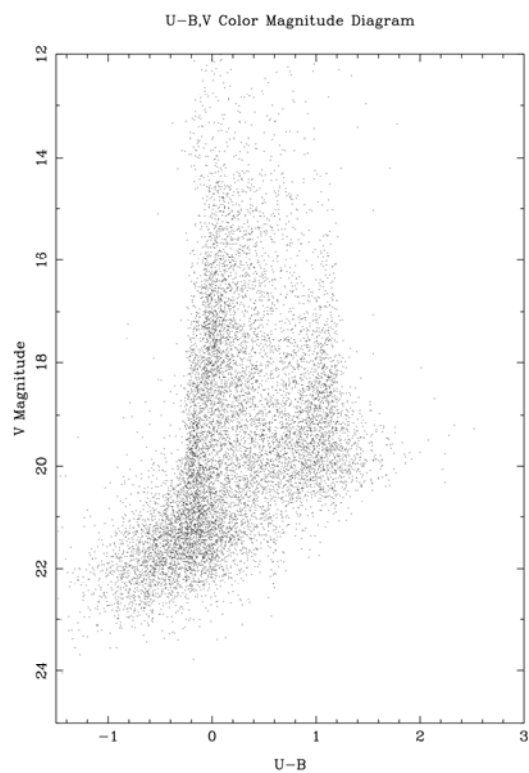
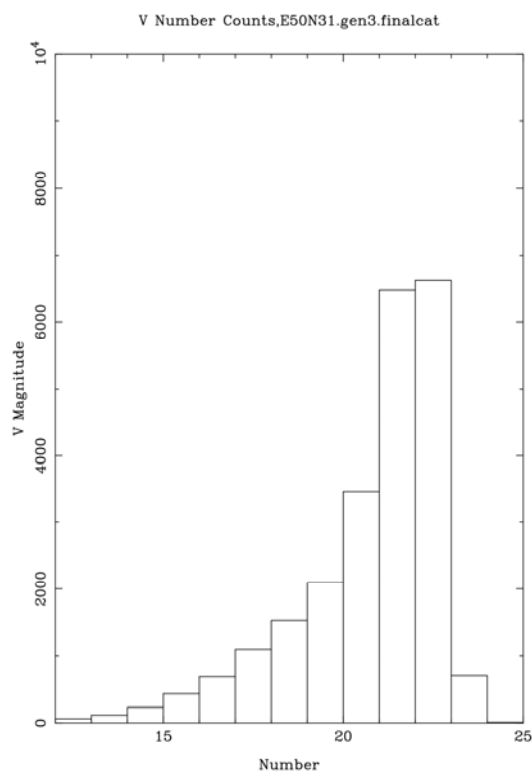
**E44N40**

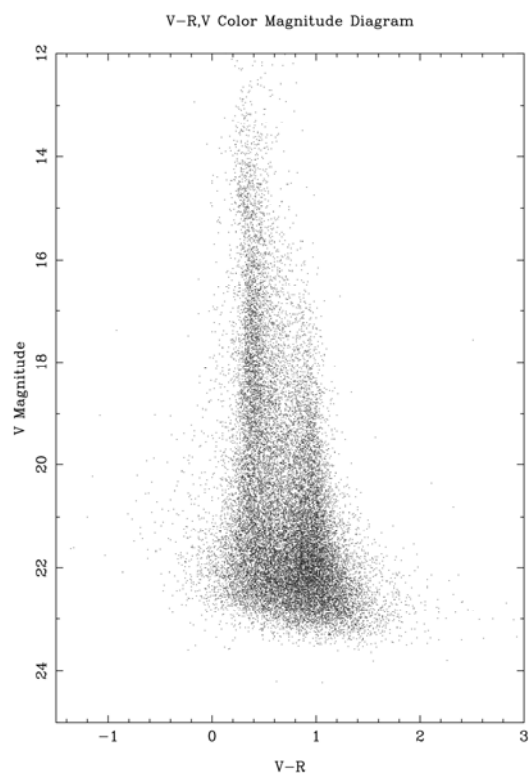
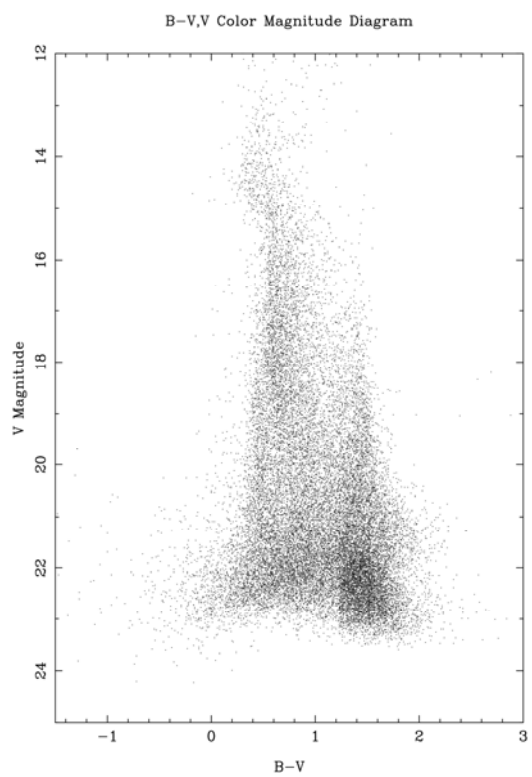
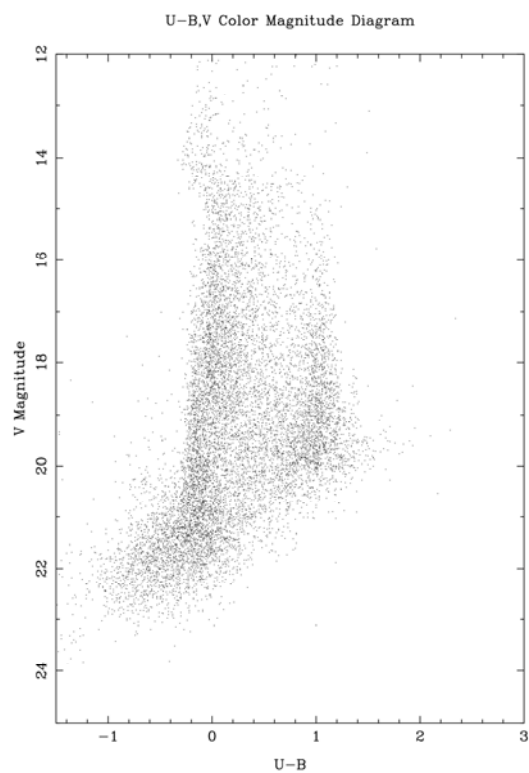
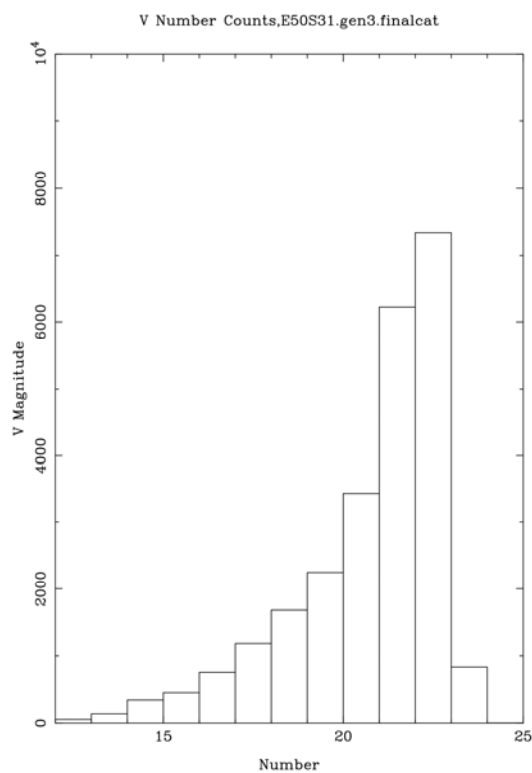
## E45N20



**E45S20**

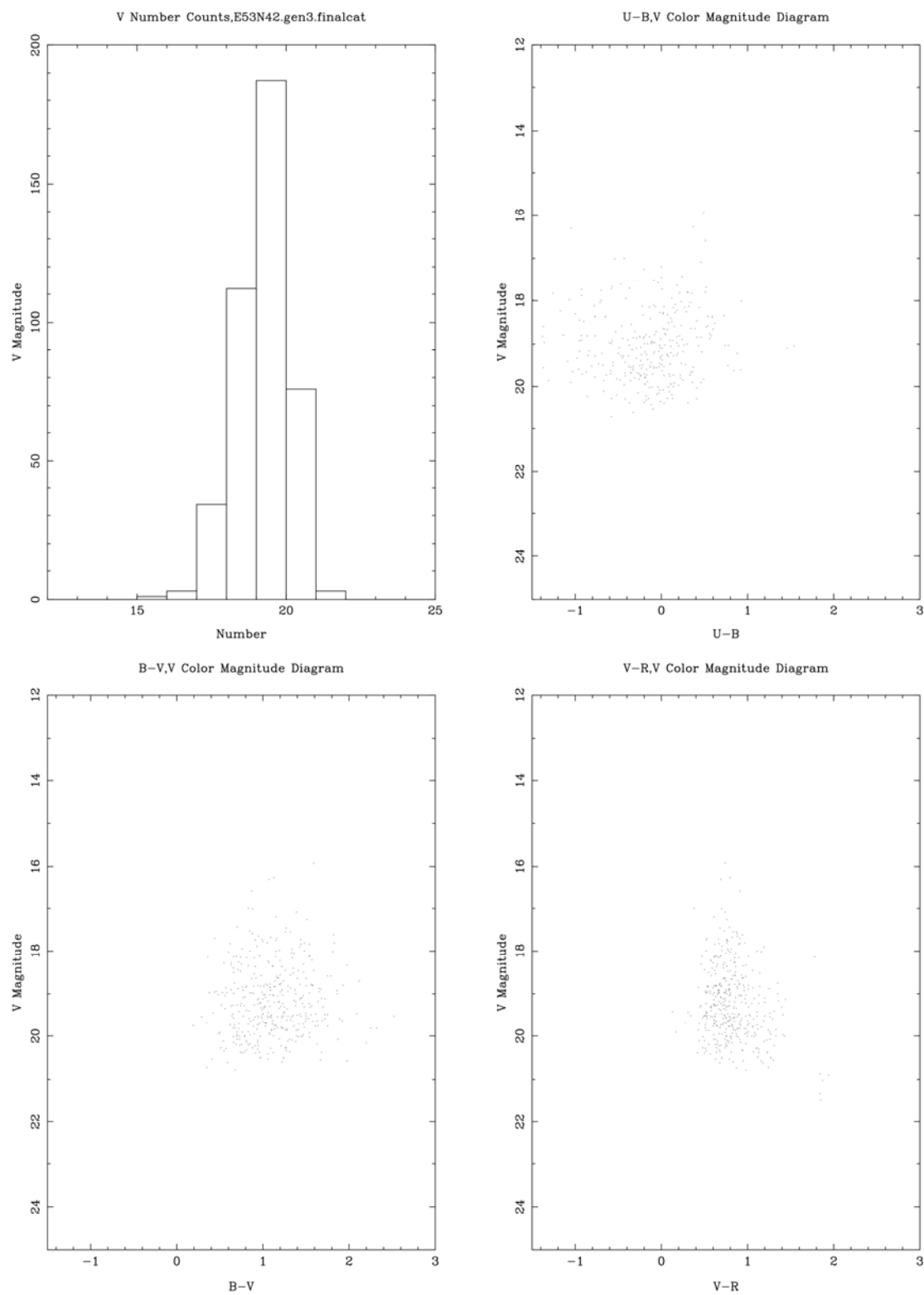
**E48N45**

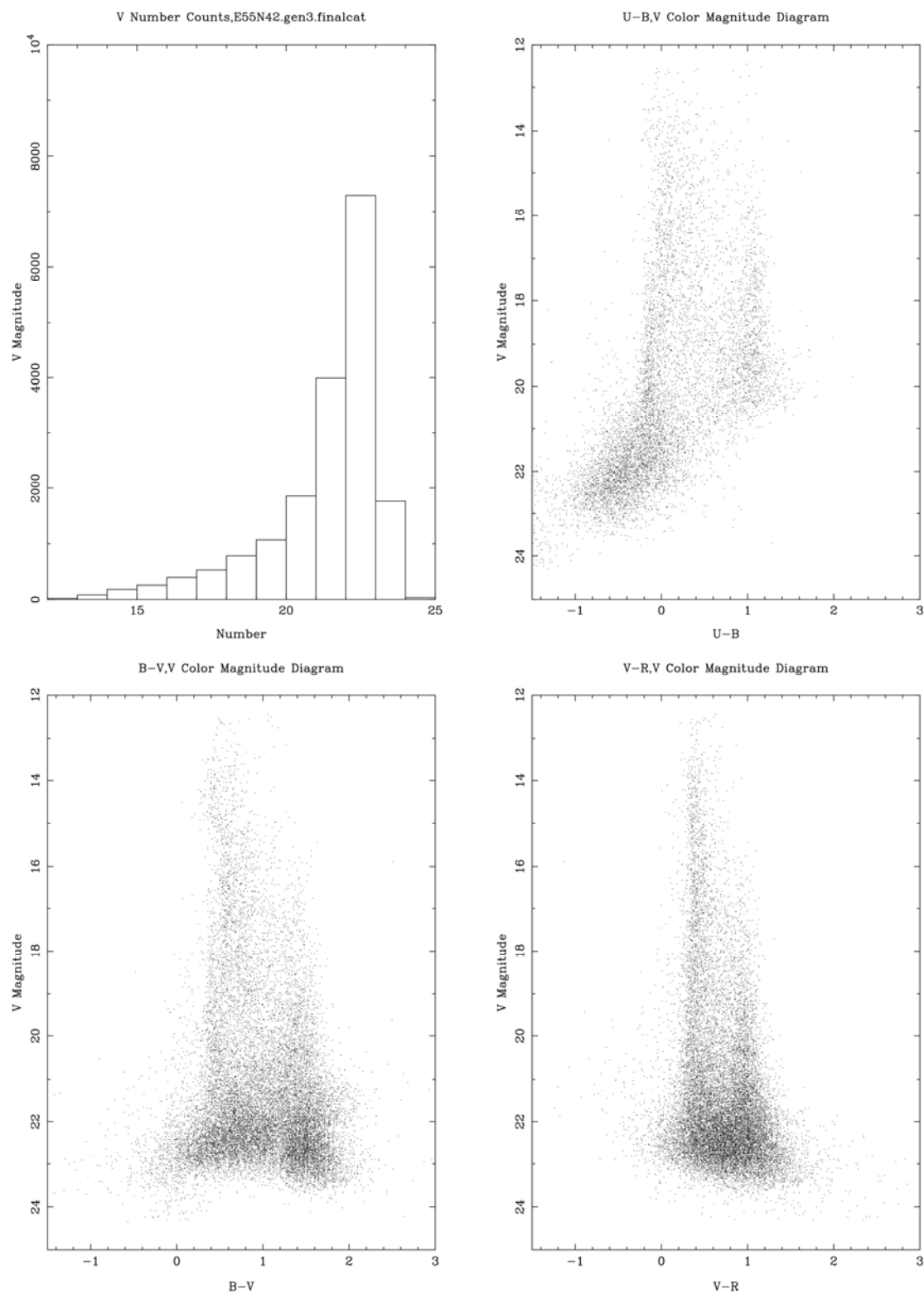
**E50N31**

**E50S31**

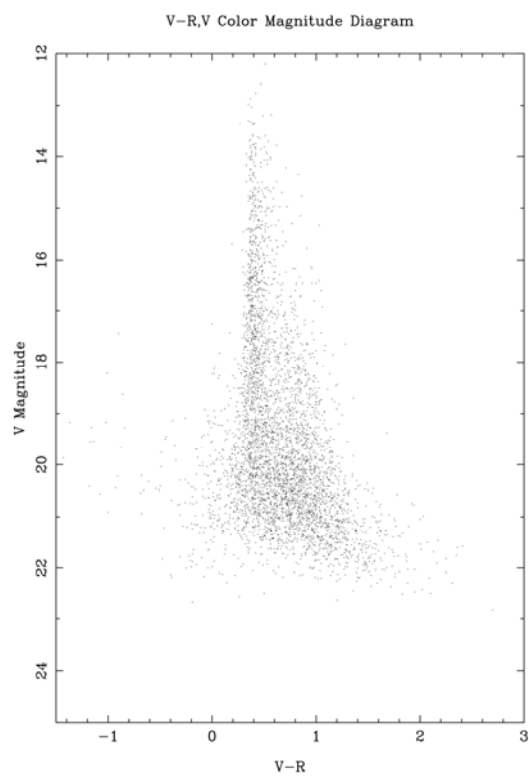
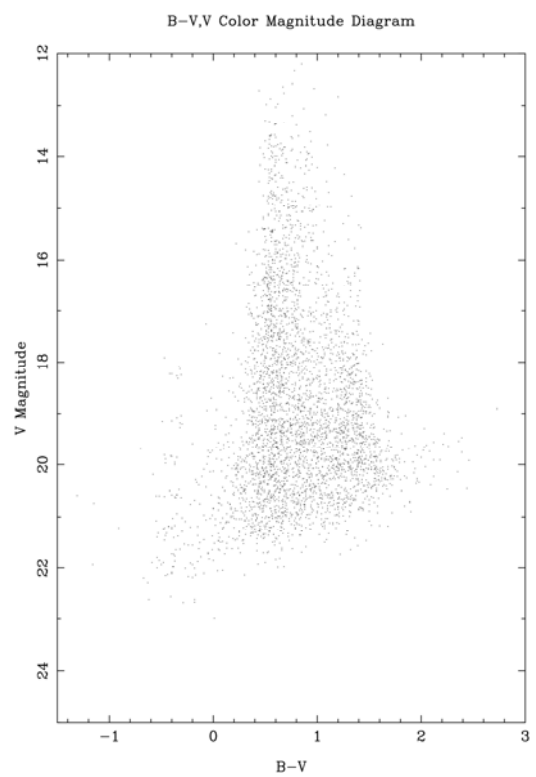
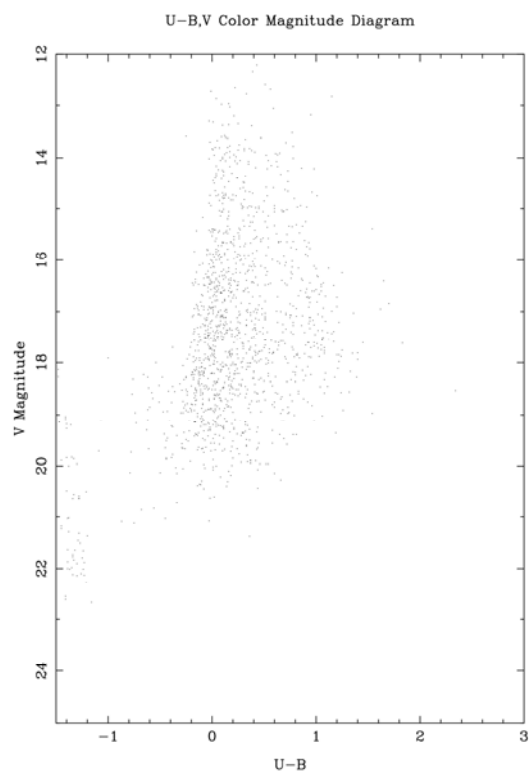
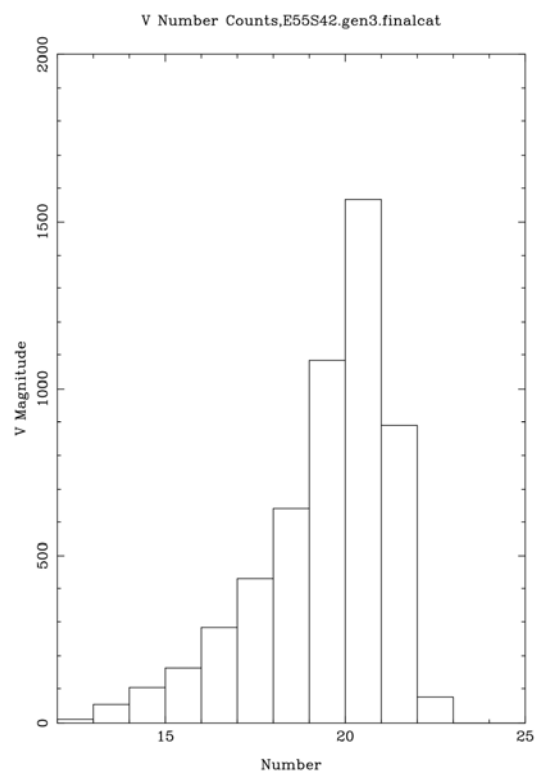


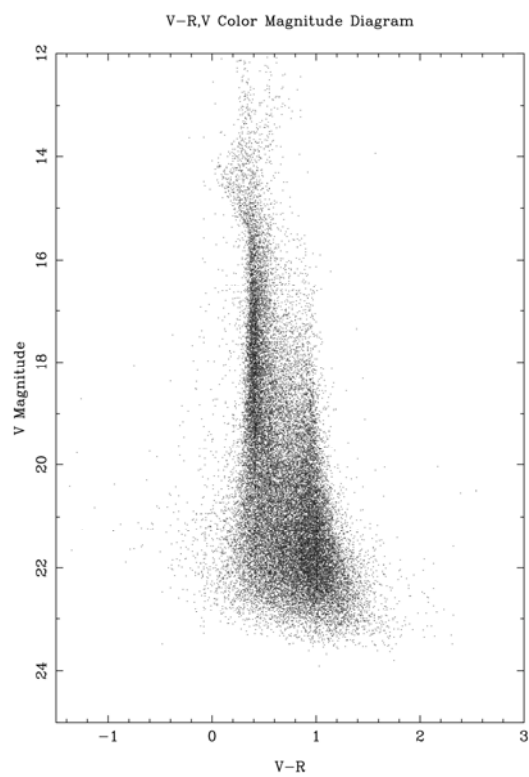
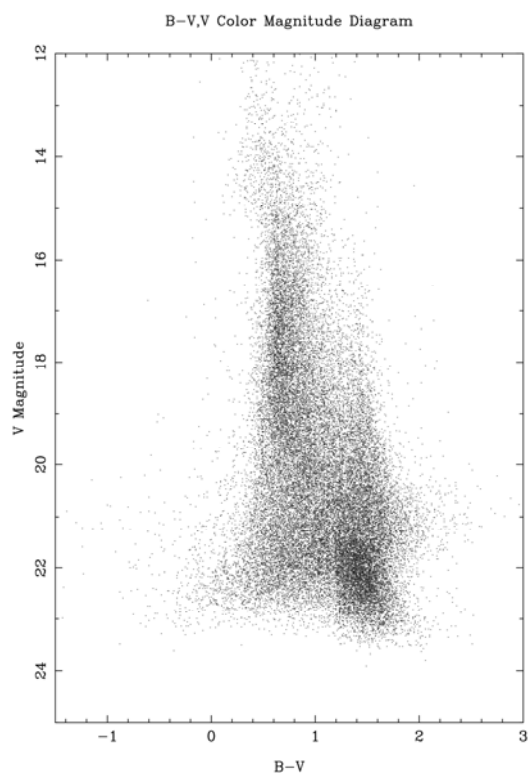
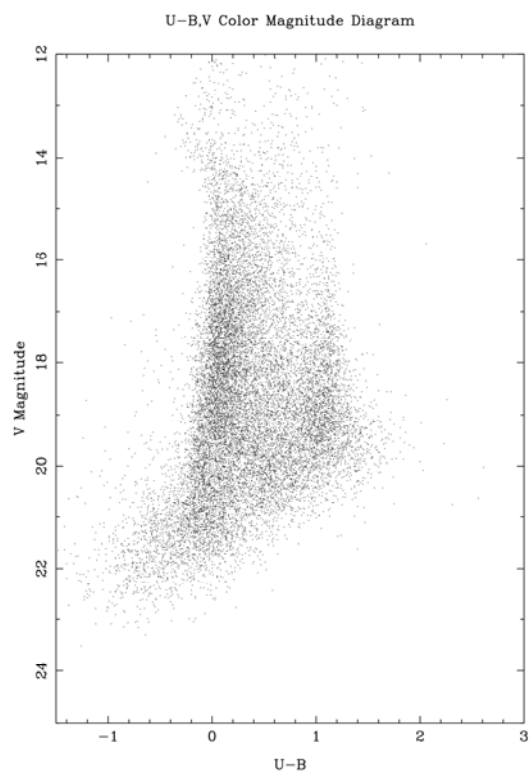
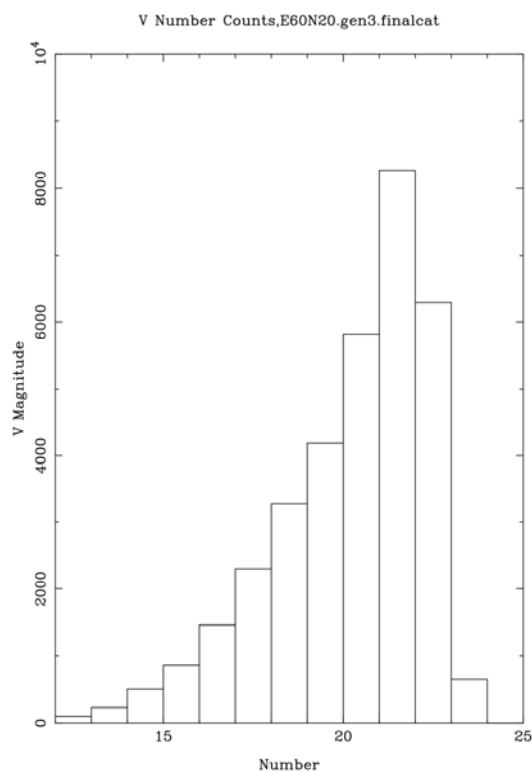
## E53N42

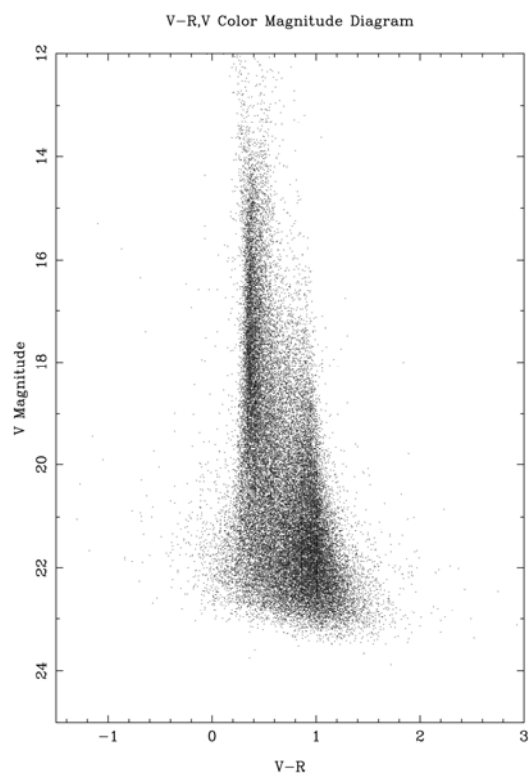
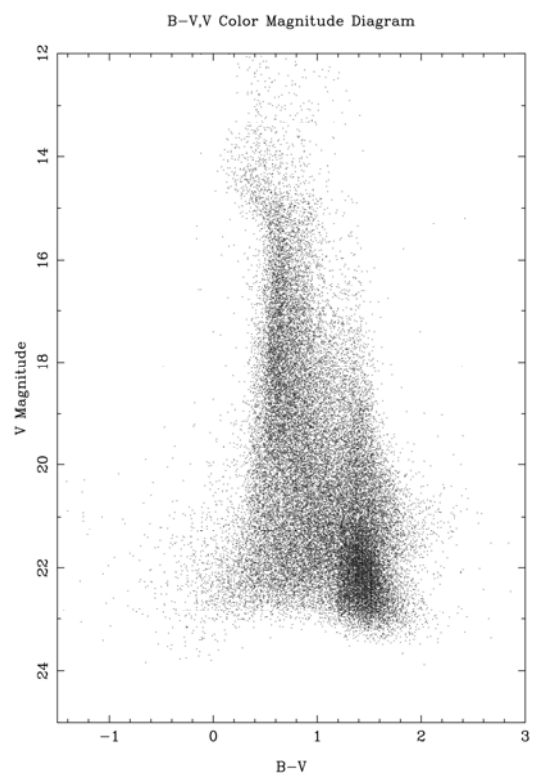
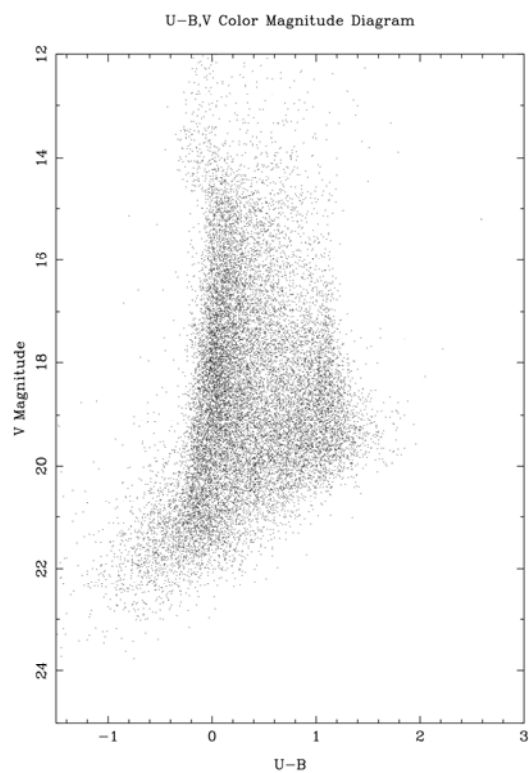
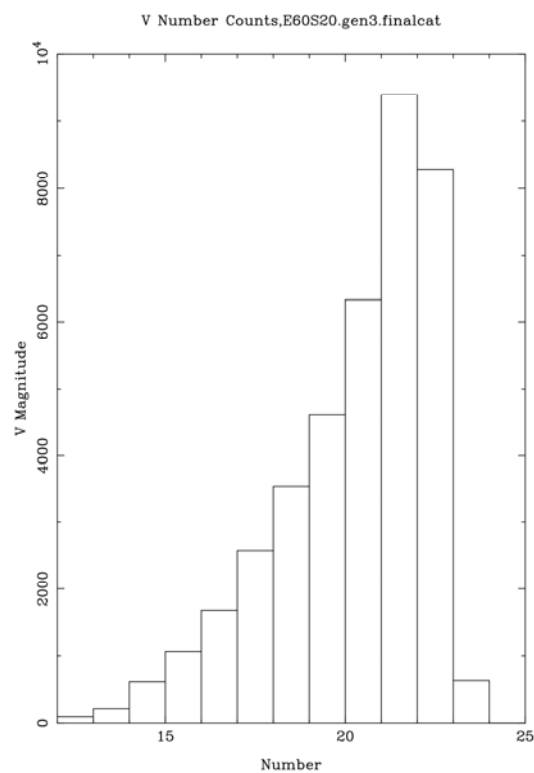


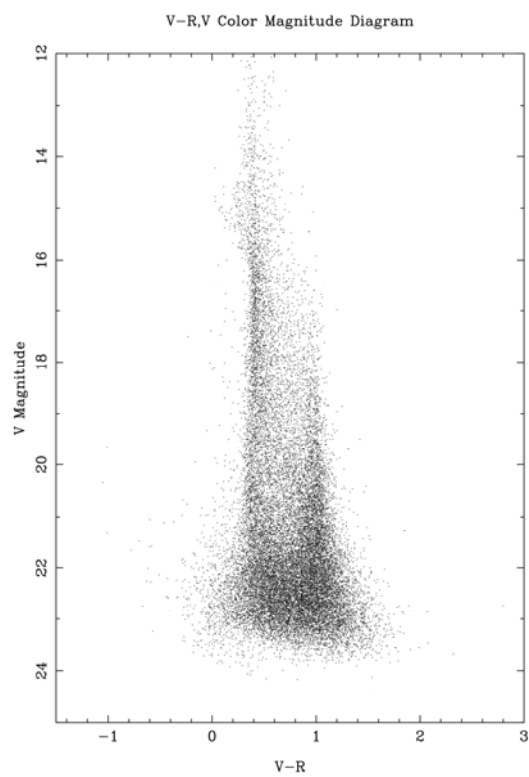
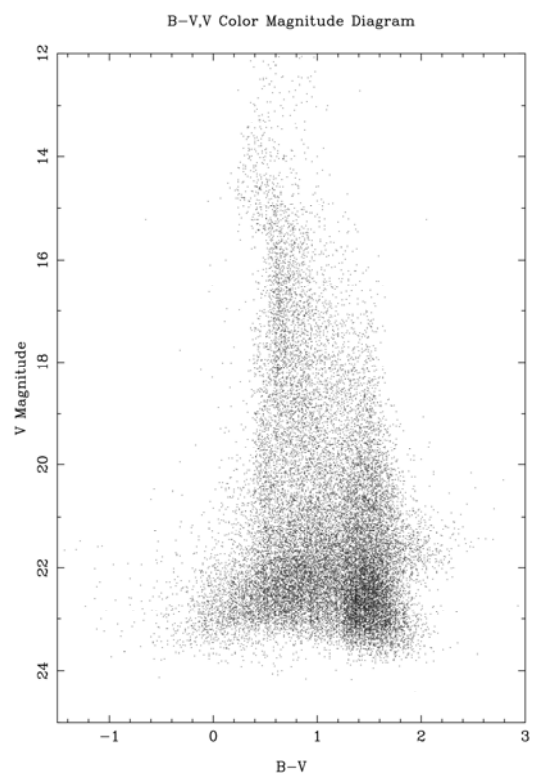
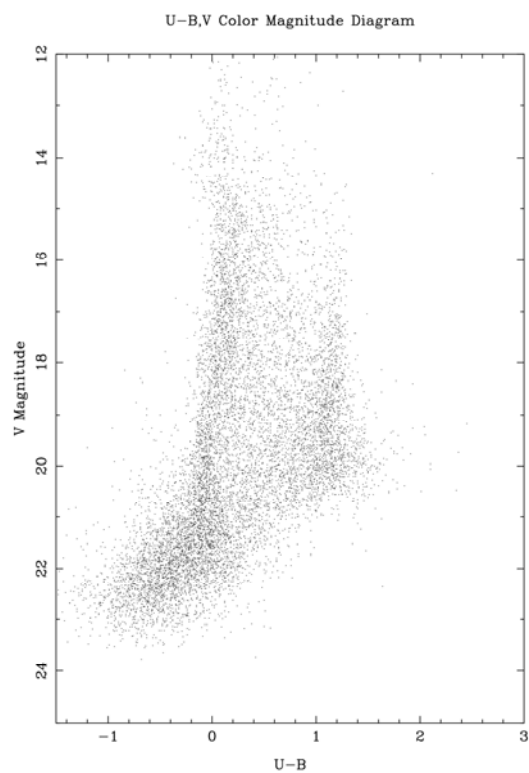
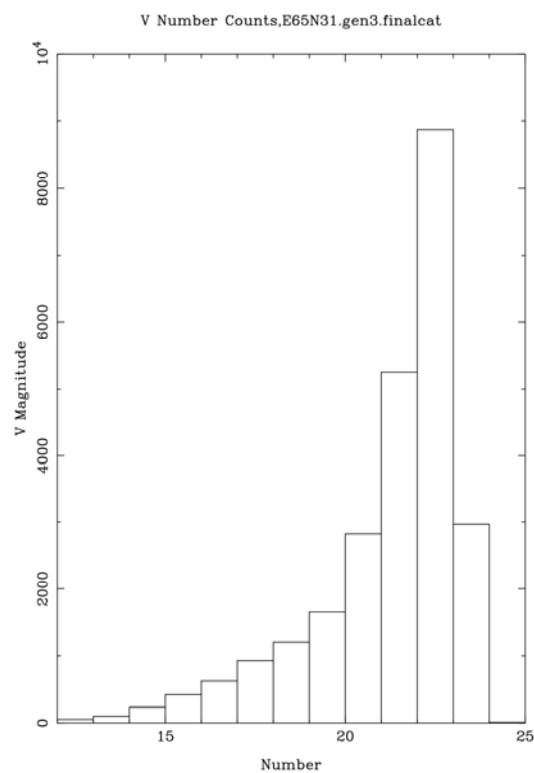
**E55N42**

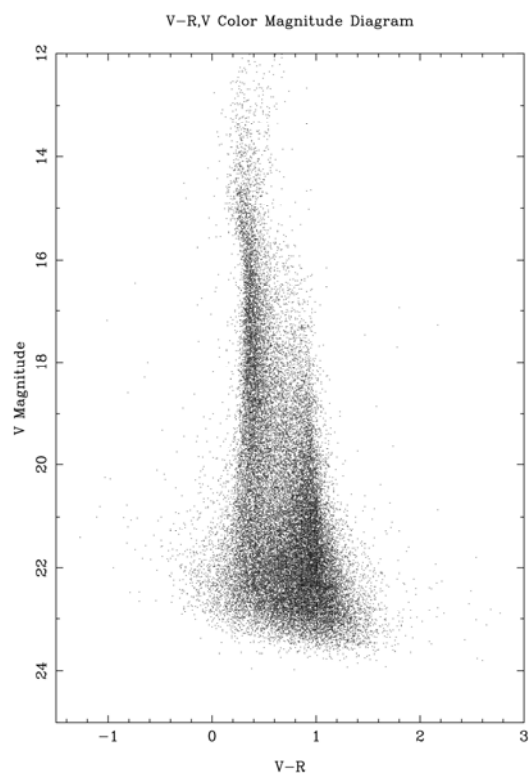
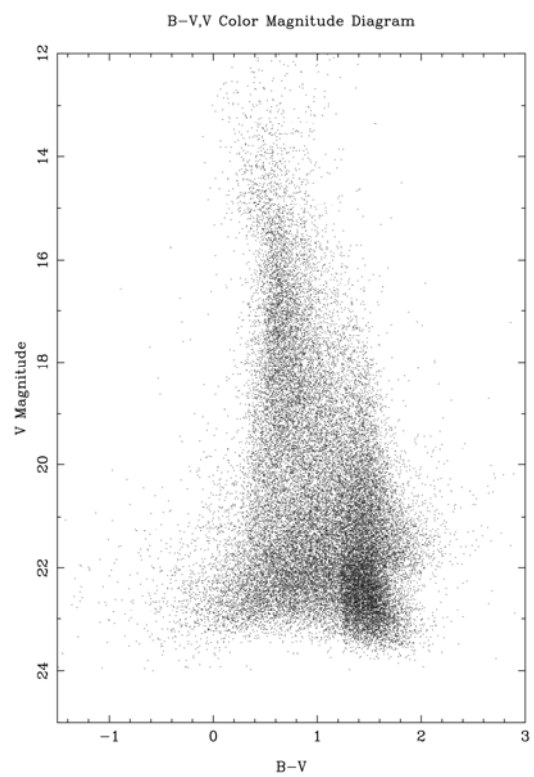
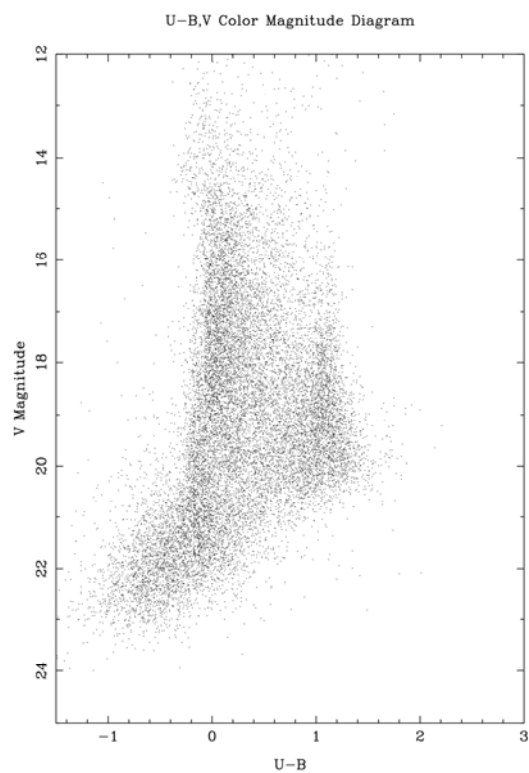
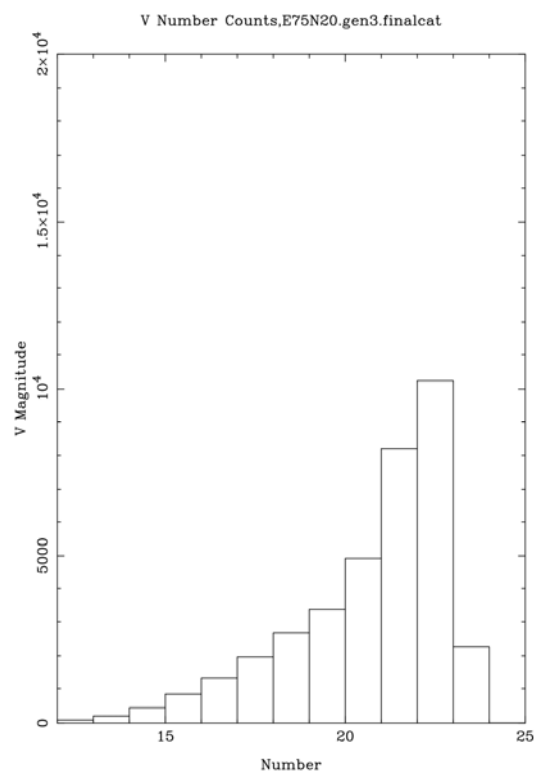
## E55S42



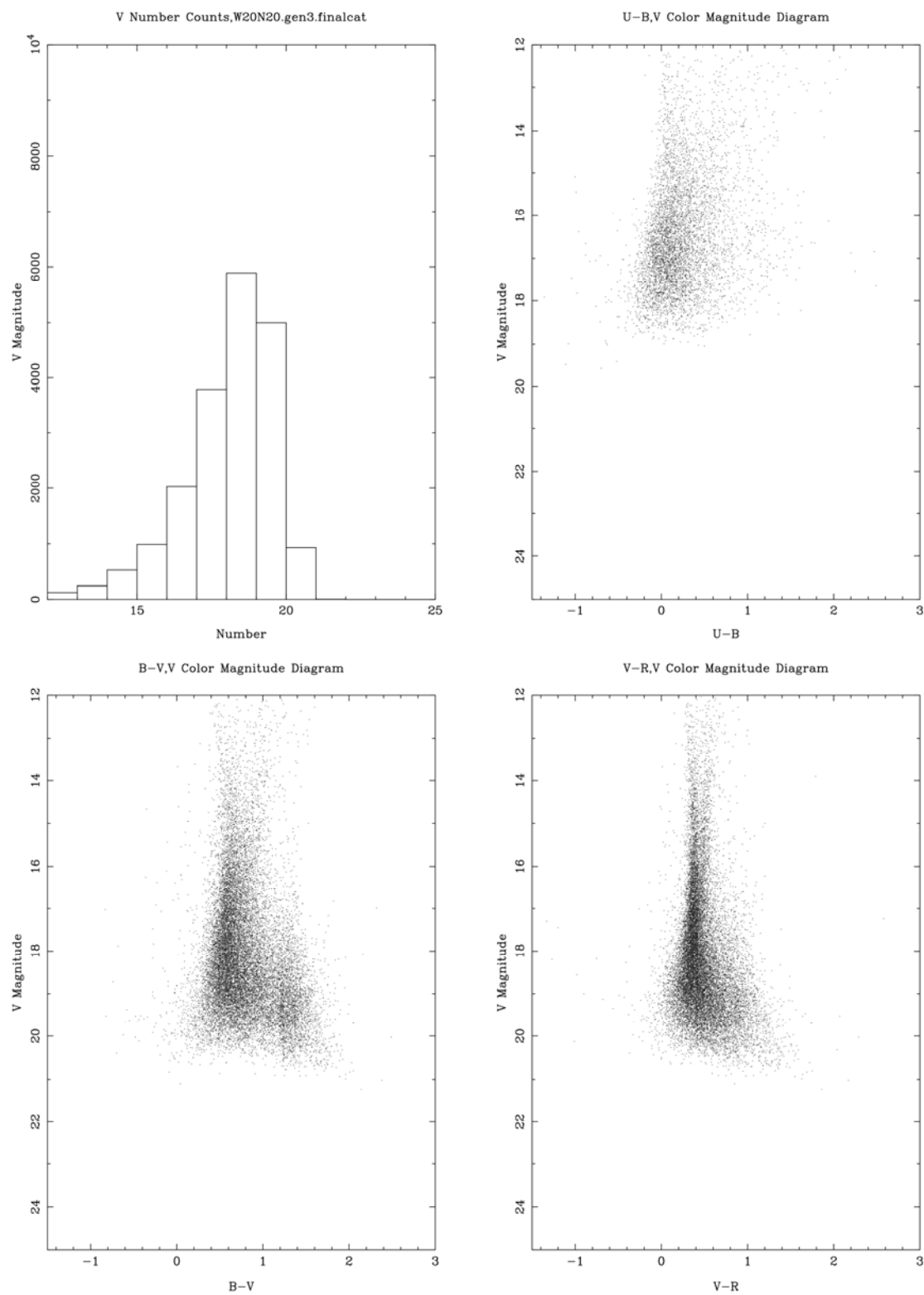
**E60N20**

**E60S20**

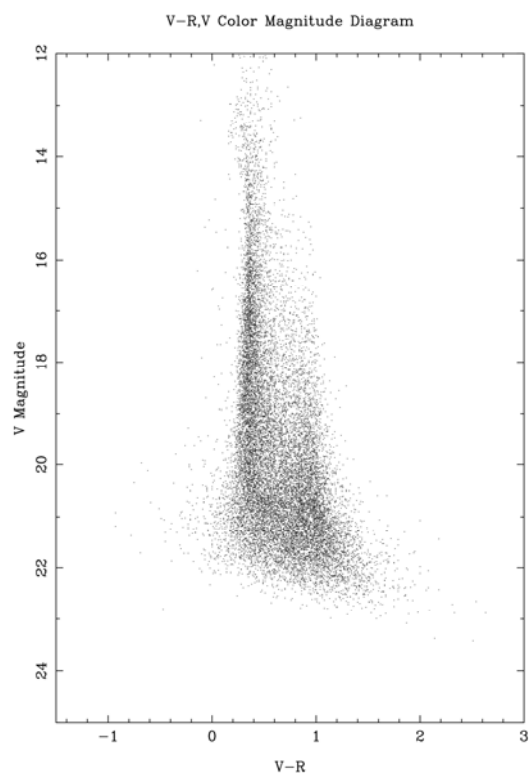
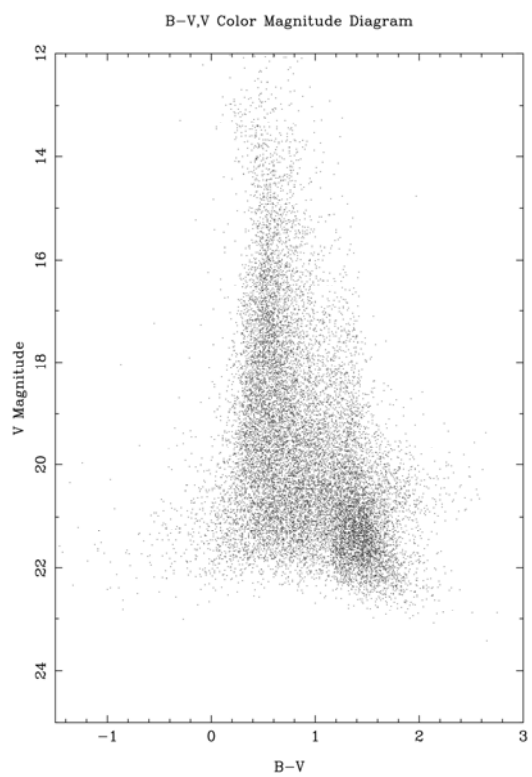
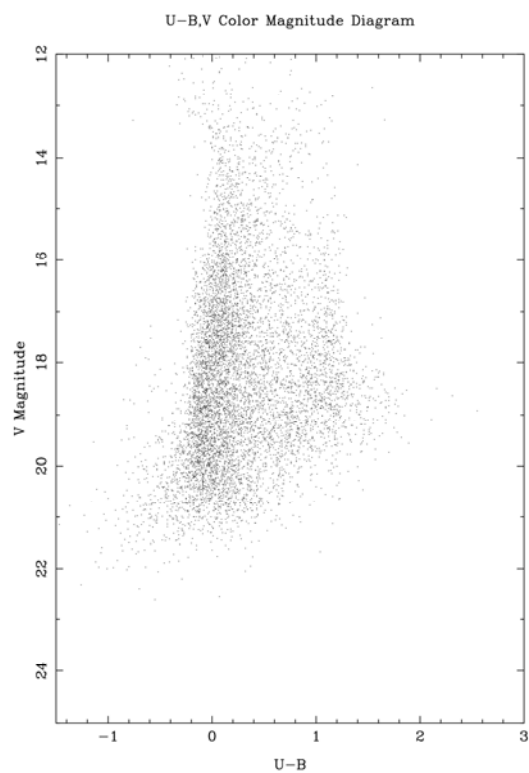
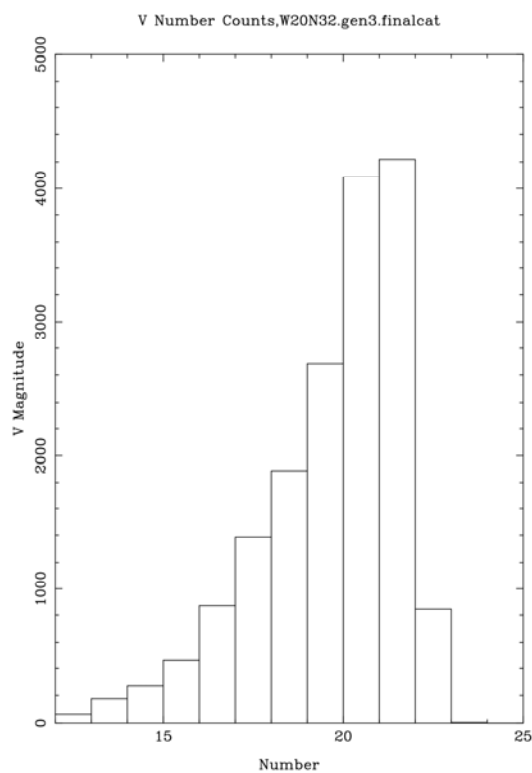
**E65N31**

**E75N20**

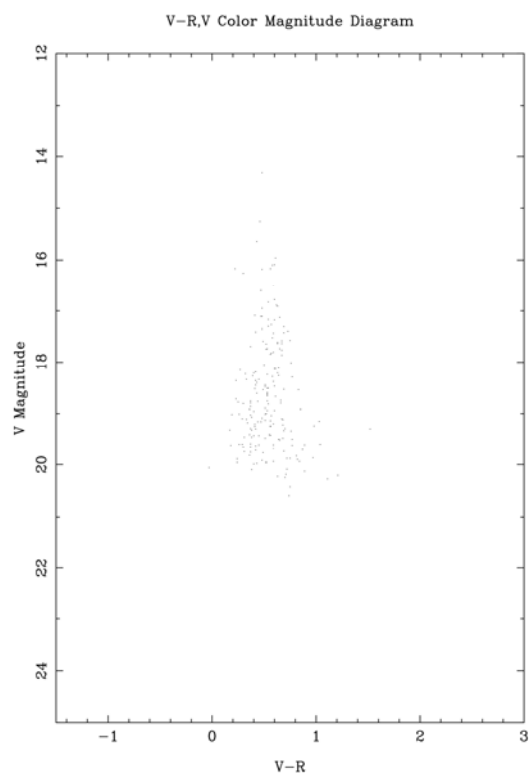
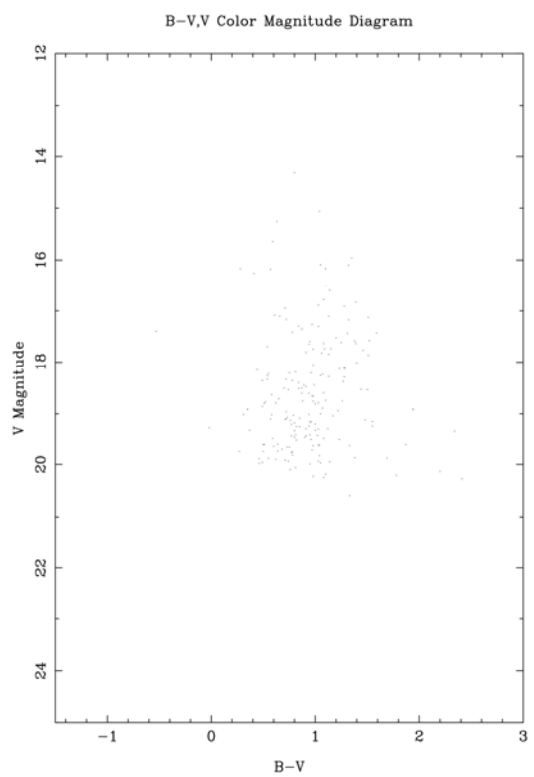
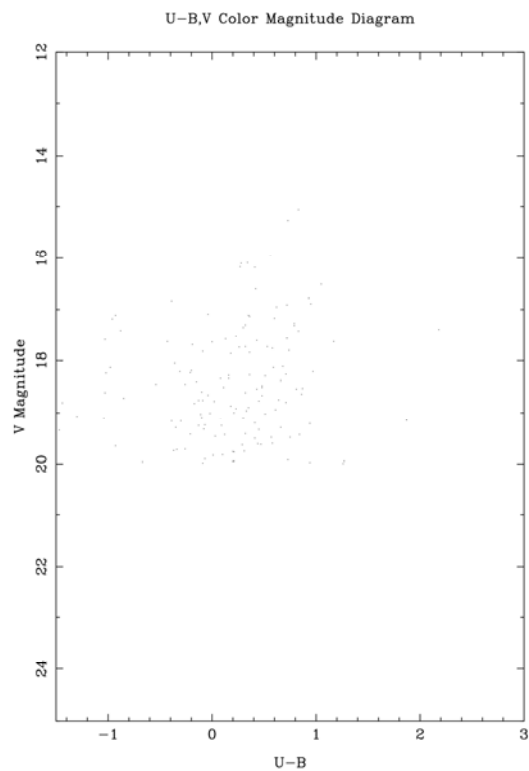
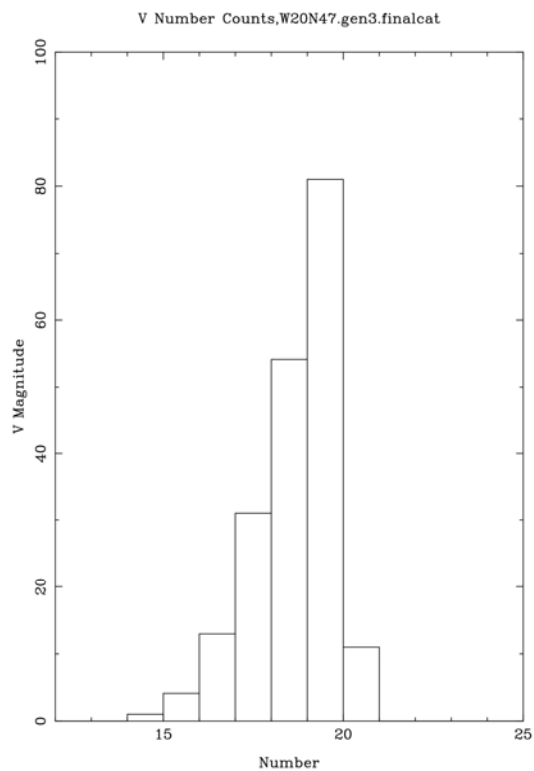
# W20N20

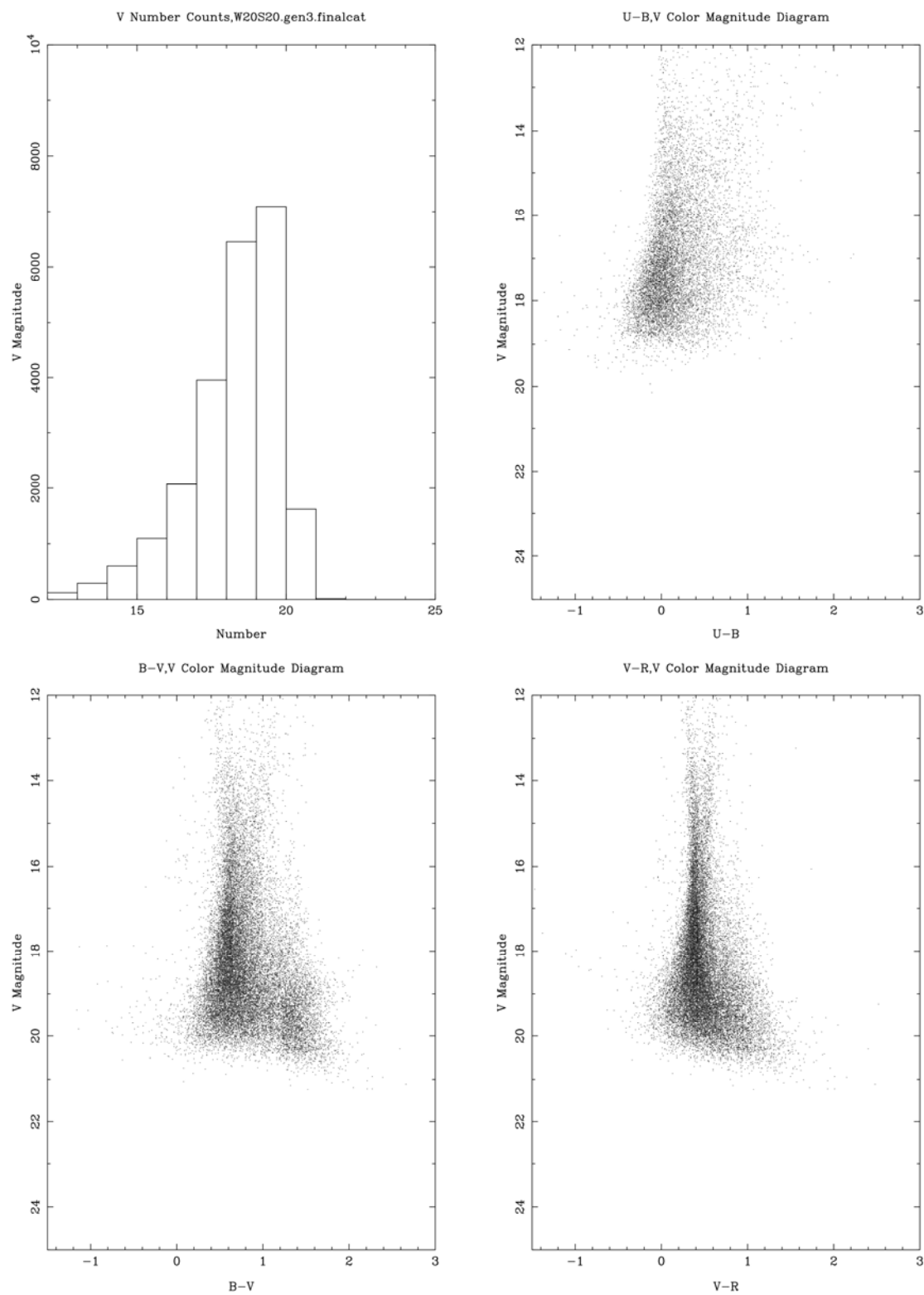


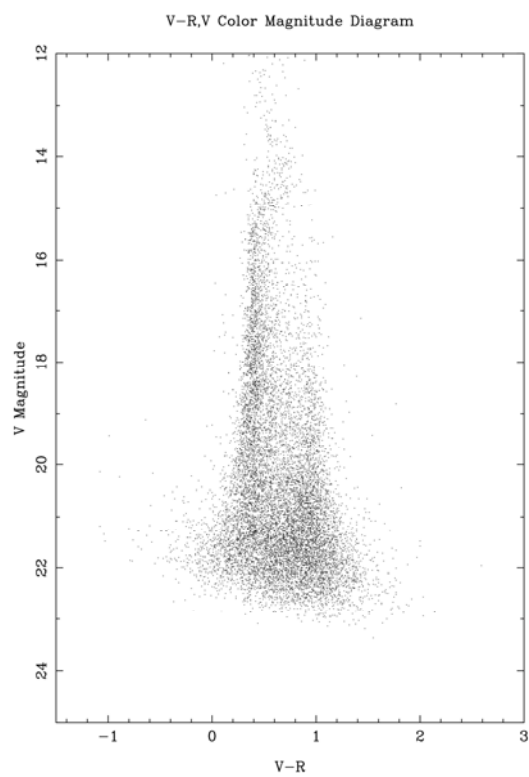
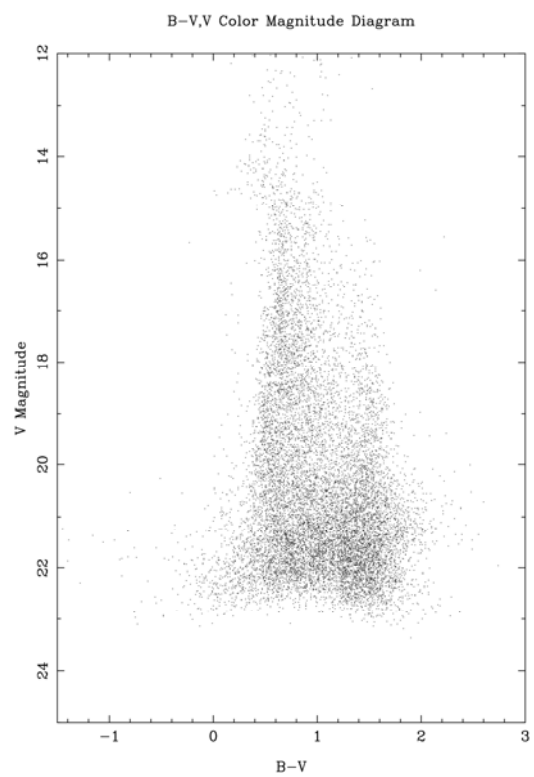
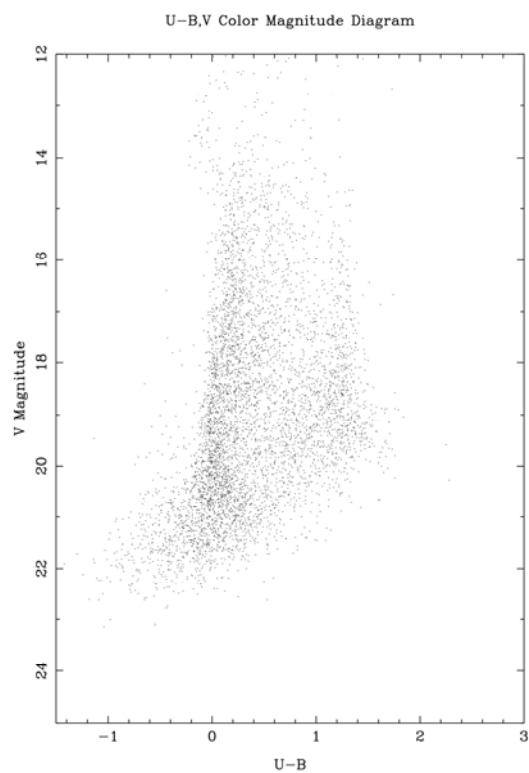
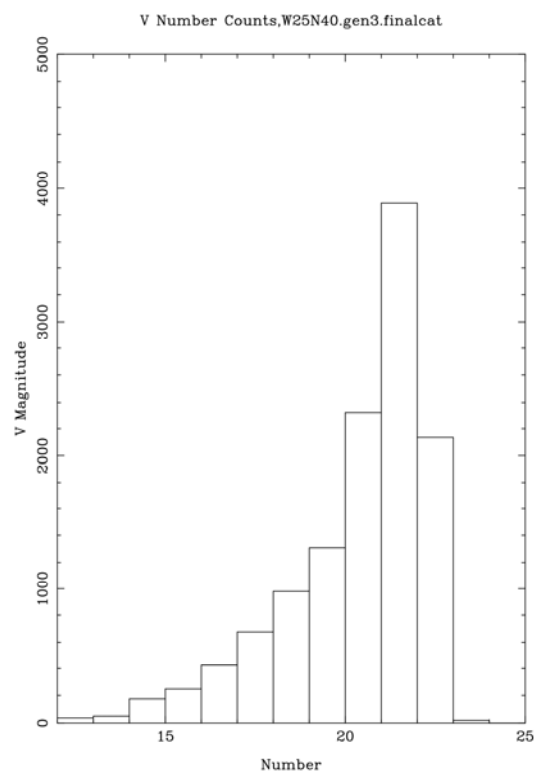


**W20N32**

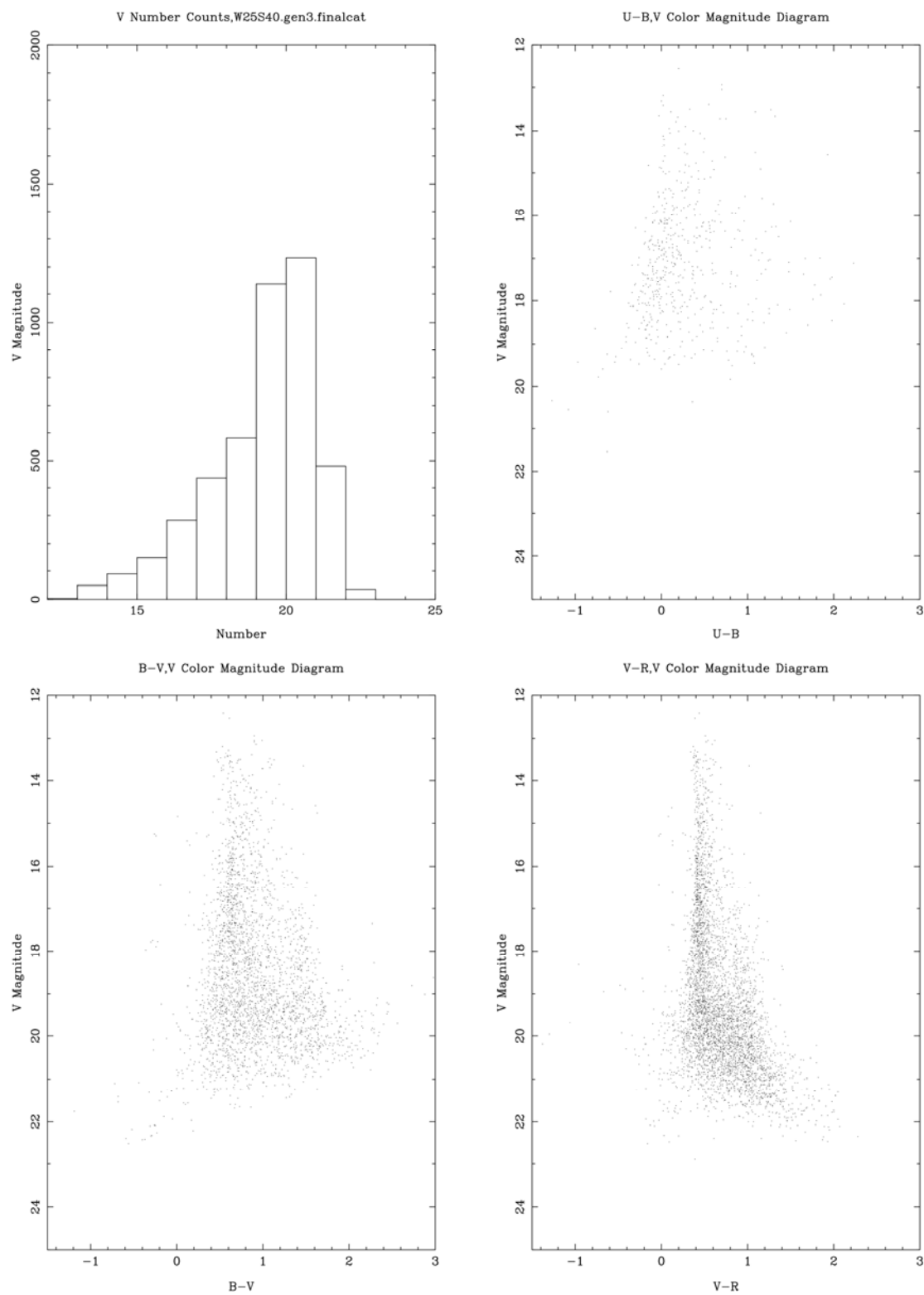
# W20N47



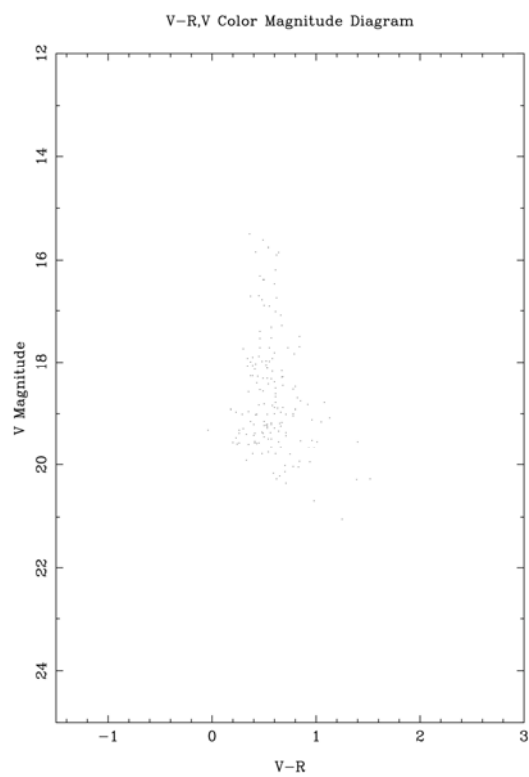
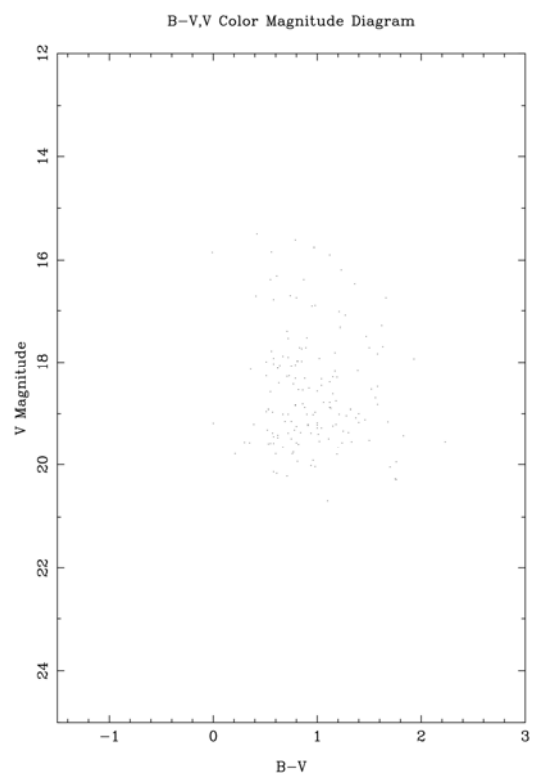
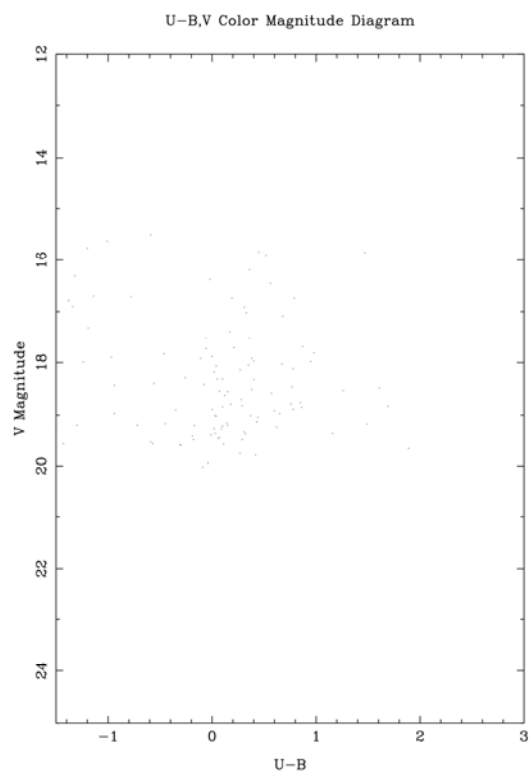
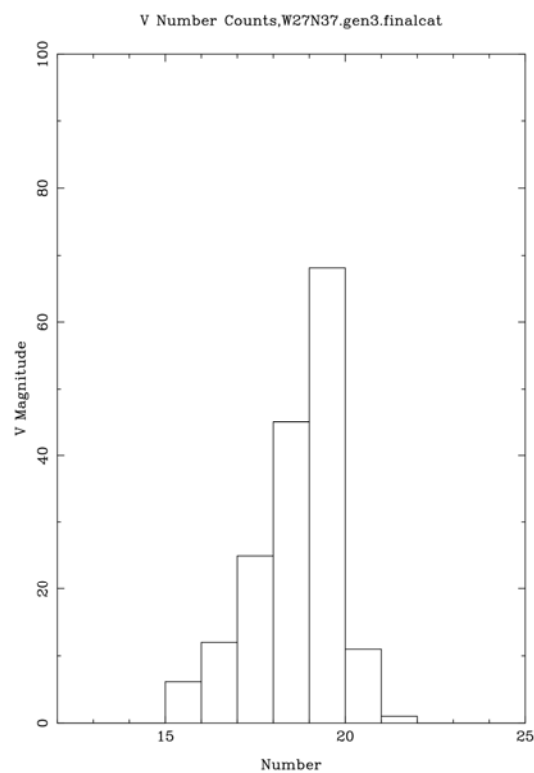
**W20S20**

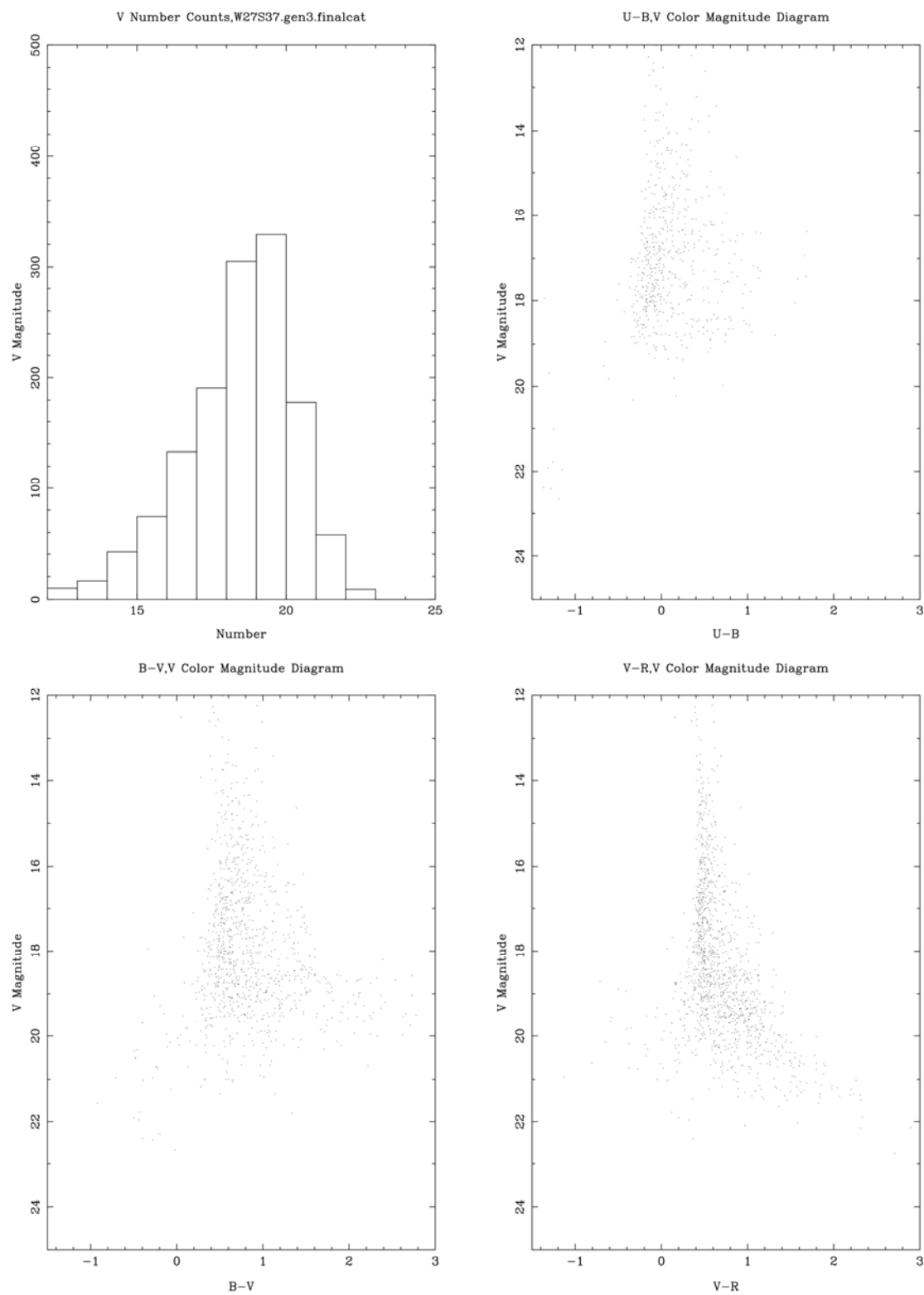
**W25N40**

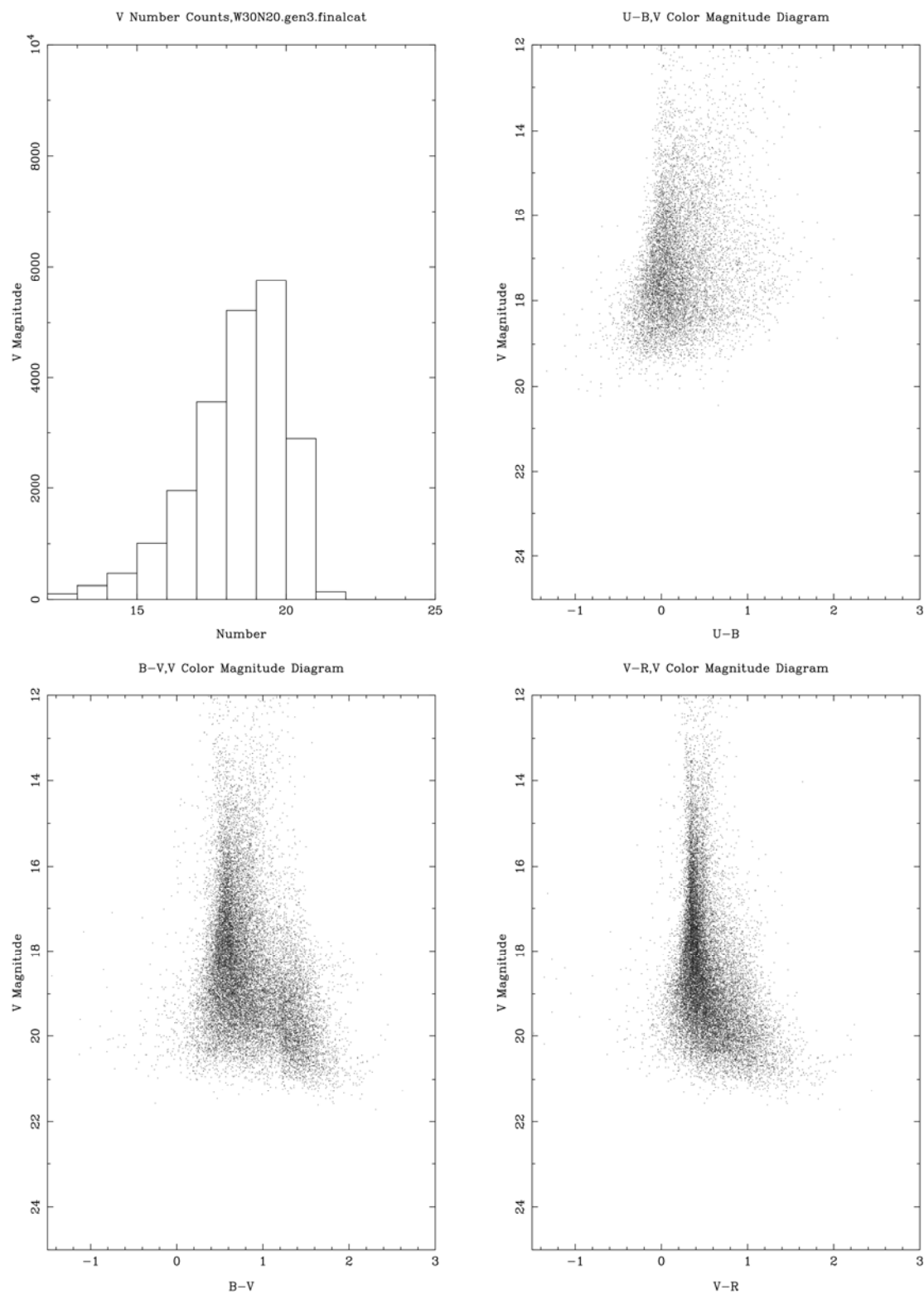
# W25S40



# W27N37

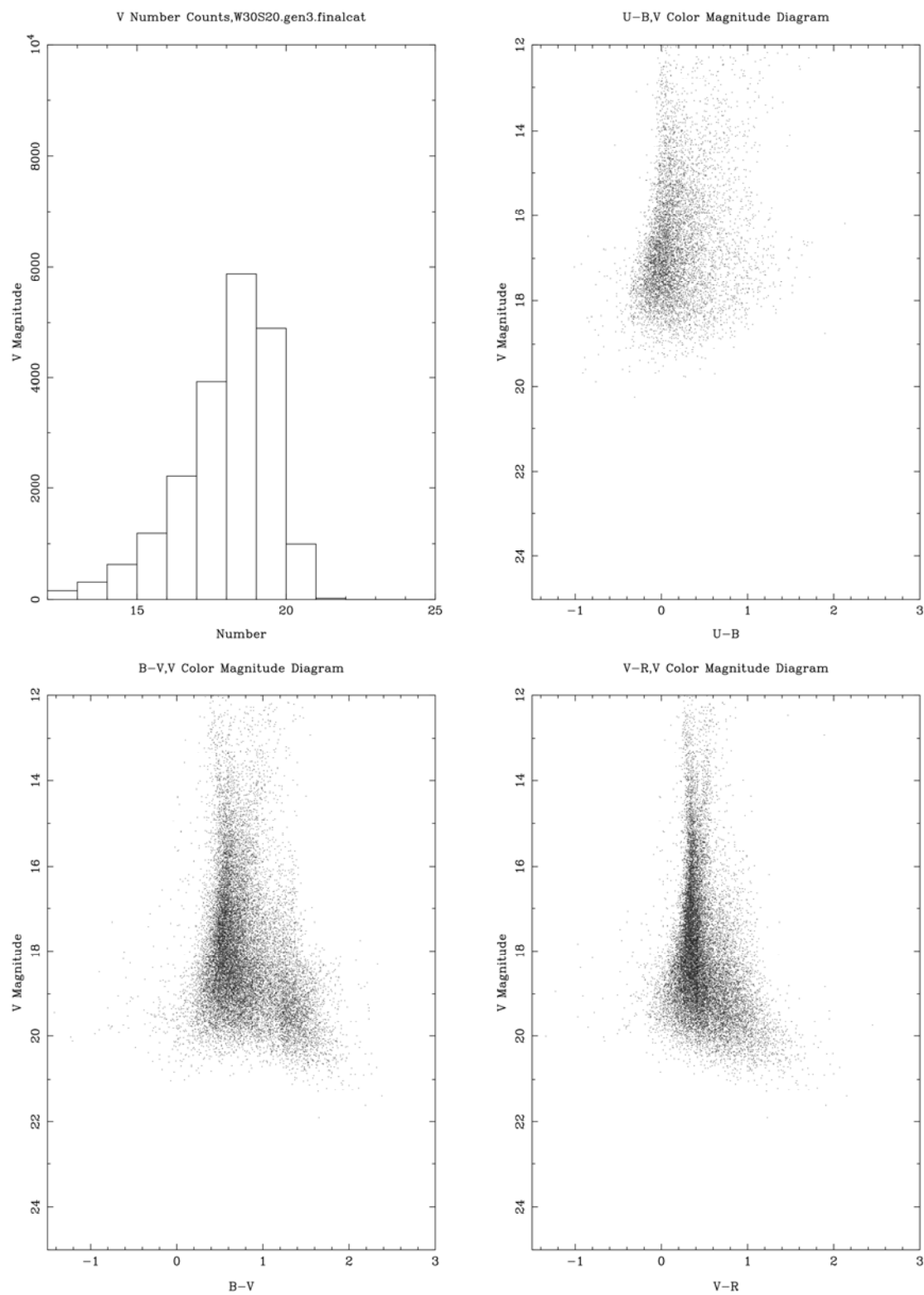


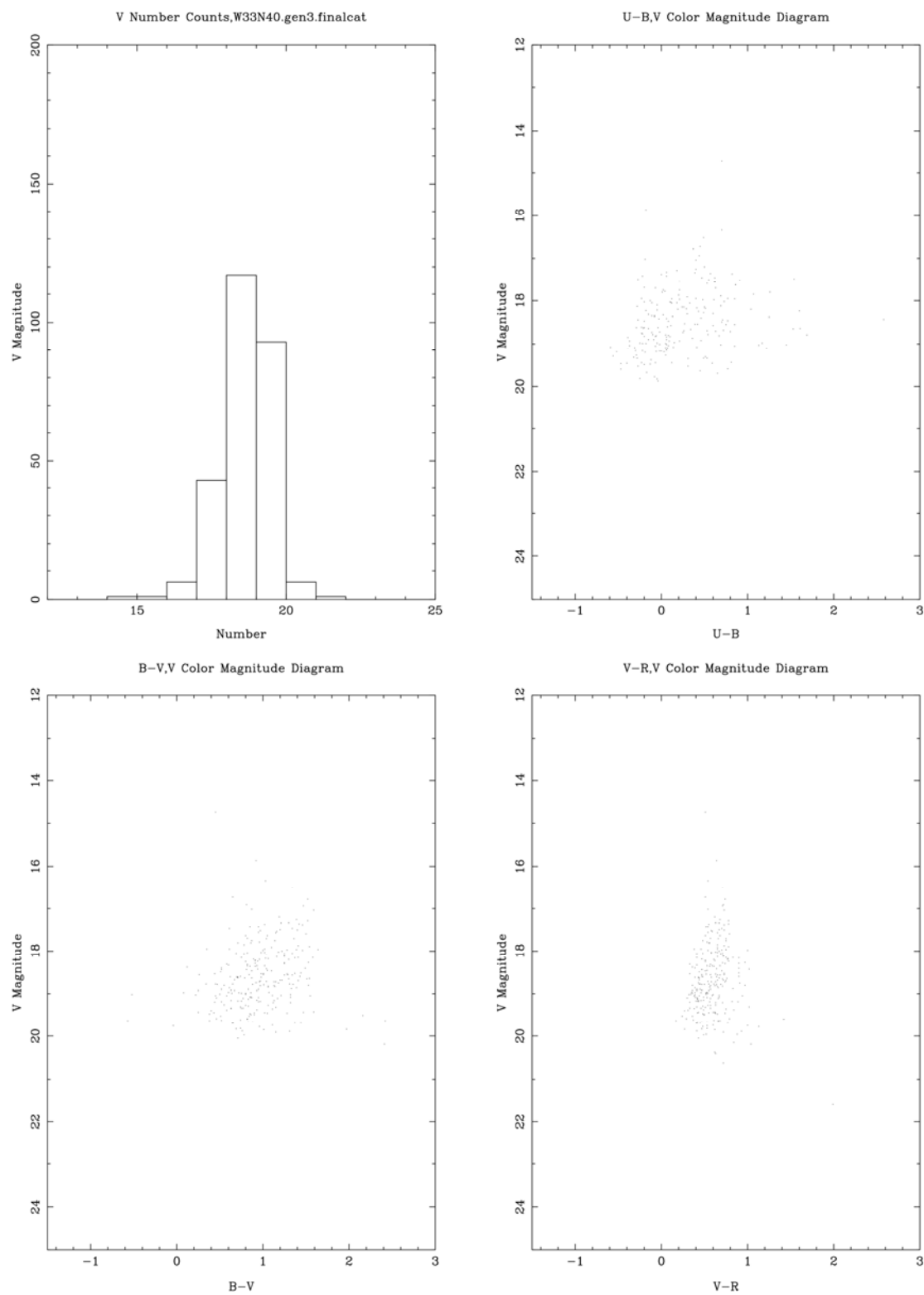
**W27S37**

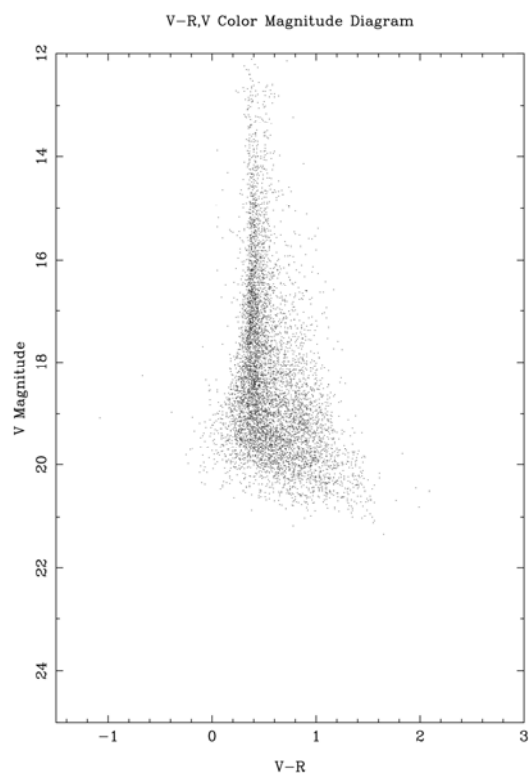
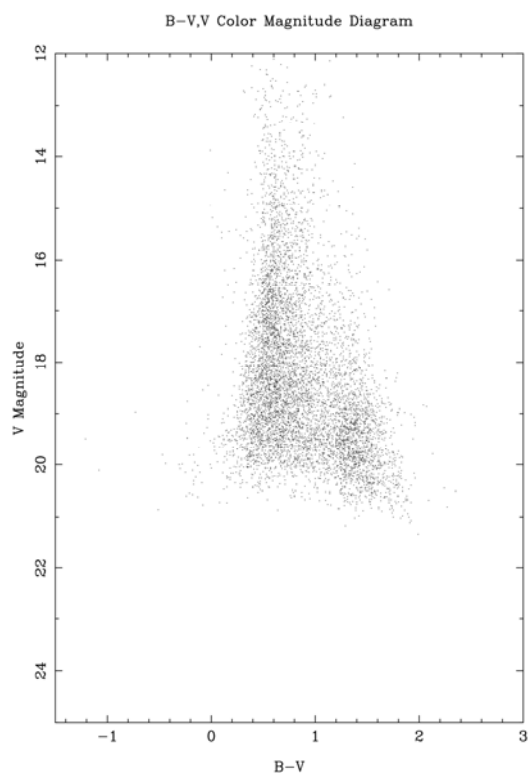
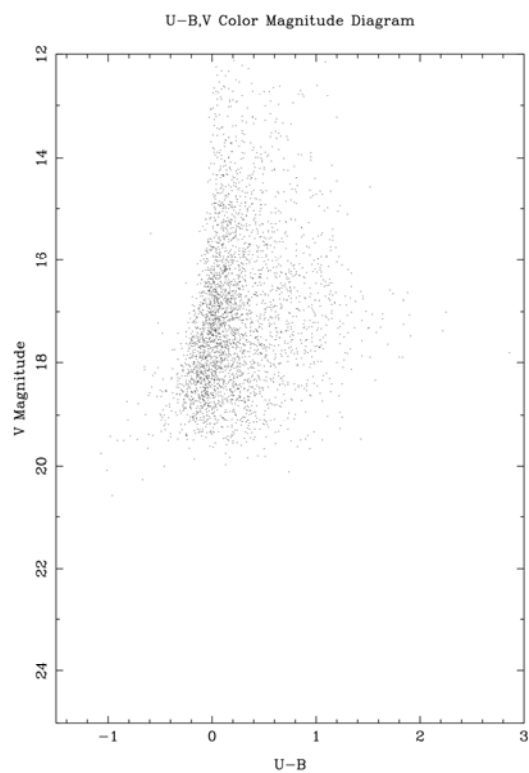
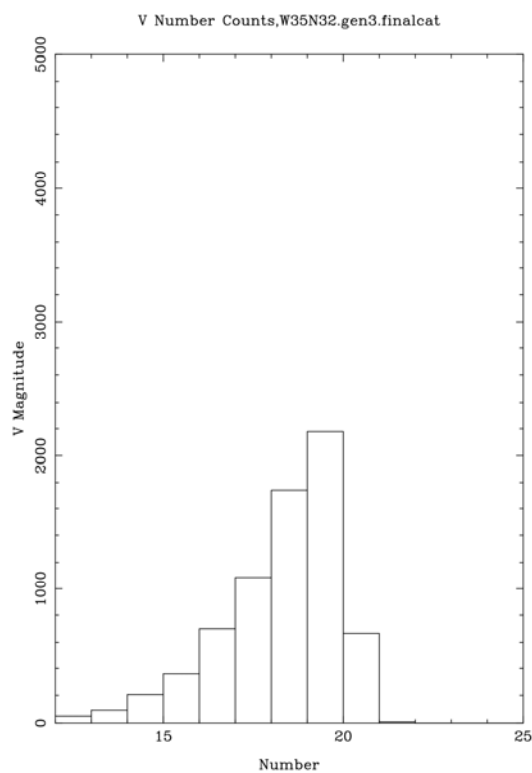
**W30N20**

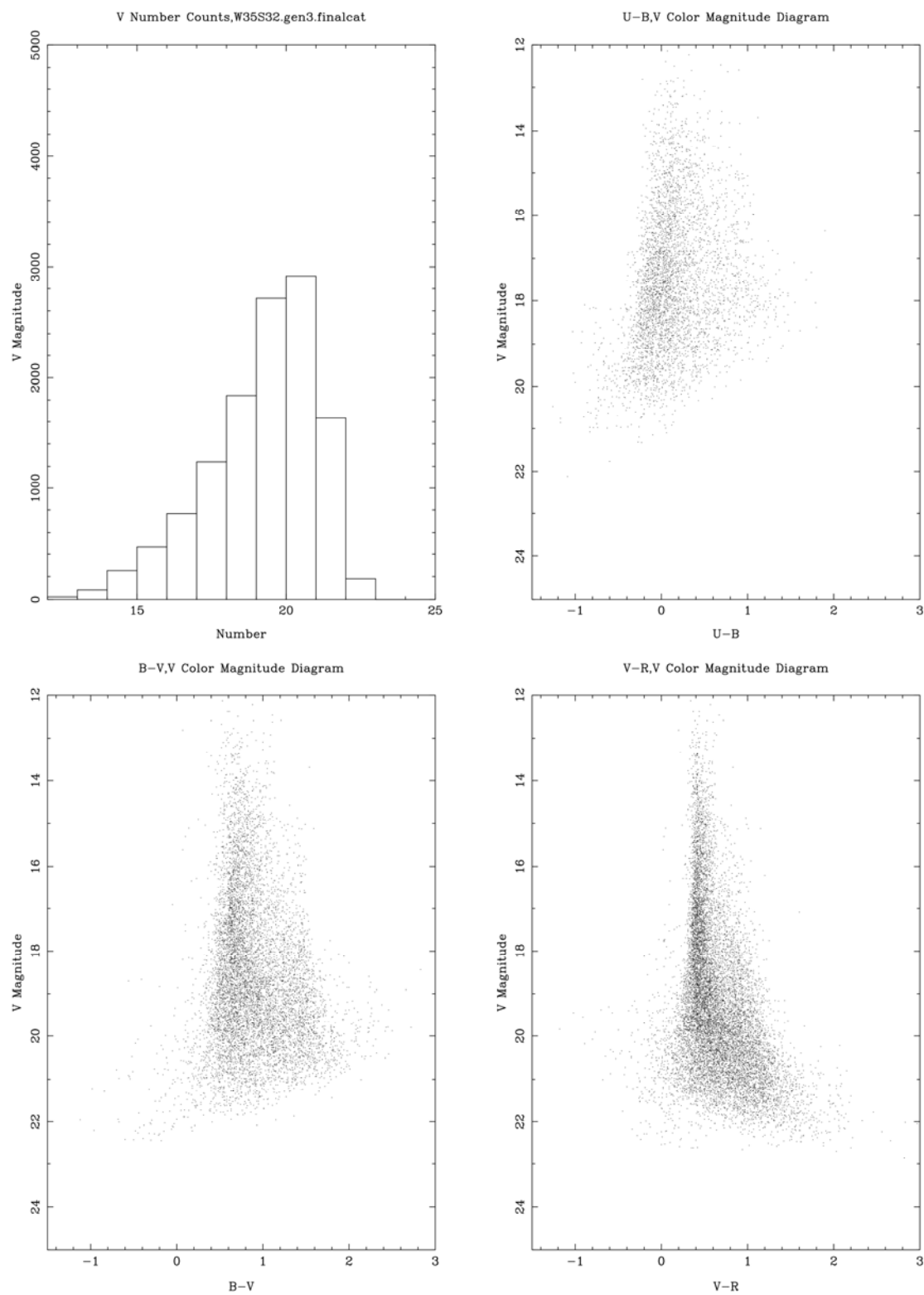


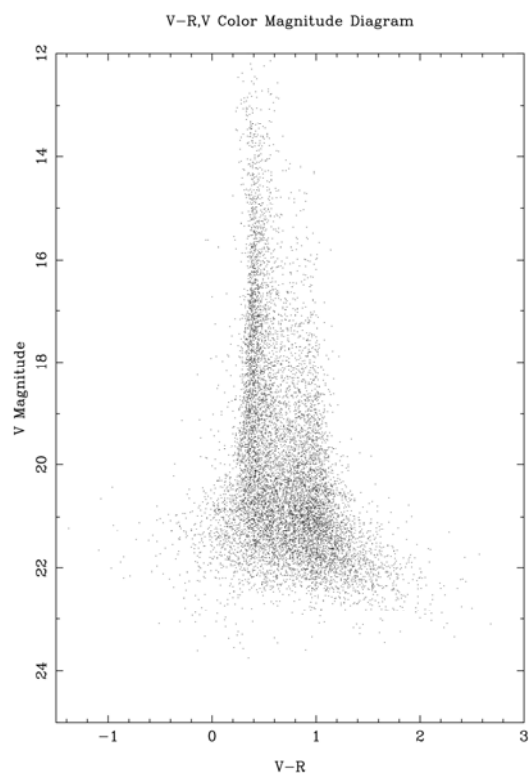
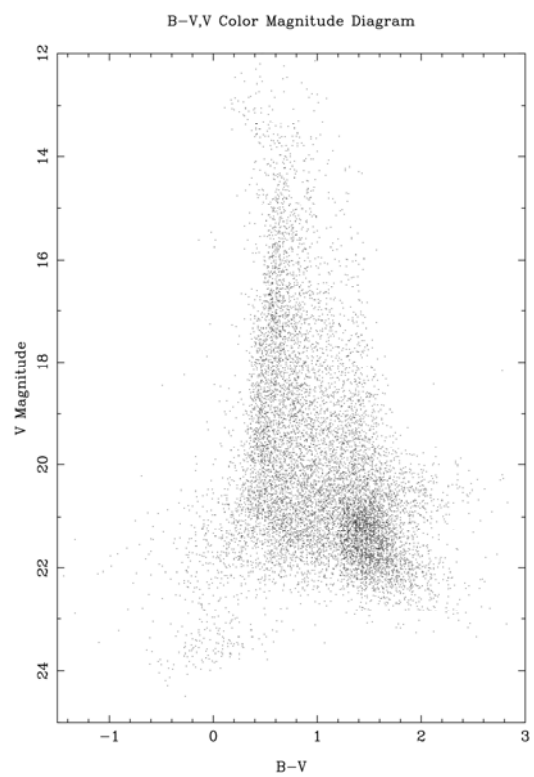
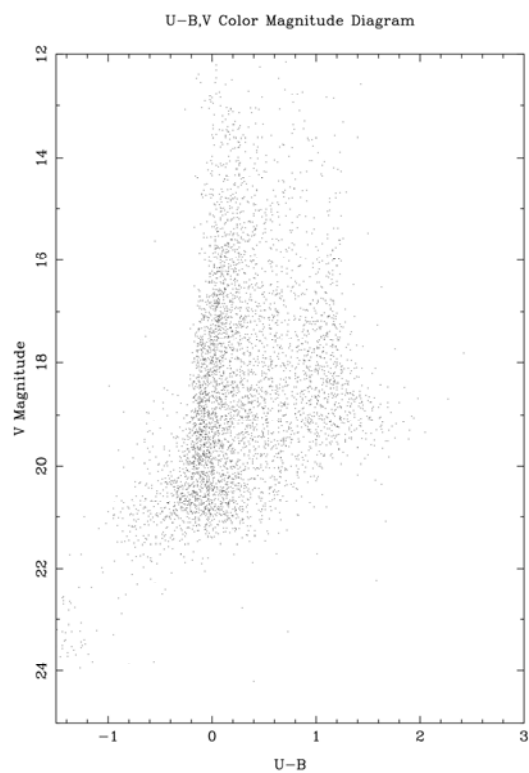
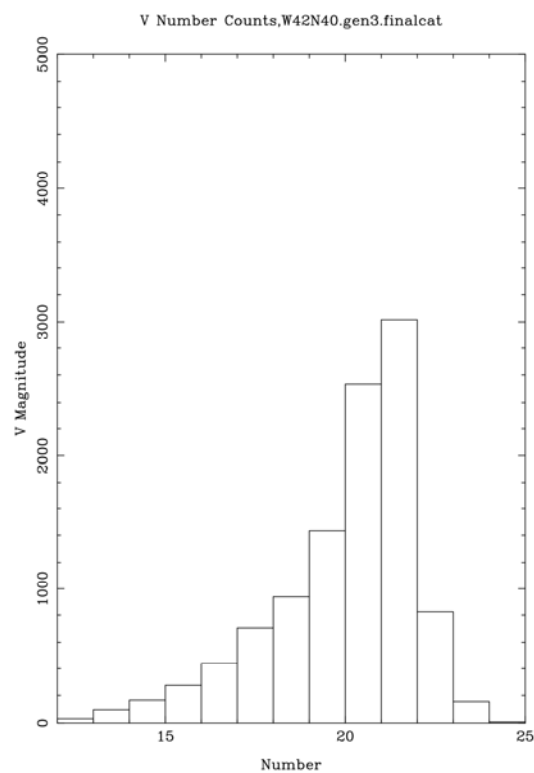
# W30S20

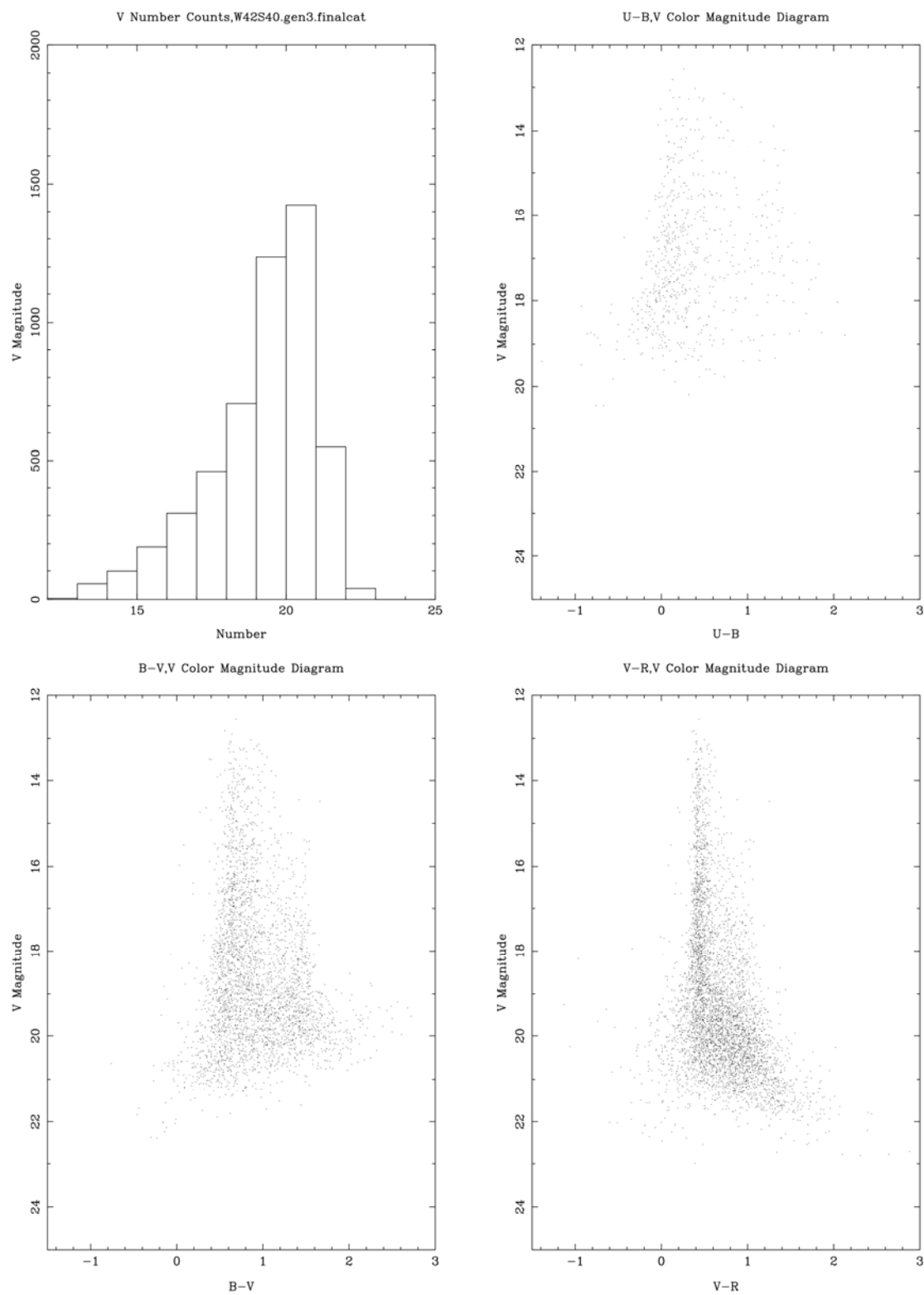


**W33N40**

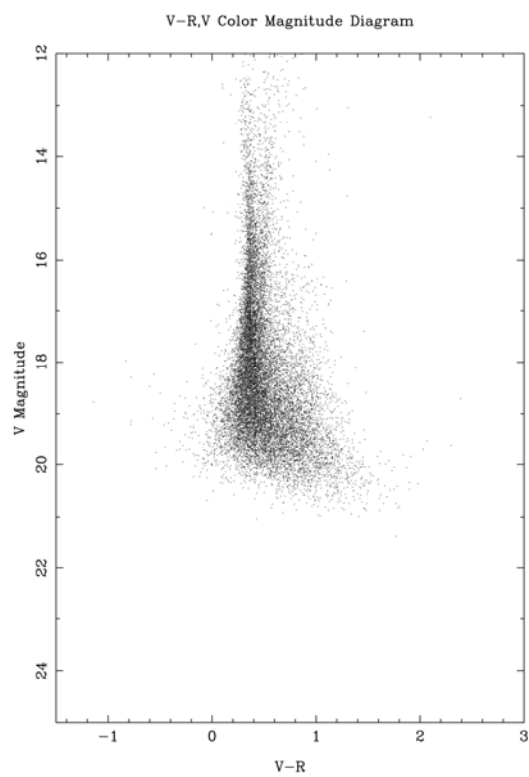
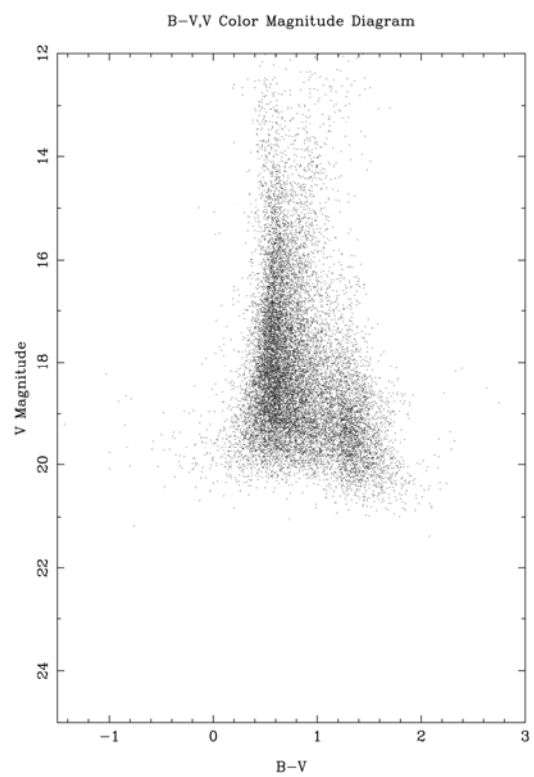
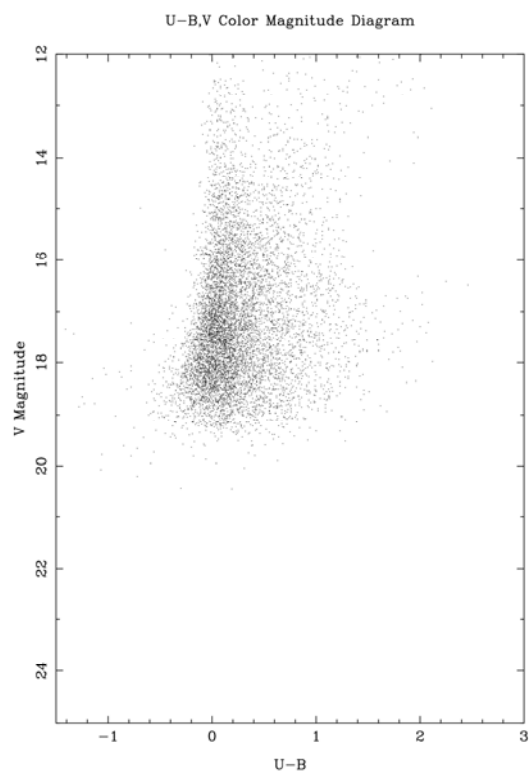
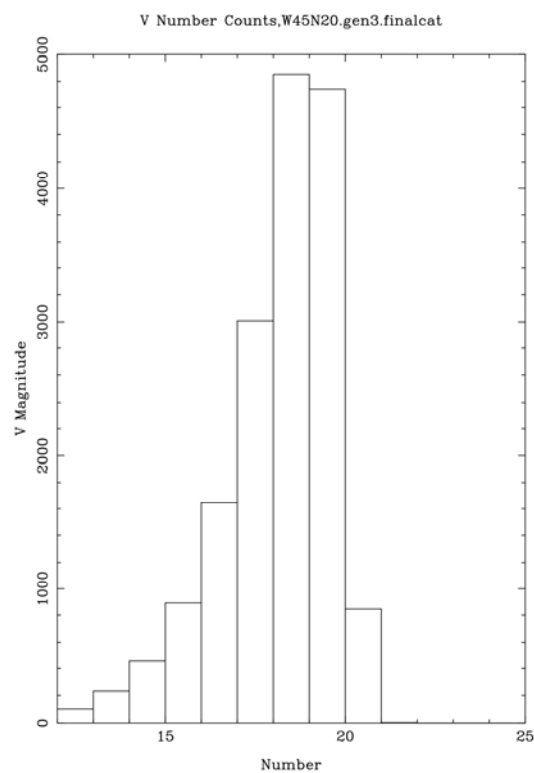
**W35N32**

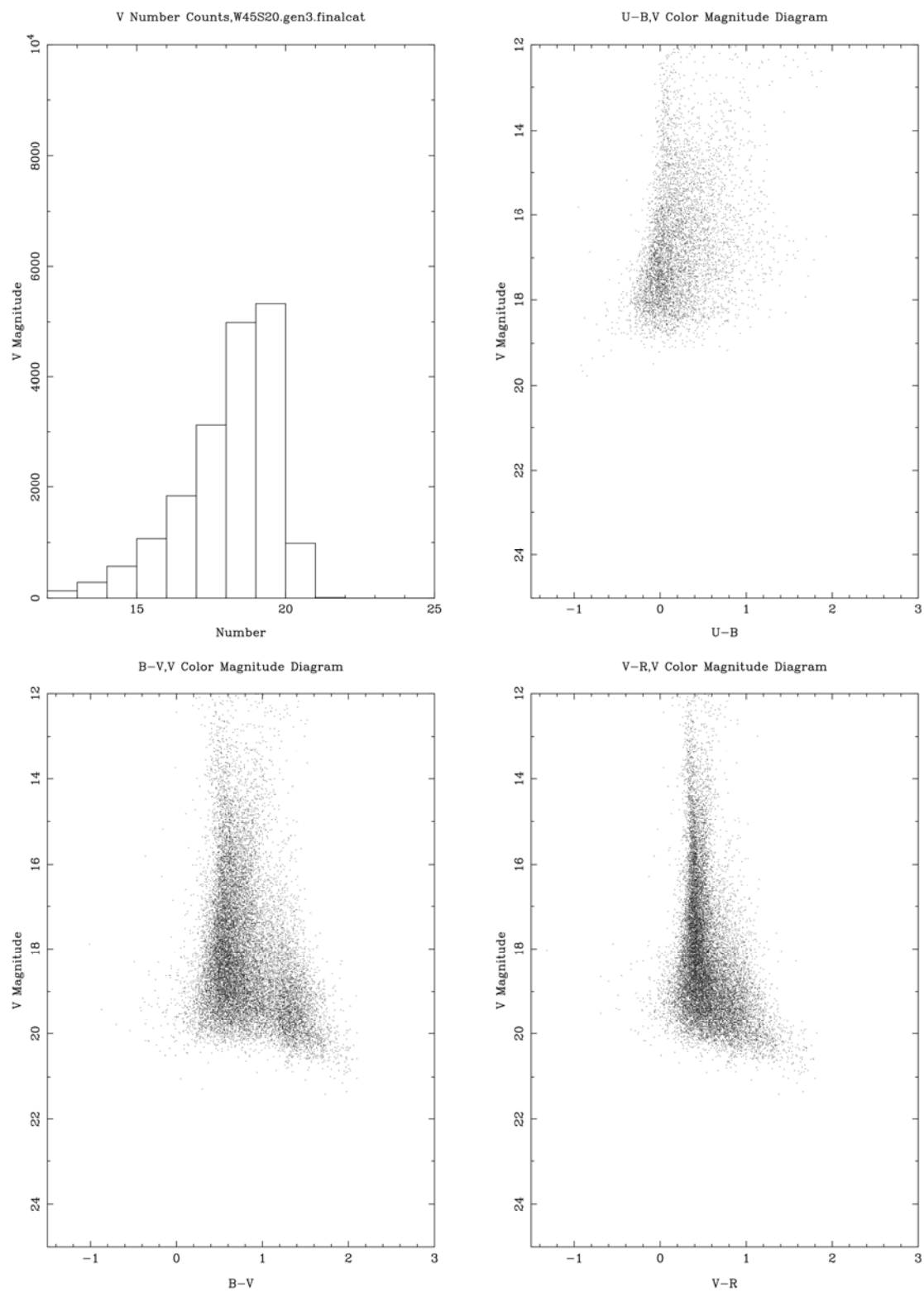
**W35S32**

**W42N40**

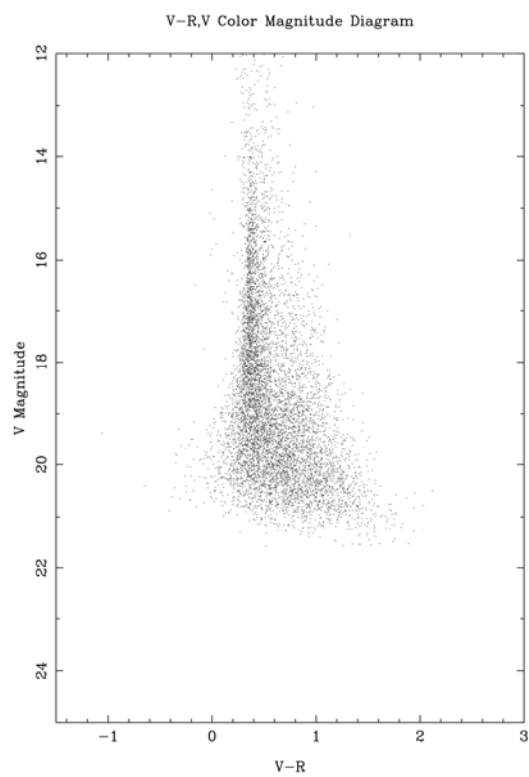
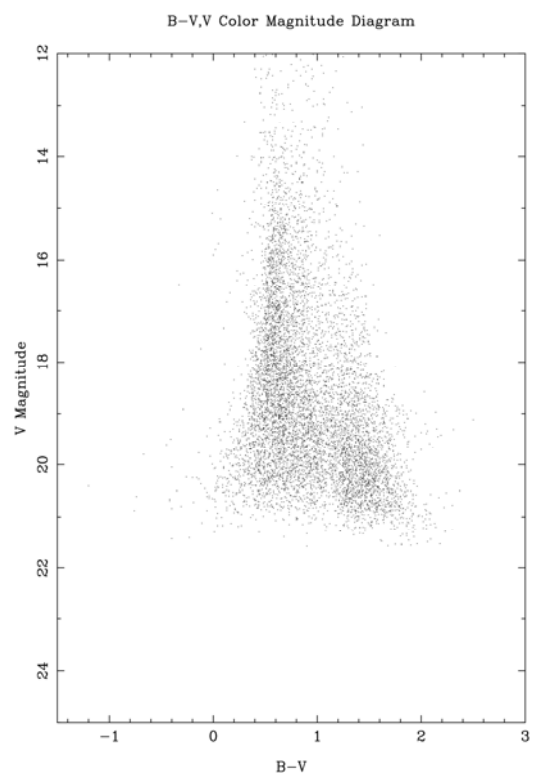
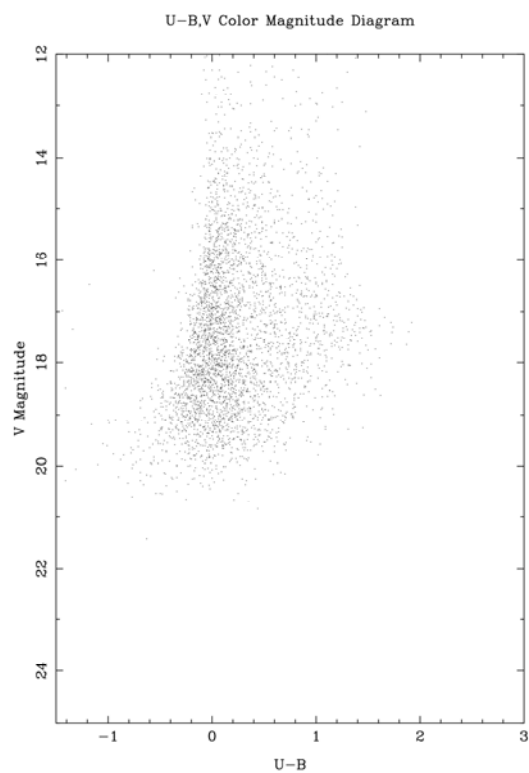
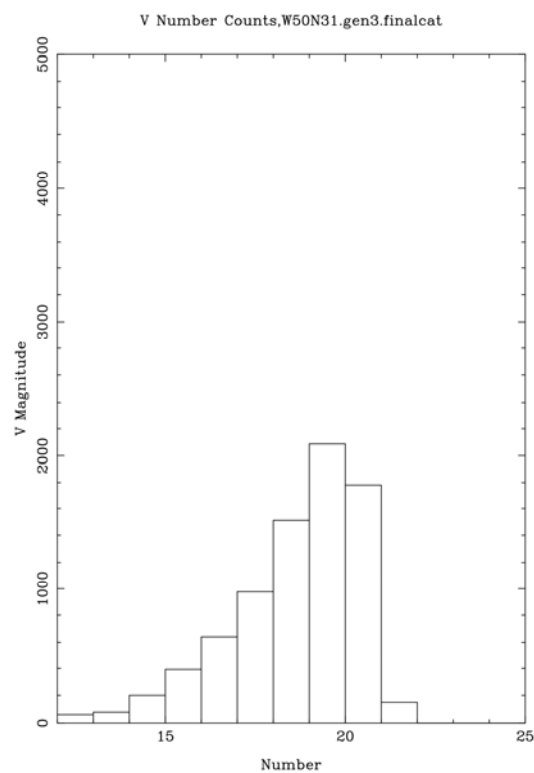
**W42S40**

# W45N20

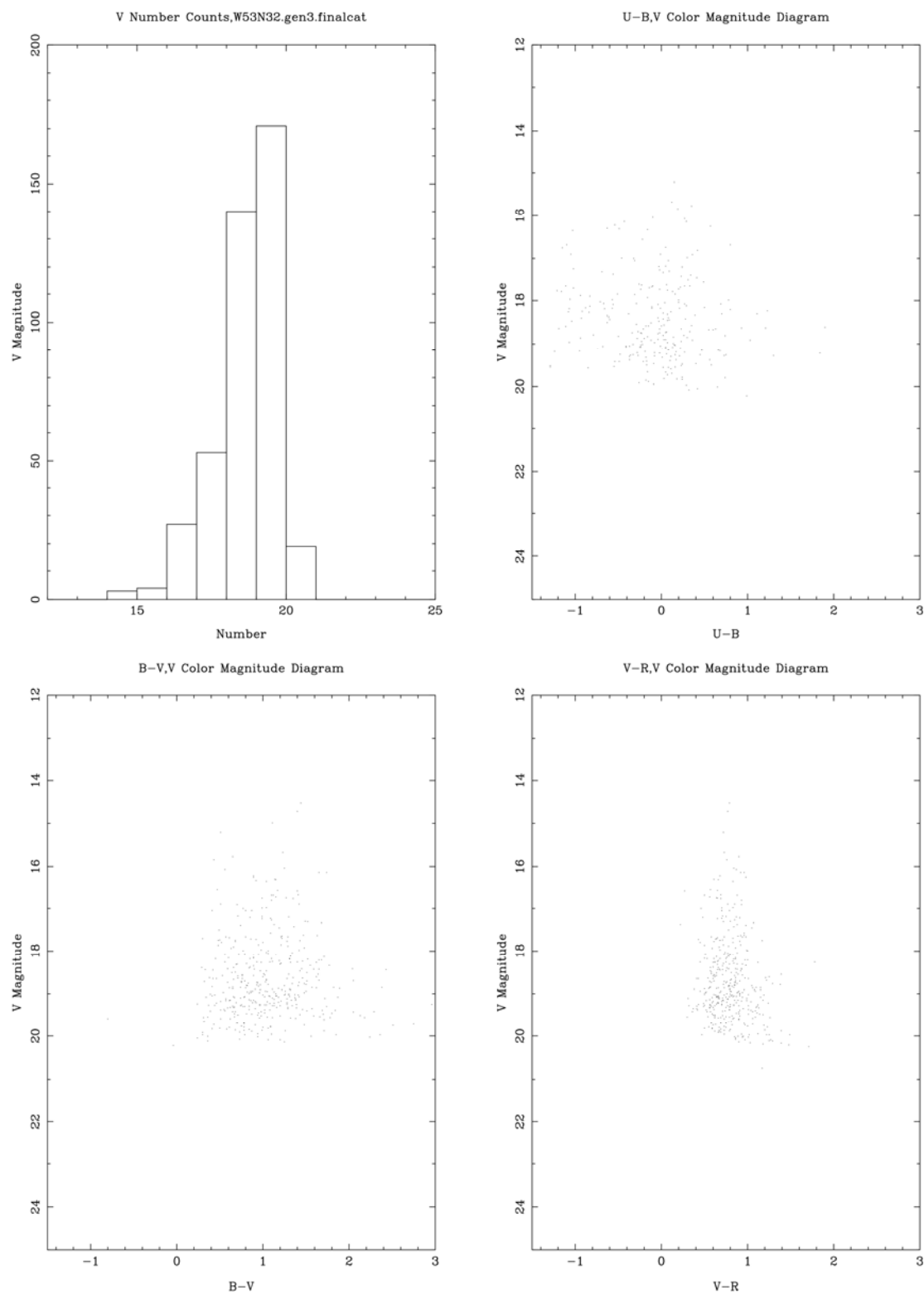


**W45S20**

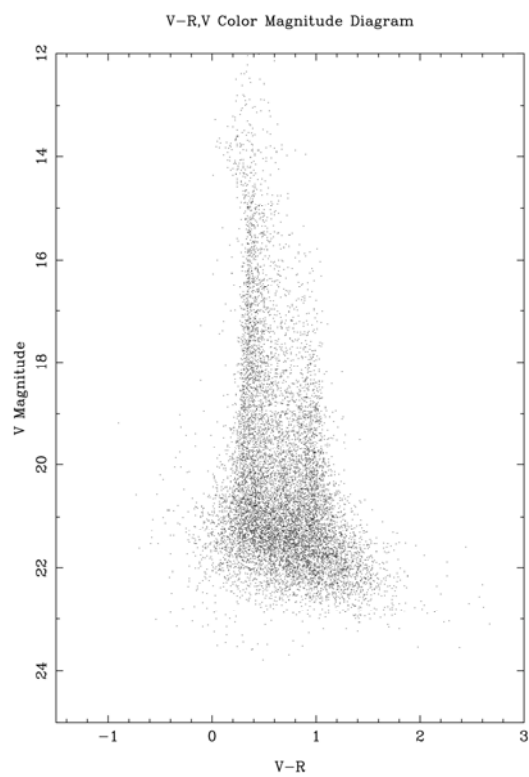
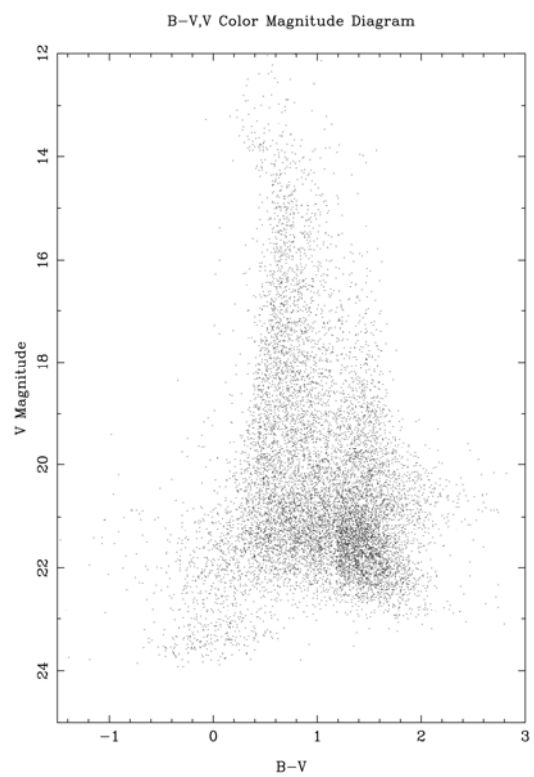
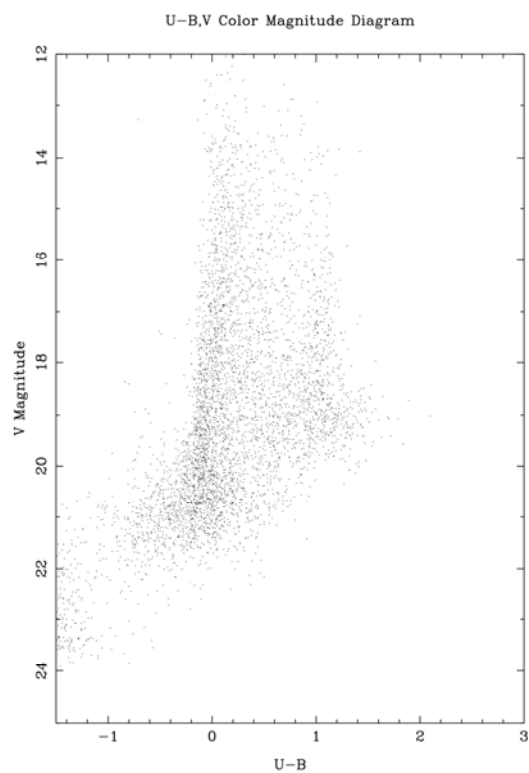
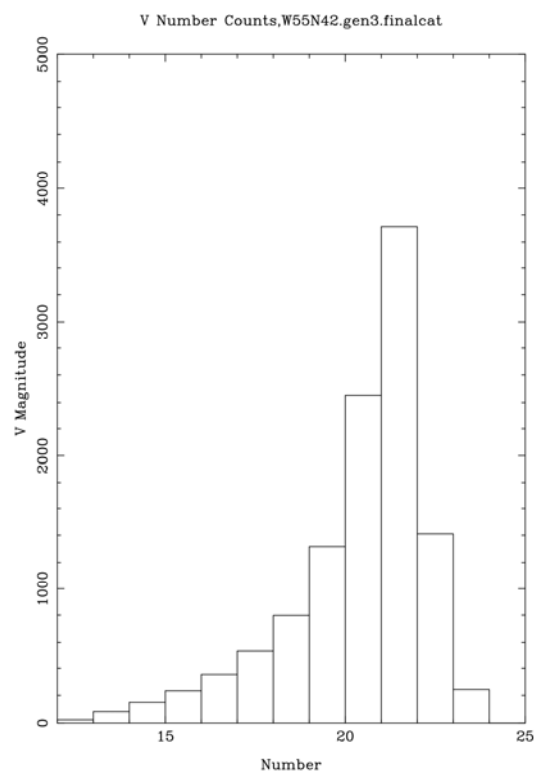


**W50N31**

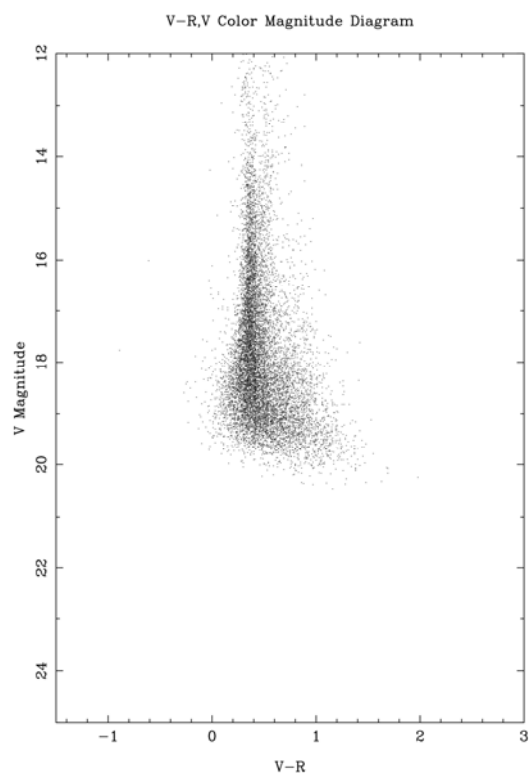
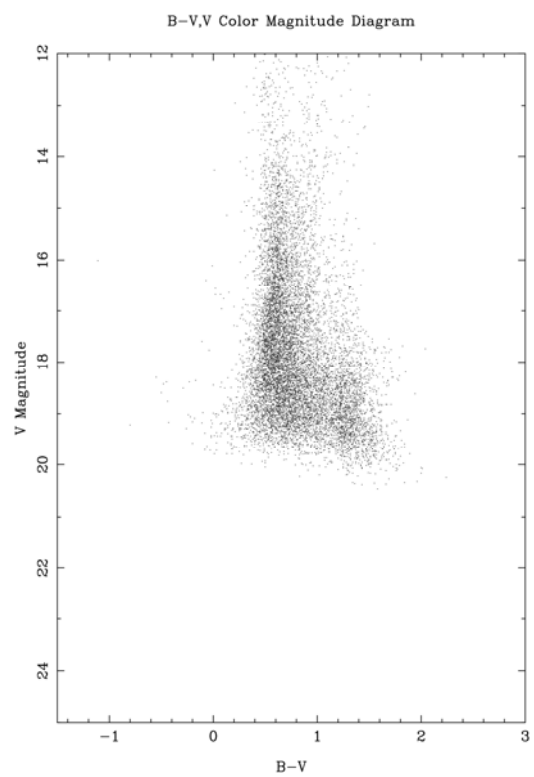
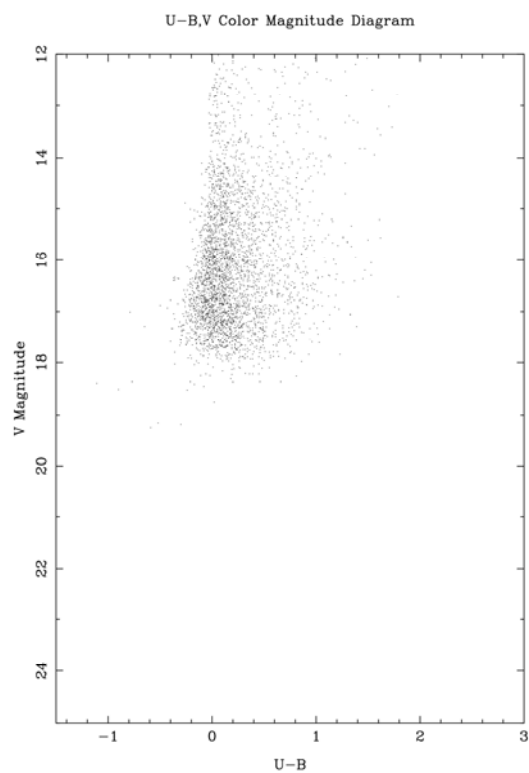
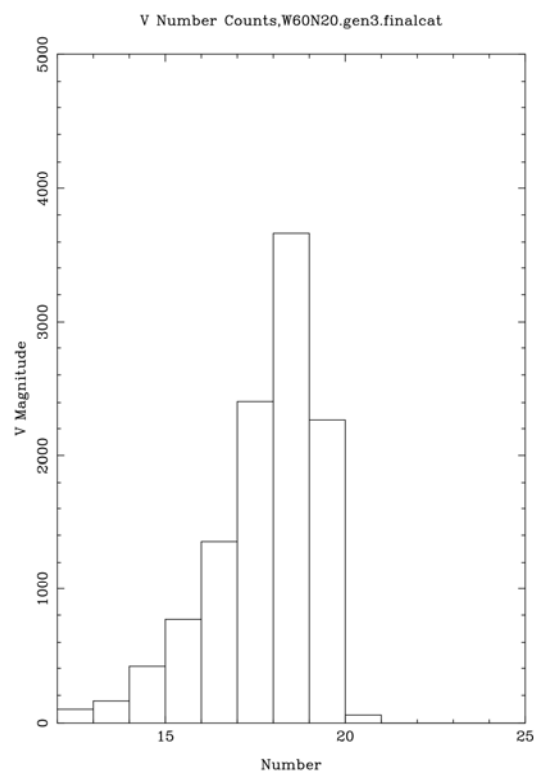
# W53N32



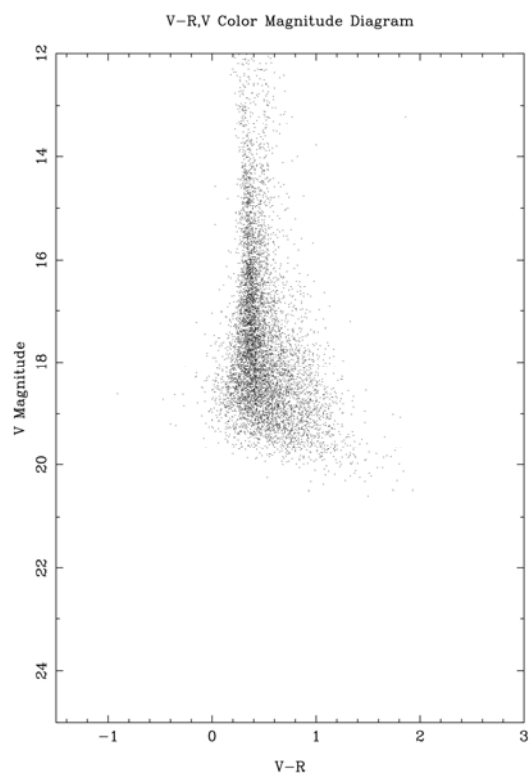
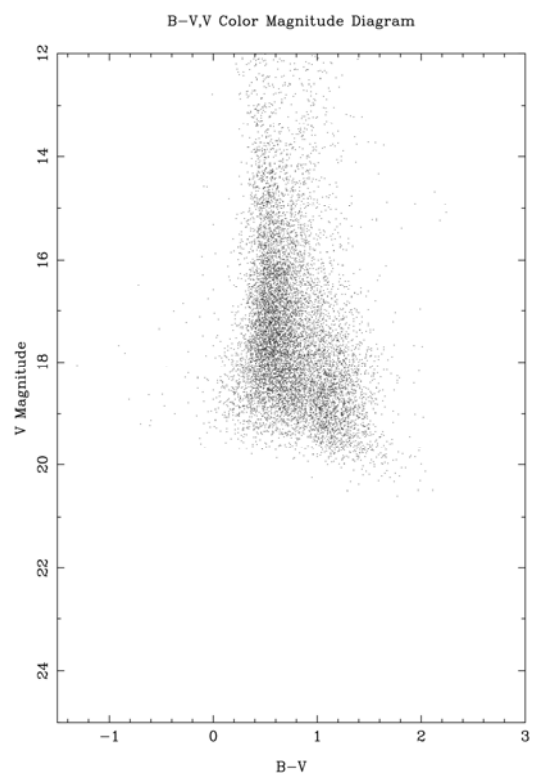
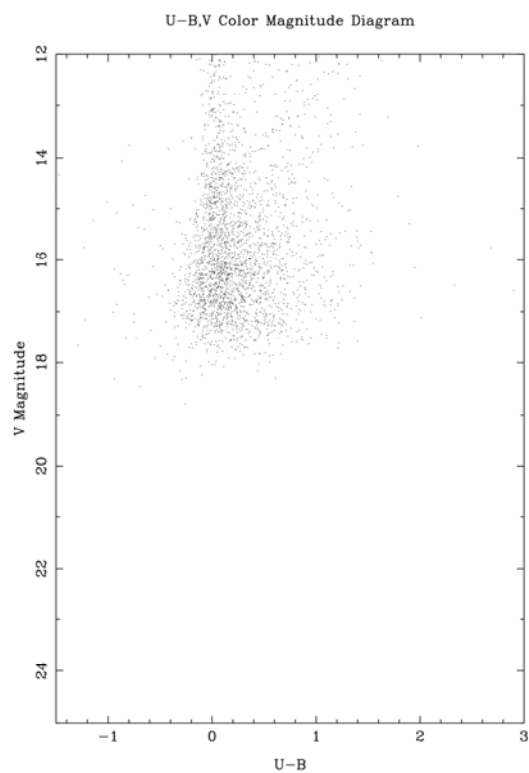
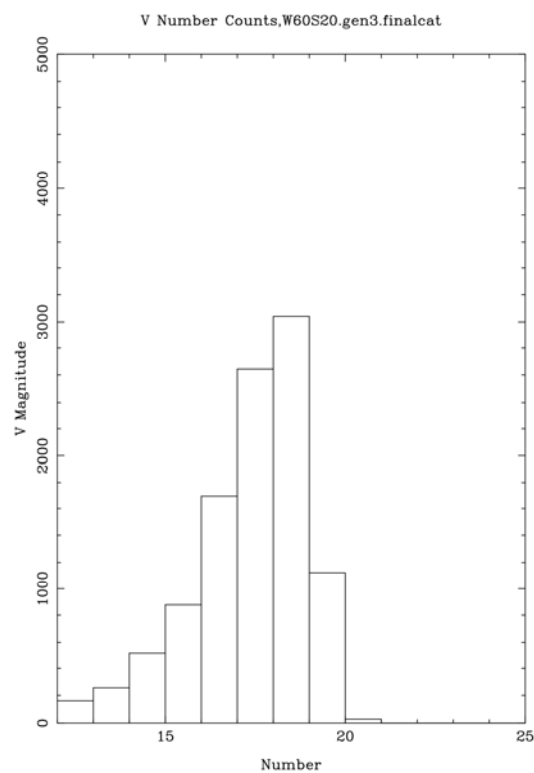
# W55N42



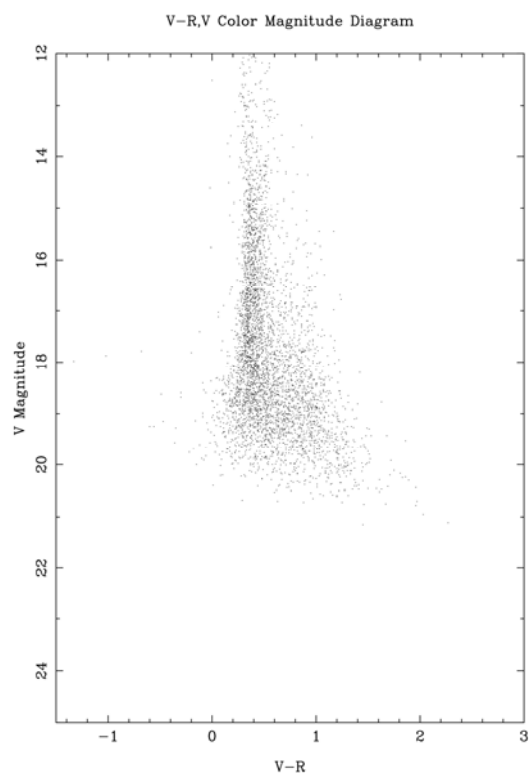
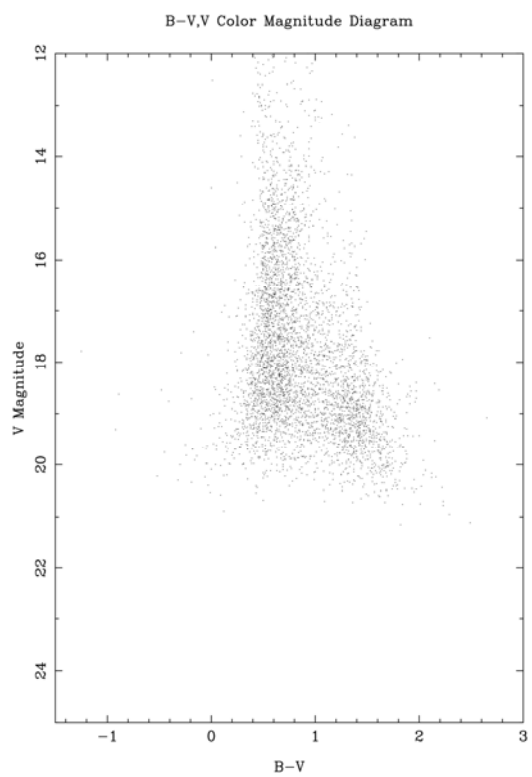
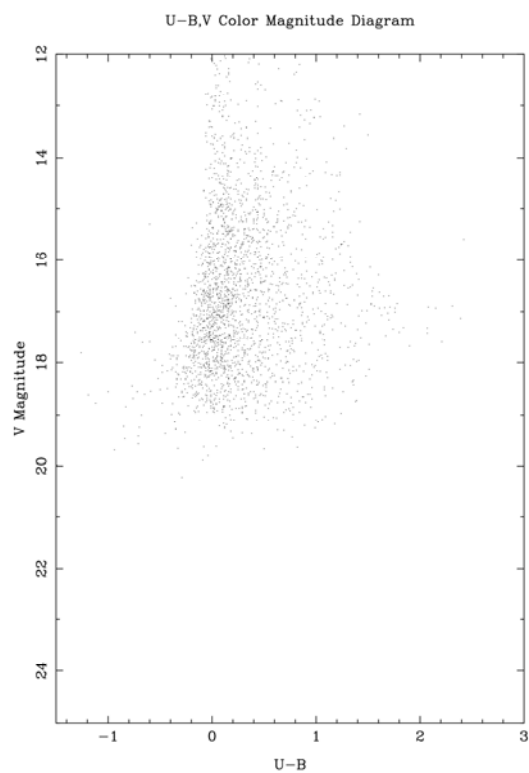
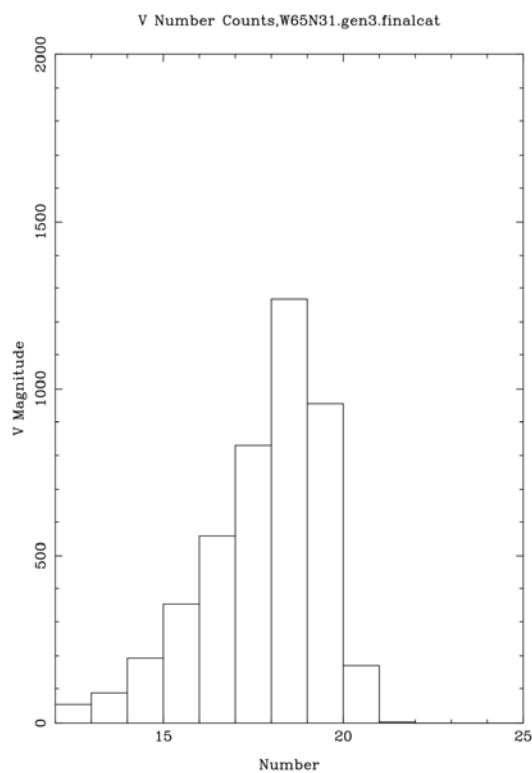
# W60N20



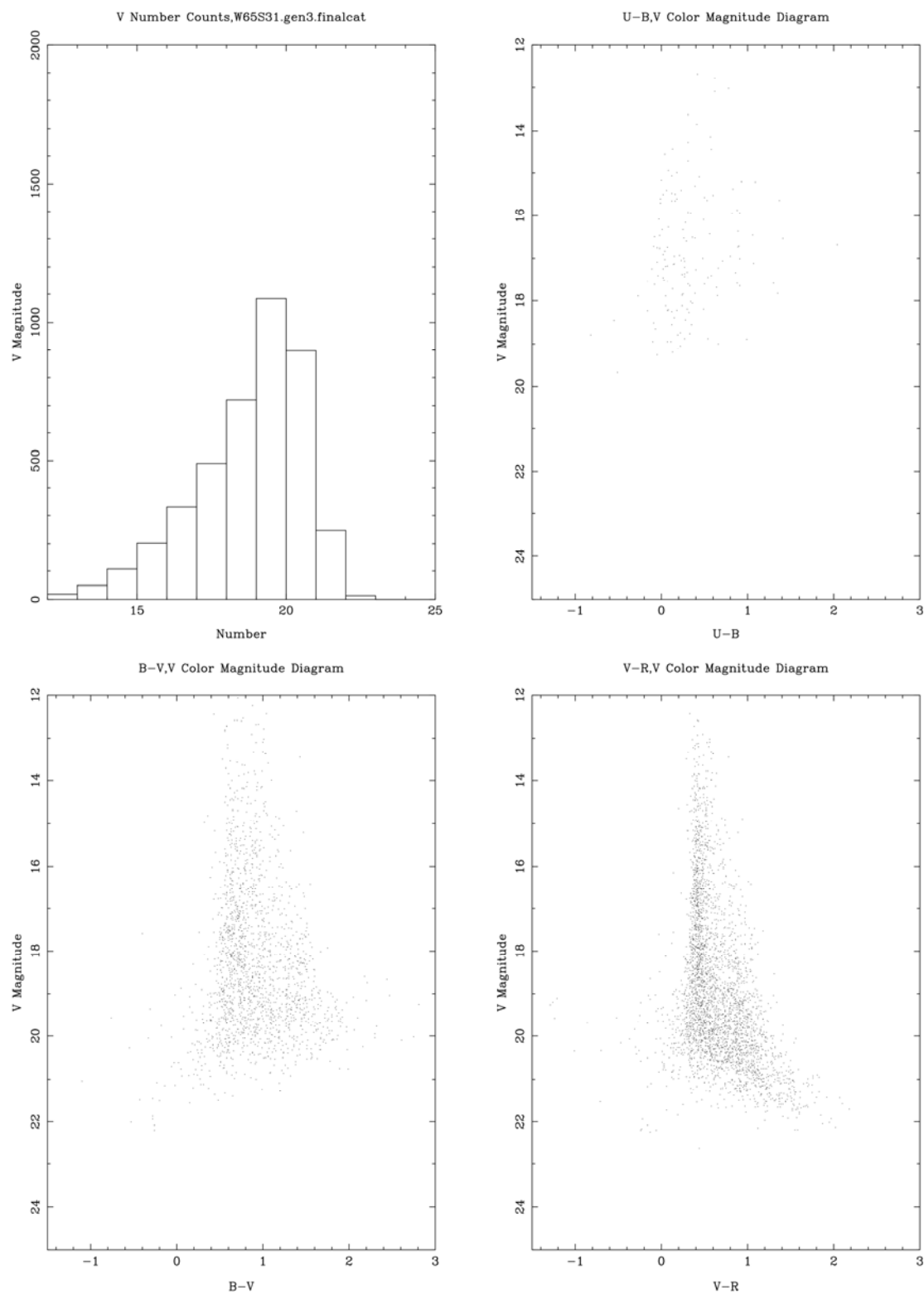
# W60S20

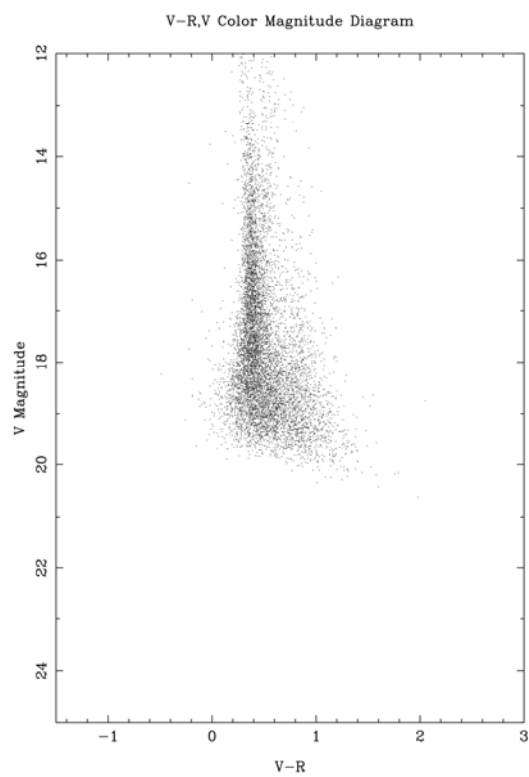
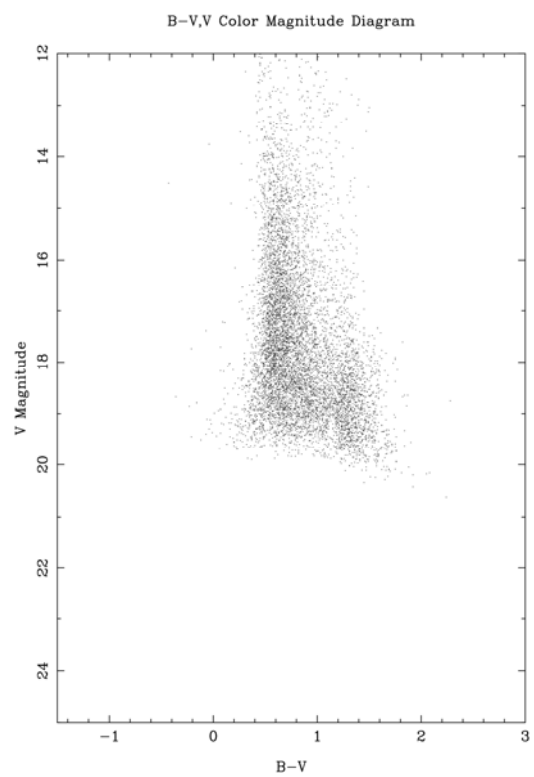
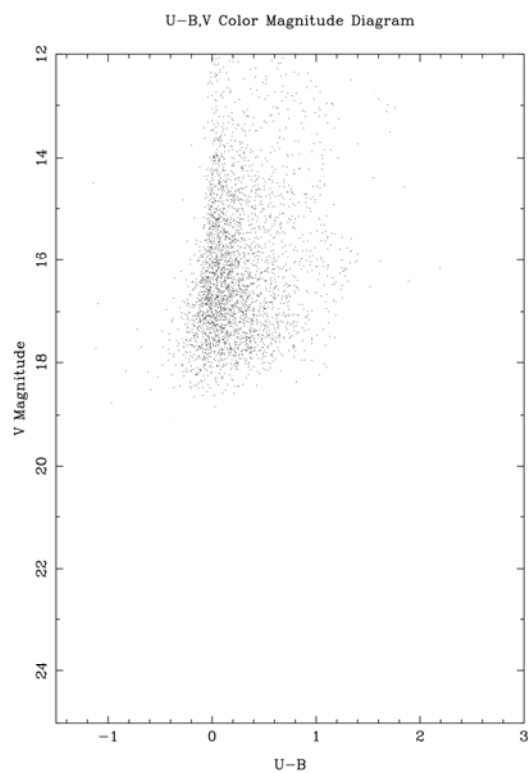
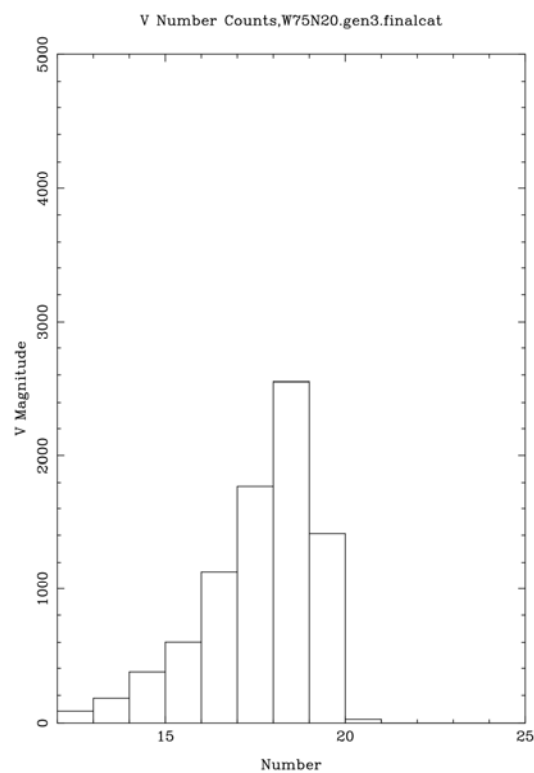


# W65N31

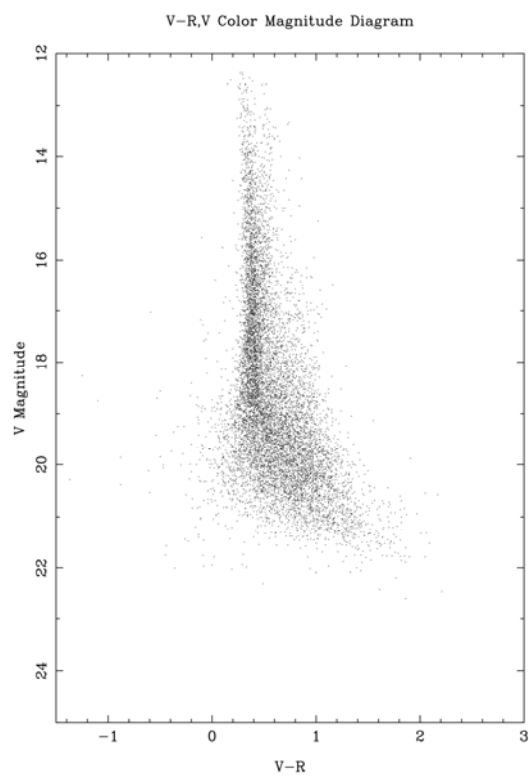
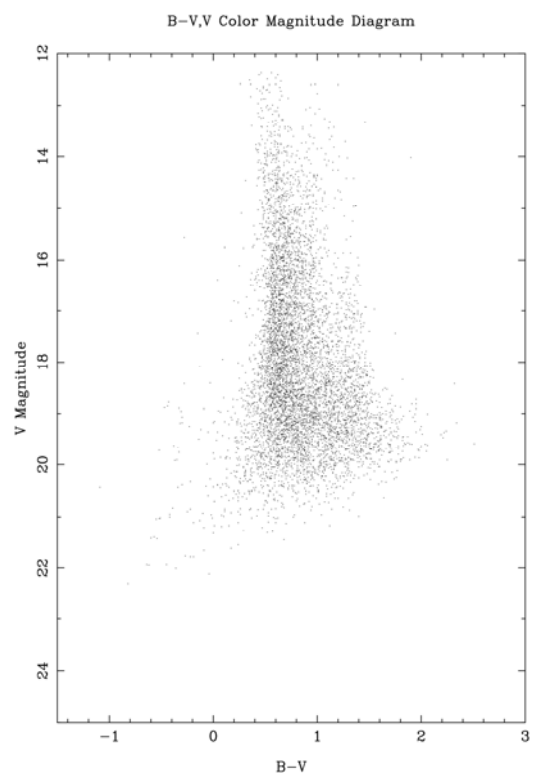
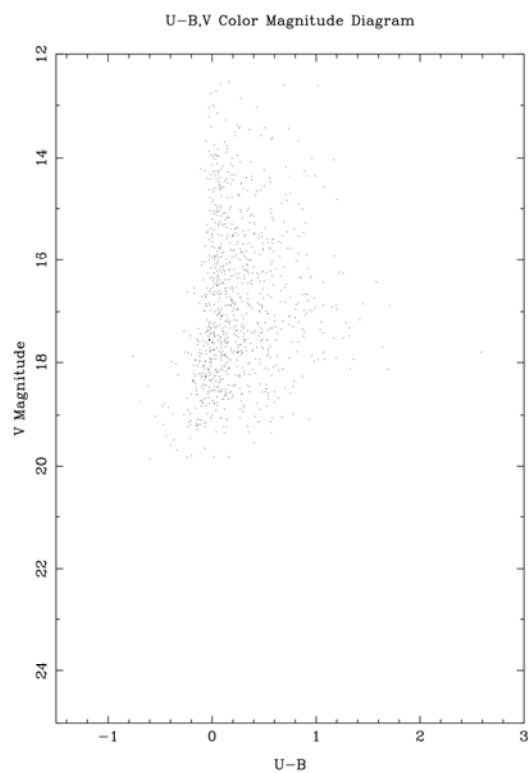
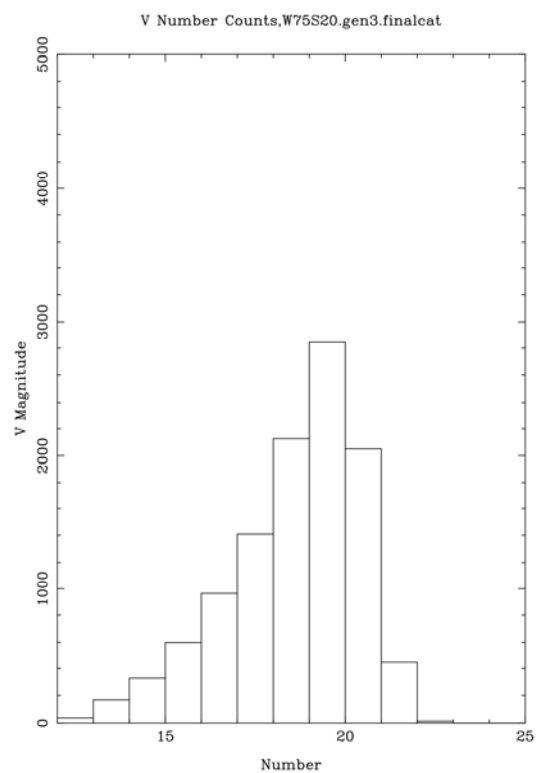


# W65S31



**W75N20**



**W75S20**

## Appendix C: PerlScript Coding for Data Analysis

### **completepeak.pl**

The program counts stars over magnitude ranges  $16 < V < 19$ ,  $16 < V < 17$ ,  $17 < V < 18$ , and  $18 < V < 19$  and gives a numerical value with positive and negative errors. We used these numbers to develop star count ratios of complementary fields of Quadrants 1 and 4, as well as the northern and southern quadrants.

```
#!/usr/bin/perl

use POSIX qw(ceil);

$dograph=1;

$maglo = 16;
$maghi = 19;

@protomag = (); @protocurve=();
open IF5, "protocurve.dat";
while ($line = <IF5>) {
    chop($line);
    @e = split(/\s+/, $line);
    $e[0] += 0.1;
    push(@protomag, $e[0]);
    push(@protocurve, $e[1]);
}
close IF5;

use PGPLOT;

# Given a final catalog, dump a bunch of usable data.....

# Data: 036429 259.867365 -01.457920 0.000020 0.000014 00.97 00.01 20.22 00.03 99.99 99.99 01.86
00.11 01.90 00.03

$infile = $ARGV[0];

open IF, "$infile";

@V=(); @BV=(); @UB=(); @VR=(); @RA=(); @DEC=(); @BVC=();
@cumV=();
@binBV=();
@binBV_color=();

for ($i = 120; $i < 240; $i++) {
    $diffV[$i]=0.0;
    $rdiffV[$i]=0.0;
}
for ($i = 1200; $i < 2400; $i++) {
    $cumV[$i]=0;
```

```

}
for ($i = 0; $i < 45; $i++) {
    $binBV[$i]=0;
    $binBV_color[$i]=0.1*($i-1)-1.5;
}

$nin = 0;
$nused = 0;
$count=0;
while ($line = <IF>) {
    $count++;
    $dcount = sprintf("%d",$count/10000);
    if ($count/10000 == $dcount) {
        printf "$count stars read...\n";
    }

    @e = split(/\s+/, $line);
    $nin++;
    if ($e[5] < 0.4) {
        push(@V,$e[7]);
        $binid = sprintf("%d",$e[7]*10);
        for ($i = 240; $i > $binid; $i--) {
            $rdiffV[$i]++;
        }
        $binid = sprintf("%d",$e[7]*100);
        for ($i = 2400; $i > $binid; $i--) {
            # if ($e[11] < 1.0) { $cumV[$i]++};
            $cumV[$i]++;
        }
        push(@UB,$e[9]);
        push(@BV,$e[11]);
        if ($e[7] > $maglo && $e[7] < $maghi && $e[11]>-1.5 && $e[11] < 4.0) {
            $binid = ($e[11]+1.5)*10.0+1;
            # $binid = ceil($binid);
            $binid=sprintf("%d",$binid);
            $binBV[$binid]++;
            $e[11]+=0.001;
            push(@BVC,$e[11]);
        }
        push(@VR,$e[13]);
        if ($e[7] > 14 && $e[7] < 22.5 && $e[11] > -1.0 && $e[11] < 3.05) {
            $vindex = sprintf("%d",($e[7]-14.0)/0.5);
            $bvindex = sprintf("%d",($e[11]+1.0)/0.05);
            # printf "$e[7] $e[11] $vindex $bvindex\n";
        }
        $nused++;
    }
}
close IF;

for ($i = 1200; $i < 2400; $i++) {
    if ($cumV[$i] > 0) {
        $cumV[$i]=0.4343*log($cumV[$i]);
    }
}
for ($i = 121; $i < 240; $i++) {

```

```

$diffV[$i]=$rdiffV[$i]-$rdiffV[$i-1];
if ($diffV[$i] > 0) {
    $diffV[$i]=0.4343*log($diffV[$i]);
}
}

#printf "Line fit between 16.0 and 18 mag\n";
$sumy = 0; $sumx = 0; $sumxx = 0; $sumxy = 0; $n = 0;
for ($i = 1600; $i < 1800; $i++) {
    $fmag = $i/100;
    $sumy += $cumV[$i];
    $sumxy += $fmag*$cumV[$i];
    $sumxx += $fmag*$fmag;
    $sumx += $fmag;
    $n++;
}

$meany = $sumy/$n;
$meanx = $sumx/$n;

$a = ($meany*$sumxx - $meanx*$sumxy)/($sumxx - $n*$meanx*$meanx);
$b = ($sumy - $n*$meanx*$meany)/($sumxx - $n*$meanx*$meanx);

$totoffset = 0; $noffset = 0;
#printf "Model match between 16 and 19 mag\n";
for ($i = 0; $i <= $#protomag; $i++) {
    #printf "$protomag[$i] $protocurve[$i]\n";
    if ($protomag[$i] > 16 && $protomag[$i] < 19.0) {
        $index = $protomag[$i]*100;
        $index = sprintf("%d",$index);
        $offset = ($cumV[$index] - $protocurve[$i]);
        $totoffset += $offset;
        $noffset += 1;
    }
}
if ($noffset > 0) {$totoffset /= $noffset;}
else {die "Unable to find the offset between the model and data.\n";}
#printf "The total offset between the curves is $totoffset in $noffset points\n";

$curcomplimit=0; $stillmatch=1;
for ($i = 0; $i <= $#protomag; $i++) {
    #printf "$protomag[$i] $protocurve[$i]\n";
    if ($protomag[$i] > 18 && $stillmatch) {
        $index = $protomag[$i]*100;
        $index = sprintf("%d",$index);
        $offset = abs($cumV[$index] - $protocurve[$i] - $totoffset);
        if ($offset > 0.15) {
            $stillmatch=0;
            $curcomplimit=$protomag[$i];
        }
    }
}

$incomplete = 0;
for ($i = 1600; $i < 2400; $i++) {

```

```

if (!$incomplete) {
    $complete = $i;
    $tmag = $i / 100;
    $y = $b*$tmag + $a;
    $test = abs($y - $cumV[$i]);
    #printf "$tmag $y $cumV[$i]\n";
    if ($test > 0.05) {
        $incomplete = 1;
        $complimit = $tmag;
    }
}

}

$max = 0;
for ($i = 0; $i < 45; $i++) {
    if ($binBV[$i] > $max) {
        $maxi=$i;
        $max = $binBV[$i];
    };
}

#$l1bin = $binBV[$maxi-1];
#$peakbin = $binBV[$maxi];
#$h1bin = $binBV[$maxi+1];
#$total = $l2bin+$l1bin+$peakbin+$h1bin+$h2bin;
#$median = $total/2.0;
#$b4 = $l1bin+$peakbin+$h1bin-$median;
#$b3 = $l1bin+$peakbin-$median;
#$b2 = $l1bin-$median;
#
# if ($b2 > 0) {
#   printf "DB: In b2\n";
#   $partial = ($l1bin-$b2)/$l1bin;
#   $fracbin = $partial - 1.0;
# }
# elif ($b3 > 0) {
#   printf "DB: In b3\n";
#   $partial = ($peakbin-$b3)/$peakbin;
#   $fracbin = $partial;
# }
# elif ($b4 > 0) {
#   printf "DB: In b4\n";
#   $partial = ($h1bin-$b4)/$h1bin;
#   $fracbin = $partial+1.0;
# }

$l2bin = $binBV[$maxi-2]*0.5;
$l1bin = $binBV[$maxi-1];
$peakbin = $binBV[$maxi];
$h1bin = $binBV[$maxi+1];
$h2bin = $binBV[$maxi+2]*0.5;
$total = $l2bin+$l1bin+$peakbin+$h1bin+$h2bin;
$median = $total/2.0;
$b5 = $l2bin+$l1bin+$peakbin+$h1bin+$h2bin-$median;
$b4 = $l2bin+$l1bin+$peakbin+$h1bin-$median;

```

```

$b3 = $l2bin+$l1bin+$peakbin-$median;
$b2 = $l2bin+$l1bin-$median;
$b1 = $l2bin-$median;

if ($b1 > 0) {
    #printf "DB: In b1\n";
    $partial = ($l2bin-$b1)/$l2bin;
    $fracbin = $partial - 2.0;
}
elseif ($b2 > 0) {
    #printf "DB: In b2\n";
    $partial = ($l1bin-$b2)/($l1bin);
    $fracbin = $partial - 1.0;
}
elseif ($b3 > 0) {
    #printf "DB: In b3\n";
    $partial = ($peakbin-$b3)/$peakbin;
    $fracbin = $partial;
}
elseif ($b4 > 0) {
    #printf "DB: In b4\n";
    $partial = ($h1bin-$b4)/$h1bin;
    $fracbin = $partial+1.0;
}
elseif ($b5 > 0) {
    #printf "DB: In b5\n";
    $partial = ($h2bin-$b5)/$h2bin;
    $fracbin = $partial+2.0;
}

#printf "DB: $median -- b: $b1 $b2 $b3 $b4 $b5\n";

#printf "DB: $median -- b: $b1 $b2 $b3 $b4 $b5\n";
#printf "DB: values: $l2bin $l1bin $peakbin $h1bin $h2bin\n";

$peakcolor=0.1*($maxi+$fracbin-1)-1.5;

#printf "\nAttempt to do a true median....\n\n";
#printf "Estimated Peak Color is $peakcolor\n";

@median=();

for ($i = 0; $i < $#BVC; $i++) {
    if ($BVC[$i] >= ($peakcolor - 0.20) && $BVC[$i] <= ($peakcolor + 0.20)) {
        push(@median,$BVC[$i]);
    }
}

@sortmedian = sort(@median);

$peakcolor = $sortmedian[$#median/2];

#for ($i = 0; $i < $#median; $i++) {
# printf "$i $sortmedian[$i]\n";
#}

```

```

$peakcolor = sprintf("%6.3f",$peakcolor);
printf "Median Peak Color is $peakcolor\n";
printf "Enter your peak value ";
$peakcolor = <stdin>;
chop ($peakcolor);
$max = $max*1.1;

if ($dograph) {

$dev = "?" unless defined $dev;

pgbegin(0,$dev,1,1);

pgscf(2);      # Set character font
pgslw(1);      # Set line width
pgsubp(2,2);
#pgsubp(1,1);

pgscf(2);      # Set character font
pgslw(1);      # Set line width
pgsch(1.2);    # Set character height
pgsls(1);
pgsch(1.0);
pgslw(1);
pghist($#BVC,\@BVC,-1.5,3,45,0);
pgsci(2);
pgmove($peakcolor,0);
pgdraw($peakcolor,10000);
$plotx = -1.4;
$ploty = $max/2;
pgsch(1.6);
pgtext($plotx,$ploty,"Median Peak: $peakcolor");
pgsch(1.2);    # Set character height
pgsci(1);
pglabel("B-V Color","Number","B-V Color Histogram,$ARGV[0]");
#pgsci(10);
#$nbin=45;
#pgmove(-1.5,0);
#pgbin($nbin,\@binBV_color,\@binBV,0);
pgsci(1);

#pghist($#V,\@V,12,25,13,0);
#pglabel("Number","V Magnitude","V Number Counts,$ARGV[0]");
#pgsci(3);
#pgmove($maglo,0); pgdraw($maglo,100000);
#pgmove($maghi,0);
#pgdraw($maghi,100000);
#$midmag = ($maglo+$maghi)/2.0;
#pgptext($midmag,5000,0,0.5,"Mag Limits");
#pgsci(1);

pgenv(-1.5,3.0,24,12,0,0);

```

```

pglabel("B-V Color","V Magnitude","B-V,V Color Magnitude Diagram");
pgpoint($#V,\@BV,\@V,-1);
pgsci(4);
pgmove($peakcolor,0);
pgdraw($peakcolor,10000);
pgtext(-0.8,13,"Blue Ridgeline");
pgsci(3);
pgmove(-1.5,$maglo);
pgdraw(3,$maglo);
pgmove(-1.5,$maghi);
pgdraw(3,$maghi);
$midmag = ($maglo+$maghi)/2.0;
pgtext(2.2,$midmag,"Mag Limits");
pgsci(1);

pgenv(12,24,0,5.5,0,0);
pglabel("V Magnitude","log10 N","Completeness Estimate,Integrated Counts");

pgsci(5);
pgmove(12,$cumV[1200]);
for ($i = 1201; $i < 2400; $i++) {
    $mmag = $i/100;
    pgdraw($mmag,$cumV[$i]);
}
pgsci(3);
pgmove($maglo,0);
pgdraw($maglo,100000);
pgmove($maghi,0);
pgdraw($maghi,100000);
$midmag = ($maglo+$maghi)/2.0;
pgptext($midmag,1.0,0,0.5,"Mag Limits");
pgsci(1);

pgsci(6);
$y = $a*12 + $b;
pgmove(12,$y);
for ($i = 12; $i < 25; $i++) {
    $y = $b*$i + $a;
    pgdraw($i,$y);
}
pgsci(7);
pgmove($complimit,0);
pgdraw($complimit,7);
$textspot = $complimit+1;
pgsch(1.6);
pgtext($textspot,3,"Completeness");
pgtext($textspot,2.7,"Limit");
pgsci(6);
pgtext($textspot,2.4,"$complimit");
pgsch(1.2);
pgsci(8);
$textspot = $protocurve[0]+$totoffset;
pgmove($protomag[0],$textspot);
for ($i = 0; $i <= $#protomag; $i++) {
    $protocurve[$i] += $totoffset;
    #printf "$protomag[$i]/$protocurve[$i]\n";
}

```



```

    pgdraw($protomag[$i],$protocurve[$i]);
}
pgsch(1.6);
$textspot = $complimit+1;
pgtext($textspot,2.1,"$scurcomplimit");
pgsch(1.2);
pgsci(1);

#Last plot-----

pgenv(12,24,0,4.5,0,0);
pglabel("V Magnitude","log10 dN/dm","Completeness Estimate, Differential Counts");

pgsci(5);
pgmove(12.1,$diffV[121]);
for ($i = 121; $i < 240; $i++) {
    $mmag = $i/10;
    pgdraw($mmag,$diffV[$i]);
}
pgsci(3);
pgmove($maglo,0);
pgdraw($maglo,100000);
pgmove($maghi,0);
pgdraw($maghi,100000);
$midmag = ($maglo+$maghi)/2.0;
pgptext($midmag,1.0,0,0.5,"Mag Limits");
pgsci(1);

pgend;
}

printf "\n\n";
printf "$ARGV[0]\n";
printf "Peak Color $peakcolor $ARGV[0]\n";
printf "V = 16-19\n";
$output = `./plinking.pl $ARGV[0] 16 19 -2 $peakcolor 0.01 0.01`;
printf "$output";
printf "V = 16-17\n";
$output = `./plinking.pl $ARGV[0] 16 17 -2 $peakcolor 0.01 0.01`;
printf "$output";
printf "V = 17-18\n";
$output = `./plinking.pl $ARGV[0] 17 18 -2 $peakcolor 0.01 0.01`;
printf "$output";
printf "V = 18-19\n";
$output = `./plinking.pl $ARGV[0] 18 19 -2 $peakcolor 0.01 0.01`;
printf "$output";

```

**countem.pl**

This program is used to count the number of stars located between two magnitudes and two B-V color values (both specified in the arguments) as well as the positive/negative error values. The star counts are used to develop the ratios.

```
#!/usr/bin/perl

if ($#ARGV != 4) {
    printf "wrong # of Args";
    exit(1);
}

$infile = $ARGV[0];
$maglo = $ARGV[1];
$maghi = $ARGV[2];
$collo = $ARGV[3];
$colhi = $ARGV[4];
$numstars = 0;

if($e[10] > $maglo++$e[10] < $maghi){
    if($e[14] > $collo++$e[14] < $colhi){
        $numstars = $numstars + 1;
    }
}
```

**photometricparallax.pl**

This program creates an image that is a top-down view of the Galactic plane from an overhead perspective (up the z-axis). The star shown in the image represent a slice of the galaxy between two z-axis positions (specified in the arguments) above or below the Galactic plane.

```
#!/usr/bin/perl

$z1 = $ARGV[1];
$z2 = $ARGV[2];
$maxstar = $ARGV[3];
$maglim = 19.5;

# Open the catalog file

# if ($#ARGV != 4) {
#   printf "wrong # of Args";
#   exit(1);
# }

use Astro::Coord;
use Astro::Time;
$infile = $ARGV[0];
$PI = 3.14159265;
$deg2rad = $PI / 180.;

@image = ();
for($i = 0; $i < 320000; $i++){
    $image[$i] = 0;
}

#$maglo = $ARGV[1];
#$maghi = $ARGV[2];
#$collo = $ARGV[3];
#$colhi = $ARGV[4];
$numstars = 0;

open IF, $infile;

# Initialize one array for each quantity we read in

@object_name=();
@ra=();
@dec=();
@err_ra=();
@err_dec=();
@stargal_class=();
@stargal_ntest=();
@vmag=();
@err_vmag=();
@ubcol=();
@err_ubcol=();
@bvc=();
@err_bvc=();
@vrc=();
```

```

@err_vrcol=();
@sg_classification=();
@d = ();
@x = ();
@y = ();
@z = ();

$n_objects = 0;

# Read the catalog in one line at a time

while ($line = <IF>) {

    # Use spaces on the line to split up the line into an array containing the
    # data we want to use.

    @e = split(/\s+/, $line);

    # Assign the split up line elements to our data array, one object at
    # a time. There are $n_objects in the catalog so after we assign all
    # of the elements taken from a given line, we now have one more object
    # in the catalog so $n_objects goes up by one.

    $object_name[$n_objects]=$e[0];
    $ra[$n_objects]=$e[1];
    $dec[$n_objects]=$e[2];
    $err_ra[$n_objects]=$e[3];
    $err_dec[$n_objects]=$e[4];
    $stargal_class[$n_objects]=$e[5];
    $stargal_ntest[$n_objects]=$e[6];
    $vmag[$n_objects]=$e[7];
    $err_vmag[$n_objects]=$e[8];
    $subcol[$n_objects]=$e[9];
    $err_ubcol[$n_objects]=$e[10];
    $bvcol[$n_objects]=$e[11];
    $err_bvcol[$n_objects]=$e[12];
    $vrcol[$n_objects]=$e[13];
    $err_vrcol[$n_objects]=$e[14];
    $source_amplifier[$n_objects]=$e[15];
    $dturn = $e[2]/360;
    $rturn = $e[1]/360;

    ($JRA, $JDec) = fk4fk5($rturn, $dturn);
    ($l, $b) = fk4gal($JRA, $JDec);
    $l = $l * 360;
    $b = $b * 360;

    $absmag = $e[11]*6 + 1;

    $d[$n_objects] = 10**((5 + $e[7] - $absmag)/5);
    # $x[$n_objects] = $d[$n_objects] * cos($e[1]*$deg2rad) * cos($e[2]*$deg2rad);
    # $y[$n_objects] = $d[$n_objects] * sin($e[1]*$deg2rad) * cos($e[2]*$deg2rad);
    # $z[$n_objects] = $d[$n_objects] * sin($e[2]*$deg2rad);
    $x[$n_objects] = $d[$n_objects] * cos($l*$deg2rad) * cos($b*$deg2rad);
    $y[$n_objects] = $d[$n_objects] * sin($l*$deg2rad) * cos($b*$deg2rad);

```

```

$z[$n_objects] = $d[$n_objects] * sin($b*$deg2rad);

# print" $e[7] $absmag $d[$n_objects] $x[$n_objects], $y[$n_objects], $z[$n_objects] $l $b\n";

#$n_objects++;

# If I wanted only stars (who have sg_classification of close to 0.00), use
# the following block instead of $n_objects++; (comment it out with a #)

if ($e[5] < 0.3 && $z[$n_objects] > $z1 && $z[$n_objects] < $z2) {
    $ix = $x[$n_objects]/25.0;
    $ix = sprintf("%d",$ix);
    $iy = (10000 - $y[$n_objects])/25.0;
    $iy = sprintf("%d",$iy);
    if ($ix > -1 && $ix < 399 && $iy > -1 && $iy < 799 && $e[7] < $maglim) {
        $image[800 * $ix + $iy] += 1;
    }
    # $n_objects++;
}

#if($e[7] > $maglo && $e[7] < $maghi){
#   if($e[11] > $collo && $e[11] < $colhi){
#       $numstars = $numstars + 1;
#   }
#}

}

# exit 0;

# Now make a plot. Need the following few lines no matter what...

use PGPLOT; # Load PGPLOT module

# "?" will prompt for device

$dev = "?" unless defined $dev;

pgbegin(0,$dev,1,1); # Open plot device , 1 plot in x, 1 plot in y

pgscf(2);          # Set character font
pgslw(2);          # Set line width

pgwnad(0,799,0,399);
@rl = (-0.50,0.00,0.10,0.30,0.50,0.70,0.90,1.00,1.70);
@rr = ( 0.0, 0.0, 0.0, 0.0, 0.0, 1.0, 1.0, 1.0, 1.0);
@rg = ( 0.0, 0.0, 0.0, 0.3, 1.0, 1.0, 0.6, 0.0, 1.0);
@rb = ( 0.0, 0.3, 0.8, 0.8, 1.0, 0.0, 0.0, 0.0, 1.0);
pgctab(\@rl,\@rr,\@rg,\@rb,9,1.0,0.5);
pgimag(\@image,800,400,1,799,1,399,1,$maxstar,[0,1,0,0,1]);
pgwedg("RI",1,3.5,1,$maxstar,'Stars per 312500 cubic parsecs');
pgswin(+10000,-10000,0,10000);
pgsch(1.0);

```

```
pglabel("Y (pc)", "X (pc)", "Star Density between $z_1$ and $z_2$ parsecs above the plane.");
pgbox("BCNTS",0,0,"BCNTS",0,0);
pgsch(1.0);
```

```
pgsch(1.0);
pgsci(5);
pgtext(8000,0400,"Quadrant 1");
pgtext(-5300,0400,"Quadrant 4");
pgsci(7);
pgsch(1.6);
pgpoint(1,0,8500,2);
pgpoint(1,0,0,9);
pgsch(1.0);
pgtext(1800,9000,"Galactic Center");
pgtext(1200,200,"Sun");
pgsch(1.0);
```

```
pgend; # Close plot
```

**scan.pl**

This program uses the companion program `photometricparallax.pl` to create a series of images overhead-view images. Each represents a 100 parsec-thick slice of stars, with the slice running parallel to the Galactic plane.

```
#!/usr/bin/perl

$maxstar = 20;
for( $z1 = 100; $z1 < 5000; $z1 = $z1 + 100){
    $z2 = $z1 + 100;
    open IF, ">ans";
    $realname = sprintf("%04d",$z1);
    print IF "$realname.gif/gif\n\n";
    close IF;
    print "at $z1 parsecs\n";
    `./photometricparallax.pl bigcat $z1 $z2 $maxstar < ans`;
}
```

## Index of Tables and Figures

- Figure 1:** Image of the Andromeda Galaxy  
Courtesy of NASA
- Figure 2:** Herschel's "grindstone model" of the Galaxy  
Astronomy Department, Ohio State University. <[http://www.astronomy.ohio-state.edu/~pogge/Ast162/Unit4/Images/Herschel\\_MW\\_1785.jpg](http://www.astronomy.ohio-state.edu/~pogge/Ast162/Unit4/Images/Herschel_MW_1785.jpg)>. Accessed 18 Jan. 2008.
- Figure 3:** Model of the Milky Way and surrounding structures  
Project Image
- Figure 4:** Hertzsprung-Russel Diagram of the Hipparcos Catalog Data  
ESA, 1997, The Hipparcos and Tycho Catalogues, ESA SP-1200.
- Figure 5:** Extinction Map develop by Schlege, Finkbeiner, and Davis.  
Schlegel, David J., Douglas P. Finkbeiner, and Marc Davis. "Maps of Dust Infrared Emission for Use in Estimation of Reddening and Cosmic Microwave Background Radiation Foregrounds." *Astrophysical Journal*, vol. 500, pp. 525.
- Figure 6:** Color magnitude diagrams in the B-V band  
Project Data
- Figure 7:** Volume calculation for the galactic model  
Larsen, Jeffrey Arthur. *The Shape of the Galaxy*. University of Minnesota, August 1996, 78.
- Figure 8:** Luminosity function used in the galactic model  
Ibid., 83.
- Figure 9:** Color Magnitude Relations used in the galactic model  
Ibid., 83.
- Figure 10:** Galactic coordinate scheme  
Project Image
- Figure 11:** Mathematical conversion between solar and galactic relative coordinates  
Larsen, *Shape*, 80.
- Table 1:** Structural parameters to be optimized by the genetic algorithm  
Larsen, *Shape*, 141.



- Figure 12:** Map of the 120 POSS I fields  
Humphreys, Roberta M., Juan Cabanela, and Jeffery A. Larsen. "Support for a Meeting on 'The Fate of the Most Massive Stars.'" National Science Foundation, 23-28 Mar. 2004, pp. 3.
- Figure 13:** Map of stellar excess against galactic ( $l$ ,  $b$ ) coordinates  
Ibid., pp. 4.
- Table 2:** Adopted and Derived Parameter Values from the galactic model  
Ibid., pp. 4.
- Figure 14:** 90-inch telescope at Kitt Peak, AZ  
Project Data
- Figure 15:** 1.0-m SMARTS Consortium telescope near La Serena, Chile  
Project Data
- Figure 16:** 1.0-m SMARTS Consortium telescope near La Serena, Chile  
Project Data
- Figure 17:** Inside the 1.0-m telescope at near La Serena, Chile  
Project Data
- Figure 18:** Raw CCD image  
Project Data
- Figure 19:** Example of Cross-Talk in a CCD image  
Project Data
- Figure 20:** Trimmed CCD image  
Project Data
- Figure 21:** Zero-Bias image  
Project Data
- Figure 22:** Flat Field  
Project Data
- Figure 23:** A final, calibrated CCD image  
Project Data
- Figure 24:** Stellar Magnitude versus Airmass  
Project Data
- Figure 25:** True Color versus Instrumental Color  
Project Data

- Table 3:** Extinction Coefficients from Kitt Peak, AZ (September 2007)  
Project Data
- Table 4:** Color Terms from Kitt Peak, AZ (September 2007)  
Project Data
- Table 5:** Extinction Coefficients from Kitt Peak, AZ (May 2008)  
Project Data
- Table 6:** Color Terms from Kitt Peak, AZ (May 2008)  
Project Data
- Table 7:** Extinction Coefficients from La Serena, Chile (October 2008)  
Project Data
- Table 8:** Color Terms from La Serena, Chile (October 2008)  
Project Data
- Figure 26:** Diagram of the Full Width at Half Maximum  
Project Image
- Figure 27:** CCD image of a galaxy  
Project Data
- Figure 28:** CCD image of a star  
Project Data
- Figure 29:** Star-Galaxy Test: Maximum Surface Brightness versus Area  
Project Data
- Figure 30:** Star-Galaxy Test: Isophotal Magnitude versus Aperture Magnitude  
Project Data
- Figure 31:** Star-Galaxy Test: XY Image Moment versus Peak Surface Brightness  
Project Data
- Figure 32:** SExtractor Identification of objects in the image  
Project Data
- Table 9:** Sample Stellar Catalog Data of E20N20  
Project Data
- Table 10:** Summary of Observed Quadrant 1 Fields in this project  
Project Data

- Table 11:** Summary of Observed Quadrant 4 Fields in this project  
Project Data
- Figure 33:** Aitoff projection of the stellar fields used for ratio study  
Project Data
- Figure 34:** Color bin analysis of E20N20  
Project Data
- Figure 35:** Color-Magnitude Diagram of E20N20 with cuts for magnitude and color  
Project Data
- Table 12:** Observed Ratios  
Project Data
- Figure 36:** Overhead view of stars in the observed fields; image developed by photometricparallax.pl.  
Project Data
- Figure 37:** X-Y scatter plot showing the objects in the fields of observation  
Project Data
- Figure 38:** Y-Z scatter plot showing the objects in the fields of observation  
Project Data
- Figure 39:** Histogram difference between E25N40 and W25N40  
Project Data
- Figure 40:** Histogram difference between E75N20 and W75N20  
Project Data
- Figure 41:** Fitness plot of the genetic algorithm  
Project Data
- Table 13:** Summary of the results of the genetic algorithm  
Project Data
- Figure 42:** Evolution of different parameters for the genetic algorithm  
Project Data
- Figure 43:** Model of predicted versus observed stars in E25N40 by color and magnitude  
Project Data
- Figure 44:** Model of predicted versus observed stars in W25N40 by color and magnitude  
Project Data

- Figure 45:** Component by component model prediction of E25N40 for  $15 < V < 15.5$   
Project Data
- Figure 46:** Component by component model prediction of E25N40 for  $16 < V < 16.5$   
Project Data
- Figure 47:** Component by component model prediction of E25N40 for  $17 < V < 17.5$   
Project Data
- Figure 48:** Component by component model prediction of E25N40 for  $18 < V < 18.5$   
Project Data
- Figure 49:** Aitoff projection showing ratio of observed data to data predicted by the  
genetic algorithm  
Project Data
- Figure 50:** Proper motions of stars in E75N20  
USNO B1.0 catalog
- Figure 51:** Color-magnitude scatter plot of E25N40  
Project Data
- Figure 52:** Color-magnitude scatter plot of W25N40  
Project Data
- Figure 53:** Color-magnitude histogram for E25N40  
Project Data
- Figure 54:** Color-magnitude histogram for W25N40  
Project Data
- Figure 55:** Histogram difference for E25N40 – W25N40  
Project Data
- Figure 56:** Image of globular cluster M2  
“Stars: The Hertzsprung-Russell Diagrams of Star Clusters,” *The Astrophysics Spectator*, <[www.astrophysicsspectator.com](http://www.astrophysicsspectator.com)> (accessed 20 April 2009).
- Figure 57:** Color-magnitude diagram of M67  
Ibid.
- Figure 58:** Color-magnitude diagram of 47 Tuc  
Ibid.

- Figure 59:** Isochrone model of stellar turnoff points  
Yi, Demarque, Kim, Lee, Ree, Lejeune, & Barnes 2001, ApJS, 136, 417
- Figure 60:** Aitoff projection of all fields observed in this project  
Project Data
- Figure 61:** Evolution of population fitness by a genetic algorithm  
Larsen, *Shape*, 138.

## Bibliography

- Belokurov, V., *et al.* “The Hercules-Aquila Cloud.” *The Astrophysical Journal*, vol. 657 (10 March 2007): pp. L89-L92.
- Bessell, M. S. “UBVRI passbands.” *Astronomical Society of the Pacific*, Publications (ISSN 0004-6280), vol. 102, Oct. 1990, p. 1181-1199.
- Cabanela, J.E., Jeffrey Larsen, and Roberta M. Humphreys. “Mapping the Asymmetric Thick Disk: A Search for Triaxiality.” Moorhead, MN: Minnesota State University, 2007.
- Carroll, Bradley W. and Dale A. Ostlie. *An Introduction to Modern Astrophysics*, Second Edition. San Francisco: Addison-Wesley, 2007.
- The Dorling Kindersley Science Encyclopedia*. London: Dorling Kindersley, 1997.
- ESA, 1997, The Hipparcos and Tycho Catalogues, ESA SP-1200.
- Gilmore, G., and N. Reid. “New light on faint stars. III – Galactic structure towards the South Pole and the Galactic thick disc.” *Royal Astronomical Society*, Monthly Notices, vol. 202, Mar. 1983, p. 1025-1047.
- Hardie, Robert H. “Photoelectric Reductions.” *Astronomical Techniques*. Edited by William A Hiltner. Chicago: Chicago Press, January 1964.
- Henbest, Nigel and Heather Couper. *The Guide to the Galaxy*. Cambridge: Cambridge University Press, 1994.
- Hester, Jeff, George Blumenthal, Bradford Smith, David Burstein, Ronald Greeley, and Howard G. Voss. *21<sup>st</sup> Century Astronomy*, Second Edition. New York: W. W. Norton & Company, 2007.
- Howell, Steve B. *Handbook of CCD Astronomy*. Cambridge: Cambridge University Press, 2000.
- Humphreys, Roberta M., Juan Cabanela, and Jeffery A. Larsen. “Support for a Meeting on ‘The Fate of the Most Massive Stars.’” National Science Foundation, 23-28 Mar. 2004.
- Ibata, R. A., G. Gilmore, and M. J. Irwin. “A Dwarf Satellite Galaxy in Sagittarius.” *Nature*, vol. 370, no. 6486/Jul 21, 1994, p. 194.

- Jurić, Mario; Ivezić, Željko; Brooks, Alyson; Lupton, Robert H.; Schlegel, David; Finkbeiner, Douglas; Padmanabhan, Nikhil; Bond, Nicholas; Sesar, Branimir; Rockosi, Constance M.; Knapp, Gillian R.; Gunn, James E.; Sumi, Takahiro; Schneider, Donald P.; Barentine, J. C.; Brewington, Howard J.; Brinkmann, J.; Fukugita, Masataka; Harvanek, Michael; Kleinman, S. J.; Krzesinski, Jurek; Long, Dan; Neilsen, Eric H., Jr.; Nitta, Atsuko; Snedden, Stephanie A.; York, Donald G.. "The Milky Way Tomography with SDSS. I. Stellar Density Distribution." *The Astrophysical Journal*, Volume 673, Issue 2. The American Astronomical Society, February 2008, pp 864-914.
- Larsen, Jeffrey Arthur. *The Shape of the Galaxy*. University of Minnesota: August 1996.
- Larsen, Jeffrey A. and Roberta M. Humphreys. "Fitting a Galactic Model to an All-Sky Survey." *The Astronomical Journal*, vol. 125 (April 2003): pp. 1346-1361.
- Martinez, Patrick and Alain Klotz. *A Practical Guide to CCD Astronomy*. Trans. by André Demers. Cambridge: Cambridge University Press, 1998.
- Michalewicz, Zbigniew. *Genetic Algorithms + Data Structures = Evolution Programs*. Second, Extended Edition. New York: Springer-Verlag, 1992.
- Mihalas, Dimitri and James Binney. *Galactic Astronomy: Structure and Kinematics*. 2<sup>nd</sup> ed. New York: W. H. Freeman and Company, 1981.
- Oort, J. H. "Some Problems Concerning the Structure and Dynamics of the Galactic System and the Elliptical Nebulae NGC 3115 and 4494." *Astrophysical Journal*, vol. 191, p. 273.
- Parker, Jennifer E., Roberta M. Humphreys, and Jeffrey A. Larsen. "The Asymmetric Thick Disk: A Star-Count and Kinematic Analysis. I. The Star Counts." *The Astronomical Journal*, vol. 126 (September 2003): pp. 1346-1361.
- Parker, Jennifer E., Roberta M. Humphreys, and Timothy C. Beers. "The Asymmetric Thick Disk: A Star-Count and Kinematic Analysis. II. The Kinematics." *The Astronomical Journal*, vol. 127 (March 2004): pp. 1567-1578.
- Quinn, P. J., and Jeremy Goodman. "Sinking satellites of spiral systems." *Astrophysical Journal*, Part 1, vol. 309, Oct. 15, 1986, p. 472-495.
- Schlegel, David J., Douglas P. Finkbeiner, and Marc Davis. "Maps of Dust Infrared Emission for Use in Estimation of Reddening and Cosmic Microwave Background Radiation Foregrounds." *Astrophysical Journal*, vol. 500, p. 525.
- Sellwood, J. A. "Bars and Dark Matter Halo Cores." *The Astrophysical Journal*, vol. 587, issue 2, pp. 638-648.

“Stars: The Hertzsprung-Russell Diagrams of Star Clusters.” *The Astrophysics Spectator*. <[www.astrophysicsspectator.com](http://www.astrophysicsspectator.com)>. Accessed 20 April 2009.

Than, Ker. “The New Tourists Guide to the Milky Way.” Space.com. 27 Feb. 2006. <[http://www.space.com/scienceastronomy/060227\\_mm\\_milky\\_way\\_tour.html](http://www.space.com/scienceastronomy/060227_mm_milky_way_tour.html)>. Accessed 18 Dec. 2007.

Tucker, Andrew R., MIDN, USN. “Exploration of Asymmetric Galactic Stellar Populations Using Star Counts, Galactic Models, and Genetic Algorithms.” United States Naval Academy, Fall 2007.

Weinberg, Martin D. “Kinematic signature of a rotating bar near a resonance.” *The Astrophysical Journal*, Part 1 (ISSN 0004-637X), vol. 420, no. 2, p. 597-611.

Yi, Sukyoung, Pierre Demarque, Yong-Cheol Kim, Young-Wook Lee, Chang H. Ree, Thibault Lejeune, and Sydney Barnes. “Toward Better Age Estimates for Stellar Populations: The  $Y^2$  Isochrones for Solar Mixture.” *The Astrophysical Journal Supplement Series*, Volume 136, Issue 2, pp. 417-437.